

PERIODIC DENSITY FUNCTIONAL STUDY ON SUPPORTED VANADIUM OXIDES

Dissertation

zur Erlangung des akademischen Grades

doctor rerum naturalium
(Dr. rer. nat.)

im Fach Chemie

eingereicht an der

Mathematisch-Naturwissenschaftlichen Fakultät I
der Humboldt-Universität zu Berlin

von

Frau Magister Tanya Kumanova Todorova
geboren am 29.01.1980 in Byala Slatina, Bulgarien

Präsident der Humboldt-Universität zu Berlin
Prof. Dr. Christoph Marksches

Dekan der Mathematisch-Naturwissenschaftlichen Fakultät I
Prof. Dr. Christian Limberg

Gutachter: 1. Prof. Dr. Joachim Sauer
 2. Prof. Dr. Hans-Joachim Freund
 3. PD. Dr. Karsten Reuter

Tag der mündlichen Prüfung: 25. September 2007

Abstract

Supported vanadium oxide catalysts are of high interest because of their potential in a wide variety of oxidation reactions. A key step to fully understand the catalytic mechanism is a profound knowledge of the microscopic structure of the vanadium oxide under various conditions and the way it is anchored to the surface of the support material. The latter is of importance in order to better understand vanadium oxide-support effects. Therefore, experimental and theoretical studies on well-defined model catalyst systems, which allow investigations at the atomic level while grasping essential aspects of the complexity of real systems, have been invoked.

In the present work, the vanadia/alumina and vanadia/silica systems are investigated using density functional theory (DFT). As for $\text{VO}_x/\text{Al}_2\text{O}_3$, low-coverage vanadia species as well as films of varying thickness on the stable $\alpha\text{-Al}_2\text{O}_3(0001)$ and the metastable $\kappa\text{-Al}_2\text{O}_3(001)$ surface are studied. Statistical thermodynamics is applied to account for the effect of oxygen partial pressure and vanadium activity at a given temperature on the stability of the supported vanadia aggregates. The role of the oxide support on the molecular and electronic structure and reducibility of the stable vanadia species is examined. The efforts have focused on finding correlations between structural properties and catalytic activity in reactions proceeding via the Mars-van Krevelen mechanism. In accord therewith, the formation energy of a lattice oxygen defect is used as an indicator of catalytic performance. The influence of the support structure on the interface vibrational modes is analyzed in an attempt to shed light on the origin of a characteristic band at $\sim 950\text{ cm}^{-1}$, observed in the experimental spectra of vanadia/alumina catalysts.

As for VO_x/SiO_2 , first, the atomic structure of the model silica support, i.e., ultrathin SiO_2 film grown on $\text{Mo}(112)$ is resolved. It consists of a monolayer of two-dimensional (2D) network of corner-sharing $[\text{SiO}_4]$ tetrahedra and is a new form of silica with a $\text{SiO}_{2.5}$ stoichiometry that does not naturally occur in bulk silica. The crucial role of combining theoretical and experimental studies for the determination of its atomic structure as well as that of the one-dimensional (1D) stripes, found to coexist with the film in perfect registry, is highlighted. A 2D diagram showing the stability of various 1D and 2D crystalline silica phases depending on the silicon coverage and oxygen pressure is derived. The formation of a new, "O-rich" phase of the $\text{SiO}_2/\text{Mo}(112)$ film is predicted, whose existence is subsequently experimentally confirmed. Finally, different VO_x species on the thin-film silica support are investigated in order to provide an understanding on the structure, stability, and vibrational spectra of the silica-supported vanadium oxides and to relate characteristic vibrational features of the experimental model catalysts to their structural features.

Keywords:

density functional theory, supported vanadium oxides, alumina, thin silica film

Zusammenfassung

Geträgerte Vanadiumoxidkatalysatoren sind wegen ihrer Vielseitigkeit bei Oxidationsreaktionen von großem Interesse. Der Schlüssel zum Verständnis der zugrunde liegenden Mechanismen ist ein tiefgreifender Einblick in die mikroskopische Struktur der Vanadiumoxide unter verschiedenen Bedingungen sowie die Art der Bindung an die Oberfläche des Trägers. Dieses ist wichtig um den Vanadiumoxid-Trägereffekt besser zu verstehen. Daher wurden experimentelle und theoretische Arbeiten an wohldefinierten Modellkatalysatoren, die Untersuchungen auf atomarem Niveau ermöglichen und trotzdem wesentliche Aspekte der Komplexität realer Katalysatoren wiedergeben, kombiniert.

In der vorliegenden Arbeit werden die Systeme Vanadiumoxid/Aluminiumoxid und Vanadiumoxid/Siliziumoxid mittels Dichtefunktionaltheorie (DFT) untersucht. Für $\text{VO}_x/\text{Al}_2\text{O}_3$ werden sowohl Vanadiumoxidspezies bei niedriger Bedeckung als auch Filme verschiedener Dicken auf der stabilen $\alpha\text{-Al}_2\text{O}_3(0001)$ -Oberfläche und der metastabilen $\kappa\text{-Al}_2\text{O}_3(001)$ Oberfläche untersucht. Der Einfluß des Sauerstoffpartialdrucks und der Aktivität von Vanadium auf die Stabilität der geträgerten Aggregate bei einer gegebenen Temperatur wird mittels statistischer Thermodynamik behandelt. Der Einfluß des oxidischen Trägers auf die atomare und elektronische Struktur und die Reduzierbarkeit der stabilen Vanadiumoxide werden untersucht. Hierbei steht die Entwicklung einer Korrelation zwischen Struktureigenschaften und katalytischer Aktivität einer Reaktion, die nach dem Mars-van Krevelen-Mechanismus abläuft, im Vordergrund. Im Einklang mit diesem Mechanismus wird die Energie für die Bildung eines Sauerstoffdefekts als Indikator für die Leistungsfähigkeit des Katalysators benutzt. Der Einfluß der Trägerstruktur auf die Schwingungsmoden des Grenzflächenbereiches wird analysiert, um Hinweise auf den Ursprung einer charakteristischen Bande, die in experimentellen Spektren von $\text{VO}_x/\text{Al}_2\text{O}_3$ Katalysatoren bei $\sim 950\text{ cm}^{-1}$ beobachtet wird, zu erhalten.

Für VO_x/SiO_2 wird zunächst die atomare Struktur des SiO_2 -Modellträgers, d. H. eines ultradünnen SiO_2 Films auf $\text{Mo}(112)$ aufgeklärt. Sie besteht aus einer Monolage eines zweidimensionalen (2D) Netzwerks aus eckenverknüpften $[\text{SiO}_4]$ -Tetraedern und stellt eine neue Form von Siliziumoxid mit der Stöchiometrie $\text{SiO}_{2.5}$, die normalerweise nicht in Siliziumoxidphasen vorkommt, dar. Die entscheidende Rolle des Zusammenwirkens von Experiment und Theorie bei der Aufklärung der atomaren Struktur des Films und von eindimensionalen (1D) Streifen, die mit dem Film koexistieren, wird hervorgehoben. Ein 2D-Phasendiagramm, das die Stabilität verschiedener kristalliner 1D und 2D SiO_2 -Strukturen in Abhängigkeit von Siliziumbedeckung und Sauerstoffdruck zeigt, wird erstellt. Es wird die Bildung einer neuen, "sauerstoffreichen" Phase des $\text{SiO}_2/\text{Mo}(112)$ Films vorhergesagt, deren Existenz anschließend experimentell gezeigt wird. Schließlich werden verschiedene VO_x -Spezies auf dem dünnen Träger untersucht, um die Struktur, Stabilität und Schwingungsspektren

von siliziumoxidgeträgerten Vanadiumoxiden zu verstehen und um charakteristische Eigenschaften der Schwingungen mit strukturellen Eigenschaften experimenteller Modelkatalysatoren zu verknüpfen.

Schlagwörter:

Dichtefunktionaltheorie, geträgerte Vanadiumoxide, Aluminiumoxid, dünner Siliziumoxid-Film

Contents

1	Introduction	1
2	Theoretical Background	5
2.1	Density Functional Theory	5
2.2	Supercell Approach and Plane-Wave Basis Set	7
2.3	The PAW Method	8
2.4	Brillouin Zone Sampling	10
3	Alumina-Supported Vanadium Oxides	13
3.1	Vanadium Oxides Supported on α -Al ₂ O ₃ (0001)	14
3.1.1	Bulk and (0001) Surface of α -Al ₂ O ₃	14
3.1.2	Vanadia Aggregates Supported on α -Al ₂ O ₃ (0001)	17
3.1.3	Thermodynamic Stability	23
3.1.4	Reducibility of Vanadia Aggregates on α -Al ₂ O ₃	27
3.1.5	V 2 <i>p</i> Surface Core-Level Shifts	32
3.1.6	Summary	35
3.2	Vanadium Oxides Supported on κ -Al ₂ O ₃ (001)	36
3.2.1	Bulk and (001) Surface of κ -Al ₂ O ₃	36
3.2.2	Vanadia Aggregates Supported on κ -Al ₂ O ₃ (001)	39
3.2.3	Reducibility of Vanadia Aggregates on κ -Al ₂ O ₃	44
3.2.4	Thermodynamic Stability	50
3.2.5	Vibrational Analysis	53
3.2.6	Summary	56
4	Thin SiO₂ Film on Mo(112) Substrate	59
4.1	Experimental Findings on the Thin Silica Film	60
4.2	Structure Models	61
4.2.1	Mo(112) Substrate	61
4.2.2	Previously Proposed Models	62
4.2.3	2 ML Silica Films	62
4.2.4	1 ML Silica Films	63
4.3	Thermodynamic Stability	65
4.4	Electronic and Vibrational Properties	66

4.4.1	Vibrational Analysis	67
4.4.2	Core-Level Shifts	75
4.4.3	STM	76
4.5	Antiphase Domain Boundaries	76
4.6	Summary	78
5	1D Silica Stripes on Mo(112) Substrate	79
5.1	Experimental Findings on the Silica Stripes	79
5.2	Structure Models	80
5.3	Thermodynamic Stability	82
5.4	Electronic and Vibrational Properties	82
5.5	Summary	85
6	Oxygen-Rich Silica Film on Mo(112)	87
6.1	Thermodynamic Stability	87
6.2	New Phase of the Silica Film	89
6.3	Summary	91
7	Oxygen Adsorption on Mo(112)	93
7.1	Genetic Algorithm Method	94
7.2	Models	95
7.2.1	$p(1 \times 2)$ -Mo(112)/ n O	96
7.2.2	$p(1 \times 3)$ -Mo(112)/ n O	97
7.3	Thermodynamic Stability	97
7.4	Properties	101
7.4.1	STM	102
7.4.2	Vibrational Frequencies	102
7.5	Summary	103
8	Vanadium Oxides on a Thin Silica Film	105
8.1	Models	106
8.1.1	Vanadium Oxides Modeled by Replacement	106
8.1.2	Vanadium Oxides Modeled by Adsorption	106
8.2	Thermodynamic Stability	111
8.3	Vibrational Analysis	113
8.4	Summary	116
9	Summary	117
	Bibliography	119

List of Figures

2.1	All-electron wavefunction in the PAW method	10
3.1	Bulk structure of α -Al ₂ O ₃	15
3.2	α -Al ₂ O ₃ (0001) surface before and after relaxation	17
3.3	Surface terminations of 6V-layer film on α -Al ₂ O ₃ (0001)	19
3.4	(2 × 2) and ($\sqrt{3} \times \sqrt{3}$)R30° vanadyl-covered surfaces	20
3.5	Low-coverage VO _x species modeled by replacement	21
3.6	Low-coverage VO _x species modeled by adsorption	22
3.7	Phase diagram for vanadium oxides on α -Al ₂ O ₃ (0001)	25
3.8	Reduction energy as a function of defect concentration	29
3.9	Reduction energy as a function of vanadia film thickness	30
3.10	Structure and electronic effects induced upon reduction	31
3.11	DOS of 1V- and 3V-layer supported films	34
3.12	Bulk structure of κ -Al ₂ O ₃	36
3.13	κ -Al ₂ O ₃ (001) surface before and after relaxation	37
3.14	Low-coverage VO _x species on κ -Al ₂ O ₃ (001)	40
3.15	V ₂ O ₅ clusters adsorbed on the κ -Al ₂ O ₃ (001) surface	41
3.16	V ₂ O ₄ clusters on the κ -Al ₂ O ₃ (001) surface	42
3.17	Vanadia films supported on κ -Al ₂ O ₃ (001)	43
3.18	Reduction of low-coverage vanadia species	45
3.19	Phase diagram for vanadium oxides on κ -Al ₂ O ₃ (001)	51
3.20	Vibrational frequencies of vanadia on κ -Al ₂ O ₃	54
3.21	Vibrational frequencies of alumina-supported vanadium oxides	55
4.1	Previously proposed models of the SiO ₂ /Mo(112) film	62
4.2	2 ML SiO ₂ /Mo(112) film models	63
4.3	1 ML SiO ₂ /Mo(112) film models	64
4.4	Stability plot for the SiO ₂ /Mo(112) film models	67
4.5	Vibrational normal modes of 1 ML model A	69
4.6	Simulated IRAS and STM of the cluster model	70
4.7	Asymmetric Si–O–Si vibrational modes	71
4.8	Symmetric Si–O–Si vibrational modes	72
4.9	Si–O–Mo vibrational modes	73
4.10	Experimental and simulated STM of the SiO ₂ /Mo(112) film	76

4.11	Antiphase domain boundaries	77
5.1	Experimental STM image of the silica stripes	80
5.2	1D crystalline silica models	81
5.3	Stability plot for the 1D silica stripe models	83
5.4	STM image of the thermodynamically stable stripes	84
5.5	IRAS spectra of silica stripes formed on Mo(112)	85
6.1	Phase digram for 1D and 2D crystalline silica on Mo(112)	88
6.2	Stability plot for the 1 ML A/nO film models	90
6.3	IRAS spectra of the “O-rich” $SiO_2/Mo(112)$ film model	92
7.1	$p(1 \times 2)$ -Mo(112)/ nO structure models	96
7.2	$p(1 \times 3)$ -Mo(112)/ nO structure models	98
7.3	Stability plot for the $p(1 \times 2)$ - and $p(1 \times 3)$ -Mo(112)/ nO models . . .	99
7.4	Combined stability plot for $p(1 \times 2)$ - and $p(1 \times 3)$ -Mo(112)/ nO . . .	100
7.5	Vibrational normal modes of the $p(1 \times 2)$ model A	104
8.1	Monomeric and dimeric VO_x species modeled by replacement	107
8.2	Monomeric and dimeric VO_x species modeled by adsorption	108
8.3	V_4O_8 and V_6O_{12} clusters on $SiO_2/Mo(112)$	109
8.4	Large vanadia clusters	110
8.5	Differently oriented V_4O_8 clusters	111
8.6	Phase diagram for vanadium oxides on $SiO_2/Mo(112)$	112

List of Tables

3.1	Al ₂ O ₃ lattice parameters	16
3.2	Interlayer distances of the α -Al ₂ O ₃ (0001) surface	16
3.3	Al ₂ O ₃ and V ₂ O ₃ lattice constants	18
3.4	V 2 <i>p</i> adlayer core-level shifts	33
3.5	Interlayer distances of the κ -Al ₂ O ₃ (001) surface	38
3.6	Reduction of the most stable V ₂ O ₅ / κ -Al ₂ O ₃ cluster	48
3.7	Reduction of vanadia films on the κ -Al ₂ O ₃ (001) surface	50
4.1	Structural parameters of the 1 ML SiO ₂ /Mo(112) film models	65
4.2	Harmonic vibrational frequencies of 1 ML <i>A</i> , <i>B</i> , and <i>C</i>	68
4.3	Symmetry transformation properties of the normal modes	74
6.1	Structural parameters of the 1 ML <i>A</i> / <i>n</i> O film models	91
7.1	Harmonic frequencies of the <i>p</i> (1 × 2)-Mo(112)/ <i>n</i> O models	103
8.1	Vibrational frequencies of selected V _{<i>n</i>} O _{<i>m</i>} /SiO ₂ /Mo(112)	114

Chapter 1

Introduction

Most of today's technologically relevant chemical reactions would not be very efficient or even possible without the use of a catalyst. Such processes are for example oil refining, the production of chemicals (e.g., ammonia synthesis) and the cleaning of exhaust gases [1]. The catalyst can be either in the same phase as the reactants (homogeneous catalysis) or in a different phase, e.g., a solid catalyst and liquid or gaseous reactants (heterogeneous catalysis). The latter is preferred by industry because of the easier separation of the catalyst and the reactants/products. The industrially applied solid catalysts are very complex materials, often consisting of a porous oxide with high thermal stability (e.g., Al_2O_3 , SiO_2 , TiO_2 , MgO , ZrO_2), which serves as support for the active component, nanometer-sized particles of transition metals (e.g., Pt, Rh, Pd, Ir, Ni, Fe) or transition metal oxides (e.g., VO_x , MoO_x , TiO_x , CrO_x), which are dispersed onto the support surface. Further additives and promoters are used to enhance the catalytic performance. Thus, in order to understand on a microscopic level why and how the catalyst works, well-defined model systems which mimic the essential properties of real catalysts at a reduced level of complexity are imperative. The transferability of the results to the real catalysis, however, is questioned by the so-called *materials gap* between the structurally rather simple model catalysts and the complex real catalysts, and the *pressure gap*, which is many orders of magnitude in pressure between the ultrahigh vacuum (UHV) conditions and the conditions applied in the catalytic reactions on an industrial scale. Under reaction conditions, the entire structure and composition of the catalyst's surface might be changed, which might thus influence its catalytic activity.

Supported vanadium oxides represent a very important class of catalytic materials because they have become the model catalyst systems for fundamental studies of supported metal oxides and are extensively employed as industrial catalysts in a variety of oxidation and reduction reactions. For example, the VO_x catalysts are used in the oxidation of *o*-xylene to phthalic anhydride, the oxidation of sulfur dioxide to sulfur trioxide in the production of sulfuric acid, the ammoxidation of aromatic hydrocarbons, the selective oxidation of methanol to formaldehyde, the

selective catalytic reduction of NO_x with NH_3 to N_2 and H_2O [2, 3]. The systems investigated in this work, $\text{VO}_x/\text{Al}_2\text{O}_3$ and VO_x/SiO_2 , are reported to be highly selective in the oxidative dehydrogenation of propane [4] and other light alkanes [5]. The importance of vanadium-based catalyst has recently been underlined by an extensive open literature search on oxide-supported catalysts, according to which about 28% of the articles published in the period 1967–2000 dealt with vanadium systems [3]. The basis for the outstanding catalytic performance of supported VO_x catalysts is determined by a large variety of geometric and electronic structure of vanadium oxides. Vanadium with its electronic configuration $[\text{Ar}]3d^34s^2$ forms the single-valency oxides VO , V_2O_3 , VO_2 , and V_2O_5 , with the formal oxidation state ranging from +2 to +5, and a series of mixed-valency oxides with the general formulas $\text{V}_n\text{O}_{2n-1}$ and $\text{V}_n\text{O}_{2n+1}$. In addition to that, vanadium ions can exhibit quite different coordination geometries described by octahedra, pentagonal bipyramids, square pyramids, and tetrahedra. They can be combined by shared corners, edges and faces, yielding an impressive variety of structural arrangements.

The vanadia-based catalysts consist of a vanadia phase deposited on the surface of an oxide support, such as SiO_2 , Al_2O_3 , TiO_2 , ZrO_2 , Nb_2O_5 , and CeO_2 . It is known that the activity of the catalysts can be modified by up to several orders of magnitude by changing the support material [6–8]. Yet, the origin of the support effect as well as the nature of the active species are far from being understood. However, this knowledge is essential for the rational design of active and selective vanadia catalysts. For that reason, experimental and theoretical studies on well-defined model systems with reduced complexity have been invoked [9, 10]. When applied to the vanadia-based systems, these models can be formally divided in two groups: (i) thin vanadium oxide films and (ii) vanadia supported on well-ordered oxide films. The atomically flat vanadium oxide films have been grown on a variety of single-crystal substrate like $\text{Cu}(100)$ [11], $\text{Au}(111)$ [12], $\text{W}(110)$ [12], $\text{Cu}_3\text{Au}(100)$ [13], $\text{Pd}(111)$ [14], and $\text{TiO}_2(110)$ [15]. It was shown that the vanadia films exhibit $\text{V}_2\text{O}_3(0001)$ structure, however, the surface exposes vanadyl ($\text{V}=\text{O}$) groups. When deposited on thin well-ordered alumina and silica films, i.e., thin Al_2O_3 film on $\text{NiAl}(110)$ and thin SiO_2 film on $\text{Mo}(112)$, respectively, at submonolayer coverage, vanadia forms three-dimensional nanoparticles [16–18]. In spite of these simplified approaches, little is known about the structure and composition of the active vanadia surfaces and even the precise atomic structure of the supporting oxide films was not known until recently.

The aim of the present work is to provide an understanding on two different vanadia-based model systems, i.e., vanadia/alumina and vanadia/silica, employing density functional theory. The alumina support in our theoretical studies is modeled using the stable $\alpha\text{-Al}_2\text{O}_3$ and the metastable $\kappa\text{-Al}_2\text{O}_3$ phases. $\alpha\text{-Al}_2\text{O}_3$ is chosen as the support because of its simplicity, which makes it a more convenient starting point for fundamental investigations of alumina-supported vanadium oxides. It is the thermodynamically stable phase of aluminum oxide and contains Al ions only in octahedral coordination. $\kappa\text{-Al}_2\text{O}_3$, on the other hand, is a metastable form of

Al_2O_3 with a moderate fraction (25%) of occupied aluminium tetrahedral sites, which is a characteristic feature of the most real alumina support material, i.e., γ - Al_2O_3 , but in contrast to the latter has a well-defined atomic structure [19]. Thus, it can be regarded as a model of more realistic alumina support material. Different low-coverage VO_x species as well as films of varying thickness deposited on these alumina surfaces are investigated. Statistical thermodynamics is applied to account for the effect of oxygen partial pressure and vanadium activity (concentration) at a given temperature on the stability of the supported vanadia aggregates. The aim is to understand how VO_x anchors to the surface of these two structurally different aluminas and to examine the role of the oxide support on the molecular and electronic structure of the stable vanadia species. The effort is to correlate structural properties with catalytic activity in reactions proceeding via the Mars-van Krevelen mechanism, in which the (rate-determining) oxidation of the reactant is decoupled from the reoxidation of the catalyst. In accord therewith, the formation energy of a lattice oxygen defect is used as an indicator of catalytic performance. Because little is known about the surface structure of supported metal oxides and vibrational spectroscopy is one of the major tools for structural characterization, the influence of the support structure on the interface vibrational modes is analyzed.

As far as the vanadia/silica model catalyst system is concerned, first the atomic structure of the model support, i.e., the thin crystalline silica film epitaxially grown on a Mo(112) substrate is investigated. Successful preparation of well-ordered silica on a metal substrate was reported first by Schroeder *et al.* [20, 21] and later by Goodman's group [22]. The crystalline phase of the silica film has not been determined and even its thickness was a matter of debate. The original study of Freund and co-workers [20] suggested an average thickness of about 6–9 Å, whereas according to Goodman and co-workers [22], the film is 3–4 Å thick, i.e., a single layer of Si and O atoms. Based on DFT calculations, Ricci and Pacchioni have proposed a β -cristobalite derived structure as the most stable model of $\text{SiO}_2/\text{Mo}(112)$ [23]. Using analogies of vibrational spectra of the film to known compounds, Chen *et al.* have suggested that it consists of a layer of isolated $[\text{SiO}_4]$ clusters arranged in a $c(2 \times 2)$ structure on the Mo(112) surface, where all oxygen atoms are bonded to the substrate [22, 24].

Fortunately, over the last 10 years it became clear that the joint effort of experiment and theory is synergetic and most valuable, if not crucial, and allows identification and characterization of complex, novel structures. Here, a successful determination of the atomic structure of the thin crystalline silica film on Mo(112) is presented, based on a combination of DFT and experimental data obtained from scanning tunneling microscopy (STM), infrared reflection absorption spectroscopy (IRAS), and X-ray photoelectron spectroscopy (XPS) [25, 26].

Interestingly, at low silicon coverages, formation of crystalline silica with even further reduced dimensionality, such as one-dimensional (1D) stripes on Mo(112), has been observed [27]. At increasing Si coverage, islands of the 2D film and stripes were found to coexist [27]. Owing to this variety of low-dimensional silica phases

formed under different conditions, various 1D and 2D silica structures are considered and a phase diagram showing their stability as a function of the silicon coverage and oxygen pressure is derived. Particularly, at elevated O_2 pressures the calculations predict formation of a new, “O-rich” phase of the 2D silica film, whose existence is subsequently experimentally confirmed [28].

The first step in the preparation of $SiO_2/Mo(112)$ film is the adsorption of oxygen on the clean $Mo(112)$ surface. Therefore, detailed knowledge of the structure and morphology of the oxidized $Mo(112)$ surface is crucial for understanding of the film formation. In addition, oxygen adsorption on metal surfaces can induce surface reconstructions or formation of thin surface oxides, which are suggested to be the active phases of many transition metal oxide catalysts [29–32]. The $p(1 \times 2)$ -O/ $Mo(112)$ phase, for instance, is an efficient catalyst in selective oxidation of methanol to formaldehyde [33, 34]. Particularly interesting is the $p(2 \times 3)$ reconstruction of the oxidized $Mo(112)$ surface that is very stable and passivates $Mo(112)$ against further oxidation in its initial stages. According to Schroeder *et al.*, it precedes the epitaxial growth of the crystalline SiO_2 film as well as the MoO_2 formation [21, 35]. In contrast, Santra *et al.* suggested that the $p(1 \times 3)$ -O/ $Mo(112)$ phase is the precursor to the epitaxial formation of $MoO_2(110)$ [36]. Our studies are aimed at determining the atomic structures of the oxidized $Mo(112)$ surface employing DFT in combination with genetic algorithm (GA) [37]. The most favorable atomic models found in our GA simulations are more stable than any other models suggested so far. The results are fully supported by a multitude of experimental data obtained from low energy electron diffraction (LEED), XPS, and STM [37].

Elucidation of the precise atomic structure of the silica support allows investigation of the VO_x/SiO_2 model catalyst systems in much greater detail. The aim is to develop an understanding of the effect of different types of aggregation on the structure, stability, and vibrational frequencies of the silica-supported vanadium oxides. The knowledge of the vibrational spectra of such well-defined systems helps to relate characteristic vibrational features of experimental systems to their structural features.

The thesis is organized as follows. A brief description of the theoretical grounds employed in this study is given in Chapter 2. In Chapter 3 a detailed analysis of low-coverage VO_x species and vanadia films of varying thickness supported on the stable $\alpha-Al_2O_3(0001)$ and the metastable $\kappa-Al_2O_3(001)$ surfaces is carried out. Resolution of the atomic structure of the thin-film silica support is presented in Chapter 4, followed by that of the silica stripes (Chapter 5). Chapter 6 is dedicated to the thermodynamic stability of the 1D and 2D crystalline silica and particularly to the “O-rich” phase of the $SiO_2/Mo(112)$ film. In Chapter 7 genetic algorithm method for automatic structure determination is presented and employed for the oxidized $p(1 \times 2)$ - and $p(1 \times 3)$ - $Mo(112)$ surfaces. Different silica-supported vanadium oxides are investigated in Chapter 8, with the focus on vibrational frequency analysis and comparison to the experimental spectra. Finally, a brief summary of the results obtained in the present work is provided in Chapter 9.

Chapter 2

Theoretical Background

Modeling of complex systems and phenomena is a powerful method towards understanding, predicting, and eventually controlling different aspects of the later. In materials science, the systems of interest typically consist of many particles of the order of Avogadro's constant $N_A = 6.022 \times 10^{23} \text{ mol}^{-1}$. The N -particle quantum-mechanical system is described by a complex-valued function of the particles' spatial and spin coordinates $\Psi(\xi_1, \xi_2, \dots, \xi_N)$, with $\xi_i = (\mathbf{r}_i, \sigma_i)$ being, respectively, the position and the spin of the i th particle. Solving the Schrödinger equation for Ψ when $N \sim N_A$ is neither useful nor possible. Fortunately, approximate methods in conjunction with today's powerful computing machinery allow the principles of quantum mechanics to be applied to real systems. The two main approaches to determine the total energy of a particular system, which is a prerequisite for its theoretical description, are either wave-function or electron-density based methods. Electronic structure calculations of solids are dominated by density functional theory (DFT), which is also the method used in the present work. The reader is referred to Refs. [38–40] for a comprehensive view on DFT.

2.1 Density Functional Theory

The origins of density functional formalism can be traced back to the Thomas-Fermi model and its extensions [41, 42]. The rigorous foundations of DFT were put forward in the pioneering work of P. Hohenberg and W. Kohn that appeared in 1964. They have formulated two theorems, which formally justified the use of the electron density as basic variable in determining the total energy and which became the foundation of modern density functional theory [43]. The first theorem states that the ground-state density $n(\mathbf{r})$ of interacting electrons in an external potential, $v(\mathbf{r})$, uniquely determines this potential, within an additive constant. This means that any observable of this system, such as the ground-state energy, can be written

as a functional of the electron density

$$E[n(\mathbf{r})] = \int n(\mathbf{r})v(\mathbf{r})d\mathbf{r} + F_{\text{HK}}[n(\mathbf{r})] \quad (2.1)$$

where $F_{\text{HK}}[n(\mathbf{r})]$ is the Hohenberg-Kohn functional, which does not depend on the external potential and is therefore universal. It contains the electron-electron interaction $E_{\text{ee}}[n]$ as well as the kinetic energy of the electrons $T_e[n]$. The theorem asserts the existence of the universal functional, but does not tell how to construct it.

The second Hohenberg-Kohn theorem proves that the variational principle holds for the minimization of the energy with respect to the electron density

$$E_0 = E[n_0] \leq E[n] \quad (2.2)$$

under the constraint of electron number conservation $\int n(\mathbf{r})d\mathbf{r} = N$. The lowest energy E_0 is only given as a functional of the true ground-state density n_0 .

A crucial step towards turning density functional theory into a practical tool for calculations is provided by a scheme for the treatment of the variational problem, proposed by Kohn and Sham [44]. The gist of their scheme is the existence of an auxiliary system of *non-interacting* particles, with kinetic energy functional and local single-particle potential, such that the ground-state density of the interacting system is equal to the ground-state density of the non-interacting system. The many-body problem is mapped onto an effective single-particle problem and all unknown terms are merged into the exchange-correlation part, E_{xc} . The latter contains the difference in the kinetic energy between the real, interacting system and the fictitious, non-interacting system as well as the exchange energy, the correlation energy, and the correction for the classical self-interaction energy. The single-particle Kohn-Sham orbitals are determined under the constraint to reproduce the density of the fully interacting many-body system. This yields the Kohn-Sham equations

$$\left[-\frac{1}{2}\nabla^2 + v_{\text{eff}}(\mathbf{r})\right]\varphi_i = \epsilon_i\varphi_i \quad (2.3)$$

$$v_{\text{eff}}(\mathbf{r}) = v(\mathbf{r}) + \int \frac{n(\mathbf{r}')}{|\mathbf{r} - \mathbf{r}'|}d\mathbf{r}' + v_{\text{xc}}(\mathbf{r}) \quad (2.4)$$

$$n(\mathbf{r}) = \sum_i^N |\varphi_i(\mathbf{r})|^2 \quad (2.5)$$

The eigenvalues ϵ_i are Lagrange multipliers that ensure the orthonormality of the Kohn-Sham orbitals. They have the dimension of an energy and are referred to as Kohn-Sham one-particle energies. The exchange-correlation potential in Eq. (2.4) is the functional derivative of $E_{\text{xc}}[n]$

$$v_{\text{xc}}(\mathbf{r}) = \frac{\delta E_{\text{xc}}[n(\mathbf{r})]}{\delta n(\mathbf{r})} \quad (2.6)$$

Since the effective potential v_{eff} depends on the density, which in turn depends on the one-particle wavefunctions φ_i , the Kohn-Sham equations have to be solved self-consistently. Once a self-consistent density is obtained, the Hohenberg-Kohn functional can be evaluated, and thus, also the ground-state total energy of the system.

It should be stressed that the DFT formalism is in principle exact. However, the exact functional for exchange and correlation is unknown. If this “divine” functional was known, all properties of a system could be calculated exactly. Over the years, a bunch of approximations have appeared. The first one is the local density approximation (LDA), in which the local exchange-correlation energy per electron is approximated by that of a homogeneous electron gas of the same density [44, 45]. The LDA is a good approximation for slowly varying densities, but it has proved to be very successful for a variety of rather inhomogeneous systems such as atoms, molecules, and solids. Attempts to remedy the neglect of the density variations are including the gradient of the electron density (generalized gradient approximation, GGA), or even higher derivatives (meta-GGA). A different approach is the construction of hybrid functionals with admixture of exact exchange (Fock exchange), as proposed by Becke [46]. Pure GGA functionals show typical deficiencies like, for example, underestimation of reaction barriers, band gaps, bulk moduli, overestimation of binding and cohesive energies, lattice constants, atomization energies of molecules and solids, overestimation of electron delocalization and metallic character (see, e.g., Refs. [40, 47–49]). Hybrid functionals usually perform better and yield very reliable results in many applications of chemistry and physics. Unfortunately, the calculation of exact exchange is computationally very expensive with plane-wave basis set. For that reason, plane-wave DFT applications usually employ a GGA type functional.

The calculations addressed in the present work have been performed using the plane-wave code Vienna Ab-initio Simulation Package (VASP) [50–52] along with the Perdew-Wang exchange-correlation functional (PW91) [53].

2.2 Supercell Approach and Plane-Wave Basis Set

A consequence of using periodic boundary conditions is that a unit cell is repeated an infinite amount of times in all three directions in space. On the other hand, a surface can be viewed as a defect in the bulk crystal, which destroys the perfect periodicity in a certain crystallographic direction. Such an aperiodic system is modeled within the supercell approach by a *slab* with a given number of atomic layers, which are separated by a vacuum region. The number of atomic layers and the vacuum thickness are system specific, but generally they should be chosen large enough so that the interaction between the two surfaces of the slab is negligible, and the vacuum thickness is sufficient not to introduce spurious results due to an interaction between the surfaces of consecutive slabs. In the following, specific details for the

supercell used in each particular calculation are explicitly given.

In practical computations, the Kohn-Sham wavefunctions have to be expanded in a finite basis set. In this work, plane waves are employed as basis functions which are particularly suitable for periodic systems due to their free-electron character. According to Bloch's theorem, the electronic wavefunctions in a periodic system can be written as a product of a plane wave and a lattice-periodic function

$$\varphi_{\mathbf{k}}(\mathbf{r}) = e^{i\mathbf{k}\cdot\mathbf{r}} u_{\mathbf{k}}(\mathbf{r}) \quad \text{with} \quad u_{\mathbf{k}}(\mathbf{r}) = u_{\mathbf{k}}(\mathbf{r} + \mathbf{R}) \quad (2.7)$$

for any lattice vector \mathbf{R} . Here, \mathbf{k} is the wave vector within the first Brillouin zone (BZ). Being a periodic function, $u_{\mathbf{k}}$ can be expanded in a Fourier series, $u_{\mathbf{k}}(\mathbf{r}) = (1/\sqrt{\Omega}) \sum_{\mathbf{G}} c_{\mathbf{k}+\mathbf{G}} \exp(i\mathbf{G}\cdot\mathbf{r})$, where in principle the sum goes over an infinite number of reciprocal lattice vectors $\mathbf{G} = m_1\mathbf{b}_1 + m_2\mathbf{b}_2 + m_3\mathbf{b}_3$, with $(\mathbf{b}_1, \mathbf{b}_2, \mathbf{b}_3)$ being the basis in the reciprocal space and $m_i = \text{integer}$. Ω is the cell volume. Substituting the expansion for $u_{\mathbf{k}}$ into Eq. (2.7) results in the following equation:

$$\varphi_{\mathbf{k}}(\mathbf{r}) = \frac{1}{\sqrt{\Omega}} \sum_{\mathbf{G}} c_{\mathbf{k}+\mathbf{G}} e^{i(\mathbf{k}+\mathbf{G})\cdot\mathbf{r}} \quad (2.8)$$

This representation of the single-particle state $\varphi_{\mathbf{k}}$ is referred to as a *plane-wave expansion*. In practice, however, one uses a truncated plane-wave expansion to include terms with kinetic energies only up to a certain cutoff, E_{cut}

$$\frac{1}{2} |\mathbf{k} + \mathbf{G}|^2 \leq E_{\text{cut}} \quad (2.9)$$

The quality of the basis set is entirely controlled by the energy cutoff – the higher the E_{cut} , the better the plane-wave representation. However, one of the difficulties associated with the use of plane-wave basis set is that the number of plane waves changes discontinuously with cutoff energy. In general, these discontinuities will occur at different cutoffs for different \mathbf{k} -points in the \mathbf{k} -point mesh. In addition, at a fixed energy cutoff, a change in the cell shape or size of the unit cell will cause discontinuation in the plane-wave basis set. This error is called ‘‘Pulay stress’’ (in analogy to Pulay forces [54]) and leads to underestimation of the equilibrium volume unless a large plane-wave cutoff is used (see Refs. [55, 56]).

The principle factor, however, that allows significant reduction of the energy cutoff in calculations using plane-wave basis set is the pseudopotential concept, which is presented next.

2.3 The PAW Method

Electronic wavefunctions show rapid oscillation in the core region due to the strong ionic potential in this region. To expand them in a plane wave basis set would require a very large number of plane waves, which would make such all-electron

calculations prohibitively expensive. A fundamental idea therefore is the *frozen-core approximation* based on the assumption that most properties of the condensed systems can be well-described by the valence electrons, while the highly localized core electrons have only minor influence. The *pseudopotential* concept exploits this by removing the core electrons and by replacing them and the strong ionic potential by a weaker pseudopotential that acts on a set of pseudo wavefunctions rather than on the true valence wavefunctions. The charge density of the core electrons is kept fixed at a value obtained from a fully self-consistent calculation for a reference state (often an isolated atom) and only the valence charge density is then self-consistently calculated for the atom in the system of interest. The pseudo wavefunctions, which are constructed to be nodeless, differ from the all-electron wavefunctions only inside a region around the nucleus. Thus, a critical parameter is the cutoff radius r_c , dividing the electron shell into a (chemically inert) core region ($r < r_c$), and a valence region ($r > r_c$) responsible for the chemical bonding. The choice of r_c should ensure that the pseudopotential describes adequately the scattering properties of the ion in different atomic environments, a property referred to as transferability. Yet, it has to be efficient in reducing the overall computational effort. Various flavors of pseudopotentials exist, such as the norm-conserving pseudopotentials derived by Hamann [57] and the ultrasoft Vanderbilt pseudopotentials [58].

Another approach is the linear methods, which in contrast to the pseudopotential method include all electrons by mapping the all-electron wavefunctions onto computationally more convenient pseudo wavefunctions by a linear transformation [59]. The projector augmented-wave (PAW) method, which is used in this work, is such an approach. The PAW method is in principle a frozen-core all-electron method. It was established by Blöchl [60] and its close connection to the ultrasoft pseudopotentials was derived by Kresse and Joubert [61].

In the PAW method, the all-electron (AE) wavefunctions $|\Psi\rangle$ are derived from pseudo (PS) wavefunctions $|\tilde{\Psi}\rangle$ by means of a linear transformation

$$|\Psi\rangle = |\tilde{\Psi}\rangle + \sum_i (|\phi_i\rangle - |\tilde{\phi}_i\rangle) \langle \tilde{p}_i | \tilde{\Psi}\rangle \quad (2.10)$$

where i goes over all atomic sites and angular momentum quantum numbers l and m . All quantities related to the PS representation of the wavefunction are indicated by a tilde. The AE partial waves ϕ_i are chosen to be solutions of the spherical (scalar-relativistic) Schrödinger equation for a non-spin-polarized atom at a specific energy ϵ_i and angular momentum l_i . The nodeless PS partial waves $\tilde{\phi}_i$ are equivalent to the AE partial waves outside the core radius r_c and match continuously onto ϕ inside the r_c . The core radius r_c is chosen approximately around half the nearest neighbor distance. The \tilde{p}_i are local projector functions that fulfill the condition within the augmentation region

$$\sum_i |\tilde{\phi}\rangle \langle \tilde{p}_i| = 1 \quad (2.11)$$

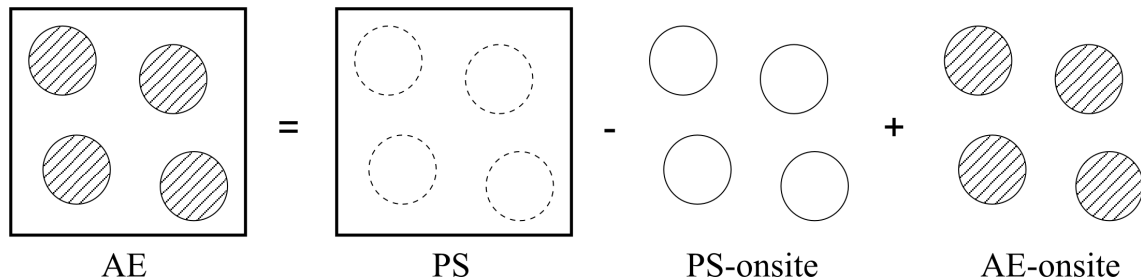


Figure 2.1: Decomposition of the all-electron wavefunction in the PAW method.

In the interstitial region between the PAW spheres, the PS wavefunctions $\tilde{\Psi}$ are identical to the AE wavefunctions Ψ . Inside the spheres, however, the pseudo wavefunctions are only a computational tool and a bad approximation to the true wavefunctions, since even the norm of the AE wavefunction is not reproduced. The decomposition of all-electron wavefunction in the PAW method is schematically shown in Figure 2.1.

The PAW method represents a balanced combination of accuracy and computational efficiency. It provides a description of the DFT ground state and related properties with an accuracy that is comparable to the full-potential linearized augmented-plane-wave (FLAPW) method [62] – regarded as the benchmark method – and combines it with the computational efficiency of (less accurate) methods based on pseudopotential approximations [63].

2.4 Brillouin Zone Sampling

One important consequence stemming from the Bloch theorem is that the physical quantities of a solid, e.g., total energy, forces, etc., can be evaluated by integration over the Brillouin zone or its *irreducible* part, when the symmetry of the system is considered. Numerically this is solved by replacing the integral by a sum over a finite number of \mathbf{k} -points:

$$\int_{\text{BZ}} \frac{1}{\Omega_{\text{BZ}}} d\mathbf{k} \rightarrow \sum_{\mathbf{k}} \omega_{\mathbf{k}} \quad (2.12)$$

The results presented in this work were obtained using the Monkhorst-Pack method [64], in which the integrations are performed as weighted sums over a grid of representative \mathbf{k} -points. Initially a homogeneous grid is constructed in the full Brillouin zone. Sets of symmetry related \mathbf{k} -points are identified by applying the symmetry operations. One representative \mathbf{k} -point is then chosen from each set of equivalent points, and assigned a weight, $\omega_{\mathbf{k}}$, equal to the number of points in the set divided by the total number of \mathbf{k} -points in the grid. These are the special points and associated weights.

For metals, where the bands cross the Fermi level, the occupation and there-

fore the integration over the Fermi surface is discontinuous. One solution to overcome this problem is the Methfessel-Paxton method [65] at a finite temperature to artificially broaden the Fermi surface. After the integration, the free energy is extrapolated back to $T = 0$ K.

Chapter 3

Alumina-Supported Vanadium Oxides

The experimental vanadia/alumina model catalysts, prepared via evaporation of vanadium in an oxygen ambient of 10^{-10} atm O_2 on a thin well-ordered alumina film grown on a NiAl(110) substrate in ultrahigh vacuum (UHV) at 300 K, consists of small, roundish vanadia particles (20–30 Å wide, 3–6 Å thick), with vanadium in an average oxidation state of V^{III} (as in V_2O_3) [16]. Using infrared spectroscopy, surface vanadyl groups have been identified, which are not a structural element of bulk-truncated V_2O_3 surfaces. Their presence implies that the surface V atoms are in a higher oxidation state (V^V), which would only be detectable if spectra are taken at grazing angles, as revealed by surface-sensitive XPS on flat $V_2O_3(0001)$ surfaces [12, 66]. For epitaxially grown V_2O_3 films on Pd(111) and Rh(111), Surnev *et al.* [14, 67–69] and Schoiswohl *et al.* [66, 70] observed different terminations, including the vanadyl one, depending on the growth conditions and film thickness. In contrast, for vanadium oxides on $Cu_3Au(100)$ support, Niehus *et al.* [13, 71] did not find evidence of vanadyl termination. A characteristic vibrational feature of the alumina-supported vanadia catalysts is a band at $\sim 950\text{ cm}^{-1}$ in the IRAS spectra of model catalysts [16] as well as in the Raman spectra of powder samples [3, 72]. It has been interpreted as being due to V–O–V vibrations and therefore used as a fingerprint for the so-called “polymeric vanadia species” [3]. Recently, this assignment has been revisited and the band was attributed to the interface-localized V–O–Al vibrations [16, 72].

In general, little is known about the structure and composition of the active vanadia surfaces and even the precise atomic structure of the thin-film alumina support was not known until recently. The alumina film has been characterized by various methods [73–78]. Results from transmission electron microscopy and phonon spectra point to a γ -like Al_2O_3 structure [73–75]. However, based on surface X-ray diffraction measurements, a κ -like structure has been derived [79]. Combining high-resolution STM images and DFT calculations, the atomic structure of the thin alumina film on NiAl(110) has finally been resolved [80, 81]. It differs from any

known Al_2O_3 bulk phase and includes a mixture of tetrahedrally and pyramidally coordinated Al ions. All the metastable bulk phases, e.g., γ -, δ -, η -, θ -, χ -, and κ -alumina, have in common Al ions not only in octahedral (Al^{O}), as in α - Al_2O_3 , but also in tetrahedral (Al^{T}) coordination. In fact, the structure of the alumina support of most real vanadia catalysts is that of γ - Al_2O_3 . A wide variety of models for the γ -phase have been proposed over the last half century, but no consensus has been reached on issues such as the arrangement of vacancies on aluminum sites and the role of hydrogen in the structure (see, e.g., Refs. [82–86]). Additionally, γ - Al_2O_3 has a high degree of disorder and shows diffuse diffraction patterns with strong structural similarities with other transition aluminas.

The aluminum oxide support in our theoretical studies is modeled using two different alumina phases, namely, the stable α - Al_2O_3 and the metastable κ - Al_2O_3 . α - Al_2O_3 is chosen as the support because of its simplicity, which makes it a more convenient starting point for fundamental investigations of $\text{VO}_x/\text{Al}_2\text{O}_3$ systems. κ - Al_2O_3 , on the other hand, is metastable Al_2O_3 with a moderate fraction (25 %) of occupied tetrahedral Al sites, which is a characteristic feature of the most real alumina support material, i.e., γ - Al_2O_3 , but in contrast to the latter has a well-defined atomic structure [19]. Thus, it can be regarded as a model of more realistic alumina support material. In this section, different low-coverage VO_x species as well as films of varying thickness deposited on these two structurally different aluminas are investigated. The aim is to understand how vanadia aggregates anchor to the alumina surface and what is the role of the oxide support on the molecular and electronic structure and reducibility of the stable vanadia species. The results described here have been published in Refs. [87, 88].

3.1 Vanadium Oxides Supported on α - $\text{Al}_2\text{O}_3(0001)$

3.1.1 Bulk and (0001) Surface of α - Al_2O_3

α - Al_2O_3 , also called (α -)alumina or sapphire is the thermodynamically stable phase of aluminum oxide. It forms a rhombohedral corundum lattice ($R\bar{3}c$ space group) with two symmetry-inequivalent atoms (Al and O) in the unit cell (see Fig. 3.1). All Al atoms are octahedrally coordinated by six oxygen atoms in the same local environment and each oxygen atom has four aluminum neighbors. Two different Al–O bondlengths occur in the crystal, 1.854 and 1.971 Å, as determined from X-ray diffraction data and the experimental lattice parameters are $a_r = 5.127$ Å and $\beta = 55.282^\circ$ [89].

The corundum structure of α - Al_2O_3 can be also described as a hexagonal unit cell with six Al_2O_3 formula units (30 atoms). The atoms are stacked along the [0001] direction in 12 planes of Al atoms and 6 planes of oxygen atoms in a sequence Al– O_3 –Al–Al– O_3 –. . .–Al (see Fig. 3.1). The oxygen atoms form hexagonal close-packed layers, and the Al atoms occupy 2/3 of the available octahedral sites between these

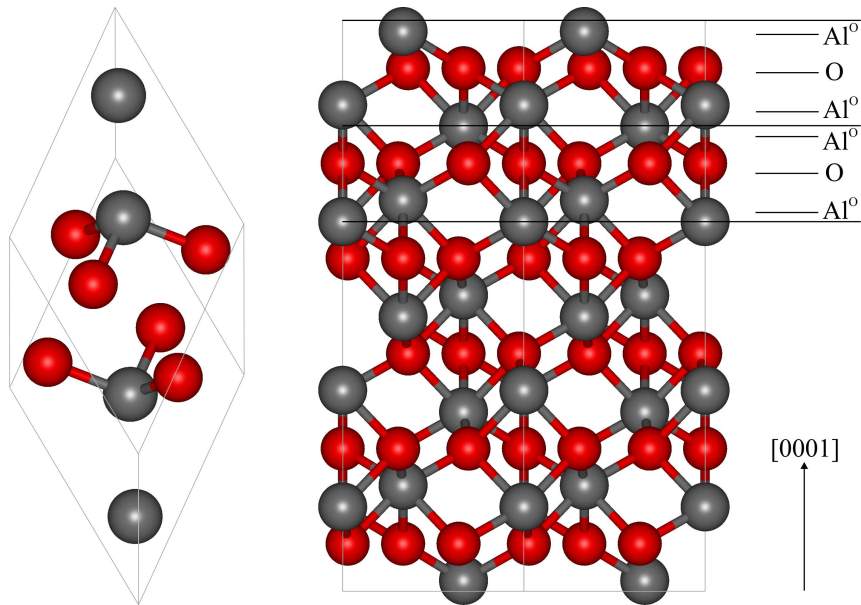


Figure 3.1: Bulk structure of $\alpha\text{-Al}_2\text{O}_3$. Left: one rhombohedral unit cell. Right: two hexagonal unit cells. The stacking sequence of aluminum and oxygen layers along the $[0001]$ direction is shown. The repeating unit of atomic layers Al-O₃-Al (*trilayer*) is indicated. Al and O atoms are depicted in dark gray and red, respectively.

layers. They are hexagonally arranged in one of the three different types of hexagonal networks, which differ in the position of the vacant octahedral sites. Moreover, due to the electrostatic repulsion arising from the face-sharing of Al octahedra in neighboring layers, the Al atoms in each layer are slightly displaced from each other, forming two separate sublayers. In the following, the term *trilayer* is used for the repeating Al-O₃-Al unit. The hexagonal unit cell includes six such trilayers and each of them maintains the bulk composition.

Cell-shape minimization that includes simultaneous optimization of the fractional coordinates at several fixed volumes is performed, and the equilibrium volume is obtained by fitting to the Murnaghan equation of state [90]. After an additional minimization of the cell shape and fractional coordinates at the calculated equilibrium volume, the optimized lattice parameters were obtained. Table 3.1 lists their values for the rhombohedral as well as for the corresponding hexagonal unit cell as a function of the k -point mesh at an energy cutoff of 800 eV. Comparison to the experimental lattice constants shows that the DFT-GGA results slightly overestimate (by 0.9%) the experimental ones. As can be also seen from Table 3.1, converged lattice parameters are obtained employing a $(3 \times 3 \times 3)$ k -mesh. Using a denser $(4 \times 4 \times 4)$ k -point grid or increasing the energy cutoff to 1200 eV result in changes of the optimized constants of about 0.001 Å.

According to experiments, the most stable alumina surface under UHV conditions is the (0001) surface, which is aluminum terminated, with oxygen in the

Table 3.1: Optimized lattice parameters of the single-crystal α -Al₂O₃ as a function of the k -point mesh at an energy cutoff of 800 eV. a_r and β are lattice parameters of the rhombohedral unit cell, a_{hex} and c_{hex} of the corresponding hexagonal unit cell.

k -mesh	a_r [Å]	β [°]	a_{hex} [Å]	c_{hex} [Å]
(3 × 3 × 3)	5.175	55.310	4.804	13.107
(4 × 4 × 4)	5.176	55.310	4.805	13.110
(5 × 5 × 5)	5.176	55.309	4.805	13.110
Experiment	5.127	55.282	4.757	12.988

next plane [91, 92]. This termination has no net dipole moment left across the surface [93] and based on Tasker’s second rule is *nonpolar* and hence stable [94]. The surface shows significant relaxation ranging from -51% [91, 93] to -63% [92]. Theoretical calculation have also identified this termination as the only stable one [95–97]. However depending on the method used large discrepancies in the size of the relaxation have been reported. For example, Hartee-Fock gives a relaxation of -40% [95], whereas density functional theory pseudopotential calculations predict the relaxation of about -87% [97–99].

Here, the Al₂O₃(0001) surface is modeled by a slab containing six *trilayers* and the vacuum region is ~ 10 Å. Test calculations indicate that this vacuum thickness is large enough to decouple the surfaces of consecutive slabs in the supercell. The lattice parameters were set to the optimized values for the bulk structure, i.e., $a_{hex} = 4.804$ Å and $c_{hex} = 13.107$ Å. The 800 eV cutoff and the (3 × 3 × 1) k -point grid that includes the $\bar{\Gamma}$ point are used for calculations on the (1 × 1) slab of six trilayers of the alumina surface. Table 3.2 lists the distances between the atomic planes of the first two topmost trilayers of the α -Al₂O₃(0001) surface in the relaxed system compared to the ideal bulk-truncated structure. The atomic planes are denoted with superscripts, e.g., Al¹, O², Al³, Al⁴, O⁵, and Al⁶. The Al atoms of the topmost

Table 3.2: Interlayer spacing (Å) of the ideal (bulk) and relaxed structure of the clean α -Al₂O₃(0001) surface as well as the distance difference Δz_{ij} and the relaxation (in %).

Interlayer distance	z_{ij} (bulk)	z_{ij} (relaxed)	Δz_{ij}	[%]
Al ⁽¹⁾ –O ⁽²⁾	0.84	0.12	–0.72	–86
O ⁽²⁾ –Al ⁽³⁾	0.85	0.88	+0.03	+4
Al ⁽³⁾ –Al ⁽⁴⁾	0.49	0.27	–0.22	–45
Al ⁽⁴⁾ –O ⁽⁵⁾	0.85	1.02	+0.17	+20
O ⁽⁵⁾ –Al ⁽⁶⁾	0.84	0.89	+0.05	+6

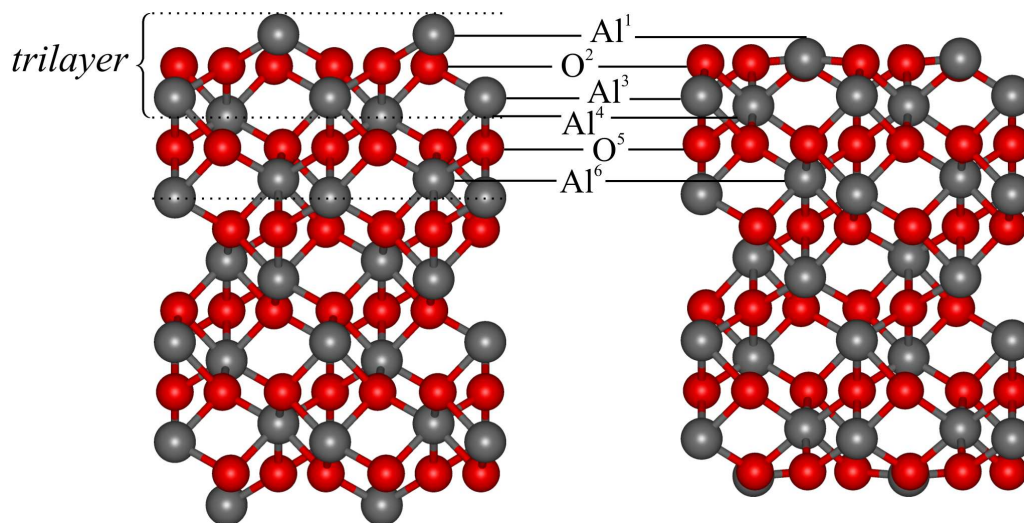


Figure 3.2: Structure of the clean $\alpha\text{-Al}_2\text{O}_3(0001)$ surface before and after relaxation (side view). The vertical lines indicate the stacking sequence of atomic layers along the $[0001]$ direction. The repeating unit (trilayer) is also marked.

metal layer (Al^1) move inwards by 86% or 0.72 \AA , whereas the oxygen layer (O^2) relaxes outwards by only 4% or 0.03 \AA (see Fig. 3.2), in very good agreement with previous DFT studies [97–102]. Thus, upon relaxation the outermost Al layer becomes almost coplanar with the oxygen layer. Despite the large relaxation, however, the $\text{Al}_2\text{O}_3(0001)$ surface remains metal terminated (see Fig. 3.2).

3.1.2 Vanadia Aggregates Supported on $\alpha\text{-Al}_2\text{O}_3(0001)$

V_2O_3 is a Mott-Hubbard system exhibiting two fascinating temperature-dependent effects: electronic and geometric [103, 104]. With increasing temperature it undergoes insulator-metal-semiconductor transitions, and in addition, changes its crystallographic structure from monoclinic to trigonal corundum structure. At temperature below 150 K it forms an antiferromagnetic insulator, in the temperature range of 150–450 K is a paramagnetic metal, whereas above 450 K it becomes a paramagnetic semiconductor. Below 150–170 K bulk V_2O_3 crystallizes as a monoclinic phase, while above this temperature it assumes trigonal geometry with the same space group ($R\bar{3}c$) as $\alpha\text{-Al}_2\text{O}_3$.

The lattice mismatch between the V_2O_3 and Al_2O_3 corundum structures is $\sim 4\%$ (experiment) and $\sim 1\%$ (DFT, this work) in the (0001) plane (see Table 3.3). Therefore, a possible way to model vanadium oxides supported on $\alpha\text{-Al}_2\text{O}_3(0001)$ is to replace Al atoms by V atoms. Vanadia films of varying thickness are thus created. The unit cell compositions have the general formula $\frac{n}{2}\text{V}_2\text{O}_3 \cdot \frac{12-n}{2}\text{Al}_2\text{O}_3$ ($n = 1\text{--}6, 12$). The thickest supported film consists of six vanadium layers on the thinnest alumina support of three trilayers (Fig. 3.3A). Decreasing the thickness of the Al_2O_3 support

Table 3.3: The lattice constants (\AA) for the hexagonal bulk Al_2O_3 and V_2O_3 structures as well as their lattice mismatch in [%].

	Al_2O_3		V_2O_3		Mismatch [%]	
	Exp. [89]	This work	Exp. [106]	This work	Exp.	This work
a_{hex}	4.757	4.804	4.940	4.856	4	1
c_{hex}	12.988	13.107	13.971	14.349	8	9

while increasing that of the V_2O_3 film does not affect the results. It was shown that the properties of the clean $\text{Al}_2\text{O}_3(0001)$ surface do not change when passing from a three- to a four-trilayer thick slab (e.g., the surface energy changes by 0.09 J/m^2) [102]. The limiting case of replacing Al atoms in all twelve metal layers of the alumina was also considered. The latter is called *V_2O_3 -like* slab because the surface unit cell has the lattice parameters of the $\alpha\text{-Al}_2\text{O}_3$ support. By adding an oxygen atom to every vanadium site in the surface layer, (1×1) vanadyl-terminated films can be created, with the general formula $\frac{1}{2}\text{V}_2\text{O}_5 \cdot \frac{n-1}{2}\text{V}_2\text{O}_3 \cdot \frac{12-n}{2}\text{Al}_2\text{O}_3$ (see e.g., Fig. 3.3D). The composition of the surface layer is V_2O_5 , but the coordination of vanadium is different from that in the single-crystal $\text{V}_2\text{O}_5(001)$ surface, where vanadium is coordinated to five oxygen atoms within the layer (one vanadyl oxygen, one 2-fold coordinated bridging oxygen, and three 3-fold coordinated bridging oxygen atoms) and there is a weak bond to the vanadyl oxygen of the layer beneath [105].

Figure 3.3A shows the supported 6V-layer vanadia film that is terminated by a single-metal layer, keeping the V_2O_3 composition. It is named $\text{V-O}_3\text{-V}(\text{V-O}_3\text{-V})$ according to the sequence of V and O atomic layers of the corundum structure from the surface into the bulk. This nomenclature includes only the atomic layers that are relevant for the following discussion, that is, those in the two outermost $\text{V-O}_3\text{-V}$ trilayers. The oxygen-terminated $\text{O}_3\text{-V}(\text{V-O}_3\text{-V})$ film (Fig. 3.3B, a total of five V layers) and the double-metal-terminated $\text{V}(\text{V-O}_3\text{-V})$ film (Fig. 3.3C, also five V layers), together with the single-metal film, belong to the so-called *intrinsic* bulk terminations. They result from the successive removal of the outermost V and O_3 layers, respectively, from the stoichiometric slab. Thus, they do not have V_2O_3 composition.

Starting from the 6V-layer film, several modifications were considered that include the (1×1) vanadyl-terminated film, $\text{O}=\text{V-O}_3\text{-V}(\text{V-O}_3\text{-V})$, cf. Fig. 3.3D. To obtain intermediate situations between a (1×1) V-terminated surface ($\Theta_{\text{O}} = 0$, in which Θ_{O} is the concentration of vanadyl oxygen atoms) and a (1×1) $\text{O}=\text{V}$ -terminated surface ($\Theta_{\text{O}} = 1$), oxygen atoms were added to $1/4$, $1/2$, or $3/4$ of the vanadium surface sites. Therefore, (2×2) unit cells with mixed $\text{O}=\text{V}$ and V terminations were considered. On the basis of the $(\sqrt{3} \times \sqrt{3})R30^\circ$ geometry, two additional oxygen coverages are possible, namely, $\Theta_{\text{O}} = 1/3$ and $2/3$ (see Figure 3.4).

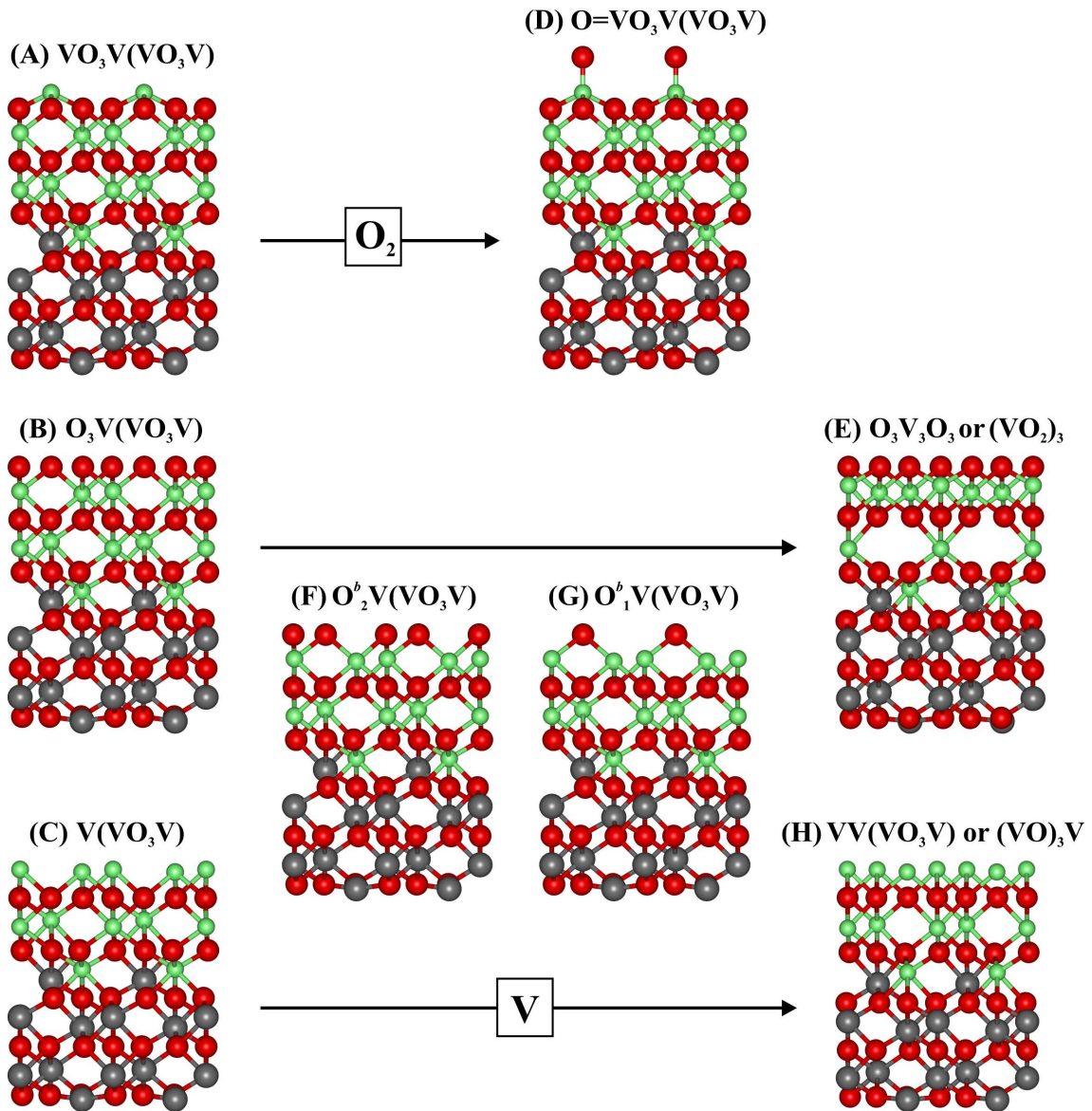


Figure 3.3: Side view of the models for differently terminated 6V-layer-supported oxide films with (1×1) periodicity. The models are labeled according to the sequence of atomic layers from the surface into the bulk. The nomenclature includes only the two outermost (V-O₃-V) trilayers. (A) V-O₃-V(V-O₃-V), (B) O₃-V(V-O₃-V), (C) V(V-O₃-V), (D) O=V-O₃-V(V-O₃-V), (E) O₃-V₃-O₃, (F) O^b₂-V(V-O₃-V), (G) O^b₁-V(V-O₃-V), (H) VV(V-O₃-V). V atoms are depicted in green, Al in gray, and O in red.

The polar (oxygen-terminated) O₃-V(V-O₃-V) surface can *reconstruct* to reduce its polarity. Figure 3.3E shows one example in which half of the vanadium atoms of the second V double layer pop into the first V double layer, leading to a O₃-V₃-O₃ sequence. This corresponds to a nonpolar hexagonal film of VO₂ composition [(VO₂)₃] on top of a single V-layer-terminated slab (V-O₃-V-Al...). This

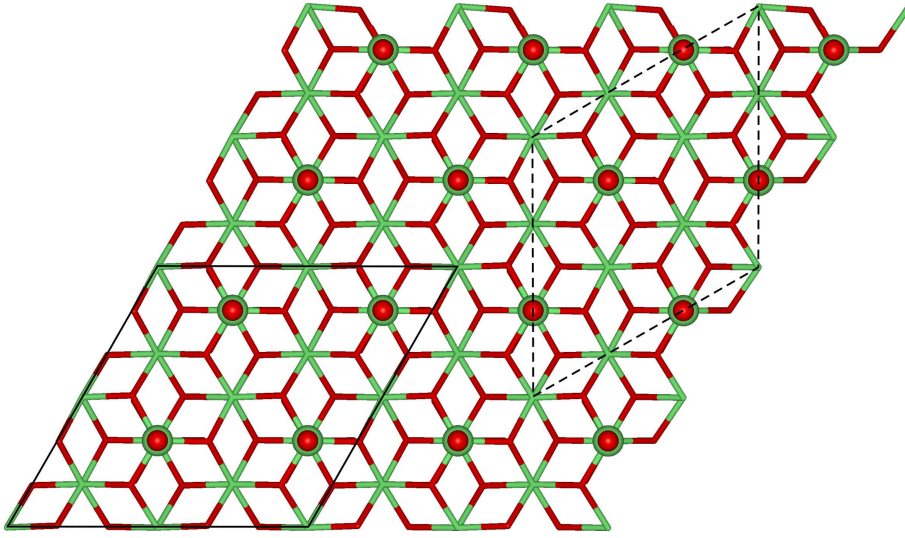


Figure 3.4: Top view of a fully vanadyl-covered surface of a vanadium oxide film supported on α - Al_2O_3 . (2×2) and $(\sqrt{3} \times \sqrt{3})R30^\circ$ unit cells are indicated by solid and broken lines, respectively.

reconstruction has recently been proposed for the (0001) surface of bulk V_2O_3 [107]. Another way of reducing the polarity is to remove 1/3 or 2/3 of the oxygen atoms from the O_3 surface layer, creating surface terminations with 2/3 (Fig. 3.3F) and 1/3 (Fig. 3.3G) monolayers (MLs) of O atoms at bridge positions. Their electronic and structural properties have recently been theoretically investigated for the $\text{V}_2\text{O}_3(0001)$ surface using cluster models [108]. The $\text{O}_2^b\text{V}(\text{V}-\text{O}_3-\text{V})$ termination (Fig. 3.3F) corresponds to the structural model of Refs. [71] and [13] for the termination of the $\text{V}_2\text{O}_3/\text{Cu}_3\text{Au}(100)$ film. An even more V-rich surface termination can be created from the double-metal-terminated film (Fig. 3.3C) by fully occupying the topmost layer with V atoms, yielding $\text{VV}(\text{V}-\text{O}_3-\text{V})$ or $(\text{VO})_3\text{V}$ (Fig. 3.3H).

The $\text{O}_3-\text{V}_3-\text{O}_3$ surface (Fig. 3.3E) discussed above can also be obtained from a fully vanadyl-covered film by removal of all of the $\text{V}=\text{O}$ groups and subsequent reconstruction. Moreover, surfaces with a $(\sqrt{3} \times \sqrt{3})R30^\circ$ periodicity, in which only part of the vanadyl groups (1/3 or 2/3) is removed and the above-described reconstruction is made, except for the sites with $\text{V}=\text{O}$ groups were considered. Their terminations are given by the general formula $(\text{O}=\text{V})_x-\text{O}_3-\text{V}_{3-x}-\text{O}_3-\text{V}_x$, with $x = 1/3$ and $2/3$ being the concentration of vanadyl groups. In the following, they will be termed $\sqrt{3}-(\text{O}=\text{V})_x$ films. The three reconstructed structures are investigated for two film thicknesses, namely, 4V and 6V layers. Removal of single vanadyl oxygen atom from these surfaces was also considered, and the corresponding surfaces are labeled $\sqrt{3}-(\text{O}=\text{V})_x^{\text{reduced}}$.

Of special interest for us are also different low-coverage VO_x species, such as monomer and dimers. Isolated VO_x sites that are created by replacing one of the outermost Al atoms in a (2×2) unit cell of the α - $\text{Al}_2\text{O}_3(0001)$ slab (surface area A

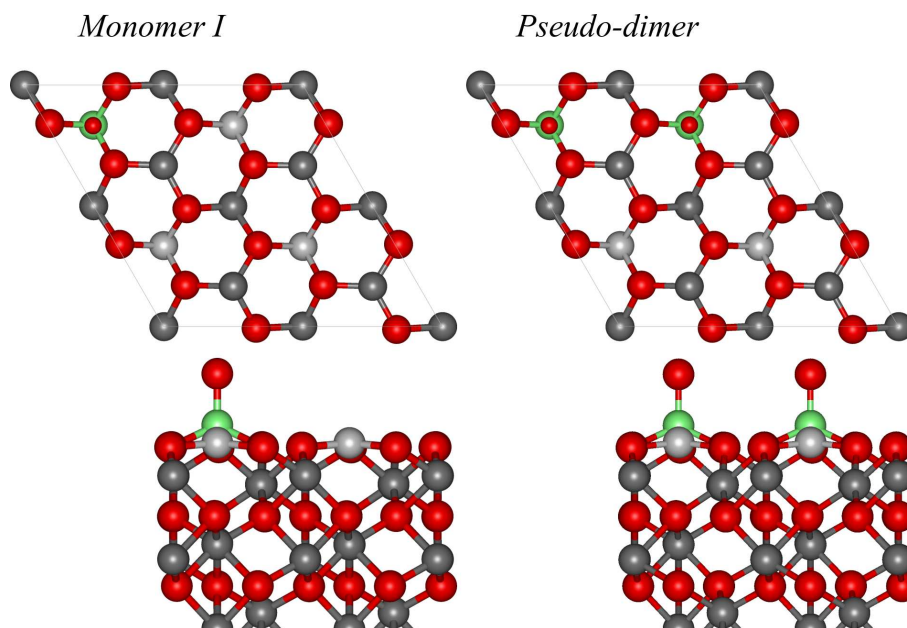


Figure 3.5: Top and side view of the monomeric and dimeric VO_x species on the $\alpha\text{-Al}_2\text{O}_3(0001)$ surface modeled by replacement. V atoms are depicted in green, O in red, Al in dark gray, whereas the topmost Al atoms are in light gray.

$= 80 \text{ \AA}^2$) by a $\text{V}=\text{O}$ group are separated by 9.60 \AA from the next-neighbor vanadyl groups. They are referred to as monomers type I. Replacement of one additional Al atom in a nearest-neighbor position results in the formation of “dimeric” vanadia sites that are separated by a distance of 4.80 \AA and are termed *pseudo-dimeric* sites because they are not connected via a direct $\text{V}-\text{O}-\text{V}$ bond. These species are anchored to the surface exclusively with $\text{V}-\text{O}^{(3)}-\text{Al}$ interface bonds and are visualized in Figure 3.5. Another approach to model low-coverage vanadia is by “landing” small (V_2O_5 or V_2O_4) gas-phase clusters on the clean α -alumina surface. Such obtained dimeric species have recently been investigated [109]. The authors reported on two very stable V_2O_5 clusters on the $\alpha\text{-Al}_2\text{O}_3(0001)$ support, which differ by only 0.12 eV , with adsorption energies of 6.80 and 6.67 eV [109]. Interestingly, the more stable one is nearly an “extension” of the bulk corundum structure, i.e., oxygen atoms follow the hexagonal stacking of the oxygen layers, whereas both V atoms occupy octahedral interstitial sites. Their reduction, giving rise to various $\text{V}_2\text{O}_4/\alpha\text{-Al}_2\text{O}_3$ clusters was also investigated. The most stable structure was obtained upon removal of a single oxygen atom from the $\text{V}-\text{O}^{(2)}-\text{Al}$ interface bond, resulting in formation of a four-membered $\text{V}-\text{O}_2-\text{V}$ ring upon lattice relaxation [109]. If one of the two V atoms in the $\text{V}_2\text{O}_4/\alpha\text{-Al}_2\text{O}_3$ structure is replaced by an Al atom, monomers are created. They are referred to as monomers type II. Figure 3.6 shows the most stable VO_x species (monomers and dimers) obtained in such a way. The major structural difference as compared to the aforementioned low-coverage species (Fig. 3.5) is the existence of twofold coordinated oxygen atoms $\text{O}^{(2)}$ at the interface ($\text{V}-\text{O}^{(2)}-\text{Al}$).

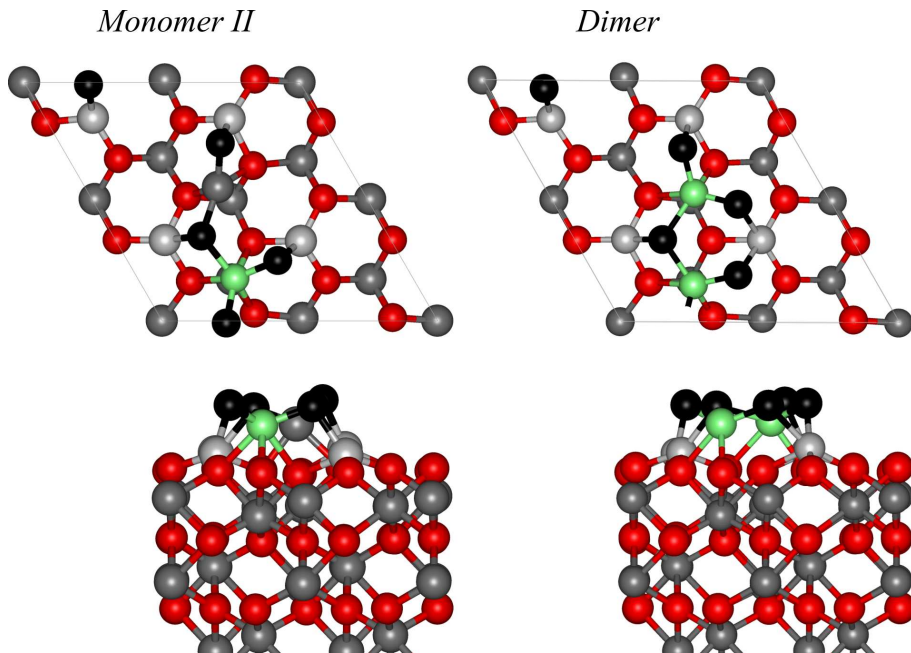


Figure 3.6: Top and side view of the monomeric and dimeric VO_x species on the $\alpha\text{-Al}_2\text{O}_3(0001)$ surface modeled by gas-phase cluster adsorption. V atoms are depicted in green, Al in dark gray, the topmost Al in light gray, O atoms from $\alpha\text{-Al}_2\text{O}_3$ are in red, whereas those from a V_2O_5 unit are in black.

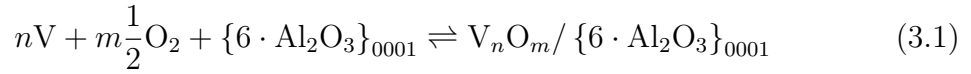
To sample the surface BZ of the vanadia/ α -alumina systems, a $(6 \times 6 \times 1)$ k -point mesh for the (1×1) hexagonal cell was used. The larger grid, as compared to the $(3 \times 3 \times 1)$ grid used for the alumina support is required because of the metallic character of V_2O_3 . For the larger (2×1) , $(\sqrt{3} \times \sqrt{3})R30^\circ$, and (2×2) surface unit cells, $(3 \times 6 \times 1)$, $(3 \times 3 \times 1)$, and $(3 \times 3 \times 1)$ grids were used, respectively. Regarding the PAW potentials, core radii of 2.3 and 1.9 au are used for V and Al, respectively. The $3p$ semi-core states of vanadium are treated as valence states to guarantee a good transferability of the potential. The O core radii are 1.2 and 1.52 au for the s and p states, respectively.

To evaluate the oxygen defect formation energies of the alumina-supported vanadium oxides investigated in this work (see Sec. 3.1.4), the total energy of the oxygen molecule is needed. A $(13 \times 14 \times 15)$ \AA^3 orthorhombic unit cell with Γ -point sampling of the BZ and 800 eV energy cutoff are employed. Both oxygen atom and molecule have triplet ground state, therefore spin-polarized calculations have been performed. The binding energy per O atom in O_2 is 3.14 eV and the bond distance is 1.222 \AA . The experimental values are 2.59 eV/atom (obtained after adding the contributions due to zero point vibrations) and 1.207 \AA , respectively [110]. The overestimation of the binding energy and the bond distance is in line with previous density functional calculations that used gradient-corrected functionals [111] (see also Ref. [48] for a comparison of different functionals).

3.1.3 Thermodynamic Stability

Supported vanadium oxides are prepared by evaporating metallic vanadium on the support in an oxygen atmosphere (see e.g., Ref. [16]). Statistical thermodynamics is applied to account for the effect of vanadium activity (concentration) and oxygen partial pressure at a given temperature on the stability of vanadia aggregates supported on the stable Al₂O₃(0001) surface [87]. The formalism has been applied to a variety of systems before (see e.g., Refs. [112–114].)

The following equilibrium reaction is considered:



with the reaction energy change:

$$\Delta E = E_{\text{V}_n\text{O}_m/\{6 \cdot \text{Al}_2\text{O}_3\}_{0001}} - E_{\{6 \cdot \text{Al}_2\text{O}_3\}_{0001}} - nE_{\text{V}}^{\text{bulk}} - m\frac{1}{2}E_{\text{O}_2} \quad (3.2)$$

Here, $E_{\text{V}_n\text{O}_m/\{6 \cdot \text{Al}_2\text{O}_3\}_{0001}}$ and $E_{\{6 \cdot \text{Al}_2\text{O}_3\}_{0001}}$ are the total energies of the alumina-supported vanadium oxide with a given composition and surface termination and the six trilayer clean α -Al₂O₃(0001) surface, respectively. Note that the energies always refer to slabs with the same amount of Al₂O₃, namely, 6 formula units. n and m are the number of V and O atoms in the supported vanadium oxide, respectively. $E_{\text{V}}^{\text{bulk}}$ and E_{O_2} are the total energies of the metallic body-centered cubic (bcc) bulk vanadium and the oxygen molecule, respectively. The accompanying change in the surface free energy $\Delta\gamma$ is

$$\Delta\gamma(T, p) = \frac{1}{A} [\Delta E - n\Delta\mu_{\text{V}} - m\Delta\mu_{\text{O}}] \quad (3.3)$$

where A is the area of the surface unit cell. Here, the chemical potential differences, $\Delta\mu_i$, are defined as

$$\Delta\mu_{\text{V}}(T, a_{\text{V}}) = \mu_{\text{V}}(T, a_{\text{V}}) - E_{\text{V}}^{\text{bulk}} \quad (3.4)$$

$$\Delta\mu_{\text{O}}(T, p) = \frac{1}{2} [\mu_{\text{O}_2}(T, p) - E_{\text{O}_2}] \quad (3.5)$$

The Gibbs free energies of the solid components, i.e., V_{*n*}O_{*m*}/Al₂O₃ and the clean Al₂O₃(0001) surface have been approximated by the calculated DFT energies at zero temperature and a given unit cell volume. This means that zero-point vibrations, vibrational entropy contributions, and enthalpy changes are neglected.

It is assumed that the number of V and O atoms removed or added to the slab varies independently. Thus, two independent extensive thermodynamic variables, μ_{V} and μ_{O_2} , control the vanadia aggregates formation. The V and O chemical potentials depend on the temperature and the vanadium activity, a_{V} (in reference to the corresponding crystalline solid), or the oxygen partial pressure, p (in reference to the molecular gas), respectively. As the surrounding O₂ atmosphere forms an

ideal gas reservoir, the pressure dependence of $\Delta\mu_{\text{O}}(T, p)$ at a given temperature is expressed as

$$\Delta\mu_{\text{O}}(T, p) = \frac{1}{2} [H(T, p^\circ) - H(0 \text{ K}, p^\circ) - TS(T, p^\circ) + RT \ln(p/p^\circ)] \quad (3.6)$$

using $\mu_{\text{O}_2}(0 \text{ K}) = E_{\text{O}_2}$. Here, p° is the pressure of the reference state ($p^\circ = 1 \text{ atm}$). For a solid component, $\Delta\mu_{\text{V}}(T, a_{\text{V}})$ is given by

$$\Delta\mu_{\text{V}}(T, a_{\text{V}}) = \Delta\mu_{\text{V}}(T_{\text{r}}) + \left[\int_{T_{\text{r}}}^T C_{\text{p}} dT - (T - T_{\text{r}}) S^\circ(T_{\text{r}}) - T \int_{T_{\text{r}}}^T (C_{\text{p}}/T) dT \right] + RT \ln(a_{\text{V}}) \quad (3.7)$$

with

$$\Delta\mu_{\text{V}}(T_{\text{r}}) = H^\circ(T_{\text{r}}) - H^\circ(0 \text{ K}) - T_{\text{r}} S^\circ(T_{\text{r}}) \quad (3.8)$$

Here, $\mu_{\text{V}}(0 \text{ K}) = E_{\text{V}}^{\text{bulk}}$ has been used. $T_{\text{r}} = 298.15 \text{ K}$ and tabulated values for the enthalpy H , entropy S , and given expressions for the temperature dependence of the specific heat $C_{\text{p}}(T)$ are used [115–117]. From a practical point of view, the vanadium activity can be varied by controlling the amount of evaporated vanadium forming the vanadium oxide and is related to the concentration through the activity coefficient, γ_{V} [114].

It is understood that the V and O particle reservoirs are in equilibrium with (metallic) bulk V and O_2 in the gas phase. To determine the most stable surface for a given set of chemical potentials ($\Delta\mu_{\text{O}}$ and $\Delta\mu_{\text{V}}$), the surface free energy is calculated for *all* systems investigated, i.e., the clean alumina surface, different low-coverage VO_x species as well as vanadium oxide films of varying thickness. The one with the lowest $\Delta\gamma$ is the thermodynamically most stable phase for the corresponding conditions. The resulting two-dimensional (2D)-surface phase diagram is shown in Figure 3.7. The $\Delta\mu_{\text{O}}$ axis is translated into an oxygen pressure scale at $T = 300$ and 800 K using Eq. (3.6) and the $\Delta\mu_{\text{V}}$ axis into an activity scale at $T = 800 \text{ K}$ using Eqs. (3.7) and (3.8).

If the V and O particle reservoirs would be in thermodynamic equilibrium with vanadia bulk phases, for example, V_2O_3 or VO_2 , the vanadium and oxygen chemical potentials will be coupled by

$$2\Delta\mu_{\text{V}} + 3\Delta\mu_{\text{O}} = \Delta E_{\text{V}_2\text{O}_3} \quad (3.9)$$

or

$$\Delta\mu_{\text{V}} + 2\Delta\mu_{\text{O}} = \Delta E_{\text{VO}_2} \quad (3.10)$$

respectively. The values of $\Delta\mu_{\text{V}}$ and $\Delta\mu_{\text{O}}$ that would correspond to V and O reservoirs in thermodynamic equilibrium with V_2O_3 bulk phase are indicated by a dotted line in Figure 3.7. $\Delta E_{\text{V}_2\text{O}_3}$ and ΔE_{VO_2} are the energies of formation of the bulk oxides:

$$\Delta E_{\text{V}_2\text{O}_3} = E_{\text{V}_2\text{O}_3}^{\text{bulk}} - 2E_{\text{V}}^{\text{bulk}} - \frac{3}{2}E_{\text{O}_2} \quad (3.11)$$

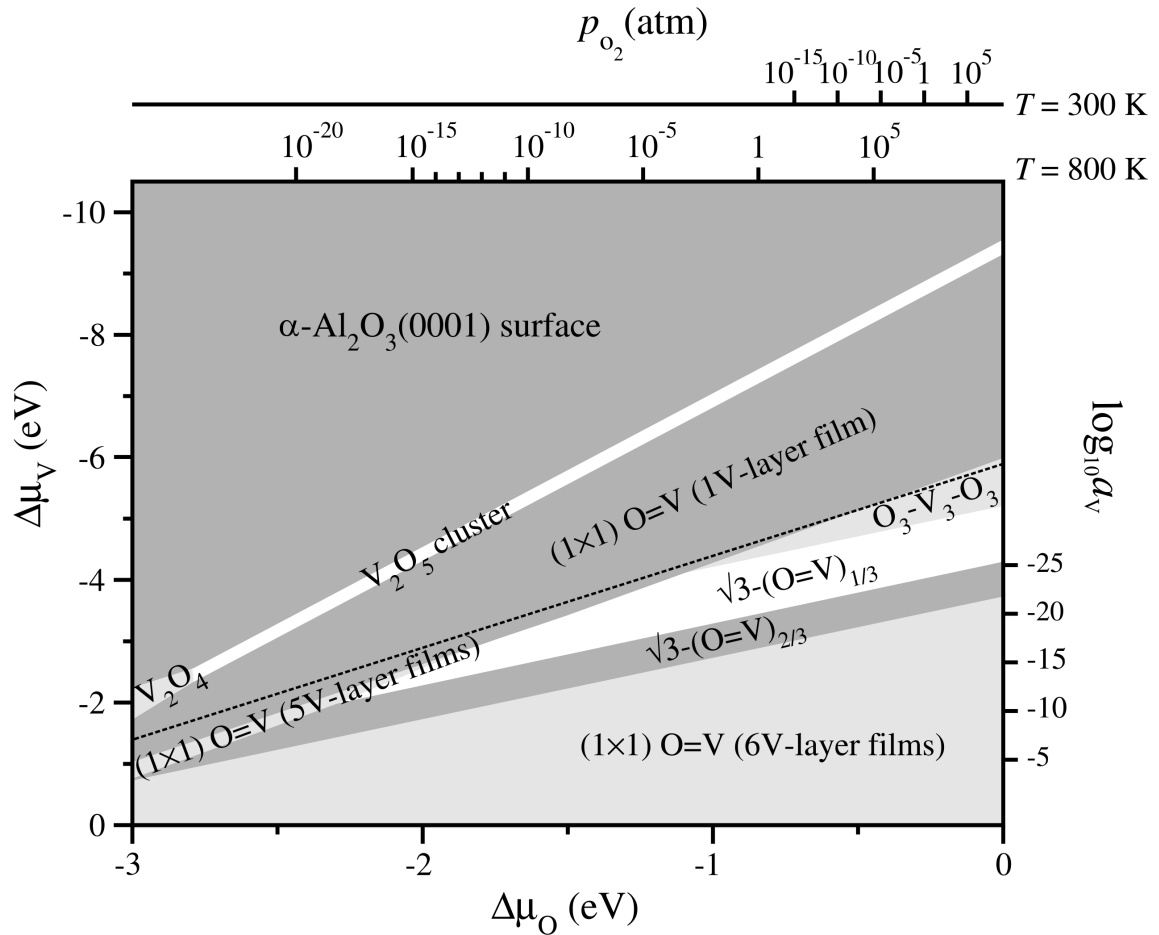


Figure 3.7: Phase diagram as a function of the $\Delta\mu_{\text{O}}$ and $\Delta\mu_{\text{V}}$ chemical potentials for vanadia aggregates supported on the $\alpha\text{-Al}_2\text{O}_3(0001)$ surface. $\Delta\mu_{\text{O}}$ and $\Delta\mu_{\text{V}}$ have been translated into a pressure scale at $T = 300$ and 800 K and an activity scale at $T = 800$ K, respectively.

$$\Delta E_{\text{VO}_2} = E_{\text{VO}_2}^{\text{bulk}} - E_{\text{V}}^{\text{bulk}} - E_{\text{O}_2} \quad (3.12)$$

for which our DFT calculations give -11.78 (V_2O_3) and -7.24 (VO_2) eV/per formula unit. The experimental results for the heat of formation at 298.15 K are -12.63 and -7.33 ($\beta\text{-VO}_2$) eV, respectively [116, 118]. A comparison of these results with those for V_2O_5 obtained from DFT (-16.41 eV) [119] and experimental determination (-16.07 eV) [116] shows that the PW91 functional overestimates the stability of the more oxygen-rich vanadia phases compared to that of the partially reduced ones.

Our calculations indicate that the only stable low-coverage vanadia species on the $\alpha\text{-Al}_2\text{O}_3(0001)$ support are dimers (V_2O_5 and its reduced counterpart V_2O_4) anchored to the alumina surface with $\text{V}-\text{O}^{(2)}-\text{Al}$ interface bonds. The reduced dimers would only become stable for oxygen chemical potential $\Delta\mu_{\text{O}} \leq -2.8$ eV, which corresponds to a pressure of 10^{-12} atm at very high temperatures (1200 K). The

structure of the α -support does not allow for the formation of differently anchored dimeric species, e.g., with V–O⁽³⁾–Al interface bonds. Interestingly, none of the two monomeric types at $\Theta = 0.25$ ML coverage (see Figs. 3.5 and 3.6) would form. Furthermore, Fig. 3.7 shows the stability of vanadium oxide films which are anchored to the alumina surface exclusively via V–O⁽³⁾–Al interface bonds. The thinnest (1×1) O=V-terminated film (~ 2 Å, 1V layer) is stable for chemical potentials of V and O that are not sufficient (not high enough) for the formation of bulk V₂O₃ oxide, that is, in the region above the dotted line. For the highest chemical potentials, the corresponding thickest possible 6V-layer film forms. In an intermediate range, the $\sqrt{3}$ -(O=V)_{1/3} and $\sqrt{3}$ -(O=V)_{2/3} terminations, which result from the (1×1) vanadyl-terminated 6V-layer film by partial removal of surface V=O groups and subsequent reconstruction, become stable. There is only a small range of oxygen and vanadium potentials for which 5V-layer films are energetically favorable, namely, (1×1) O=V (5V layers) and O₃–V₃–O₃ (Fig. 3.3E). Hence, for the thicker films, the same possible terminations as those recently predicted for the single-crystal V₂O₃(0001) surface were obtained [107]. It is noteworthy that no other vanadium oxide films with thicknesses between the thinnest and thickest ones are predicted to form. A thicker slab (number of trilayers > 6), allowing thicker vanadia films, would result in the same phase diagram with respect to the stability regions of thin vs. thick films. That is, the stability regions for the thicker films in Figure 3.7 will be replaced by those of even thicker films and the same surface structures will be present for the latter.

The 2–6 Å thickness range for the vanadia aggregates investigated in this work is well within the thickness of the experimental vanadia model systems of Ref. [16]. They were prepared at room temperature (300 K) in UHV (10^{-13} atm), whereas typical reducing conditions are UHV and elevated temperatures (e.g., 800 K). The corresponding $\Delta\mu_{\text{O}}$ values are approximately -0.66 and -1.88 eV, respectively. In UHV and 300 K, the calculations favor (mostly) vanadyl-terminated surfaces independent of the film thickness, which is consistent with the analysis of the IR spectra of the experimental vanadia particles [16]. The phase diagram indicates that V=O groups are stable up to at least 800 K, which, in turn, is consistent with the experimental results [12].

For a given oxygen pressure and temperature, the precise surface structure depends on the vanadium chemical potential. For large $\Delta\mu_{\text{V}}$ values (high vanadium activity), the (1×1) fully vanadyl-covered, 6V-layer surface is the stable phase. As the V coverage decreases, the reconstructed $\sqrt{3}$ -(O=V)_{*x*} phases with $x = 2/3$ and, in turn $1/3$ become more favorable. The values of $\Delta\mu_{\text{V}}$ for which these transitions occur are approximately 1 eV smaller in UHV at $T = 300$ K than at $T = 800$ K. These terminations have less vanadyl groups and are more vanadium-poor (more oxygen-rich) compared to the (1×1) O=V phase. For even lower $\Delta\mu_{\text{V}}$ values in UHV and 300 K, the whole surface reconstructs, yielding a O₃–V₃–O₃ termination and no V=O groups. This VO₂ termination is also stable at 800 K, but at higher O₂ pressure (~ 1 atm). For $\Delta\mu_{\text{V}} < \frac{1}{2} [\Delta E_{\text{V}_2\text{O}_3} - 3\Delta\mu_{\text{O}}]$, that is, values above the

dotted line in Fig. 3.7, the ultrathin films (1V layer) stabilize at the (1×1) O=V termination. At 300 K and UHV, a $\Delta\mu_V$ value approximately 2 eV lower than at 800 K is required to stabilize this 1V-layer film. Upon further reduction of $\Delta\mu_V$, low-coverage dimeric VO_x species on the alumina support are favored.

Our calculations suggest that the termination of vanadium oxide films with thickness of $\geq 6 \text{ \AA}$ grown on $\alpha\text{-Al}_2\text{O}_3(0001)$ surface may be varied either by changing the temperature at a given O_2 pressure (V supply switched off) or by varying the vanadium activity while controlling T and the oxygen pressure. For instance, if UHV and room temperature are assumed, *five* terminations are possible at varying values of $\Delta\mu_V$. These surface terminations are likely to be present among the vanadia particles ($\sim 6 \text{ \AA}$) grown on alumina at these conditions [16]. Thus, the presence of vanadyl species, as observed in the IR spectra, does not necessarily imply a complete coverage with V=O groups (1×1 termination).

As mentioned above, at a temperature of 300 K, a partial pressure of approximately 10^{-13} atm corresponds to $\Delta\mu_O \approx -0.66$ eV, which is not significantly different from the values that correspond to conditions typically employed in oxidation reactions, namely, atmospheric pressure and a temperature of 500–600 K ($\Delta\mu_O = -0.50$ and -0.61 eV, respectively). Thus, the results of the present study suggest that the discussed stable terminations are expected to also exist at catalytically relevant conditions.

Finally, it is important to mention that the PW91 functional tends to overestimate formation and binding energies, which means that the calculated chemical potentials may shift by several hundred meV. Thus, the absolute pressures and activities may change by 2–3 orders of magnitude. Moreover, the overestimation of the stability of the more oxygen-rich bulk vanadia phases mentioned above also applies to the theoretically predicted stability ranges of the $\sqrt{3}\text{-(O=V)}_x$ terminations of the supported films. Theory puts the subsequent transitions between the (1×1) O=V, $\sqrt{3}\text{-(O=V)}_{2/3}$, and $\sqrt{3}\text{-(O=V)}_{1/3}$ terminations at somewhat lower (i.e., more negative) $\Delta\mu_O$ values. This was recently shown for the $\text{V}_2\text{O}_3(0001)$ surface, for which theory [107] and experiment [66] agree that vanadyl groups are progressively removed from the surface with increasing oxygen pressure; however, they disagree on the range in which the (1×1) O=V and $\sqrt{3}\text{-(O=V)}_x$ terminations are stable.

3.1.4 Reducibility of Vanadia Aggregates on $\alpha\text{-Al}_2\text{O}_3$

Isotopic-labeling studies of supported vanadia catalysts have shown that lattice oxygen atoms take part as reactive intermediates in Mars-van Krevelen-type oxidation reactions [120, 121]. If we accept that the activity of the heterogeneous catalyst depends on its ability to release lattice oxygen, the energy of *surface* oxygen defect formation may be used as an indicator of its catalytic activity. Note that the trends in the enthalpy of this reduction reaction are not to be compared with the reducibility trends as deduced from temperature programmed reduction experiments. In this technique, the catalyst is heated in a flow of hydrogen while monitoring the

hydrogen consumption leading to the reduction of *all* reducible species, i.e., not only those at the surface. The results yield information on the kinetics of this reduction process.

In view of the relation between the catalytic performance of supported vanadia catalysts and surface reducibility, the dissociation of the surface vanadyl bonds of the ultrathin 1V- and thick 6V-layer films on the α -Al₂O₃(0001) surface is first examined. The results are vanadyl oxygen defects at different concentrations $\Theta_{\text{def}} = N_{\text{def}}/N_{\text{tot}}$. The values N_{def} and N_{tot} are the actual and maximum possible number of vanadyl oxygen defects in the unit cell, respectively.

The average vacancy formation energy, $E_f(\Theta_{\text{def}})$ is given by

$$E_f(\Theta_{\text{def}}) = E_{\text{red}}(\Theta_{\text{def}}) - E_{\text{O=V}} + N_{\text{def}} \frac{1}{2} E_{\text{O}_2} \quad (3.13)$$

in which $E_{\text{red}}(\Theta_{\text{def}})$ and $E_{\text{O=V}}$ represent the total energies of the reduced and the vanadyl-terminated surface slab, respectively. Using Eq. (3.13), the energy required to create defect structures with $\Theta_{\text{def}} = 1/4, 1/3, 1/2, 2/3, 3/4,$ and 1 employing (2×2) and $(\sqrt{3} \times \sqrt{3})R30^\circ$ unit cells is calculated. The creation of an isolated oxygen defect at the fully vanadyl-terminated surfaces corresponds to $\Theta_{\text{def}} = 1/4$ and $1/3$ for the respective surface cells. The energy cost for the consecutive removal of such defects is given by

$$\Delta E_f(\Theta_{\text{def}}) = \begin{cases} E_f(\Theta_{\text{def}}) - E_f(\Theta_{\text{def}} - \frac{1}{4}) & \Theta_{\text{def}} = 1/4, 1/2, 3/4, \text{ and } 1 \\ E_f(\Theta_{\text{def}}) - E_f(\Theta_{\text{def}} - \frac{1}{3}) & \Theta_{\text{def}} = 1/3 \text{ and } 2/3 \end{cases} \quad (3.14)$$

For example, $\Delta E_f(\Theta_{\text{def}} = \frac{1}{2})$ is the energy for removal of a second vanadyl oxygen from a (2×2) surface cell.

Figure 3.8 shows the results for the ultrathin 1V- and thick 6V-layer films. For both films, it is easiest to create the first defect. Thus, the formation of additional defects becomes more difficult with increasing defect concentration, Θ_{def} . Furthermore, the calculations suggest a somewhat *less* facile reduction of the ultrathin 1V-layer film. For instance, the creation of a single defect ($\Theta_{\text{def}} = 1/4$) for the 1V-layer film (4.11 eV) is by ~ 0.5 eV more costly than that for the thick 6V-layer film (3.59 eV). This may relate to the insulating nature of the vanadyl-terminated 1V-layer system (see Fig. 3.11A). Moreover, the Θ_{def} dependence due to repulsive interactions is less pronounced for the thin film, for which the difference between the defect formation energies at $\Theta_{\text{def}} = 1/4$ and 1 is 0.37 eV.

For other film terminations that are likely to be stable, namely, the $\sqrt{3}$ -(O=V)_x phases, the energy cost to remove a single vanadyl oxygen is 3.75 eV for $x = 2/3$ and 3.90 eV for $x = 1/3$. These values lie between the $\Delta E_f(\Theta_{\text{def}} = \frac{1}{4})$ for the 6V-layer (3.59 eV) and 1V-layer (4.11 eV) O=V films with (1×1) periodicity. It is noteworthy that this sequence of defect formation energies follows exactly the order of stable terminations in the calculated phase diagram, as the oxygen pressure decreases while the vanadium chemical potential is kept constant (see Fig. 3.7 for the

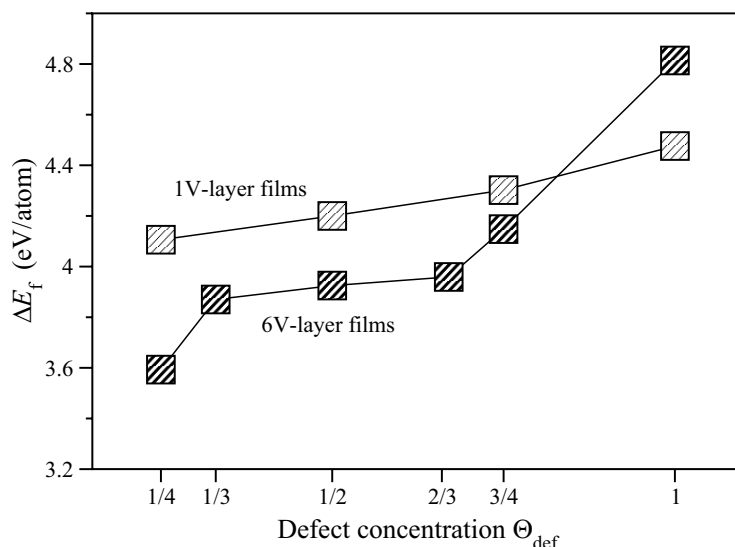


Figure 3.8: Vanadyl oxygen vacancy formation energies in eV/atom for a single defect as a function of the defect concentration Θ_{def} for 1V- and 6V-layer films.

example of $\Delta\mu_{\text{V}} \approx -2.5$ eV). Note that phases that are stable at low oxygen pressure are those that most strongly resist oxygen release (or defect formation) into the gas phase, whereas phases that easily release oxygen require high oxygen pressure for stabilization.

Furthermore, the complete reduction of alumina-supported vanadium oxides by means of removal of all vanadyl oxygen atoms from the (1×1) O=V-terminated films resulting in fully reduced single-metal terminated ones is considered. The reaction energy for this process is given by Eq. (3.13), where $\Theta_{\text{def}} = 1$ and $N_{\text{def}} = 1$. Figure 3.9 shows the vacancy formation energy as a function of vanadia film thickness, with n being the number of V layers in the film ($n = 1-6, 12$). For the thinnest 1V-layer film ($n = 1$), the largest value is obtained (4.27 eV/atom). Gradually increasing the thickness of the vanadia film leads to energy oscillations with decreasing amplitude. The lowest value corresponds to the 2V-layer film with the sequence (V-O₃-V)-(Al-O₃-Al); that is, it contains a V-Al double-metal layer at the V₂O₃/Al₂O₃ interface. For a 3V-layer film, (V-O₃-V)(V-O₃-Al), a value of 4.11 eV/atom is obtained, which differs from that of the V₂O₃-like surface ($n = 12$) by only 0.2%. The $\sim 4\%$ in-plane lattice mismatch between the V₂O₃ and $\alpha\text{-Al}_2\text{O}_3(0001)$ single-crystal surfaces results in a value for the limiting V₂O₃-like case that is 0.07 eV/atom larger than that for the V₂O₃(0001) surface. Thus, with respect to the removal of the vanadyl oxygen atoms from all surface vanadyl groups, a 3V-layer film already behaves like the single-crystal V₂O₃(0001) surface. However, films of intermediate thickness, such as the 3V-layer film, do not show up in the stability plot.

Regarding creation of oxygen defects at the surface of low-coverage α -alumina-

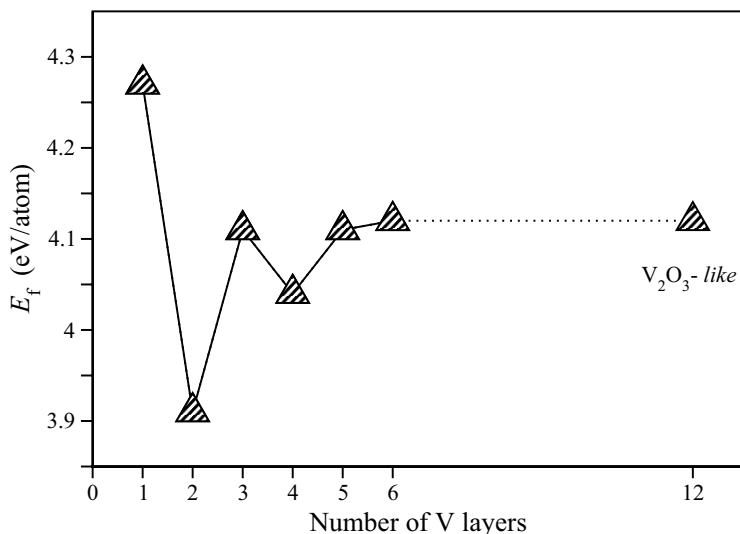


Figure 3.9: Vanadyl oxygen vacancy formation energies in eV/atom for a complete reduction as a function of the number of V layers for (1×1) O=V-terminated vanadia films on α -Al₂O₃.

supported vanadia aggregates (Figs. 3.5 and 3.6), the following results are obtained. Reduction of the isolated VO_x sites created by replacement of an outermost Al atom in the clean (2×2) alumina surface by a vanadyl group and referred to as monomers type I costs 4.56, which upon relaxation is lowered to 4.47 eV and the surface is left metal-terminated. This monomer has exclusively V–O⁽³⁾–Al interface bonds. In contrast, the monomer which resulted from replacement of an Al atom in the most stable V₂O₄ cluster adsorbed on the α -alumina surface (monomer type II) is characterized by the presence of two differently coordinated interface oxygen atoms and no V=O groups. Removal of a bridging oxygen atom at the V–O⁽²⁾–Al interface costs 4.16 eV, whereas 5.53 eV are required for reduction of a bridging oxygen at the V–O⁽³⁾–Al interface. The initial defect formation energy of pseudo-dimeric sites (see Fig. 3.5) is 4.34 eV with a relaxation contribution of only ~ 0.1 eV. In contrast, in the *real* dimer modeled by gas-phase (V₂O₅) cluster adsorption on the clean α -alumina surface, reduction of the least bound oxygen atom, which is a bridging oxygen of the V–O⁽²⁾–Al interface, costs 2.79 eV [109]. The reason is the formation of a new V–O⁽³⁾–V bond at the vanadia/alumina interface upon creation of the defect, resulting in a four-membered V–O₂–V ring. Much larger is the energy cost to remove the vanadyl (3.77 eV) or the bridging V–O⁽²⁾–V (3.70 eV) oxygen atoms from the 0.12 eV less stable V₂O₅/Al₂O₃ structure [109]. The 3.70 eV value for the removal of the bridging O⁽²⁾ is comparable to that of the bridging O⁽²⁾ atoms from the V₂O₅(001) surface.

In summary, formation of isolated oxygen defects at the stable surfaces of supported vanadium oxide films requires between 4.11 (1V-layer film) and 3.59 eV (6V-layer film), which is much larger than the 1.93 eV obtained for the single-crystal

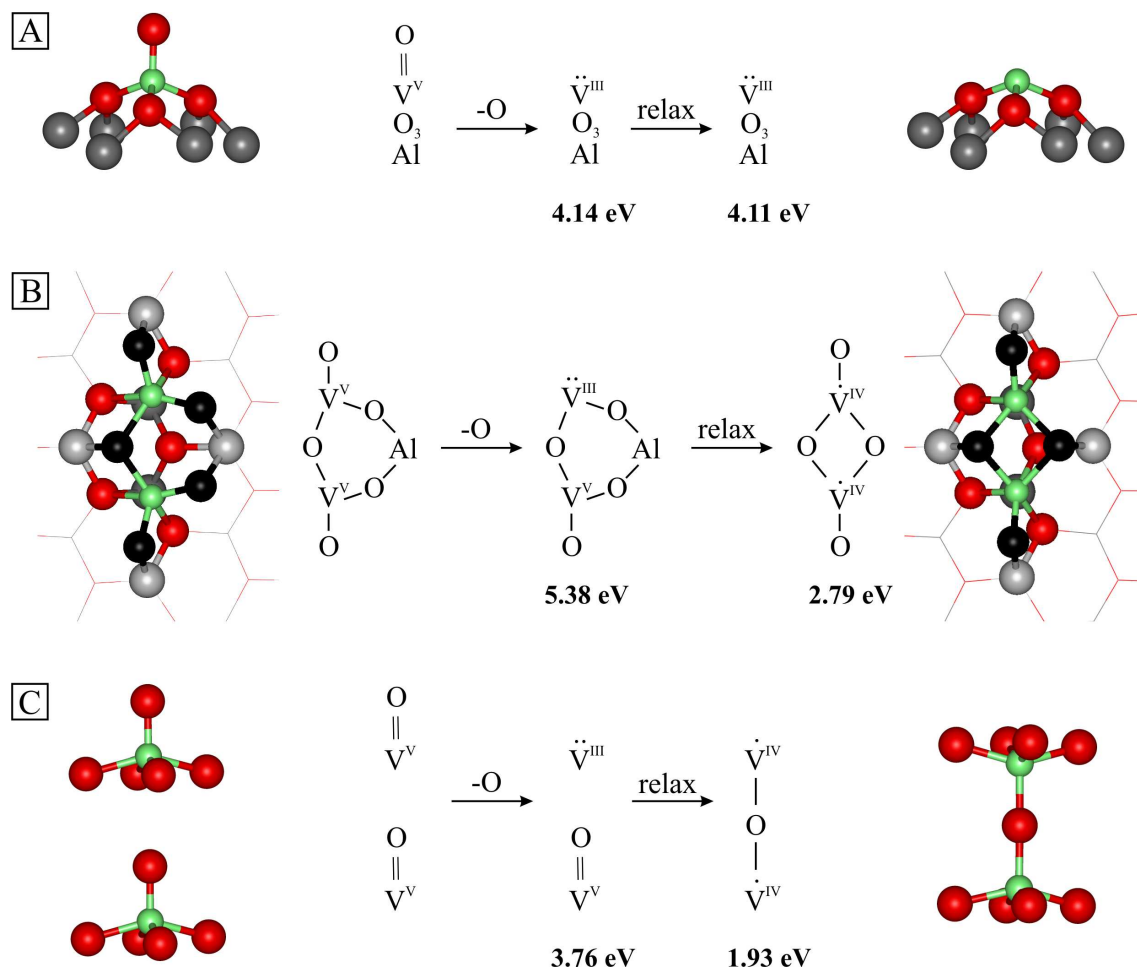


Figure 3.10: Schematic representation of the oxygen-induced structure and electronic effects at the 1V-layer film supported on $\alpha\text{-Al}_2\text{O}_3$ (A), dimeric species on $\alpha\text{-Al}_2\text{O}_3$ (B), and $\text{V}_2\text{O}_5(001)$ single-crystal surface (C). The defect formation energies correspond to those for single defects.

$\text{V}_2\text{O}_5(001)$ [119]. However, as already mentioned, reduction of the only stable low-coverage VO_x species on the $\alpha\text{-Al}_2\text{O}_3(0001)$ support (dimers) costs 2.79 eV, which is 1.3 eV lower than for the ultrathin vanadyl-terminated films and about 0.9 eV larger than for $\text{V}_2\text{O}_5(001)$. The reason is the following: on the supported films, defect formation converts a $\text{O}=\text{V}^{\text{V}}(d^0)$ site into a $\text{V}^{\text{III}}(d^2)$ site (cf. Fig. 3.10A). The lattice relaxations are very small and there is no way of stabilizing the reduced center by forming new bonds. In contrast, oxygen defect formation at the V_2O_5 cluster/ $\alpha\text{-Al}_2\text{O}_3$ as well as at the $\text{V}_2\text{O}_5(001)$ single-crystal surface is accompanied by significant lattice-induced relaxation effects, resulting in formation of new V–O–V bonds. In the former model, this is a V–O⁽³⁾–V bond at the interface, giving rise to a four-membered V–O₂–V ring (Fig. 3.10B), whereas in the later, it is a V–O⁽²⁾–V bond with the V_2O_5 layer beneath the surface layer (Fig. 3.10C). Consequently,

the defect formation energy is lowered from 5.38 to 2.79 eV (dimeric species) and from 3.76 to 1.93 eV (crystalline $V_2O_5(001)$). Interestingly, for both structures, the initially formed upon reduction $V^{III}(d^2)/V^V(d^0)$ pairs are converted into more stable pairs of $V^{IV}(d^1)$ sites. The unrelaxed values are well within the range of values obtained for the alumina-supported vanadia films. Therefore, the creation of oxygen defects at the vanadia surfaces is significantly facilitated by lattice relaxations and as for the V_2O_5 cluster/ α - Al_2O_3 and crystalline $V_2O_5(001)$ by formation of new bonds and $V^{IV}(d^1)$ pairs.

3.1.5 V 2p Surface Core-Level Shifts

As has already been mentioned, surface-sensitive XPS helped solve the apparently conflicting results of Ref. [16], namely, the observation of a characteristic vanadyl stretch frequency and vanadium atoms in the oxidation state of V^{III} . Indeed, for the vanadium atoms at the vanadyl terminated $V_2O_3(0001)$ surface, a shift of the V 2p core levels of ~ 2 eV toward higher binding energies compared to those for the reduced films (i.e., single-metal-terminated) has been observed [12] and confirmed by calculations [107] and additional experiments [66].

In the following, the V 2p adlayer core-level shift (Δ_{ACLS}) for the V atoms in the surface layer induced by the presence of the vanadyl oxygen atoms for differently terminated vanadia films is examined. As mentioned in Sec. 3.1.4, a 3V-layer film behaves like a $V_2O_3(0001)$ single-crystal surface with respect to vanadyl oxygen removal. Therefore, the (1×1) O=V-terminated (metallic) surfaces with three (or more) V layers and the reconstructed $\sqrt{3}$ -(O=V) $_x$ structures are considered.

The oxygen-induced V 2p core-level shift is the difference between the core ionization energies at the vanadyl-terminated surface and at the reduced one. Using the Slater-Janak transition state approach [122, 123], the total shift (Δ_{ACLS}) is approximated as

$$\Delta_{ACLS} \approx -(\varepsilon_{0.5}^{vanadyl} - \varepsilon_{0.5}^{reduced}) \quad (3.15)$$

This shift is decomposed into an initial state contribution ($\Delta_{ACLS}^{initial}$) and a screening contribution (Δ^{scr}). The $\Delta_{ACLS}^{initial}$ component is evaluated as

$$\Delta_{ACLS}^{initial} = -(\varepsilon^{vanadyl} - \varepsilon^{reduced}) \quad (3.16)$$

where $\varepsilon^{vanadyl}$ and $\varepsilon^{reduced}$ are the Kohn-Sham eigenvalues of the V 2p core-states of a V atom at the vanadyl-terminated and reduced surfaces, respectively. The values $\varepsilon_{0.5}^{vanadyl}$ and $\varepsilon_{0.5}^{reduced}$ are the corresponding eigenvalues after the removal of half of an electron from the 2p states. The eigenvalues refer to the Fermi level. The considered systems have a Fermi reservoir of electrons. Thus, to describe the transition state, spin-polarized, self-consistent calculations using a modified PAW potential were performed under the constraint of charge neutrality. This implies that half of a valence electron was added at the Fermi level. By generation of the core-excited PAW potentials, half of a core electron is excited. The other core

Table 3.4: Oxygen-induced V $2p$ adlayer core-level shifts and their initial-state and screening contributions (in eV) for the three outermost V layers of the 3V-layer-supported V_2O_3 film and the $\text{V}_2\text{O}_3(0001)$ surface.

	3V-layer film			$\text{V}_2\text{O}_3(0001)^1$			$\text{V}_2\text{O}_3(0001)^2$
	Δ_{ACLS}	$\Delta_{\text{ACLS}}^{\text{initial}}$	Δ^{scr}	Δ_{ACLS}	$\Delta_{\text{ACLS}}^{\text{initial}}$	Δ^{scr}	Δ_{ACLS}
V_1	1.53	1.34	0.19	1.66	1.20	0.46	0.91
$\text{V}_2\text{-V}_3$	0.18	0.38	-0.20	0.09	0.19	-0.10	0.12

¹This work: spin-polarized calculations²Ref. [107]: non-spin-polarized calculations

electrons are not allowed to relax, whereas the screening by the valence electrons is included. The impurity problem of the localized core-hole is treated using the supercell approach. For the smallest (1×1) cell, atoms with core-holes are separated by $\sim 4.8 \text{ \AA}$.

Table 3.4 shows the vanadyl-induced V $2p$ core-level shift and its initial and screening contributions for the 3V-layer (1×1) O=V-terminated film. Values are given for the atom of the surface layer (V_1), to which oxygen is directly bonded, and average values are given for the atoms in the second and third layers (V_2 and V_3). DFT predicts that, in the outermost V layer (V_1), V $2p$ core electrons are, by 1.53 eV, more bound for the vanadyl-terminated surface than for the single-metal-terminated surface. However, a much smaller shift is predicted for the atoms of the double V-layer beneath. Since screening is small, this is basically an initial state effect. Increasing the film thickness from three to, for example, five V layers results in a 0.19 eV larger shift for the V_1 atoms. For the limiting V_2O_3 -like case, the value is 1.65 eV.

Figure 3.11 displays the contribution of the d -states on the vanadium atoms (in the outermost metal layers) to the total density of states (DOS) for the vanadyl-terminated (Figure 3.11 A.1, B.1) and reduced (panels A.2 and B.2) films. A and B refer to the 1V- and 3V-layer films, respectively. Figure 3.11 C.1, C.2 shows the difference between the spin-up and spin-down DOS for the surface V sites (V_1) for the vanadyl-terminated and reduced 3V-layer films. The integration of these curves (up to the Fermi level) yield 0.03 (vanadyl) and 1.91 (reduced) electrons, which reflects the vanadyl-induced change in the oxidation state of the surface atoms. The positive initial-state contribution to the shift is due to the increase in the oxidation state of vanadium from V^{III} to V^{V} upon oxygen adsorption leading to V=O bond formation. The gain of local charge at the reduced V sites makes the electrostatic potential repulsive and core-level binding energies decrease. The more efficient screening of the core-hole by intraatomic polarization at the reduced surface correlates with the higher d -DOS of the V_1 atom about the Fermi level.

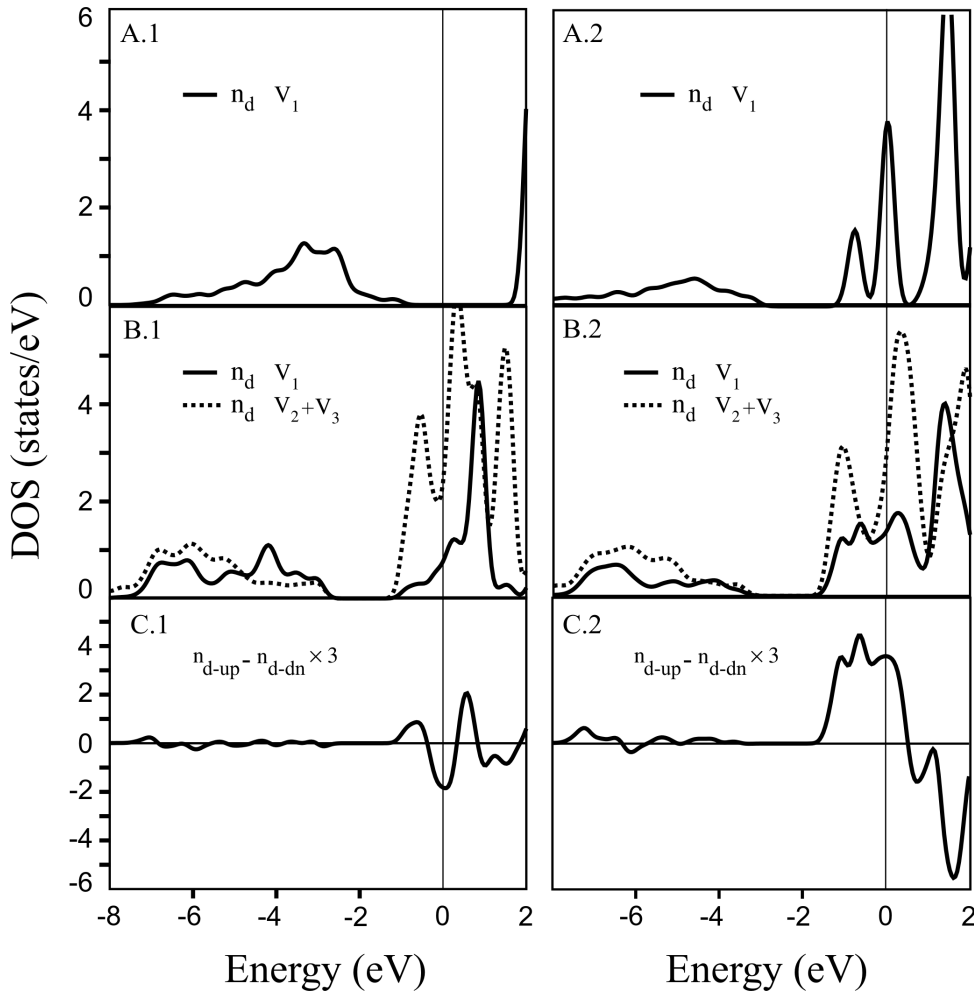


Figure 3.11: d -orbital-projected DOS, n_d for the V atoms in the outermost metal layers. A and B refer to the 1V- and 3V-layer films, respectively. Full lines correspond to the topmost V layer, whereas the dotted lines to the sum of the V atoms in the double-metal layer beneath. A.1/B.1/C.1 and A.2/B.2/C.2 refer to the (1×1) vanadyl and the reduced single-metal terminations, respectively. The d -orbital projected spin density, $(n_{d\text{-up}} - n_{d\text{-dn}})$ for the V_1 atom of the 3V-layer films are shown in C.1/C.2 panels. The curves are smoothed by a Gaussian level broadening of 0.2 eV. The energy zero is at the Fermi level.

The value of 1.53 eV calculated for a 3V-layer film differs only by 0.13 eV from that calculated for the single-crystal $V_2O_3(0001)$ surface atoms (see Table 3.4). The latter compares well with the experimentally observed shift of ~ 2 eV [12]. A non-spin-polarized calculation for the $V_2O_3(0001)$ yields only 0.91 eV, whereas employing the LDA+U method, the shift is 1.86 eV [107]. For the reconstructed $\sqrt{3}-(O=V)_x$ terminations, similar vanadyl oxygen-induced V $2p$ shifts are obtained, namely, 1.73 and 1.69 eV for $x = 1/3$ and $2/3$, respectively. In the experimental work of Ref. [66],

no difference between the measured V 2*p* shift of vanadyl-terminated sites at different structures is reported. The calculated small differences support this observation.

3.1.6 Summary

Combining DFT and statistical thermodynamics, a detailed study on vanadium oxides supported on the α -Al₂O₃(0001) surface has been presented. The calculated phase diagram as a function of vanadium activity and oxygen partial pressure shows that the only stable low-coverage VO_{*x*} species are dimers (V₂O₅ and its reduced counterpart) anchored to the surface via V–O⁽²⁾–Al interface bonds. At room temperature and UHV, (1 × 1) O=V-terminated ultrathin films (thickness ~ 2 Å) are stable for low vanadium chemical potentials. As the $\Delta\mu_V$ values increase, films become as thick as the vanadium supply allows and different surface structures having exclusively V–O⁽³⁾–Al interface bonds are possible, namely, a reconstructed oxygen-terminated (O₃–V₃–O₃) surface, two partially covered by vanadyl groups exhibiting a $(\sqrt{3} \times \sqrt{3})R30^\circ$ geometry, and an unreconstructed surface completely covered by V=O groups. These terminations were also predicted to be stable for the V₂O₃(0001) single-crystal surface [107]. Moreover, all of them are likely to be present not only in UHV and 300 K, but also at catalytically relevant conditions (1 atm, ~500-600 K). The phase diagram indicates that the presence of vanadyl groups is a prevalent feature of the film terminations rendering the oxidation state of vanadium V^V for the surface atoms and V^{III} for the atoms in the bulk, and that V=O groups are stable up to at least 800 K in UHV. For both alumina-supported vanadia films and crystalline V₂O₃(0001), a shift of about 2 eV for the V 2*p* core levels of the surface vanadium atoms verifies the existence of terminating vanadyl oxygen atoms. However, observation of this shift does not necessarily imply complete coverage with V=O groups (1 × 1 termination).

The supported vanadium oxide catalysts are characterized by the ability to release lattice oxygen in Mars-van Krevelen-type oxidation reactions. If we accept that the catalytic activity of the vanadia catalyst depends on its reducibility, the energy of oxygen defect formation may be used as an indicator of its catalytic performance. Reducing the stable α -alumina-supported vanadia films requires energies in the range of 4.11 (ultrathin 1V-layer film) and 3.59 eV (thick 6V-layer film). The defect formation converts a V^V(*d*⁰) site into a V^{III}(*d*²) one and the relaxation effects are very small. It is noteworthy that the sequence of defect formation energies follows exactly the order of stable terminations in the calculated phase diagram as the oxygen pressure decreases, while the vanadium chemical potential is kept constant. In contrast, oxygen defect formation at the only stable low-coverage VO_{*x*} species on the α -Al₂O₃ support (dimers) costs 2.79 eV, which is about 0.9 eV larger than for the V₂O₅(001) single-crystal surface. In both cases, the facile reduction is due to substantial structure relaxations when the defect is created, that involve formation of an additional V–O–V bond and convert a V^{III}(*d*²)/V^V(*d*⁰) pair into a more stable pair of V^{IV}(*d*¹) sites.

3.2 Vanadium Oxides Supported on κ -Al₂O₃(001)

3.2.1 Bulk and (001) Surface of κ -Al₂O₃

κ -Al₂O₃ crystallizes in an orthorhombic structure (40 atoms) within the space group $Pna2_1$ [124]. Although a metastable phase, κ -alumina appears to be very stable, maintaining its structural identity up to temperatures of ~ 1200 K, where it transforms to α -Al₂O₃. For a long time, experimental determination of the structure has been hampered by the poor degree of crystallinity, the difficulty to obtain significant amounts of phase-pure samples, and the metastability. Based on high-resolution electron microscopy studies [125] and X-ray powder diffraction, transmission electron microscopy, and nuclear magnetic resonance results [126], the κ -Al₂O₃ structure has been resolved. Performing thorough DFT calculations on all possible structure candidates consistent with the $Pna2_1$ symmetry (estimated to be 60), Lundqvist and co-workers have found the experimental model as the most stable for κ -Al₂O₃ [19]. In the unit cell, 75% of the Al atoms are Al^O and 25% are Al^T coordinated, which leads to two different types of Al layers alternating along the [001] direction (see Figure 3.12). The first type (“octahedral”) is composed only of Al^O ions, whereas the second contains equal amount of Al^O and Al^T and is called a “mixed” layer. The presence of Al^T sites creates large holes in the octahedral Al layers making the structure much more open compared to that of the α -phase.

The experimental lattice parameters and atomic coordinates were used as a starting point for the structure optimization [126]. The cell parameters and the internal coordinates were simultaneously optimized by a stress tensor calculation, employing

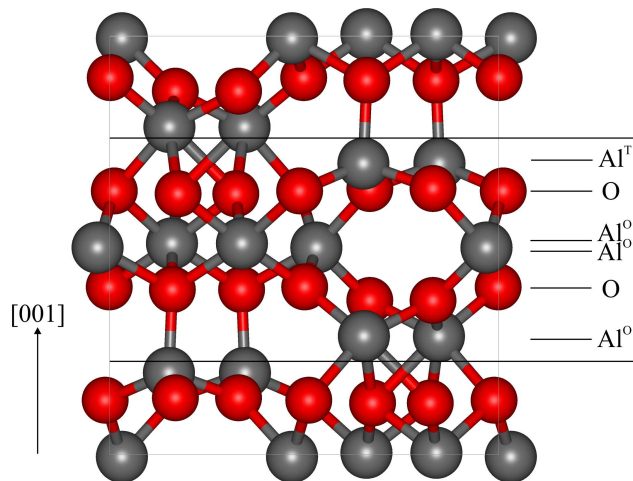


Figure 3.12: Bulk structure of κ -Al₂O₃. The stacking sequence of oxygen and aluminum layers along the [001] direction is shown. One *sixlayer* with the following sequence of atomic layers Al₂^T-O₆-Al₂^O-Al₂^O-O₆-Al₂^O is indicated. O and Al atoms are depicted in red and dark gray, respectively.

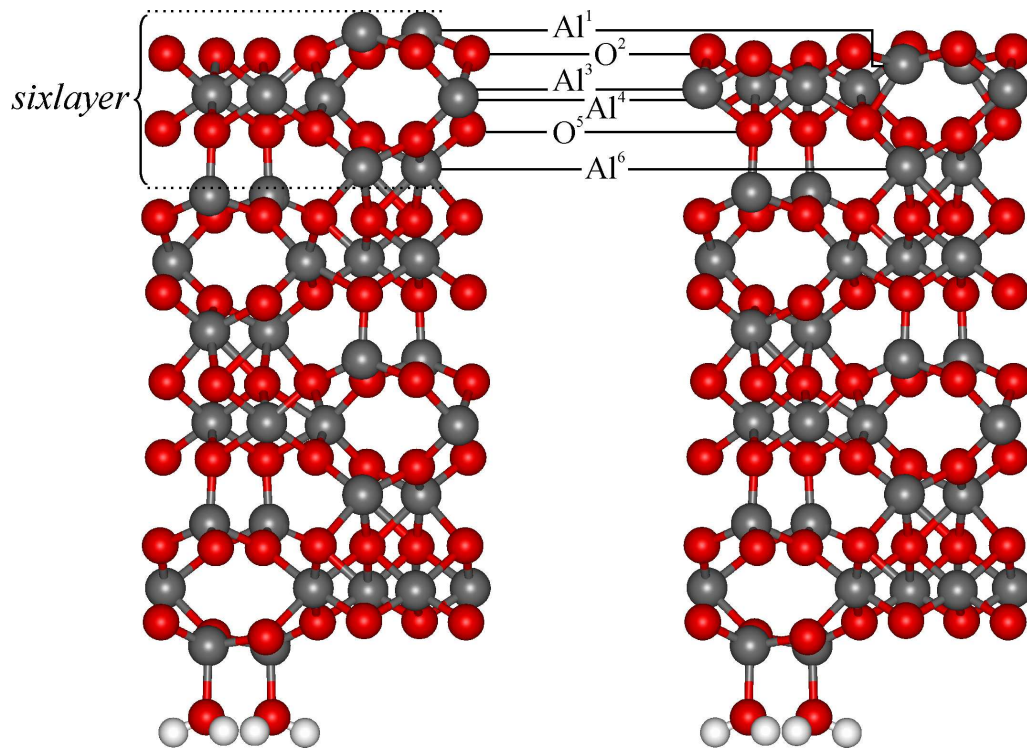


Figure 3.13: Structure of the clean κ -Al₂O₃(001) surface before and after relaxation (side view). The vertical lines indicate the stacking sequence of atomic layers along the [001] direction. The repeating unit (sixlayer) is also marked. The (00 $\bar{1}$) surface is terminated by H₂O molecules.

an energy cutoff of 500 eV and a $(4 \times 2 \times 2)$ k -point mesh. The optimized lattice constants are: $a = 4.882 \text{ \AA}$, $b = 8.393 \text{ \AA}$, and $c = 9.021 \text{ \AA}$, which are in excellent agreement with the experimental lattice constants $a_{\text{exp}} = 4.844 \text{ \AA}$, $b_{\text{exp}} = 8.330 \text{ \AA}$, and $c_{\text{exp}} = 8.955 \text{ \AA}$ as well as with previously reported DFT results [99, 127].

The [001] and [00 $\bar{1}$] are the preferential growth directions of chemical-vapor deposited κ -Al₂O₃ [128]. The atoms in the unit cell are stacked along the [001] direction in a sequence Al₂^T-O₆-Al₂^O-Al₂^O-O₆-Al₂^O...-Al₂^T (see Fig. 3.13). In the following, the term *sixlayer* is used for the repeating unit (Al₂^T-O₆-Al₂^O-Al₂^O-O₆-Al₂^O). The κ -Al₂O₃(001) surface is modeled by a slab consisting of four such sixlayers (16 planes of Al atoms and 8 planes of O atoms) and the vacuum region is $\sim 10 \text{ \AA}$. It has a dipole moment perpendicular to the surface due to the nonsymmetrical interlayer distances around the middle plane of each sixlayer. Thus, according to Tasker's third rule the surface is *polar* [94]. Actually, none of the conceivable terminations that can be obtained upon cleavage along the [001] direction is nonpolar and significant relaxations contribute to the surface stabilization [99, 127]. It was shown that the most stable surface termination, i.e., the one with the lowest separation energy, defined as the energy needed to cleave the infinite crystal and separate the two re-

sulting half-infinite crystals from each other, is terminated by a single aluminum layer (before relaxation) and has no tetrahedral Al ions in its immediate subsurface layers [99, 127]. It resembles the nonpolar single-metal termination of the corundum α -phase, but has two outermost Al atoms per surface unit cell.

In contrast to α -Al₂O₃, κ -Al₂O₃ lacks mirror symmetry through the (001) plane, making the two (001) and (00 $\bar{1}$) surfaces inequivalent. As a consequence, the existence of a one-dimensional metallic surface state on κ -Al₂O₃(00 $\bar{1}$) was predicted [127]. It has recently been suggested that it may have useful applications in carbon nanotubes fabrication because of its affinity to strongly interact and chemisorb graphite sheets [129]. Test calculations indicate that such metallic state would have a dramatic effect on the reducibility of the vanadia aggregates supported on the (001) surface of the slab. Therefore, the bottom (00 $\bar{1}$) surface was terminated by water molecules, thus “quenching” the metallic state and keeping the Al₂O₃ composition unchanged.

The relaxed κ -Al₂O₃(001) supercell was constructed in the following way. First, the coordinates of the two topmost sixlayers at the (001) surface were kept fixed at their bulk positions, while the bottom (00 $\bar{1}$) surface was terminated by two H₂O molecules (one per surface Al ion) and the two bottom sixlayers were fully relaxed. Second, the optimized coordinates of the (00 $\bar{1}$) surface were kept fixed and the (001) surface relaxed. A plane-wave cutoff of 250 eV and a (4 × 2 × 1) Monkhorst-Pack k -point sampling of the Brillouin zone are used for the (1 × 1) slab. Table 3.5 lists the distances between the atomic planes of the topmost sixlayer of the κ -Al₂O₃(001) surface in the relaxed system compared to the ideal bulk-truncated structure. The atomic planes are denoted with superscripts, e.g., Al¹, O², Al³, Al⁴, O⁵, and Al⁶. The Al atoms of the topmost metal layer (Al¹) move inward by 153% or 0.90 Å, i.e., they move inside the holes of the octahedral Al layer. Similarly, the oxygen layer (O²) relaxes inward by 21% or 0.24 Å forming a buckled oxygen layer (see Fig. 3.13). Thus, upon relaxation the clean κ -Al₂O₃(001) surface becomes oxygen-terminated and the outermost Al atoms recover their bulk tetrahedral coordination.

Table 3.5: Interlayer spacing (Å) of the ideal (bulk) and relaxed structure of the clean κ -Al₂O₃(001) surface as well as the distance difference Δz_{ij} .

Interlayer distance	z_{ij} (bulk)	z_{ij} (relaxed)	Δz_{ij}
Al ⁽¹⁾ –O ⁽²⁾	0.59	0.31	–0.90
O ⁽²⁾ –Al ⁽³⁾	1.13	0.89	–0.24
Al ⁽³⁾ –Al ⁽⁴⁾	0.09	0.09	±0.00
Al ⁽⁴⁾ –O ⁽⁵⁾	0.96	1.10	+0.14
O ⁽⁵⁾ –Al ⁽⁶⁾	0.95	1.03	+0.08

3.2.2 Vanadia Aggregates Supported on κ -Al₂O₃(001)

In the same way as employed for vanadium oxides on α -Al₂O₃ (see Sec. 3.1.2), vanadia supported on κ -Al₂O₃(001) can be modeled by subsequent replacing of Al by V atoms or by “landing” small gas-phase clusters on the clean κ -alumina surface. Monomeric and polymeric species as well as vanadia films of varying thickness are thus created. The surface vanadium coverage is defined as $\Theta = N/N_{max}$, where N and N_{max} are the actual and the maximum number of vanadium atoms per surface area A . Depending on the Θ values, two types of supported vanadium oxides are considered: low-coverage VO_x species ($\Theta \leq 1$ ML) and vanadia films ($\Theta > 1$ ML).

Low-Coverage VO_x Species Modeled by Replacement

Figure 3.14 visualizes the low-coverage vanadia species with $\Theta \leq 1$ ML created by replacement of Al atoms by V atoms, namely monomers at $\Theta = 0.25$ and 0.5 ML, dimers ($\Theta = 0.5$ ML), trimers ($\Theta = 0.75$ ML), and 1D vanadia zigzag rows along the [100] direction at $\Theta = 1$ ML. All of them are anchored to the alumina surface exclusively via V–O⁽³⁾–Al interface bonds.

The isolated V sites at $\Theta = 0.25$ ML (Fig. 3.14A) and $\Theta = 0.5$ ML (Fig. 3.14B) are obtained by replacing one of the outermost Al atoms by V in the clean κ -Al₂O₃ surface with a (2×1) and (1×1) periodicity, respectively. Two neighboring V sites are separated by 9.77 and 4.88 Å, respectively. The dimeric ($\Theta = 0.5$ ML) and trimeric ($\Theta = 0.75$ ML) species are modeled in a (2×1) cell by replacing two and three out of the four topmost Al atoms by V, respectively (Figs. 3.14 C and D). The dimer is a *real* dimer because the two V sites share an oxygen atom (V–O⁽³⁾–V bond). Further replacement of all topmost Al atoms results in a 1D vanadia row (Fig. 3.14E). Formally, it is a 1V-layer film ($\Theta = 1$ ML), but the neighboring rows are not connected by V–O–V bonds. The dimers and trimers as well as the 1D vanadia rows are referred to as polymeric VO_x species. Again, by adding oxygen atoms to the vanadium centers, vanadyl groups are created. For all structures with the (2×1) periodicity, a $(2 \times 2 \times 1)$ k -point grid is employed.

The coordination of the outermost Al ions of the vanadyl-terminated low-coverage VO_x species varies with respect to that of the clean κ -Al₂O₃(001) surface (4-fold): monomers at $\Theta = 0.25$ ML and dimers ($\Theta = 0.5$ ML) have only one 5-fold coordinated Al atom, whereas for monomers at $\Theta = 0.5$ ML and trimers all surface Al atoms are 5-fold coordinated.

Low-Coverage VO_x Species Modeled by Adsorption

Another way of creating low-coverage VO_x species is by adsorption of small gas-phase clusters on the clean κ -Al₂O₃(001) surface. For instance, by “landing” V₂O₅ and V₂O₄ clusters on the surface, dimeric vanadia species are obtained. They are modeled using a (2×1) unit cell and the vacuum region is increased to 15 Å.

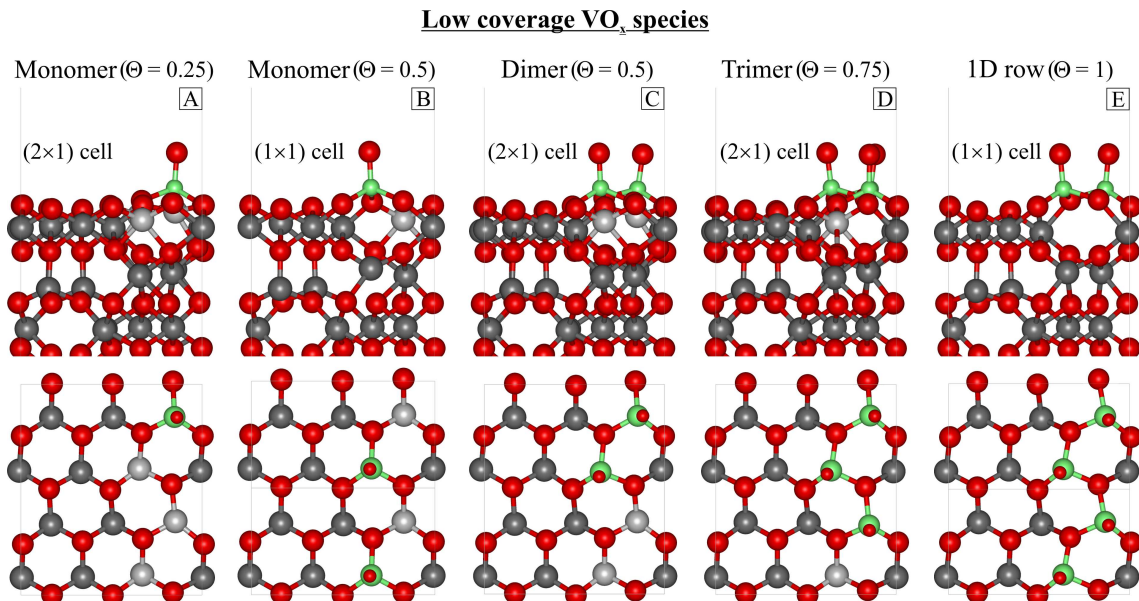


Figure 3.14: Side and top view of vanadyl-terminated low-coverage VO_x species ($\Theta \leq 1$ ML) supported on the κ -Al₂O₃(001) surface: monomers, dimers, trimers, and 1D vanadia rows. V atoms are depicted in green, O in red, Al in dark gray, whereas the topmost Al atoms are in light gray.

Figure 3.15 shows the three most stable V₂O₅ on κ -Al₂O₃ configurations. Model A is energetically the most favorable one and has one V=O bond, one V–O⁽²⁾–V bond, and three interface V–O⁽²⁾–Al bonds. Such V–O⁽²⁾–Al interface-bridging bonds are only obtained when vanadia clusters are adsorbed on the alumina surface, whereas all species created by replacement of Al atoms by V have only 3-fold coordinated oxygen atoms at the interface (see Sec. 3.2.2). Similar to the clusters on α -alumina, a V₂O₅ unit tends to bind as much as possible to the surface, thereby increasing the coordination of the undercoordinated surface Al and O atoms. One V atom (V1) is 5-fold coordinated and the other (V2) is 6-fold. Both of them occupy octahedral sites above Al atoms of the Al³ and Al⁴ layers. The oxygen atoms are approximately in one plane that follows the stacking sequence of oxygen layers. Moreover, its structure resembles that of the most stable V₂O₅ on α -alumina [109] (see Fig. 3.6). Closer inspection of the two models, however, shows that there are some differences. On α -Al₂O₃, the cluster has no vanadyl groups, the V–O–V bond contains a 3-fold coordinated oxygen atom, and two of the V–O⁽²⁾–Al bonds from the V₂O₅ unit are very short (1.67 and 1.68 Å), whereas in the V₂O₅ cluster on κ -Al₂O₃ the V–O⁽²⁾–Al bonds are in the 1.72–1.76 Å range.

The second most stable structure (Figure 3.15B) is obtained from the initial configuration that led to structure model A after a short (0.8 ps) simulated annealing run and subsequent structure optimization at $T = 0$ K. It is ~ 0.4 eV less stable and has two V=O bonds, one V–O⁽²⁾–V bond, and two V–O⁽²⁾–Al bonds. Both

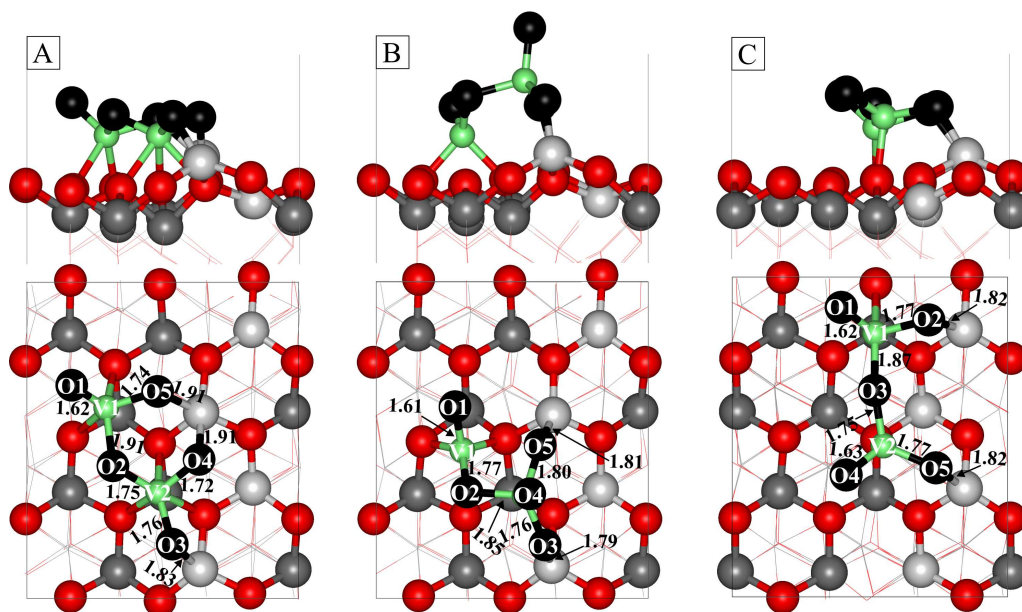


Figure 3.15: Side and top view of the most stable V₂O₅ clusters adsorbed on the κ -Al₂O₃(001) surface. V atoms are depicted in green, Al in dark gray, the topmost Al in light gray, O atoms from the κ -Al₂O₃ surface are in red, whereas those from a V₂O₅ unit are in black. Bond lengths are in Å.

vanadium atoms are 4-fold coordinated. The V1 atom is bound to two surface O atoms and two (O1 and O2) of the V₂O₅ unit, whereas V2 is connected only to cluster oxygen atoms. The latter is in nearly perfect tetrahedral surrounding and forms two interface bonds with the outermost Al atoms from the κ -Al₂O₃ support.

The third V₂O₅ cluster (Figure 3.15C) is only 0.12 eV higher in energy than model B. Again, there are two V=O bonds, one V–O⁽²⁾–V bond, and two V–O⁽²⁾–Al bonds and V1 and V2 atoms are in 4-fold coordination. However, in contrast to model B, each vanadium atom forms an interface bond with one of the topmost Al atoms and V1–O2/V2–O5 and O2–Al/O5–Al have the same bond lengths (1.77 and 1.82 Å), respectively.

The adsorption energy of the V₂O₅ cluster on the κ -Al₂O₃(001) surface, E_{ad} , is defined as

$$E_{\text{ad}} = E_{\text{V}_2\text{O}_5/\text{Al}_2\text{O}_3} - E_{\text{Al}_2\text{O}_3} - E_{\text{V}_2\text{O}_5(\text{gas})} \quad (3.17)$$

where $E_{\text{V}_2\text{O}_5/\text{Al}_2\text{O}_3}$, $E_{\text{Al}_2\text{O}_3}$, and $E_{\text{V}_2\text{O}_5(\text{gas})}$ are the total energies of the supported vanadia slab, the clean κ -Al₂O₃(001) surface, and the most stable V₂O₅ cluster in the gas phase, respectively. The two different V₂O₅ structures, i.e., the linear and the cyclic one are calculated in a cubic box with $a = 15$ Å using only the Γ -point. The cyclic V₂O₅ is by 0.96 eV more stable than the linear one. The obtained geometries are in very good agreement with the previously reported B3LYP (TZVP basis set) [130] and plane wave PW91 [109, 131] results.

For all three structures shown in Figure 3.15, the adsorption of the V_2O_5 cluster on $\alpha\text{-Al}_2\text{O}_3(0001)$ is an exothermic process: -6.47 (model A), -6.09 (model B), and -5.96 eV (model C). The coverage of V atoms per surface Al atoms is 0.5 ML and the surface area is $\sim 82 \text{ \AA}^2$. Note that for the two most stable clusters on the $\alpha\text{-Al}_2\text{O}_3(0001)$ support, adsorption energies of -6.80 and -6.67 eV are obtained [109]. The vanadium dispersion is also 0.5 ML and the surface area of 80 \AA^2 is very similar. Model B and C will not be considered any further and the discussion continues with the most stable cluster A regarded as yet another type of model for dimeric vanadia species on κ -alumina support.

Removing one oxygen atom from the V_2O_5 cluster A (cf. Figure 3.15A) results in five different $V_2O_4/\kappa\text{-Al}_2\text{O}_3$ dimeric structures. They differ in the oxygen atom that has been removed, i.e., a vanadyl oxygen (O1), a bridging $V\text{-O}^{(2)}\text{-V}$ oxygen (O2), and three inequivalent interface $V\text{-O}^{(2)}\text{-Al}$ oxygen atoms (O3, O4, and O5). Figure 3.16 shows their relaxed geometries.

To evaluate the adsorption energies of the V_2O_4 cluster on $\kappa\text{-Al}_2\text{O}_3$, the energy of the gas-phase V_2O_4 is needed. Similar to V_2O_5 , the V_2O_4 clusters are placed in a cubic box with $a = 15 \text{ \AA}$ and the calculations are performed using only the Γ -point. The energetically most favorable V_2O_4 structure is the cyclic isomer with a $V\text{-O}_2\text{-V}$ ring and two vanadyl oxygen atoms in trans configuration. As has been pointed out in Ref. [132], the lowest-spin state is an open-shell singlet with one d -electron at each vanadium atom. It is 173 meV more stable than the triplet state, which is in good agreement with the previous PW91 calculations (177 meV) [109] and in qualitative agreement with the more reliable B3LYP results (112 meV) [132]. The energy is obtained from the energy of the broken symmetry solution and the triplet state at the same geometry assuming $\langle \hat{S}^2 \rangle = 1$.

Finally, replacement of one of the two V atoms by an Al atom in a V_2O_4 cluster

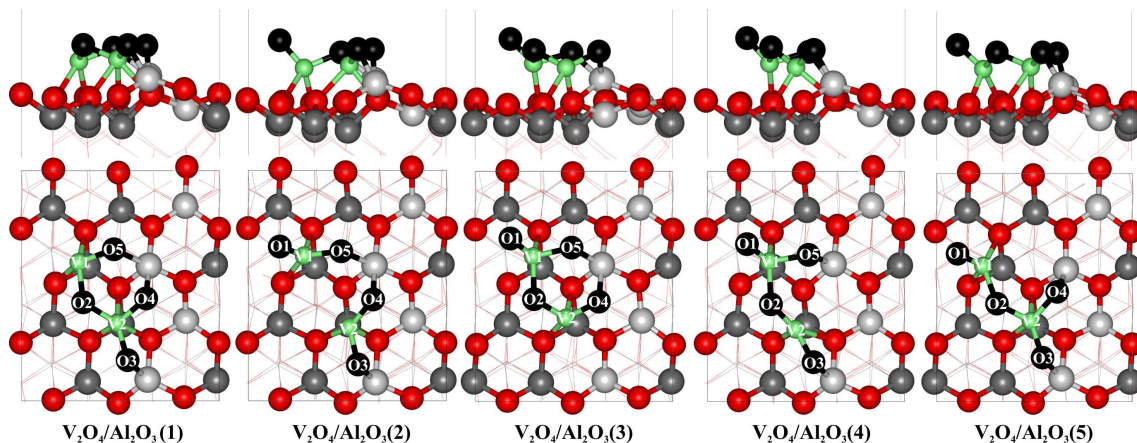


Figure 3.16: Optimized structures of the V_2O_4 clusters on the $\kappa\text{-Al}_2\text{O}_3(001)$ surface obtained upon removal of a single oxygen atom (number in parenthesis) from the most stable $V_2O_5/\kappa\text{-Al}_2\text{O}_3$ cluster.

on the κ -Al₂O₃(001) surface creates VO_{2.5}AlO_{1.5} species, i.e., monomers at $\Theta = 0.25$ ML that are structurally different from those shown in Figure 3.14A. In both monomeric types, however, vanadium is in V^V oxidation state.

Vanadia Films

Vanadia films with (1×1) periodicity and coverage $\Theta > 1$ ML have been considered. The unit cell compositions have the general formula $\frac{n}{2}\text{V}_2\text{O}_3 \cdot \frac{32-n}{2}\text{Al}_2\text{O}_3$ ($n = 4, 6, 8,$ and 10), whereas the composition of the fully vanadyl-terminated films is $\frac{n}{2}\text{V}_2\text{O}_5 \cdot \frac{32-n}{2}\text{Al}_2\text{O}_3$, respectively. Figure 3.17 shows the vanadyl-covered vanadia films supported on the κ -Al₂O₃(001) surface with thicknesses of up to five vanadium layers. Similar to the V₂O₃(0001) surface [107] as well as thick vanadia films supported on α -Al₂O₃(0001) [87], vanadia films supported on κ -Al₂O₃(001) may reconstruct. On the basis of the structure of 4V- and 5V-layer films, two models were built, in which one or two of the surface vanadyl groups are removed and the vanadium atom(s) from the fourth V-layer pop into the hole of the outermost octahedral layer. The unit cell size, however, does not change.

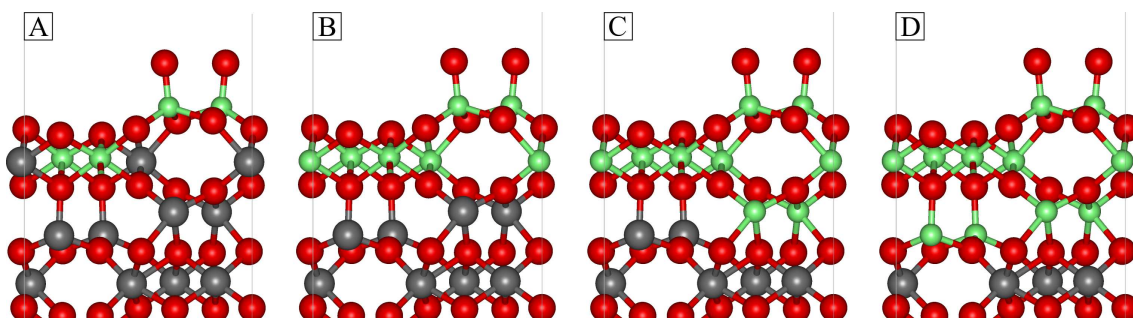


Figure 3.17: Side view of vanadyl-terminated vanadia films ($\Theta > 1$ ML) supported on the κ -Al₂O₃(001) surface: (A) 2V-layer film, (B) 3V-layer film, (C) 4V-layer film, and (D) 5V-layer film, respectively. See Figure 3.14 for color coding.

The oxygen defect formation energies of the κ -alumina-supported vanadium oxides are calculated as the difference between the defect formation energy with respect to the oxygen atom (calculated at a 250 eV cutoff) and half the dissociation energy of the O₂ molecule in the gas phase. The latter has been obtained using a 400 eV cutoff and smaller radii for the *s* and *p* states of oxygen by 0.30 and 0.38 a.u., respectively. The accuracy of this approach is verified by test calculations performed entirely at a 400 eV cutoff, which have shown systematic changes in the defect formation energy of about 0.1 eV. The calculated dissociation energy of O₂ is 6.29 eV, whereas the experimental value is 5.17 eV (obtained after adding the contributions due to zero point vibrations) [110].

3.2.3 Reducibility of Vanadia Aggregates on κ -Al₂O₃

We have previously shown that the crystalline α -V₂O₅(001) surface is much more reactive (in terms of surface oxygen defect formation) than the epitaxial vanadia films on the α -Al₂O₃(0001) support ($E_f \sim 2$ vs. 4 eV/atom) [87, 119]. This is due to the stabilization of the reduced surface V sites by forming new V–O–V bonds with the V₂O₅ crystal layer underneath. Moreover, dimeric species on α -Al₂O₃ are still more difficult to reduce ($E_f \sim 3$ eV/atom) than the α -V₂O₅(001) surface, but significantly easier than the supported vanadia films [109]. The reason is the formation of a new V–O⁽³⁾–V bond at the vanadia/alumina interface upon creation of the defect resulting in a four-membered V–O₂–V ring.

Here, the energy to remove surface lattice oxygen atoms from vanadia aggregates supported on the metastable κ -Al₂O₃(001) surface is evaluated and compared with the results obtained for the stable α -Al₂O₃(0001), thus gaining further insight into the role of the support structure.

Low-Coverage VO_x Species Modeled by Replacement

We start by considering the initial reduction of low-coverage vanadia species ($\Theta \leq 1$ ML) by creating a single vanadyl oxygen defect. Figure 3.18 illustrates the structural relaxations induced by the subsequent removal of vanadyl oxygen atoms, starting from fully vanadyl-covered monomeric and polymeric species supported on the κ -Al₂O₃(001) surface until their complete reduction.

Upon relaxation, the energy to remove a vanadyl oxygen atom from the isolated VO_x site at $\Theta = 0.25$ ML is lowered from 3.32 to 2.74 eV. The reduced V-center (V1) relaxes inward into the hole in the octahedral layer and forms one new V–O bond with an oxygen atom from the O⁵ layer beneath (see Fig. 3.13 for layers labeling), thus recovering its tetrahedral coordination. The three topmost Al atoms (shown as light gray in Fig. 3.18A) are also tetrahedrally coordinated. As a result, the κ -Al₂O₃ surface with the reduced monomeric VO_x sites becomes oxygen terminated. The defect formation energy of similarly dispersed monomers on α -Al₂O₃ (monomers type I, cf. Section 3.1.4) is 4.47 eV, that is, about 1.7 eV more costly (relaxation effects amount to ~ 0.1 eV), and the surface is metal-terminated.

Increasing the coverage of monomeric species to $\Theta = 0.5$ ML on κ -Al₂O₃ does not influence the initial reduction of vanadyl oxygen atoms and the calculated defect formation energy is 2.77 eV. In this case, half of the outermost Al atoms become tetrahedrally coordinated. Thus, decreasing the separation of the monomers on the κ -alumina surface from 9.77 to 4.88 Å (cf. Fig. 3.14A, B) results in a very small change in the initial defect formation energy.

True dimeric species on κ -Al₂O₃ at $\Theta = 0.5$ ML (Fig. 3.14C), which have a direct V–O–V bond, are by 0.56 eV *less* stable than the monomeric species at the same V-coverage (Fig. 3.14B). In the latter, the two outermost Al atoms are 5-fold coordinated, whereas in the former they are 4- and 5-fold, respectively. Thus, low-

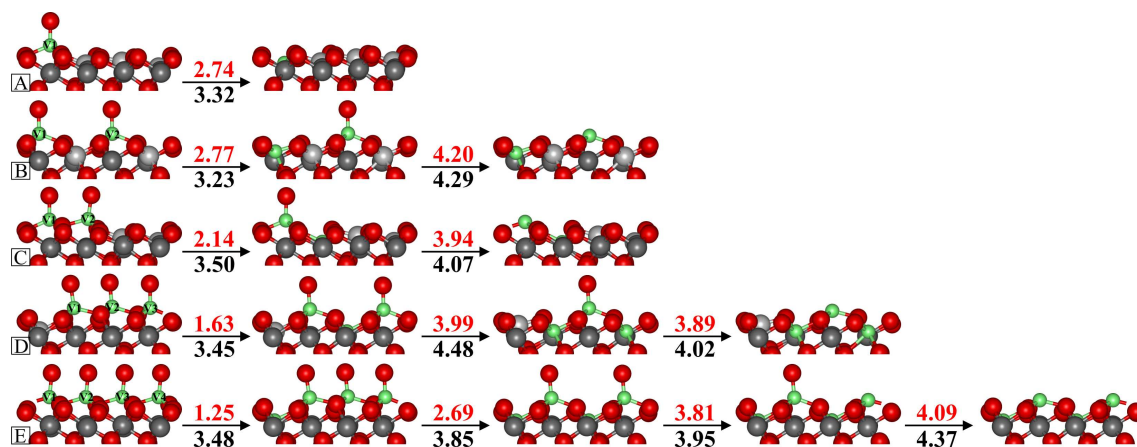


Figure 3.18: Reduction of low-coverage vanadia species: (A) monomers at $\Theta = 0.25$ ML, (B) monomers at $\Theta = 0.5$ ML, (C) dimers at $\Theta = 0.5$ ML, (D) trimers at $\Theta = 0.75$ ML, and (E) 1D vanadia rows at $\Theta = 1$ ML. The vanadyl oxygen vacancy formation energies are given in eV. Relaxed and unrelaxed values are in red and black, respectively.

coverage VO_x when supported on the κ -Al₂O₃ surface prefer to be as dispersed as possible. At higher VO_x coverages, however, formation of oligomeric species cannot be avoided. Upon removal of a single vanadyl oxygen atom, the dimeric species undergo a larger structure relaxation than the monomeric ones, which lowers the vacancy formation energy from 3.50 to 2.14 eV. The reduced V-center becomes octahedrally coordinated due to the formation of three V–O bonds with oxygen atoms of the oxygen layer O⁵ beneath, while the two outermost Al atoms remain tetrahedrally and pyramidally coordinated, respectively. The initial defect formation energy of pseudo-dimeric sites on α -Al₂O₃ is 4.34 eV with a relaxation contribution of only ~ 0.1 eV. The values of 2.74 and 2.14 eV compared to 4.47 and 4.34 eV for vanadia species at coverages up to 0.5 ML on the κ - and α -Al₂O₃, respectively, demonstrate that the initial reduction of small aggregates on the metastable support is much more facile than on the stable one.

Upon the reduction of trimers, the energy decreases from 3.45 to either 1.63 or 2.02 eV depending on whether the central or a terminal vanadyl oxygen has been removed (V2 and V1 in Fig. 3.18D, respectively). In all cases, the reduced V-atoms become octahedrally coordinated. However, relaxation effects change the coordination of the topmost aluminum atom to tetrahedrally when the reduced site is at the end of the trimer, and remains pyramidally otherwise. Further decrease of the initial defect formation energy is found for the 1D vanadia rows (1.25 eV only). The unrelaxed value is 3.48 eV, and structure relaxation results in octahedrally coordinated reduced sites. As the length of the polymeric species increases from two to three and finally to 1D zigzag rows, the initial reduction becomes more and more facile.

As a next step, the subsequent reduction of low-coverage vanadia species on the

metastable support is considered. The formation of additional vanadyl oxygen defects becomes more difficult (about 4 eV) partly because of the repulsive interactions between defects (see Figure 3.18). The energy is approximately the same regardless of the size (i.e., length) of the aggregates. Specifically, subsequent reduction of the monomeric species at $\Theta = 0.5$ ML, which leaves the surface metal terminated (Fig. 3.18B), requires 4.20 eV (relaxation effects amount to less than 0.1 eV). The resulting fully reduced $\text{VO}_x/\kappa\text{-Al}_2\text{O}_3$ surface is buckled. Comparison of the initial and subsequent defect formation energies indicates that despite the large separation between two V centers of 4.88 Å, these monomers cannot be regarded as isolated species. In contrast, on the stable $\alpha\text{-Al}_2\text{O}_3$ support the V-sites forming pseudo-dimers at $\Theta = 0.5$ ML can be considered to be isolated with an energy difference between the initial and subsequent reduction of 0.12 eV. The subsequent reduction of dimeric species on $\kappa\text{-Al}_2\text{O}_3$ at $\Theta = 0.5$ ML yields a metal-terminated surface that is buckled. The inward relaxation of two neighboring V-sites into the octahedral hole running along the [100] direction is *not* observed.

As far as the trimers are concerned, in the most stable structure the two reduced sites are not closest neighbors. The reduced centers (V1 and V3 in Fig. 3.18D) do relax inward while increasing their coordination to 5-fold. Complete reduction of the trimer does not cause significant lattice relaxation and the surface is left metal-terminated (Fig. 3.18D). This indicates that starting from the initially reduced polymeric species, further reduction would preferentially take place on next-nearest neighbors along the zigzag row resulting in the formation of a buckled layer of *up* and *down* metal sites. This is confirmed by the subsequent removal of vanadyl oxygen atoms from the 1D vanadia rows. That is, the creation of a second oxygen defect favors the alternation of defect sites. The reduced structure has two vanadium sites that moved inward in the octahedral hole (V1 and V3 in Fig. 3.18E) and became 5-fold coordinated. These significant lattice rearrangements are accompanied by a decrease of the subsequent defect formation energy from 3.85 to 2.69 eV. Further reduction of the third (V2) and fourth (V4) vanadyl oxygen atoms is calculated to be as costly as for the neighboring sites of already reduced centers (~ 4 eV). Those V centers stay *up* maintaining the buckled layer of *up* and *down* metal sites. This is in contrast to γ - and $\alpha\text{-V}_2\text{O}_5(001)$, for which starting from an isolated defect site the subsequent removal of *neighboring* vanadyl oxygen atoms along rows in the [010] direction is favored [119, 133].

Two conclusions can be drawn. First, the removal of lattice oxygen atoms from the low-coverage vanadia species supported on $\kappa\text{-Al}_2\text{O}_3(001)$ is favored by the open structure of the metastable alumina support that facilitates relaxation and formation of new V–O bonds. Second, the (initial) reduction of polymeric VO_x species is more facile than that of monomeric ones. The longer polymeric species are likely to be particularly easy to reduce. This might be correlated with the observed effect of vanadia surface density on the initial rate of alkene formation [7, 134].

It is noteworthy that monomeric and polymeric vanadia species on an ultrathin alumina film grown on NiAl(110) are predicted to show very similar behavior in

terms of reducibility trends as the corresponding VO_x species on the metastable κ -Al₂O₃ [135], which validates and further strengthens our choice of support material and the results obtained in this work.

Low-Coverage VO_x Species Modeled by Adsorption

As a next step, the reduction of low-coverage vanadia ($\Theta \leq 0.5$ ML) created by adsorption of gas-phase V₂O₅ clusters on the κ -Al₂O₃(001) surface is considered. In contrast to the VO_x species discussed in the previous section, these low-coverage vanadia are anchored to the alumina surface with V–O⁽²⁾–Al interface bonds. Table 3.6 compiles the corresponding defect formation energies before and after relaxation. It also contains the adsorption energy of the V₂O₄ clusters on κ -Al₂O₃ given with respect to the gas-phase V₂O₄ cyclic-trans isomer. Removal of the vanadyl oxygen O1 bound to the V1 site costs 2.69 eV, which upon relaxation is lowered to 2.27 eV. The resulting structure, V₂O₄/Al₂O₃(1), is very similar to the unrelaxed one, i.e., it preserves the V1–O2–V2–O4–Al–O5 ring and all oxygen species from the V₂O₄ unit are in a plane parallel to the surface (cf. Figure 3.16). No new bonds are formed; the V1–O2, V1–O5, and O5–Al bonds are shortened by 0.07, 0.05, and 0.10 Å, respectively, while the V2–O2 bond is stretched by 0.06 Å. The other bond lengths change by less than 0.02 Å. As a result of the bonding to the κ -Al₂O₃ surface, the V₂O₄ cluster is stabilized by 6.71 eV.

The structure obtained upon removal of the O3 atom, V₂O₄/Al₂O₃(3), is quite similar to the former one. However, it undergoes significant lattice rearrangements accompanied by a decrease of the defect formation energy from 4.31 to 2.73 eV. In particular, the V1 atom loses one bond with a surface oxygen atom, while the coordination of the V2 site is reduced from 6-fold to 4-fold. This is caused by the large inward relaxation of the outermost Al directly bound to the O3 atom and consequent inward movement of the lattice oxygen connected to it. Thus, both vanadium sites become tetrahedrally coordinated and are no longer in the same plane. Similar to the V₂O₄/Al₂O₃(1) cluster, this V₂O₄ cluster is very strongly adsorbed on the κ -surface (6.25 eV).

Removing the O2 atom from the V–O⁽²⁾–V bridge breaks the V1–O2–V2–O4–Al–O5 ring and yields a linear surface cluster V₂O₄/Al₂O₃(2) (see Fig. 3.16). The same effect is obtained upon removal of O4 or O5 atoms from the interface V–O⁽²⁾–Al bonds. The large relaxation of the V₂O₄/Al₂O₃(2) structure lowers the vacancy formation energy from 3.73 to 2.56 eV. Here, the V2 atom moves upward and the bond with the lattice oxygen centered in the middle of the V1–O2–V2–O4–Al–O5 ring breaks up (cf. Fig. 3.16). As a result, the coordination of both V1 and V2 sites is reduced to 4-fold. This V₂O₄ cluster is also strongly bound to the alumina surface, with a similar value for the adsorption energy (6.42 eV) as the other reduced clusters (see Table 3.6).

Interestingly, a very small amount of energy is required to remove one of the interface O4 and O5 atoms, i.e., 1.42 and 1.45 eV, respectively. Those oxygen atoms

Table 3.6: Oxygen vacancy formation energy E_f in eV for the most stable $V_2O_5/\kappa\text{-Al}_2O_3$ cluster A as well as the adsorption energy E_{ad} (eV) of the V_2O_4 clusters on the $\kappa\text{-Al}_2O_3(001)$ surface. The values in parenthesis correspond to the formation energy of the unrelaxed structures.

O vacancy type	E_f	E_{ad}
V=O (O1)	2.27 (2.69)	6.71
V-O ⁽²⁾ -V (O2)	2.56 (3.73)	6.42
V-O ⁽²⁾ -Al (O3)	2.73 (4.31)	6.25
V-O ⁽²⁾ -Al (O4)	1.42 (3.20)	7.55
V-O ⁽²⁾ -Al (O5)	1.45 (3.23)	7.53

are bound to the outermost Al atom (4-fold coordinated in the bulk) that upon adsorption of the vanadia cluster became 5-fold coordinated. Significant structure relaxation upon oxygen removal is accompanied by ~ 1.8 eV decrease in the vacancy formation energy. All bond lengths change by less than 0.02 Å except for the bonds that involve the overcoordinated Al atom. In case of O4 removal, the O5–Al bond is shortened by 0.09 Å to a value of 1.82 Å, a typical Al^T–O distance in bulk $\kappa\text{-Al}_2O_3$. The same happens when the O5 atom is removed, i.e., O4–Al bond is shortened to 1.79 Å, while the V2–O2 is stretched by 0.07 Å. As a result, in both cases the Al ion nearly recovers its perfect tetrahedral bulk coordination. Hence, the larger values (7.55 and 7.53 eV) calculated for the adsorption energies of those two V_2O_4 clusters appear in line with the additional structure stabilization.

Removal of the vanadyl oxygen atom from the most stable monomeric site obtained by replacing one V atom by an Al atom in the $V_2O_4/Al_2O_3(4)$ requires 1.72 eV. In comparison with the reduction of the corresponding dimer (1.42 eV, cf. Table 3.6), reduction of such a monomeric V-site is by 0.3 eV more costly. This trend is confirmed for similarly modeled low-coverage vanadia species on the $\alpha\text{-Al}_2O_3$ support (see Section 3.1.4). The most stable monomer, (monomer type II, cf. Figure 3.6) is characterized by the presence of two differently coordinated interface oxygen atoms and no vanadyl groups. Removal of a bridging oxygen atom at the V–O⁽²⁾–Al interface costs 4.16 eV, whereas 5.53 eV are required for reduction of a bridging oxygen at the V–O⁽³⁾–Al interface. The formation energy of a defect at the V–O⁽²⁾–Al interface of the corresponding dimer is 2.79 eV [109], which again indicates a more facile reduction of alumina-supported dimeric species as compared to monomeric ones.

In regard to the energy for creating oxygen defects at the surface of low-coverage alumina-supported vanadia aggregates, the following conclusions can be drawn. Reduction of monomers and dimers modeled by clusters adsorbed on the $\kappa\text{-Al}_2O_3(001)$ surface requires between 1.42 and 2.73 eV per $1/2O_2$ molecule. These low-coverage species ($\Theta \leq 0.5$ ML) are anchored to the surface with V–O⁽²⁾–Al interface bonds.

For low-coverage species ($\Theta \leq 1$ ML), but a different nature of the interface (V–O⁽³⁾–Al), the energy varies between 1.25 and 2.77 eV with the reduction of the monomer being the most difficult (see Figure 3.18). On the stable α -Al₂O₃(0001) surface, the energy cost for the formation of a single oxygen defect at the V–O⁽²⁾–Al interface lies in the range of 2.79 – 4.77 eV [109], whereas for species with V–O⁽³⁾–Al interface bonds, the energy varies between 4.34 and 5.53 eV (see Sec. 3.1.4). Thus, oxygen defects can be more easily created on small vanadia aggregates supported on the metastable κ -Al₂O₃ than on the stable α -Al₂O₃ surface.

Formation of an oxygen defect in all vanadia species supported on κ -Al₂O₃(001) leaves two electrons in the system, which occupy *d*-states localized on one V-site that becomes V^{III}(*d*²), while the second V-site remains in a V^V(*d*⁰) configuration. This is different from the reduction of V₂O₅(001) single-crystal surface as well as dimeric species on α -Al₂O₃, for which lattice relaxations result in a pair of V^{IV}(*d*¹) sites. The vacancy formation energy is 1.93 eV [119] and 2.79 eV [109], respectively, whereas for dimeric species on the κ -Al₂O₃ support, a much lower value (1.42 eV) is predicted. This shows that low-defect formation energies can be obtained when substantial relaxation effects occur that not necessarily yield to the formation of a V^{IV}(*d*¹) pair.

Vanadia Films

Finally, the reducibility of vanadia films supported on κ -Al₂O₃(001) is discussed and compared with the results previously obtained for such films on α -Al₂O₃ (see Section 3.1.4 and Ref. [87]). The corresponding vacancy formation energies are summarized in Table 3.7. Removal of a single vanadyl oxygen atom from the 2V-layer film costs 3.31 eV, which is significantly higher than the energy required for the initial reduction of low-coverage VO_x species. This reduction is less costly when thicker vanadium oxide films are formed. For instance, creation of a single defect requires 2.96 eV for the 3V-layer film, and 2.49 and 2.37 eV for the 4V- and 5V-layer films, respectively. In all cases, the reduced V-center relaxes inward into the octahedral hole and increases its coordination to 5-fold by forming two new V–O bonds with oxygen atoms of the O⁵ layer underneath.

We have shown that for the vanadia films on α -Al₂O₃ formation of an oxygen defect varies between 4.11 eV (ultrathin 1V-layer film) and 3.56 eV (thick 6V-layer film). Hence, similar to the low-coverage vanadia aggregates, the oxygen defects are more easily created in “epitaxially grown” vanadia films on the metastable κ -Al₂O₃(001) than on the stable α -Al₂O₃(0001) surface. This is due to the presence of tetrahedrally coordinated Al sites in the κ -alumina resulting in a much more open support structure that facilitates lattice relaxations.

Subsequent oxygen removal that yields a metal-terminated surface, however, requires ~ 4 eV regardless of the film thickness (see Table 3.7) and the support structure (κ - and α -Al₂O₃ phases differ by less than 0.1 eV). For the removal of a vanadyl oxygen atom terminating the reconstructed 4V- and 5V-layer films (from which one

Table 3.7: Oxygen vacancy formation energy E_f in eV per $1/2\text{O}_2$ molecule for the initial and subsequent reduction of the vanadia films on the $\kappa\text{-Al}_2\text{O}_3(001)$ surface.

Structure	E_f^{initial}	$E_f^{\text{subsequent}}$
2V-layer film	3.31	4.00
3V-layer film	2.96	4.07
4V-layer film	2.49	3.93
5V-layer film	2.37	4.03
4V-layer film (reconstructed)	3.98	
5V-layer film (reconstructed)	3.98	

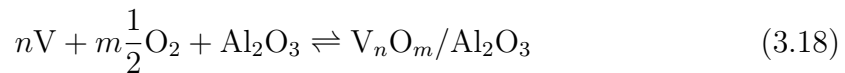
vanadyl group is missing), a value of 3.98 eV is obtained. The similarity between this value and those corresponding to the subsequent reduction of the unreconstructed films with the same thickness is related to the equal composition of the topmost atomic layers, namely $\text{O}=\text{V}-\text{O}_6-\text{V}_2-\text{V}_2-\text{V}-\text{O}_6-$ with one additional vanadium atom placed in the octahedral layer. It pops up from the V^6 layer (reconstructed films) or, as in case of the unreconstructed films, it drops from the topmost V-layer (V^1).

Thus, the effect of the structure of the alumina support on the reducibility of vanadium oxide films is suggested to be particularly significant at the *initial* reduction step (removal of first vanadyl oxygen) independent of the V-concentration.

3.2.4 Thermodynamic Stability

As with our studies on vanadium oxides supported on the $\alpha\text{-Al}_2\text{O}_3(0001)$ surface (cf. Section 3.1.3 and Refs. [87, 109]), statistical thermodynamics is applied to account for the effect of oxygen partial pressure and vanadium concentration at a given temperature on the stability of the vanadia aggregates supported on the metastable $\kappa\text{-Al}_2\text{O}_3(001)$ surface.

Using the same notation as in Section 3.1.3, the following equilibrium reaction is considered



with the accompanying change in the surface-related free energy $\Delta\gamma$ defined in Eq. (3.3). The reaction energy ΔE is the energy required to form the alumina-supported vanadium oxide from the $\kappa\text{-Al}_2\text{O}_3$ support, metallic vanadium and oxygen. In calculating $\Delta\gamma$, DFT total energies of the supported vanadia slab, the clean $\kappa\text{-Al}_2\text{O}_3(001)$ surface, the oxygen molecule, and the bcc bulk vanadium were used, neglecting zero-point vibrations, vibrational entropy contributions, and enthalpy changes. The chemical potential differences $\Delta\mu_i$ ($i = \text{V}$ and O) are defined in Eqs. (3.4) and (3.5). The most favorable structure for a given set of vanadium and oxygen chemical potentials is the one that minimizes the surface free energy

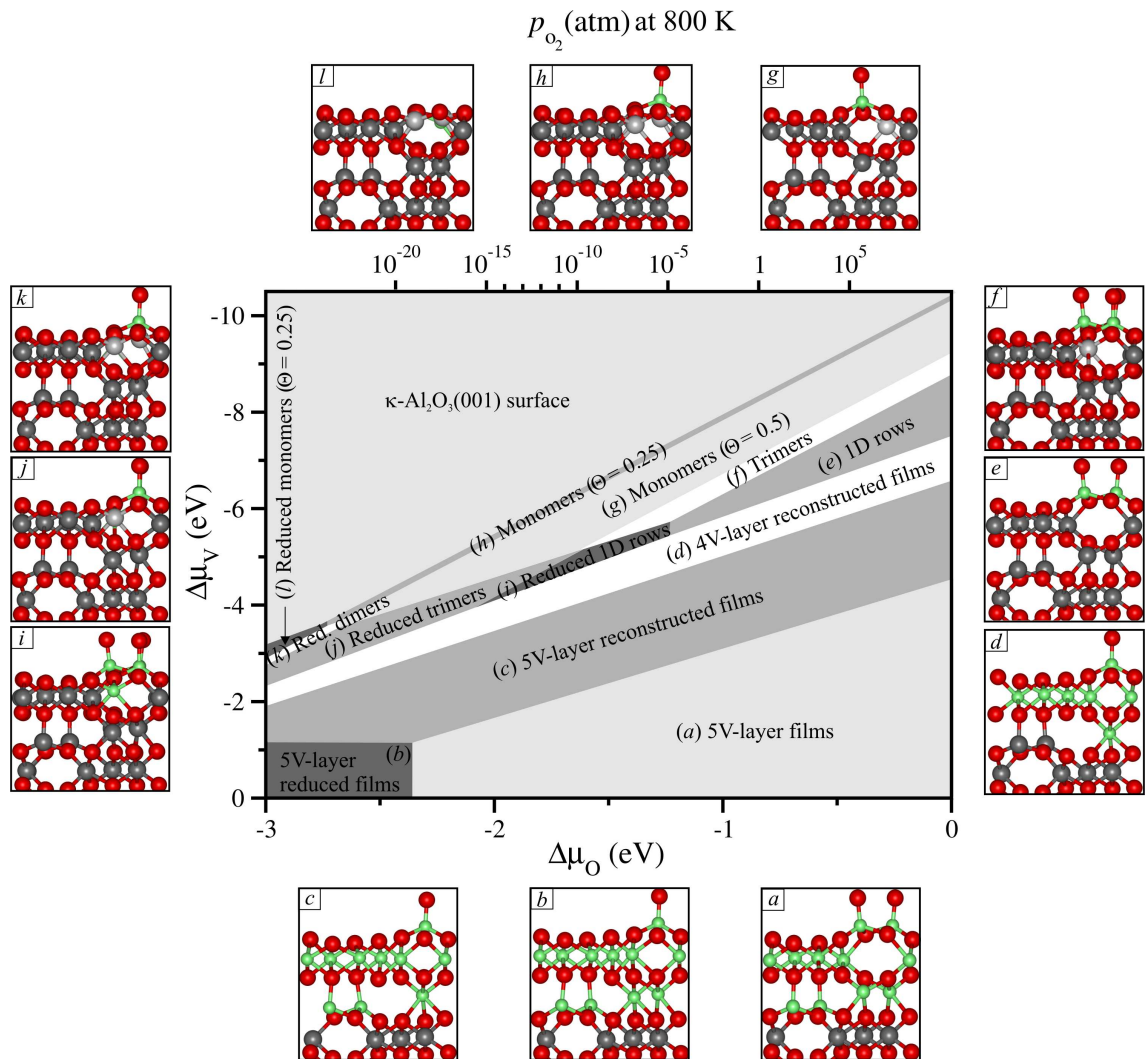


Figure 3.19: Phase diagram as a function of the $\Delta\mu_{\text{O}}$ and $\Delta\mu_{\text{V}}$ chemical potentials for vanadia aggregates supported on the $\kappa\text{-Al}_2\text{O}_3(001)$ surface. $\Delta\mu_{\text{O}}$ is translated into a pressure scale at $T = 800$ K.

$\Delta\gamma$. The resulting phase diagram is shown in Figure 3.19 with values of the oxygen potential related to the oxygen pressure at $T = 800$ K.

At the highest vanadium chemical potentials, the thickest film considered forms (i.e., 5V-layer film, cf. Fig. 3.19a). The same result was found for the vanadia films on the $\alpha\text{-Al}_2\text{O}_3$ surface (cf. Figure 3.7). At very reducing conditions ($\Delta\mu_{\text{O}} \leq -2.4$ eV) and still high $\Delta\mu_{\text{V}}$ values, the film obtained upon removal of a single vanadyl O-atom from this fully vanadyl-covered thick film becomes stable (Fig. 3.19b). Upon gradually decreasing the $\Delta\mu_{\text{V}}$ values, a reconstructed film with the same thickness (5V layers) is stable (Fig. 3.19c). As was mentioned before, this vanadia film has the same composition of the outermost layers ($\text{O}=\text{V}-\text{O}_6-\text{V}_2-\text{V}_2-\text{V}-\text{O}_6^-$) as the reduced

unreconstructed one (Fig. 3.19*b*) as well as a very similar vacancy formation energy (3.98 eV). Further decreasing the vanadium potential leads to stabilization of the reconstructed thinner 4V-layer films (Fig. 3.19*d*). Again, we note similarities with the calculated phase diagram for the vanadia films on α -Al₂O₃ support where in an intermediate range of $\Delta\mu_V$ values similarly reconstructed structures are predicted to form [87]. Further reducing the $\Delta\mu_V$ values results in formation of 1 ML thick structures. That is, similar to α -Al₂O₃, no aggregates with intermediate thicknesses are observed and the film becomes as thick as the vanadium supply allows.

However, the plots differ significantly at low-vanadium chemical potential that is not sufficient for the formation of vanadia bulk phases. Figure 3.19 shows all stable low-coverage VO_x species on the κ -Al₂O₃(001) surface. As $\Delta\mu_V$ decreases, for high $\Delta\mu_O$ values ($\Delta\mu_O \geq -1.25$ eV, which corresponds to $p \geq 10^{-5}$ atm at 800 K), fully vanadyl-terminated 1D vanadia rows (Fig. 3.19*e*), trimers (Fig. 3.19*f*), and monomers at $\Theta = 0.5$ and 0.25 ML (Fig. 3.19*g* and 3.19*h*, respectively) are predicted to be thermodynamically stable. Note that the monomeric species at $\Theta = 0.5$ ML (Fig. 3.14B) compete with the dimeric ones at the same coverage (Fig. 3.14C), but are 0.56 eV more stable. Thus, the vanadyl-covered dimers do not show up in the stability plot. Moreover, there are regions at which the *partially reduced* 1D rows (Fig. 3.19*i*) and trimers (Fig. 3.19*j*) are energetically favorable under UHV conditions. At even lower oxygen pressure, the partially reduced dimers (Fig. 3.19*k*) and monomers at $\Theta = 0.25$ ML (Fig. 3.19*l*) are also stabilized.

All low-coverage vanadia species on κ -Al₂O₃(001) that appear in the stability plot are anchored to the surface with V–O⁽³⁾–Al interface bonds. Despite the facile reduction of species with V–O⁽²⁾–Al bonds, they (and their reduced counterparts) are not predicted to be thermodynamically stable. This is a major difference compared to vanadia on α -Al₂O₃, for which dimeric species with V–O⁽²⁾–Al interface bonds are energetically favorable [109]. However, the structure of α -support does not allow for the formation of differently anchored dimers. Additionally, our calculations indicate that none of the two monomeric species at $\Theta = 0.25$ ML would form, and thus the only stable low-coverage vanadia on the α -Al₂O₃ support are dimers. This is another major difference compared to the κ -alumina for which monomers at two different VO_x loadings are stable. Hence, the present study demonstrates that the support structure *does* affect the structure of the catalyst.

An important difference between the low-coverage VO_x species on α -Al₂O₃ and those on κ -Al₂O₃ is the stability of the reduced systems. The α -alumina-supported reduced dimers would only become stable for $\Delta\mu_O \leq -2.8$ eV, which corresponds to a pressure of 10⁻¹² atm at very high temperatures (1200 K). In contrast, partially reduced polymeric VO_x species on κ -Al₂O₃ are stable in UHV and 800 K. This correlates with the more facile reduction of κ -alumina-supported vanadia compared to α -alumina.

Characteristic features of the experimental model catalysts prepared by vanadium evaporation under UHV conditions [16] are the presence of V in an average oxidation state of V^{III} (as in V₂O₃) and the existence of surface vanadyl groups.

The oxidation state of V^V of the surface V-atoms is only detectable on a flat V₂O₃ surface if spectra are taken at grazing angles [12, 66]. For vanadia aggregates on κ -Al₂O₃, low-coverage polymeric species are predicted to be partially reduced in UHV and $T \geq 800$ K (i.e., to have V^V and V^{III} centers). As the V-coverage increases and three-dimensional structures (films) form, V^{III} centers become prevalent in the bulk, but will not be accessible for reactant molecules.

3.2.5 Vibrational Analysis

Vibrational spectroscopy is a very useful tool for structural characterization, but the interpretation of the measured spectra is not always straightforward. Complex systems, such as supported vanadium oxides, appear to be particularly challenging. In this section, the calculated vibrational frequencies of selected κ -alumina-supported vanadia, e.g., monomers at $\Theta = 0.5$ ML and 1D vanadia rows having exclusively V–O⁽³⁾–Al interface bonds as well as the dimeric V₂O₅ and V₂O₄ clusters anchored to the κ -Al₂O₃(001) surface with V–O⁽²⁾–Al bonds are discussed. The influence of the support structure on the interface vibrational modes is analyzed.

Figure 3.20 shows the frequencies¹ of the IR active vibrations² of the clean κ -Al₂O₃(001) and both the fully reduced and the vanadyl-terminated monomers and 1D rows. For the clean κ -surface, the most intense broad band at 678 cm⁻¹ is assigned to the Al₂O₃ bulk modes and the two weak bands at 882 and 846 cm⁻¹ to Al^T–O stretching modes. The vibration at 882 cm⁻¹ involves exclusively the tetrahedrally coordinated Al atoms. It is shifted by ~ 45 cm⁻¹ toward higher wavenumbers as compared to the highest IR active mode of the clean α -Al₂O₃ surface (837 cm⁻¹). This is because the Al^T–O bond distances (1.75–1.79 Å), which occur only in κ -Al₂O₃, are much shorter than the Al^O–O distances (1.84–1.99 Å) that are common for both Al₂O₃ phases.

Upon creation of monomeric V sites, a very sharp and intense band at 870 cm⁻¹ emerges, which is assigned to V–O⁽³⁾–Al coupled with Al–O stretching modes of the whole slab. Additionally, the intensity of the broad Al₂O₃ bulk peak significantly decreases. When the surface is oxidized and covered with vanadyl oxygen atoms, the calculated vibrational spectrum shows a new band at 1044 cm⁻¹, which is the typical vanadyl bond stretch. It is lower than that calculated for the V₂O₅(001) single-crystal surface (1079–1095 cm⁻¹) [102] and the thin films on the α -Al₂O₃(0001) surface (1058, 1076 cm⁻¹) [102]. A very broad peak with two maxima at 820 and 786 cm⁻¹ is assigned to V–O⁽³⁾–Al vibration strongly coupled with Al–O stretching modes (red-shifted as compared to the metal-terminated model), and to pure Al–O stretching modes, respectively.

¹The vibrational frequencies (here and in the following) were calculated within the harmonic approximation by numerical differentiation of the forces using 0.02 Å displacements of the atoms in each Cartesian direction.

²The intensities were obtained from the derivatives of the dipole moment component perpendicular to the surface.

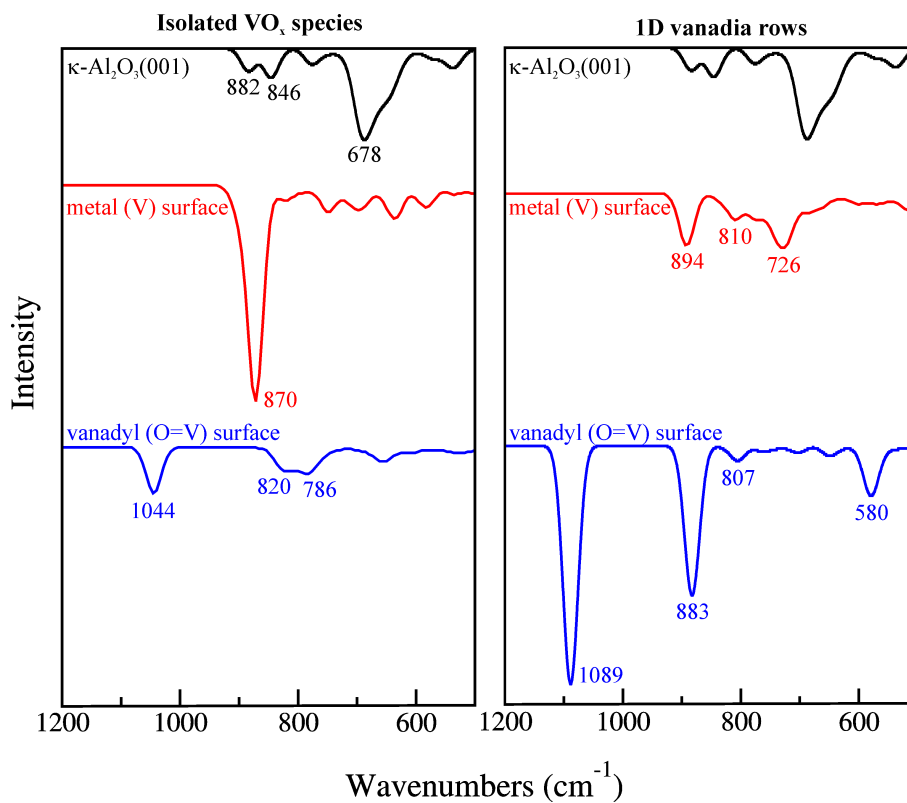


Figure 3.20: Calculated frequencies for the IR active vibrations of the monomeric species at $\Theta = 0.5$ ML (left panel) and 1D vanadia rows at $\Theta = 1$ ML (right panel) supported on the κ - $\text{Al}_2\text{O}_3(001)$ surface. The spectrum of clean surface is drawn in black, the fully reduced metal (V) and the vanadyl-terminated surfaces are in red and blue, respectively.

Calculated IR spectra of the 1D vanadia rows do not show IR active $\text{V}-\text{O}^{(3)}-\text{V}$ modes. For the metal-terminated surface, the highest frequency at 894 cm^{-1} is a pure $\text{Al}-\text{O}$ stretching, mainly involving tetrahedral Al^{T} sites, whereas the one at 810 cm^{-1} includes all Al atoms in the slab. Similar to the isolated sites, a very intense band at 1089 cm^{-1} appears in the spectrum of the vanadyl-terminated vanadia rows. It is due to the in-phase stretching of the two vanadyl groups and is shifted toward higher wavenumbers as compared to the $\text{V}=\text{O}$ mode of monomers ($\Theta = 0.5$ ML). Slightly less intense is the band at 883 cm^{-1} , which is assigned to $\text{V}-\text{O}^{(3)}-\text{Al}$ vibrations coupled with stretching of $\text{Al}-\text{O}$ bonds that extend up to the Al^{T} layer (cf. Fig. 3.13). The largest displacements within the alumina framework correspond to stretching of the tetrahedrally coordinated aluminum atoms.

Furthermore, neither the dimer nor its reduced counterpart anchored to the surface via $\text{V}-\text{O}^{(2)}-\text{Al}$ interface bonds show bands above 900 cm^{-1} . Similar to the 883 cm^{-1} band for the 1D vanadia rows (with $\text{V}-\text{O}^{(3)}-\text{Al}$ bonds), these systems show bands at 858 cm^{-1} (V_2O_5) and 856 and 888 cm^{-1} (V_2O_4) assigned to interface vibrations coupled with $\text{Al}-\text{O}$ stretching. However, the nature of the interface bonds

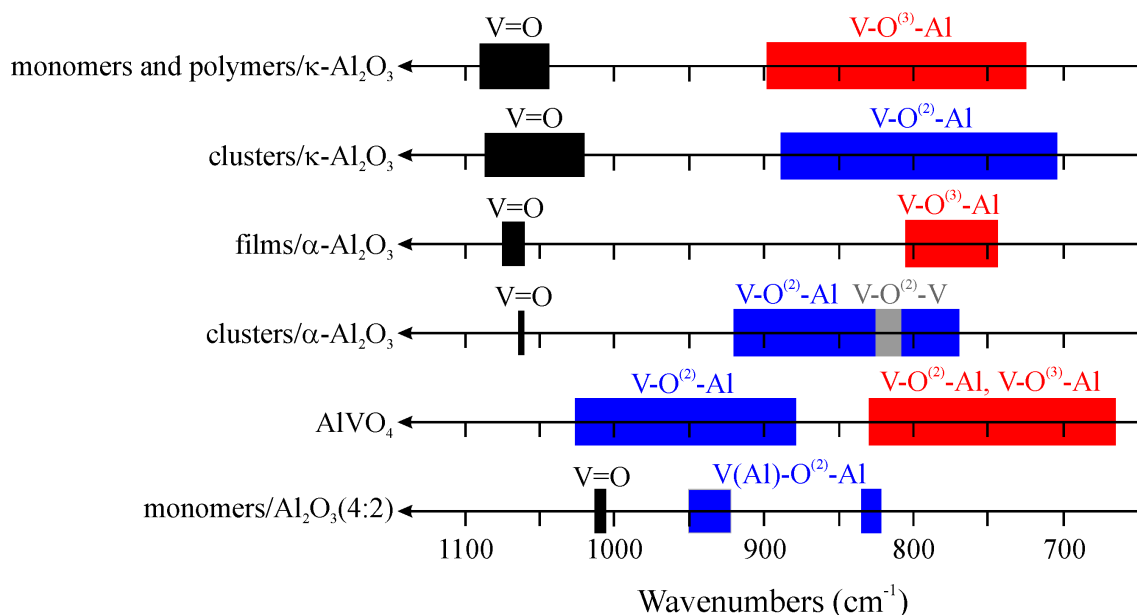


Figure 3.21: Harmonic vibrational frequencies of monomeric and polymeric vanadia species and clusters on the metastable κ -Al₂O₃(001) surface (this work), vanadia films and clusters on the stable α -Al₂O₃(0001) surface [109], bulk AlVO₄ [136], and a cluster model for O=V(OAl)₃ sites on alumina with 4-fold coordinated Al and 2-fold coordinated O atoms (4:2 coordination) [72].

is different. Additionally, vanadyl bond stretch at 1020 (V₂O₅) and 1087 cm⁻¹ (V₂O₄) as well as V-O⁽²⁾-Al vibrations strongly coupled with Al-O stretching of the whole slab appear at \sim 715 cm⁻¹.

Frequency calculations of thin vanadia films supported on α -Al₂O₃(0001) surface [102], did not give rise to bands above 805 cm⁻¹ (cf. Figure 3.21). In bulk AlVO₄, in which oxygen atoms are 2-fold coordinated and form V-O⁽²⁾-Al bonds, vibrations in the 1025–882 cm⁻¹ region (Fig. 3.21) were obtained and indeed assigned to V-O⁽²⁾ stretch [136]. The shortest V-O⁽²⁾ bonds are 1.67 Å and belong to rings composed of alternating oxygen and metal atoms. Moreover, a surface-localized V-O⁽²⁾-Al vibration at 922 cm⁻¹ was obtained for the most stable V₂O₅ cluster adsorbed on the α -Al₂O₃(0001) surface, which arises from the presence of short V-O⁽²⁾ bonds (1.67 and 1.68 Å) at the interface [109]. The bands at 858 cm⁻¹ for the V₂O₅ cluster on κ -Al₂O₃ reveal that the structure of the support and in particular the presence of tetrahedral sites affects the interface vibrations. These dimeric species have a similar structure to the corresponding ones on α -Al₂O₃; however, they do not have any short V-O⁽²⁾ bonds (see Figure 3.15). Their vibration in contrast to V₂O₅/ α -Al₂O₃ is *not* interface-localized.

One puzzling question concerning alumina-supported vanadia catalysts is the nature of the \sim 950 cm⁻¹ band observed in the IR spectra of model systems as well as in the Raman spectra of powder samples [3, 16, 72]. It was claimed that this

mode is due to V–O–V vibrations and therefore used as a fingerprint for the so-called “polymeric vanadia species” [3]. Indeed, a Raman active mode at 963 cm^{-1} attributed to V–O⁽²⁾–V stretching vibrations exists in bulk V₂O₅ [137]. In Ref. [16], however, it was suggested that the band is localized at the interface and involves V, O, and Al ions. A vibrational study of alumina-supported vanadium oxides modeled by a cluster containing an O=V(OAl)₃ unit with 2-fold coordinated oxygen atoms at the V–O–Al interface and tetrahedrally coordinated aluminum atoms, revealed strong vibrational coupling between the in-phase V–O⁽²⁾–Al mode and the Al–O–Al framework [72]. The authors reported four intense vibrations involving the V–O–Al interface in the $925\text{--}955\text{ cm}^{-1}$ region, with the V–O⁽²⁾ bonds of 1.77 and 1.78 Å (cf. Figure 3.21).

Thus, based on the vibrational spectra summarized in Figure 3.21, the presence of V–O⁽²⁾–Al interface bonds as a structural element of alumina-supported vanadia catalysts can *not* guarantee the appearance of a band at $\sim 950\text{ cm}^{-1}$ and that additional factors, such as the V–O⁽²⁾ bond lengths, couplings, and the specific support structure play a role. For vanadia species supported on κ -alumina, both V–O⁽²⁾–Al and V–O⁽³⁾–Al interface bonds give rise to bands in the same range (below $\sim 900\text{ cm}^{-1}$). This discussion also indicates that on the basis of the structure of models that produced the $\sim 950\text{ cm}^{-1}$ band, the nature of the interface cannot be unequivocally assigned.

3.2.6 Summary

Low-coverage vanadia species (monomers, dimers, trimers, and 1D vanadia rows) as well as vanadia films of varying thickness supported on the κ -Al₂O₃(001) surface have been investigated by DFT combined with statistical thermodynamics. The results are compared to those obtained for α -Al₂O₃-supported species.

The vanadia/ κ -alumina phase diagram as a function of oxygen partial pressure and vanadium activity shows that at high values of the vanadium chemical potential, vanadia films would become as thick as the vanadium supply allows. The presence of vanadyl groups is a prevalent feature of the film termination rendering the oxidation state of vanadium V^V for the surface atoms and V^{III} for the atoms in the bulk of these 3D structures. This is similar to what has been predicted for the α -Al₂O₃(0001) support. A major difference appears at low $\Delta\mu_V$ values. On κ -alumina, low-coverage monomeric and polymeric species are anchored exclusively via V–O⁽³⁾–Al interface bonds, whereas on α -alumina only species with V–O⁽²⁾–Al bonds are stabilized. Moreover, under typical reducing conditions (UHV and high temperatures, e.g., $T \geq 800\text{ K}$), low-coverage aggregates on κ -Al₂O₃ are partially reduced, i.e., they expose V^V and V^{III} centers. This correlates with defect formation energy values for the initial removal of lattice oxygen in the range of 1.25–2.74 eV. The reduction energy decreases as oligomers of increasing length form and reaches a minimum (1.25 eV) for the 1D rows. In contrast, on the α -Al₂O₃(0001) surface, the only stable low-coverage VO_x species are dimers with V–O⁽²⁾–Al interface bonds and a

defect formation energy of 2.8 eV.

The supported vanadia catalysts are characterized by the ability to release lattice oxygen in Mars-van Krevelen-type oxidation reactions. If we accept that the catalytic activity depends on the catalyst's reducibility, the energy of oxygen defect formation may be used as an indicator of its catalytic performance. Hence, systems with low thermodynamic stability of lattice oxygen (i.e., small defect formation energy) are likely to perform better. Our findings indicate that the vanadyl-terminated low-coverage species on κ -Al₂O₃, which possess significantly labile oxygen atoms, are expected to exist at catalytically relevant conditions, namely atmospheric pressure and a temperature range of 500–800 K ($\Delta\mu_{\text{O}} = -0.50$ to -0.85 eV). Thus, the present study suggests that the VO_x/ κ -Al₂O₃ species are likely to show higher reactivity than the stable species on the α -Al₂O₃ support.

At a given vanadia loading, the reactivity of the supported VO_x species is influenced by the alumina support structure. Compared to α -Al₂O₃, the presence of tetrahedrally coordinated Al sites (25 %) in κ -Al₂O₃ results in a much more open structure that facilitates significant defect-induced lattice relaxations. Similar results are expected to be obtained for vanadia supported on other metastable alumina phases such as γ -Al₂O₃ and on the unique structure of the ultrathin aluminum oxide film on NiAl(110).

Using the calculated vibrational spectra of dimeric species anchored via V–O⁽²⁾–Al interface bonds at the α - and κ -Al₂O₃ supports, the studies show that the sole presence of such bonds at the vanadia/alumina interface does *not* necessarily lead to surface-localized vibrations at ~ 950 cm⁻¹, and that the existence of tetrahedral sites affects the spectra.

Chapter 4

Thin SiO₂ Film on Mo(112) Substrate

Surface science techniques, such as scanning tunneling microscopy or photoemission spectroscopy, cannot be applied directly to insulating bulk-like materials, because of the requirement of electrical conductivity of the samples. This limitation is overcome in ultrathin oxide films epitaxially grown on metal substrates. Additionally, the reduced complexity of well-ordered supports, as compared to the industrially used porous bulk materials, facilitates the structural characterization of model catalyst systems at the atomic level. However, the atomic structure of crystalline films could only be resolved in a few cases [29, 32, 80].

Silica is widely used as a support material in heterogeneous catalysis. Amorphous SiO₂ has been grown on Mo(100) and Mo(110) surfaces [138, 139], but the preparation of well-ordered films on metal supports remained an experimental challenge until very recently, when the first crystalline silica epilayers were reported on a Mo(112) substrate by Schroeder *et al.* [20, 21, 140, 141] and later by Goodman and co-workers [22, 24, 142–144]. In the first structure model [21], a SiO₄ tetrahedron is assumed to be the building unit for the epilayer silica film. The proposed structure involves a maximum coordination of oxygen atoms to the Mo(112) surface, i.e., three O atoms of each tetrahedra are bonded to the Mo atoms. The fourth (“apical”) oxygen atom must be stabilized either by hydrogen, thus forming silanol (Si–OH) groups, or shared with further silica layers. Since neither silanol nor hydroxyl species were observed on these films [21], this implied that the silica film was of several layers in thickness. Based on attenuation of the substrate signals in the Auger electron spectra (AES) and angular-resolved XPS spectra, Schroeder *et al.* [20] came to the conclusion that the film is 5–8 Å thick.

The first attempt to employ DFT calculations for resolving the structure of the SiO₂/Mo(112) film was made by Ricci and Pacchioni [23]. The authors investigated the stability and adhesion energies of OH-terminated and fully dehydroxylated three-layer thick films of known silica phases, i.e., β -cristobalite, β -tridymite, α -quartz, and β -quartz epitaxially grown on Mo(112). They concluded that the silica films

(~ 11 Å thickness) grow preferentially with the β -cristobalite structure because this provides the strongest adhesion to the Mo(112) surface and the smallest strain in the epilayer. The dehydroxylated surfaces of these phases undergo strong reconstructions, resulting in the formation of two-membered silica rings in the case of the cristobalite and tridymite structures, and in three-membered rings in the case of quartz [23]. The presence of the strained two-membered silica rings at the surface of the cristobalite-derived model (cf. Figure 4.1A) should result in films which are highly reactive towards adsorption of water or metal clusters. However, this is in contrast to experimental observations, which indicate that the film is inert towards H₂O, CO, and O₂ [145]. Furthermore, vibrational frequencies calculated within the harmonic approximation revealed a broad band in the 1000–1100 cm⁻¹ region, which is inconsistent with the sharp band at 1048 cm⁻¹ measured in IRAS [21] and high-resolution electron energy loss spectrometry (HREELS) [22] experiments.

Following analysis of the HREELS spectra of the SiO₂/Mo(112) film and various Si and Mo oxide compounds reported in the literature, Goodman and co-workers [22] suggested that this prominent absorption band at 1048 cm⁻¹ must be attributed to the Si–O–Mo vibration. The absence of a band in the 1150–1250 cm⁻¹ region, which is characteristic of the asymmetric Si–O–Si stretching vibration in bulk silica systems, led the authors to conclude that the film does not exhibit Si–O–Si bonds. Hence, they proposed a model consisting of a layer of isolated [SiO₄] clusters arranged in a $c(2 \times 2)$ structure on the Mo(112) surface, with all oxygen atoms bonded to the Mo substrate [22, 24] (cf. Figure 4.1B). The film is one layer thick, in agreement with the thickness of ~ 3 Å determined by AES. It is noteworthy that experimentally synthesized thicker films lack long-range order and decompose upon high temperature annealing to yield the monolayer structure. Thus, in spite of extensive efforts from both experiment and theory to elucidate the atomic structure of the ultrathin silica film epitaxially grown on Mo(112) surface, none of the models proposed so far could successfully explain all the available experimental data.

In this chapter, first-principle DFT calculations are employed to determine the atomic structure of the crystalline SiO₂/Mo(112) film, demonstrating an excellent agreement with the experimental STM, XPS, and IRAS results. The structure consists of a two-dimensional (2D) network of corner-sharing [SiO₄] tetrahedra and is a new form of SiO₂ which resembles the sheet structure of monolayer silicates [146]. The work presented here has been performed in collaboration with the experimental group of Prof. Hans-Joachim Freund at the Fritz-Haber-Institut der Max-Planck-Gesellschaft and the results have been published in Refs. [25, 26, 147].

4.1 Experimental Findings on the Thin Silica Film

First, the most important experimental findings for the ultrathin crystalline silica film grown on the Mo(112) substrate are briefly summarized.

The preparation of thin well-ordered SiO₂ films included Si deposition in an

oxygen environment onto an oxygen-precovered Mo(112) surface and subsequent annealing in vacuum. The ordering strongly depends on the annealing temperature, such that high temperature annealing at ~ 1250 K produces a sharp LEED pattern showing a $c(2 \times 2)$ -Mo(112) structure.

Large-scale STM images revealed atomically flat films, free of holes and silica particles, with smooth terraces of 20–50 nm in width. In addition, well-resolved images of antiphase domain boundaries (APDB) propagating along the $[\bar{1}10]$ direction, as predicted by Schroeder *et al.* [20] on the basis of LEED results, were obtained. High-resolution STM images show a honeycomb-like structure of the silica film with a periodicity of ~ 5.2 Å in the $[\bar{3}11]$ direction and ~ 5.5 Å in the $[\bar{1}\bar{1}0]$ direction, in agreement with the $c(2 \times 2)$ structure observed by LEED. Interestingly, the atomic structure seen in STM depends on the tunneling conditions, which indicates that different electronic states can be involved in the tunneling process.

The IRAS spectra for these films showed a sharp and strong signal at 1059 cm^{-1} with the full width half maximum (FWHM) of only 12 cm^{-1} , suggesting a high ordering of the film and a single phonon excitation as well as two weak bands at 771 and 675 cm^{-1} .

Finally, the XPS study revealed a single peak in the Si $2p$ region with a binding energy (BE) of 103.2 eV, which is characteristic for the Si^{IV} oxidation state. The O $1s$ region, on the other hand, showed two components centered at 531.2 and 532.5 eV, which suggest the presence of two different oxygen species. Their intensity ratio is estimated to be 3:2. Both BEs are significantly higher than those observed for MoO_x films formed on the Mo(112) surface (~ 530 eV), and therefore cannot be assigned to the oxidation of the Mo substrate underneath the film.

4.2 Structure Models

In constructing possible structure models for the thin $\text{SiO}_2/\text{Mo}(112)$ film, criteria based on the following experimental evidence have been used: (i) periodicity consistent with the LEED and STM data, (ii) hexagonal arrangement of the building units indicated by STM, (iii) simple atomic structure and/or high symmetry of the film suggested by the XPS and IRAS data, (iv) coordinatively saturated and oxygen-terminated surface, based on the chemical inertness of the film towards H_2O , O_2 , and CO [145], and (v) an average thickness of the film of about 3–4 Å, as determined by AES [22].

4.2.1 Mo(112) Substrate

The Mo(112) substrate was constructed from the relaxed bulk bcc Mo structure with a calculated lattice constant $a = 3.155$ Å, in excellent agreement with the experimental value of 3.147 Å. The surface was modeled using an orthorhombic (2×2) unit cell with the lattice constants $a_0 = 5.464$ Å and $b_0 = 8.923$ Å. The slab

contains seven Mo layers, which reproduce well the band structure of bulk Mo. During the geometry optimization, all atoms in the four surface layers were relaxed, while the three bottom layers were kept frozen at their bulk positions. An energy cutoff of 400 eV and a $(8 \times 4 \times 1)$ Monkhorst-Pack grid were employed throughout this work. Regarding the PAW potentials, core radii of 1.9 and 2.6 au are used for Si and Mo, respectively. The O core radii are 1.2 and 1.52 au for the *s* and *p* states, respectively.

4.2.2 Previously Proposed Models

Figure 4.1 shows the previously proposed models of thin crystalline silica films grown on Mo(112), i.e., (A) the three SiO₂ layers of β -cristobalite-like structure with the composition (SiO₂)₁₀·3O [23] and (B) the monolayer of isolated $c(2 \times 2)$ -[SiO₄] tetrahedra with surface unit cell composition (SiO₂)₂·4O [22]. However, as has already been mentioned, they could not successfully explain the experimental findings, and thus, none of them correspond to the structure of the epitaxially grown ultrathin SiO₂ film.

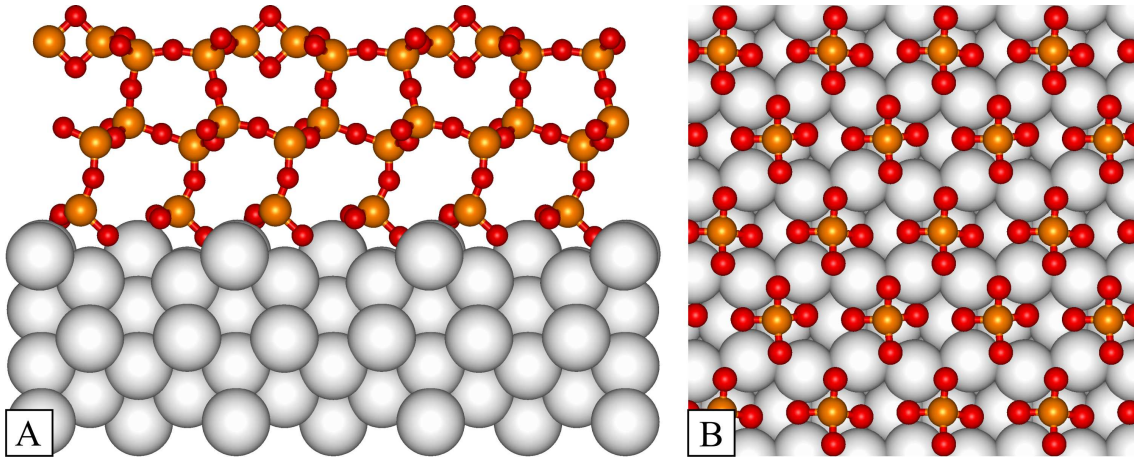


Figure 4.1: (A) Side view of the β -cristobalite derived structure [23] and (B) Top view of the isolated $c(2 \times 2)$ -[SiO₄] tetrahedra structure [22].

4.2.3 2 ML Silica Films

Inspired by the structures of layered silicates [146], models consisting of two monolayers (2 ML) of [SiO₄] tetrahedra, with an average thickness of about 7–9 Å were constructed. None of them has dangling Si–O bonds or edge-shared SiO₄ tetrahedra strained at the film surface. 2 ML structure models with a precise SiO₂ stoichiometry as well as models with an excess of one, two, and three oxygen atoms per surface unit cell and the composition (SiO₂)₈·O, (SiO₂)₈·2O, and (SiO₂)₈·3O, respectively, were considered.

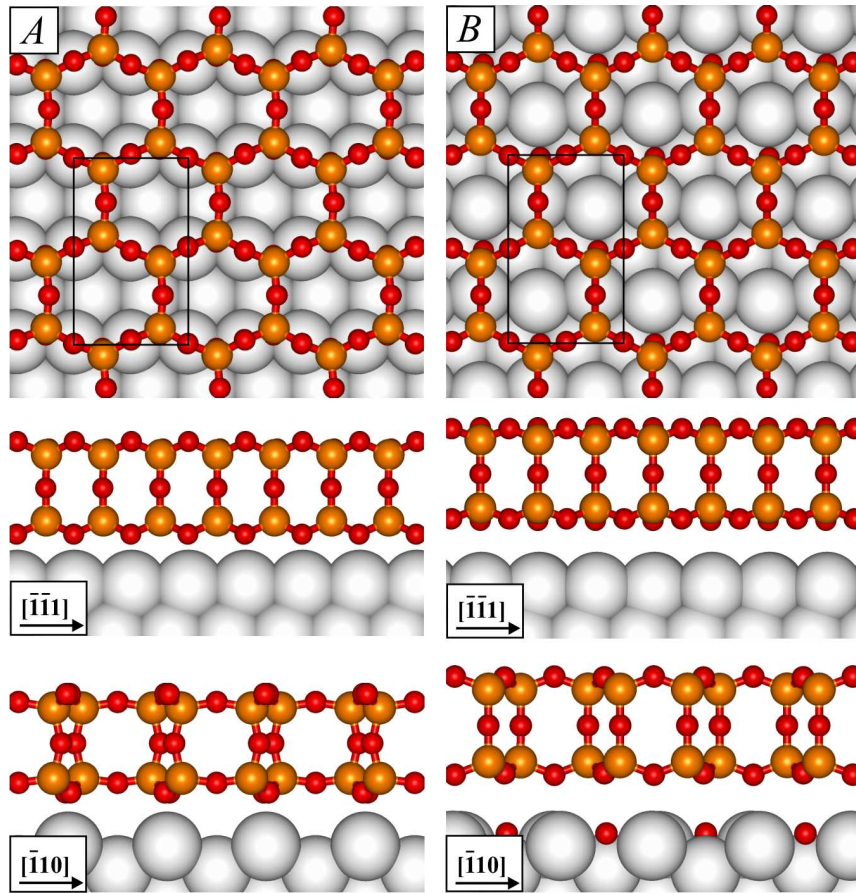


Figure 4.2: The 2 ML $\text{SiO}_2/\text{Mo}(112)$ film models: (A) stoichiometric $(\text{SiO}_2)_8/\text{Mo}(112)$ film and (B) $(\text{SiO}_2)_8 \cdot 2\text{O}/\text{Mo}(112)$ model with excess of two oxygen atoms in bridge sites located in the trenches. Black rectangle indicates the unit cell.

Figure 4.2 shows the two most stable 2 ML $\text{SiO}_2/\text{Mo}(112)$ film structures. The stoichiometric $(\text{SiO}_2)_8/\text{Mo}(112)$ film has oxygen atoms (O2) in the top position with respect to the protruding Mo atoms running along the $[\bar{1}\bar{1}1]$ direction (cf. Figure 4.2A). As a result of full valence saturation of the bottom and top sides of the silica layer, this film stays unbound to the substrate and is separated by 2.4 Å from the topmost Mo atoms of the $\text{Mo}(112)$ surface. Attempts to bind the film to the substrate by introducing excess oxygen resulted in an unbound silica film (3.2 Å distance from the substrate) and an oxidized $\text{Mo}(112)$ surface. Figure 4.2B shows the most stable example of such a film, with the surface unit cell composition $(\text{SiO}_2)_8 \cdot 2\text{O}$ and the excess of two oxygen atoms located in bridge positions in the trenches.

4.2.4 1 ML Silica Films

Even thinner films, such as monolayer (1 ML) models, can be constructed by cutting off the bottom Si and O atomic layers of a 2 ML stoichiometric film in such a

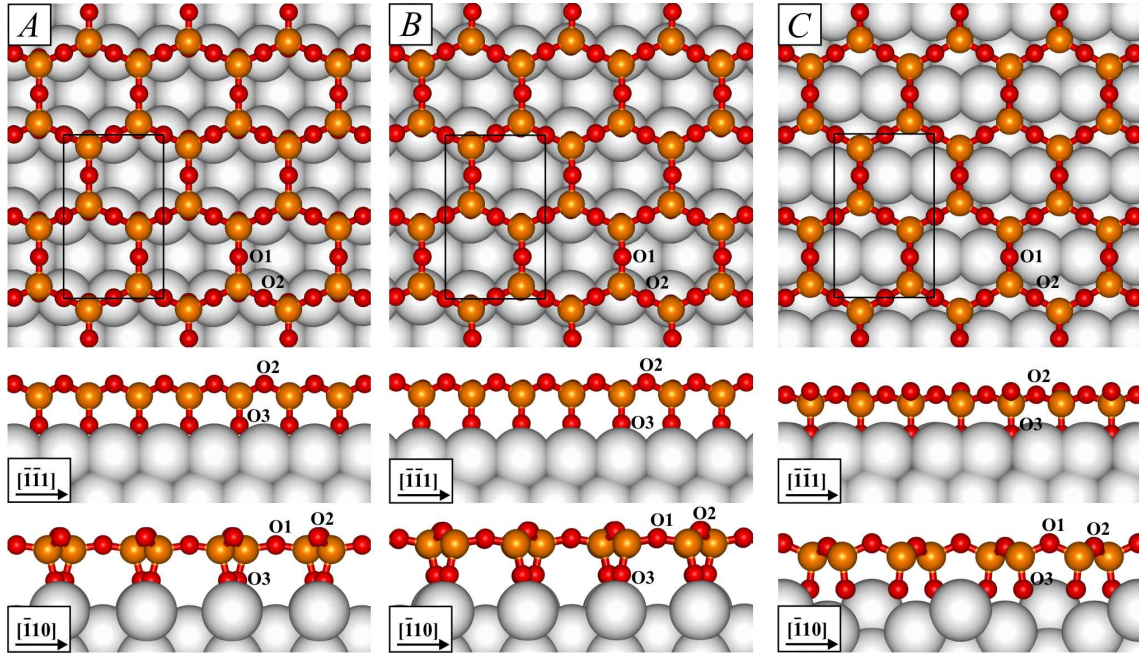


Figure 4.3: The three 1 ML models of the SiO₂/Mo(112) film. Black rectangle indicates the (SiO₂)₄·2O unit cell.

way that the oxygen atoms are pointing to the metal substrate. The three models presented in Figure 4.3 differ by the adsorption site of the interface oxygen atom (O3) on Mo(112), i.e., bridge (model A), top (model B), or pseudo threefold hollow (model C) sites with respect to the protruding Mo rows running along the $[\bar{1}\bar{1}1]$ direction. The formal surface unit cell composition of all three models is (SiO₂)₄·2O or Si:O ratio of 1:2.5, which suggests non-stoichiometric films. However, one oxygen atom of each SiO₄ tetrahedron forms an O–Mo bond and formally shares one electron with the metal surface. Thus, the structure of the film can also be interpreted as a stoichiometric layer of molybdenum silicate deposited on the Mo(112) surface. It should be mentioned that these structures show some similarities with the proposed, but rejected model 4 of Ref. [22].

Table 4.1 presents selected calculated structural parameters for the three 1 ML SiO₂/Mo(112) film models (cf. Figure 4.3 for atom labeling). The distance between the plane of the topmost O2 atoms and the plane between the Mo atoms of the topmost rows and those in the furrows is ~ 4.5 Å, in agreement with the experimentally estimated film thickness based on AES results. In all models, the Si–O bond lengths show only a small variation in the range of 1.62–1.65 Å. On the other hand, the bonds between Mo and interface oxygen (O3) atoms differ significantly among the three models. They range from 1.91 Å for the 1 ML model B to 2.32 Å for 1 ML model C. The Si–O1–Si bond angle shows much larger variation (131.5–163.2°) than the Si–O2–Si angle (132.9–145.3°). The Si–O–Mo bond angle varies in a range of 121.1–177.3°. Note that the 1 ML model B with top positions of interface

Table 4.1: Selected structural parameters (Å, deg) of the 1 ML SiO₂/Mo(112) film models.

Model	Si–O1	Si–O2	Si–O3	Mo–O3	Si–O1–Si	Si–O2–Si	Si–O–Mo
1 ML <i>A</i>	1.62	1.64	1.65	2.11	163.2	132.9	139.2–139.6
1 ML <i>B</i>	1.62	1.64	1.64	1.91	157.1	134.4	177.3
1 ML <i>C</i>	1.63	1.63	1.65	2.22–2.32	131.5	145.3	121.1–152.1

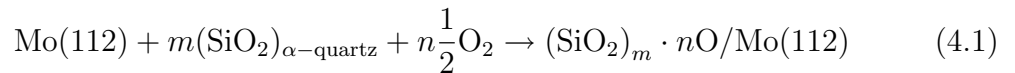
oxygen atoms with respect to the protruding Mo rows corresponds to the model independently found by Giordano *et al.* [148].

In addition, the structural parameters for the $c(2 \times 2)$ -[SiO₄] tetrahedra structure of Chen *et al.* [22] were calculated. It consists of isolated SiO₄ tetrahedra located in the trenches of the Mo(112) substrate, with all four oxygen atoms bound to the metal surface. Two of the oxygen atoms bind to Mo atoms of the protruding rows and the other two are located in the trenches (cf. Figure 4.1B). The Si atoms from every SiO₄ unit are positioned downwards with respect to the topmost pairs of O atoms. The Si–O bond lengths are in the range of 1.65–1.73 Å, slightly longer than the bonds in the 1 ML SiO₂/Mo(112) models, whereas the Mo–O bonds (2.14–2.28 Å) are similar. The Si–O–Mo bond angles that involve Mo atoms from the protruding rows are much smaller (75.3–107.7°) than the corresponding ones in the monolayer films, and increase to 119.6–162.4° for the angles involving Mo atoms from the trenches.

Very recently, Chen and Goodman have revisited their structure model, so that the isolated SiO₄ clusters are rotated with respect to those in the original model to better fit the observed STM images [149].

4.3 Thermodynamic Stability

The stability of the silica structure models is compared using the formation energy, ΔE_{form} , from a clean Mo(112) surface, bulk α -quartz, and oxygen:



where m and n are the numbers of SiO₂ units and excess oxygen atoms in a surface unit cell, respectively. The ΔE_{form} is given as

$$\Delta E_{\text{form}} = E_{(\text{SiO}_2)_m \cdot n\text{O}/\text{Mo(112)}} - (E_{\text{Mo(112)}} + mE_{(\text{SiO}_2)_{\alpha\text{-quartz}}} + n\frac{1}{2}E_{\text{O}_2}) \quad (4.2)$$

where $E_{(\text{SiO}_2)_m \cdot n\text{O}/\text{Mo(112)}}$ corresponds to the energy of a given SiO₂/Mo(112) structure model, $E_{\text{Mo(112)}}$, $E_{(\text{SiO}_2)_{\alpha\text{-quartz}}}$, and E_{O_2} are the energies of the clean Mo(112) surface, bulk α -quartz, and an oxygen molecule, respectively.

The most stable stoichiometric 2 ML film (Figure 4.2A) has a positive value of the formation energy ($\Delta E_{\text{form}} = 0.8$ eV; $m = 8, n = 0$). The model with a partially oxidized Mo(112) surface (Fig. 4.2B, $m = 8, n = 2$) is a quite stable 2 ML structure, with a formation energy of -6.5 eV. The increasing stability with increasing the oxygen content in the unit cell is certainly connected with the high oxidation energy of Mo. Among the 1 ML models, the highest stability is shown by model A ($\Delta E_{\text{form}} = -10.8$ eV; $m = 4, n = 2$), which is 2 eV more stable than model B ($\Delta E_{\text{form}} = -8.8$ eV) and C ($\Delta E_{\text{form}} = -8.7$ eV). The β -cristobalite-like (three SiO₂ layers) film structure proposed by Ricci and Pacchioni is 1.7 eV less stable ($\Delta E_{\text{form}} = -9.1$ eV; $m = 10, n = 3$) than the 1 ML model A, whereas the model of isolated $c(2 \times 2)$ -[SiO₄] clusters of Chen *et al.* is slightly more stable ($\Delta E_{\text{form}} = -11.5$ eV; $m = 2, n = 4$).

Since these structure models differ by their chemical composition, the relative stability has to be compared at a given oxygen pressure corresponding to experimental conditions. Thus, the quantity of interest is the surface-related free energy of reaction (4.1), $\Delta\gamma$, defined as

$$\Delta\gamma(T, p) = \frac{1}{A} [\Delta E_{\text{form}} - n\Delta\mu_{\text{O}}(T, p)] \quad (4.3)$$

where A is the surface area and $\Delta\mu_{\text{O}}(T, p)$ is given by Eq. (3.5) in Section 3.1.3. The oxygen chemical potential is related to temperature (T) and oxygen partial pressure (p) assuming that the surface is in thermodynamic equilibrium with the gas phase O₂ [113].

Figure 4.4 plots the surface-related free energy $\Delta\gamma$ as a function of the oxygen chemical potential at $T = 300$ and 1200 K for the most stable SiO₂/Mo(112) structure models. Our calculations suggest that 1 ML model A is thermodynamically the most favorable structure at all experimentally relevant oxygen pressures. The free energy of formation of the second most stable 1 ML model B is with 43 meV/Å² larger and differs only by 0.6 meV/Å² from the 1 ML model C. Since these models have the same content of excess oxygen n (see Eq. (4.1)), the three lines in the plot are parallel. The isolated $c(2 \times 2)$ -[SiO₄] tetrahedra model is energetically more favorable than the β -cristobalite-like film for oxygen chemical potential values higher than about -2.5 eV. However, when compared to the 1 ML model A, it becomes more stable only at very high oxygen partial pressures (e.g., $\sim 3 \times 10^8$ atm. at $T = 1200$ K). Thus, statistical thermodynamics indicates that 1 ML A is the most probable candidate for the atomic structure of the SiO₂/Mo(112) film.

4.4 Electronic and Vibrational Properties

In order to verify whether the model of the 2D network of [SiO₄] tetrahedra indeed agrees with the experimental findings, the IR spectra and O 1s core-level shifts as well as STM images at different tunneling conditions were calculated for all three

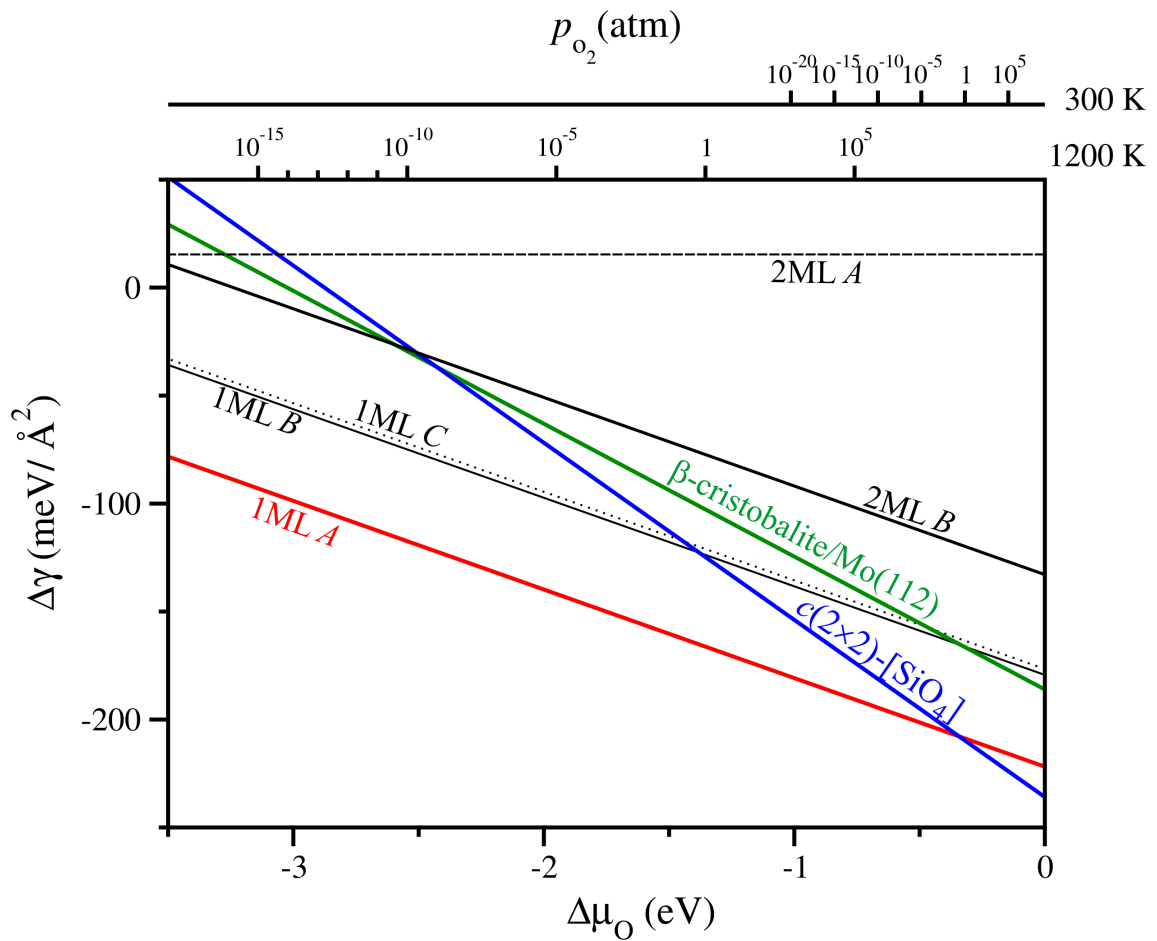


Figure 4.4: Surface-related free energy of formation $\Delta\gamma(T, p)$ as a function of the oxygen chemical potential for the most stable $\text{SiO}_2/\text{Mo}(112)$ film models: 1 ML and 2 ML films, β -cristobalite-like film (Ref. [23]), and the isolated $c(2 \times 2)$ - $[\text{SiO}_4]$ tetrahedra model (Ref. [22]). The $\Delta\mu_{\text{O}}$ axis has been translated into an oxygen pressure scale at $T = 300$ and 1200 K.

1 ML structures *A*, *B*, and *C*. In addition, the electronic and vibrational properties of the isolated $c(2 \times 2)$ - $[\text{SiO}_4]$ tetrahedra model are discussed, unambiguously demonstrating that it does not correspond to the atomic structure of the silica film.

4.4.1 Vibrational Analysis

It is known that the agreement between calculated harmonic vibrational frequencies and observed fundamentals can be improved using an empirical scaling factor derived from calculated and observed frequencies of known compounds [150]. α -quartz was chosen as the reference substance and the lattice constants and internal coordinates were simultaneously optimized by a stress tensor calculation using the same setup as for the $\text{SiO}_2/\text{Mo}(112)$ films, except for the higher plane wave energy cutoff of 800 eV. For the final configuration, the relaxation of atomic positions and calculation of

Table 4.2: Calculated scaled [scaling factor 1.0312] harmonic vibrational frequencies (cm⁻¹) and IR intensities (in parentheses, normalized to 1.00) for the most intense vibrational modes of the 1 ML *A*, *B*, and *C* models. Experimental IRAS frequencies are given for comparison.

1 ML <i>A</i>		1 ML <i>B</i>		1 ML <i>C</i>		Experiment	
Si ¹⁶ O ₂	Si ¹⁸ O ₂	Si ¹⁶ O ₂	Si ¹⁸ O ₂	Si ¹⁶ O ₂	Si ¹⁸ O ₂	Si ¹⁶ O ₂	Si ¹⁸ O ₂
1061(0.91)	1021	1132(1.00)	1085	978(0.58)	948	1059	1018
779(0.07)	770	781(0.04)	774	804(0.004)	795	771	764
672(0.09)	650	709(0.13)	689	646(0.09)	616	675	656
312(0.02)	307	335(0.02)	326	290(0.006)	284		

harmonic frequencies were performed employing a 400 eV cutoff. The experimental phonon frequencies of α -quartz in the range of 400–1200 cm⁻¹ were taken from Refs. [151, 152]. Using a least square fitting procedure, the scaling factor of 1.0312 was derived, with the root mean square error (rms) between the calculated and observed frequencies of 13.6 cm⁻¹.

Table 4.2 shows the calculated scaled harmonic frequencies for the most intense vibrational modes of the 1 ML film models *A*, *B*, and *C* as well as those obtained by IRAS. In agreement with experiment, the calculations reveal only three IR active modes above 400 cm⁻¹ with non-negligible intensity. While for models *B* and *C* the calculated frequencies deviate by up to 80 cm⁻¹ from the experimental values, for the 1 ML model *A* the positions and relative intensities of the calculated bands corroborate the experimental results. Moreover, for the same film model the calculations reproduce even the experimental ¹⁸O isotopic shifts (cf. Table 4.2).

The normal modes for the three most intense vibrations of the 1 ML *A* are visualized in Figure 4.5. The mode at 1061 cm⁻¹ is the in-phase combination of asymmetric Si–O–Mo stretching modes originating from the Si–O bonds pointing downwards to the Mo(112) substrate. The mode at 779 cm⁻¹ is the Si–O–Si symmetric stretching coupled with Si–O–Si bending, and the third mode at 672 cm⁻¹ is a coupling of Si–O–Si bending with a small contribution of the Si–O–Si symmetric stretching modes. The vibration with a low IRAS intensity at 312 cm⁻¹ corresponds to a vertical motion of the entire silica film. On the other hand, the calculated IRAS inactive vibrations include combinations of Si–O–Si asymmetric stretching modes in the range of 1008–1195 cm⁻¹, out-of-phase combinations of Si–O–Mo asymmetric stretching vibrations between 863 and 912 cm⁻¹ as well as coupled Si–O–Si symmetric stretching and Si–O–Si bending modes between 676 and 821 cm⁻¹. Vibrations in the range of 325–557 cm⁻¹ include complicated couplings of bending modes. Generally, the assignment of vibrational modes below 900 cm⁻¹ is difficult because of the strong coupling between different stretching and bending modes.

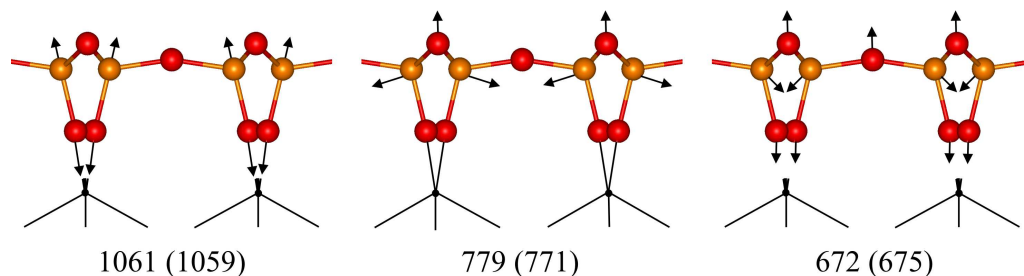


Figure 4.5: Vibrational normal modes viewed along the $[\bar{1}\bar{1}\bar{1}]$ direction of the 1 ML model A. Calculated and experimental (in parentheses) vibrational frequencies (cm^{-1}) are shown for comparison. O and Si atoms are depicted in red and orange, respectively. For clarity, the Mo(112) surface is drawn as sticks.

The vibrational spectrum calculated for the monolayer film of isolated $c(2 \times 2)$ - $[\text{SiO}_4]$ units (cf. Figure 4.6c) shows two almost equally intense bands at 706 (coupled symmetric O–Si–O stretching and O–Si–O bending modes) and 532 cm^{-1} (coupled Mo–O stretching and O–Si–O bending modes) as well as a less intense band at 403 cm^{-1} (Mo–O stretching and O–Si–O bending), which clearly disagree with the experimental IRAS and HREELS spectra. The O–Si–O asymmetric stretching modes at 929 and 939 cm^{-1} involving the topmost oxygen atoms bound to the protruding Mo rows as well as the O–Si–O asymmetric stretching modes at 760 and 762 cm^{-1} involving oxygen atoms located in the furrows of the Mo(112) surface are IRAS inactive.

Recently, Yakovkin reported a vibrational frequency calculation for the same model of isolated $c(2 \times 2)$ - $[\text{SiO}_4]$ tetrahedra, but using only a small cluster model containing just one $[\text{SiO}_4]$ unit cut from the optimized periodic structure [153]. Such a model cannot adequately describe the Mo conduction band electrons nor the coupling of the silica vibrational modes with those of the substrate. Moreover, the Hartree-Fock method applied by the author along with a minimal STO-3G basis set are known to be particularly inaccurate in describing transition metal containing compounds. In that paper, the 2D network of SiO_4 tetrahedra has not been considered and the analysis was restricted to isolated $[\text{SiO}_n]$ structures. In that respect, the study does not provide any comparison of the possible silica film models, but simply assumes the structure proposed by Chen *et al.* as correct [22]. However, the calculated Si–O stretching frequency at 1044 cm^{-1} , reported to be in excellent agreement with the experimental mode at 1048 cm^{-1} , actually corresponds to the IRAS inactive modes at 929 and 939 cm^{-1} in our slab calculation. Given the crude approximations in this calculation, the agreement is entirely accidental and cannot be taken seriously as a support in favor of the isolated $c(2 \times 2)$ - $[\text{SiO}_4]$ tetrahedra structure. In fact, we have demonstrated that this model does not account for the observed vibrational spectra [26, 147], in contrast to the 2D network of corner-sharing $[\text{SiO}_4]$ tetrahedra. The latter is the same film model independently proposed by Giordano *et al.* [154] based on periodic DFT calculations, which further strengthened the

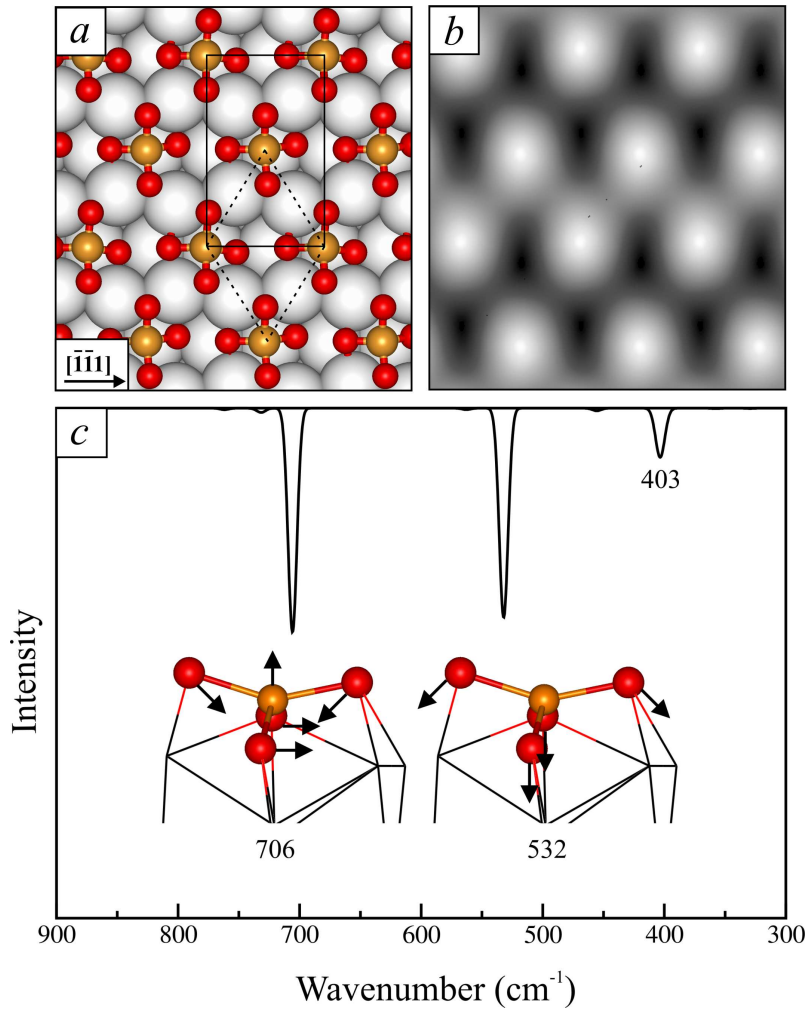


Figure 4.6: (a) Isolated $c(2 \times 2)$ -[SiO₄] tetrahedra structure of Chen *et al.* [22]. Black rectangle indicates the (SiO₂)₂·4O surface unit cell; (b) simulated STM image at $V_s = 0.65$ V; (c) simulated IRAS spectrum and the IR active vibrational modes. O and Si atoms are depicted in red and orange, respectively. The Mo(112) surface is drawn as black sticks.

arguments in favor of the 2D-network structure.

The absence of the characteristic Si–O–Si absorption bands in the monolayer SiO₂/Mo(112) film at ~ 1176 cm⁻¹ in HREELS or in the range of 1200–1250 cm⁻¹ in IRAS does not necessarily mean the absence of Si–O–Si bonds as postulated by Chen *et al.* [22]. The effect can be rationalized on the basis of the selection rules applied to refractory metal surfaces. The selection rule states that only vibrational modes with a component of the dynamic dipole moment perpendicular to the metal surface will contribute to the IR absorption [155]. These vibrational modes are, in general, only the totally symmetric modes of the film [156, 157].

To apply the selection rules to the 2D-network model, we first note that the surface unit cell belongs to the two-dimensional $cm\bar{m}$ space group, which is charac-

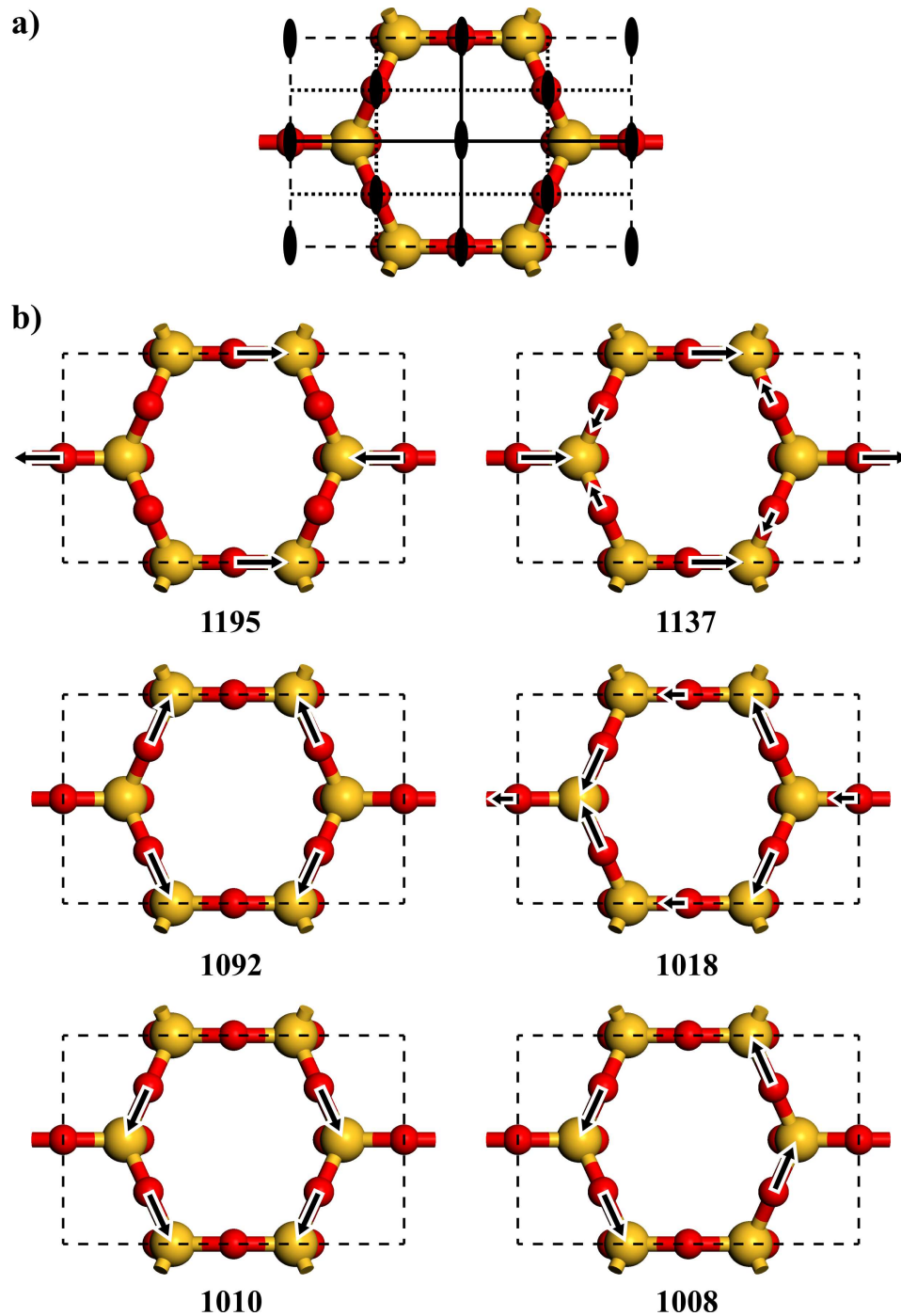


Figure 4.7: (a) Symmetry elements of the $cm\bar{m}$ surface unit cell of the 2D-network model of the $\text{SiO}_2/\text{Mo}(112)$ film (top view). The ellipsoids represent the twofold symmetry axes (C_2), solid lines - the symmetry planes (σ), and dotted lines - the glide planes (σ'); (b) Schematic representation of the normal modes involving coupled asymmetric Si-O-Si stretching vibrations along with the calculated frequencies in cm^{-1} .

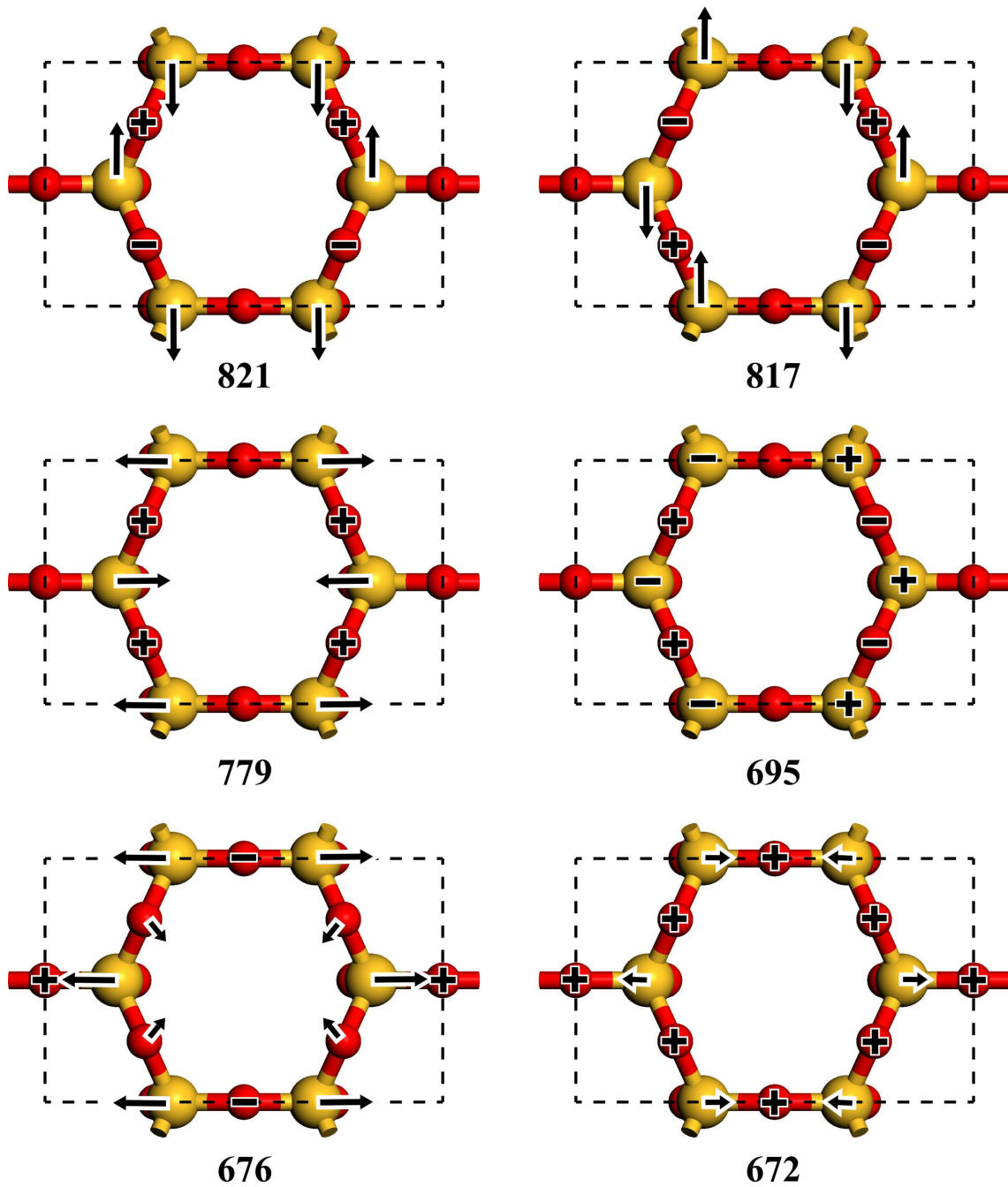


Figure 4.8: Schematic representation of the normal modes involving coupled symmetric Si-O-Si stretching vibrations along with the calculated frequencies in cm⁻¹. The plus and minus signs indicate atomic motions perpendicular to the surface.

terized by eight symmetry elements as shown in Figure 4.7a and listed in Table 4.3. Moreover, since the unit cell contains four Si and ten O atoms, there are six normal modes involving coupled asymmetric Si-O-Si stretching vibrations, six modes in-

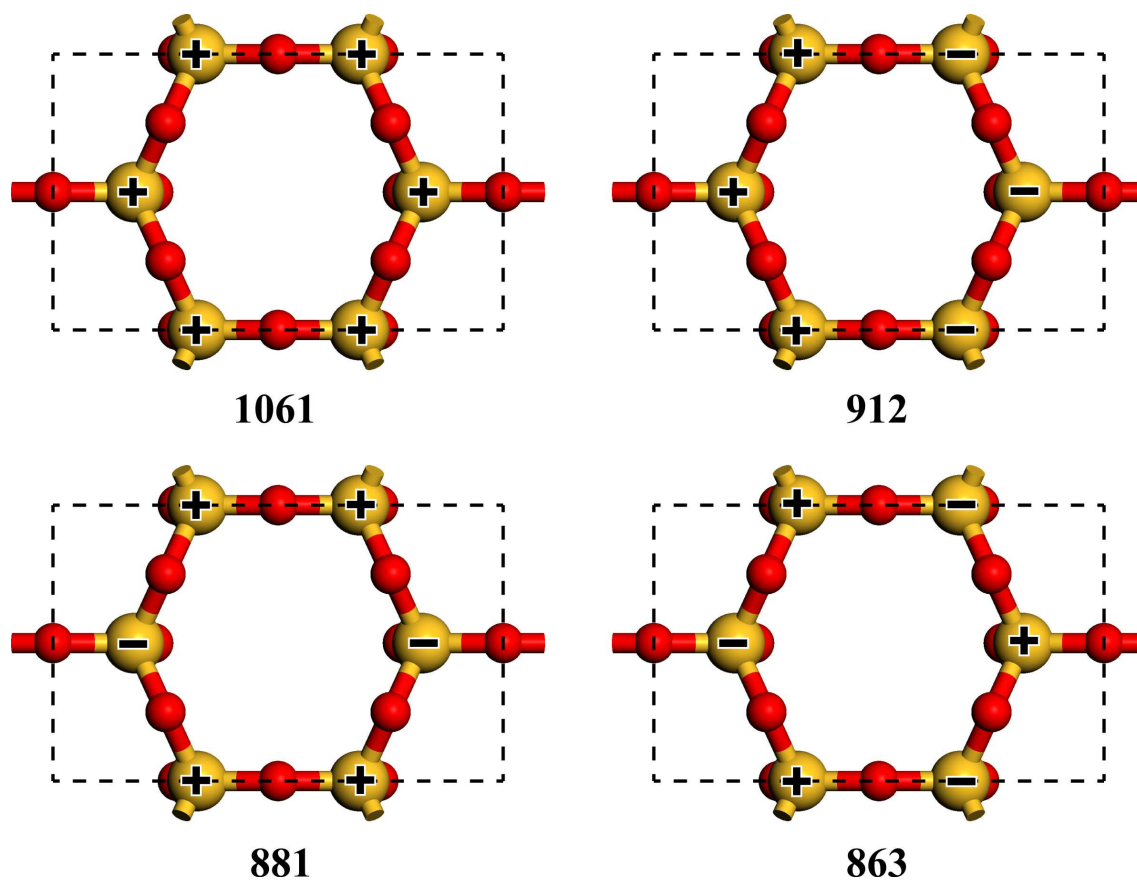


Figure 4.9: Schematic representation of the normal modes involving coupled Si–O–Mo stretching vibrations along with the calculated frequencies in cm^{-1} .

volving coupled symmetric Si–O–Si stretching vibrations, and four modes involving coupled asymmetric Si–O–Mo stretching vibrations. They are schematically represented in Figures 4.7b, 4.8 and 4.9, along with the corresponding calculated scaled frequencies. Table 4.3 shows their transformation properties with respect to all symmetry elements of the $cm\bar{m}$ space group, i.e., E - identity, C_2 - twofold symmetry axis, σ - symmetry plane, σ' - glide plane, τ - translational period. Note that only the frequency values are obtained from the DFT calculations. The normal modes themselves are deduced from the composition of the unit cell and its symmetry alone.

The six asymmetric Si–O–Si stretching vibrations shown in Fig. 4.7b are IRAS inactive because there is no dynamic dipole moment component perpendicular to the surface associated with any of these modes. The only vibrations that can result in the IR absorption are the symmetric Si–O–Si and the asymmetric Si–O–Mo stretching modes. Table 4.3 demonstrates that there are only three such modes with frequencies at 1061, 779, and 672 cm^{-1} that are symmetric with respect to all symmetry operations of the $cm\bar{m}$ space group (cf. Figs. 4.8 and 4.9). Hence, according

Table 4.3: Calculated scaled [scaling factor 1.0312] harmonic vibrational frequencies of the 2D-network model *A* and transformation properties of the normal modes with respect to the eight symmetry operations of the two-dimensional *cm̄m* space group (E - identity, C₂ - twofold symmetry axis, σ - symmetry plane, σ' - glide plane, τ - translational period).

Modes (cm ⁻¹)	E	C ₂	$\sigma(xz)$	$\sigma(yz)$	1/2 τ	C ₂ '	$\sigma'(xz)$	$\sigma'(yz)$
<i>Asymmetric Si-O-Si</i>								
$\nu_1 = 1195$	1	-1	-1	1	-1	1	1	-1
$\nu_2 = 1137$	1	-1	-1	1	1	-1	-1	1
$\nu_3 = 1092$	1	1	1	1	-1	-1	-1	-1
$\nu_4 = 1018$	1	-1	-1	1	1	-1	-1	1
$\nu_5 = 1010$	1	-1	1	-1	1	-1	1	-1
$\nu_6 = 1008$	1	1	-1	-1	-1	-1	1	1
<i>Asymmetric Si-O-Mo</i>								
$\nu_1 = 1061$	1	1	1	1	1	1	1	1
$\nu_2 = 912$	1	-1	-1	1	-1	1	1	-1
$\nu_3 = 881$	1	1	1	1	-1	-1	-1	-1
$\nu_4 = 863$	1	-1	-1	1	1	-1	-1	1
<i>Symmetric Si-O-Si</i>								
$\nu_1 = 821$	1	-1	1	-1	-1	1	-1	1
$\nu_2 = 817$	1	1	-1	-1	1	1	-1	-1
$\nu_3 = 779$	1	1	1	1	1	1	1	1
$\nu_4 = 695$	1	-1	-1	1	-1	1	1	-1
$\nu_5 = 676$	1	1	1	1	-1	-1	-1	-1
$\nu_6 = 672$	1	1	1	1	1	1	1	1

to the symmetry selection rule, they should be IRAS active. These are in-phase couplings of the asymmetric Si-O-Mo stretching vibrations as well as out-of-phase and in-phase couplings of the symmetric Si-O-Si ones, respectively (the latter two can also be interpreted as Si-O-Si symmetric stretching coupled with Si-O-Si bending modes). These are precisely the three bands observed in the IRAS experiments (cf. Section 4.1 and Refs. [25, 26, 147]).

Symmetry analysis for the vibrational modes of the isolated $c(2 \times 2)$ -[SiO₄] tetrahedra structure is very simple. The symmetry of the [SiO₄] units (Fig. 4.6a) is C_{2v}, suggesting that there are only two symmetric and two asymmetric combinations of Si-O stretching vibrations. Only the two symmetric modes are completely symmetric with respect to all symmetry operations of the C_{2v} group and therefore can be observed by IRAS. This is in agreement with the DFT results [26], which show only two IR active modes at 706 and 532 cm⁻¹, assigned to symmetric O-Si-O vibrations (see Fig. 4.6c). In contrast, Chen and Goodman claim that the asymmetric Si-O vibrations should always be IR active [149, 158]. However, in a dipole scattering

regime, HREELS obeys the same selection rule that applies to infrared spectroscopy, i.e., when the electrical field of the incoming electron interacts with the vibrational dipole moment of the film, only the totally symmetric vibrations are allowed. As a result, the HREELS experiments performed for the monolayer silica film reveal the same three vibrational modes in the range of 600–1200 cm^{-1} as observed by IRAS [22].

Finally, the following issue needs to be clarified. It is well-known that in the inelastic scattering regime of HREELS, the bands associated with vibrations parallel to the metal surface can also be observed. They show much weaker intensity than the dipole scattered ones and are best detected at off-specular angles. The absence of asymmetric Si–O–Si vibrational features in the off-specular HREELS spectra for the $\text{SiO}_2/\text{Mo}(112)$ film was interpreted by Chen and Goodman as the absence of Si–O–Si bonds essentially parallel to the substrate surface and was used as an argument to reject the 2D-network as the most viable model for the silica film. However, the following symmetry selection rules apply to the off-specular HREELS. (i) First, if the plane of incidence of the electron beam coincides with a plane of symmetry, a vibration that is antisymmetric with respect to that plane is forbidden in both specular and non-specular directions. Such modes could be observed only in off-specular directions, in the plane perpendicular to the incident plane [156]. (ii) Second, if a vibration is antisymmetric with respect to a twofold axis of symmetry, or a plane of symmetry perpendicular to the surface and to the plane of incidence of the electrons, the mode is forbidden in the specular direction [156]. It is evident from Table 4.3 that all modes, except the totally symmetric ones at 1061, 779, and 672 cm^{-1} , are antisymmetric with respect to at least one twofold axis or a symmetry plane. Therefore, it is not surprising that the intensity of the asymmetric Si–O–Si vibrations is extremely low and renders their detection impossible even in off-specular HREELS measurements.

4.4.2 Core-Level Shifts

Furthermore, the difference in binding energies of O 1s core levels between different oxygen atoms present in the 1 ML film models was calculated. For the surface O1 and O2 atoms in Si–O–Si bridging positions (cf. Figure 4.3), the BEs are nearly equal (± 0.1 eV). The BE difference between O1(O2) and interface oxygen atoms O3 is much larger and found to be 1.3, 1.9, and 1.1 eV for the models *A*, *B*, and *C*, respectively. The experimental value for the O 1s core-level shift of 1.3 eV again favors the monolayer model *A*. The intensity ratio of (O1+O2):O3 is exactly 3:2, in perfect agreement with the ratio estimated from integration of the enclosed area in the XPS spectrum. On the other hand, the largest BE difference between the inequivalent oxygen atoms in the $c(2 \times 2)$ -[SiO_4] isolated cluster model was calculated to be 0.8 eV, which is in clear disagreement with the XPS data.

4.4.3 STM

Finally, STM images of the most stable 1 ML *A* structure were simulated at tunneling conditions applied in the experiments. The images (here and in the following) were obtained from the self-consistent charge density employing the Tersoff-Hamann approach [159]. In this method, the unknown tip states are assumed to have *s*-like character and the tip is modeled by a locally spherical potential centered at it. Thus, the tunneling current is given by the properties of the surface alone, i.e., tip-surface interactions do not influence the measured current. The latter is proportional to the local density of states *of the surface* at the position of the STM tip¹.

Figure 4.10 shows the atomically resolved STM images (left) and simulated images (right) when the tunneling gap was set to 4 Å at 0.65 V in (a) and 6 Å at 1.2 V in (b). Interestingly, the protrusions imaged by STM are attributed to the bridging oxygen atoms at a small tip-surface distance (Fig. 4.10a) and to the silicon atoms at a larger distance (Fig. 4.10b). In both cases, the simulated images match very well the experimental ones, thus providing further strong evidence for the 1 ML model *A*.

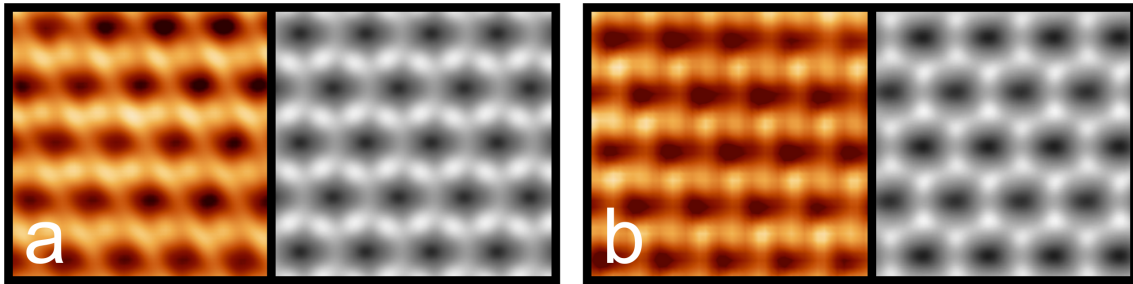


Figure 4.10: Atomically resolved STM images (left) and simulated images (right). The tunneling gap is set 4 Å at 0.65 V in (a) and 6 Å at 1.2 V in (b).

The simulated STM image of the isolated $c(2 \times 2)$ -[SiO₄] cluster model shows no dependence on the tip-surface separation. The image differs substantially from the experimental data, showing basically the whole [SiO₄] units as bright protrusions (see Figs. 4.6a and b).

4.5 Antiphase Domain Boundaries

As mentioned in Section 4.1, the atomically resolved STM images revealed surface dislocations in the form of antiphase domain boundaries (APDB). Here, as a final piece of evidence, it is demonstrated that our 1 ML model *A* of the SiO₂/Mo(112) film provides a straightforward explanation of their structure.

¹The tunneling current is given as $I(\mathbf{r}, U) = \sum_{E_F \leq \epsilon_i \leq E_F + eU} n_d(\mathbf{r}, \epsilon_i) = \sum_{E_F \leq \epsilon_i \leq E_F + eU} |\phi_i(\mathbf{r})|^2$, where U is the applied voltage, eU is the difference between the Fermi energies (E_F) of the tip and the surface, and $n_d(\mathbf{r}, \epsilon_i)$ is the local density of states of the surface.

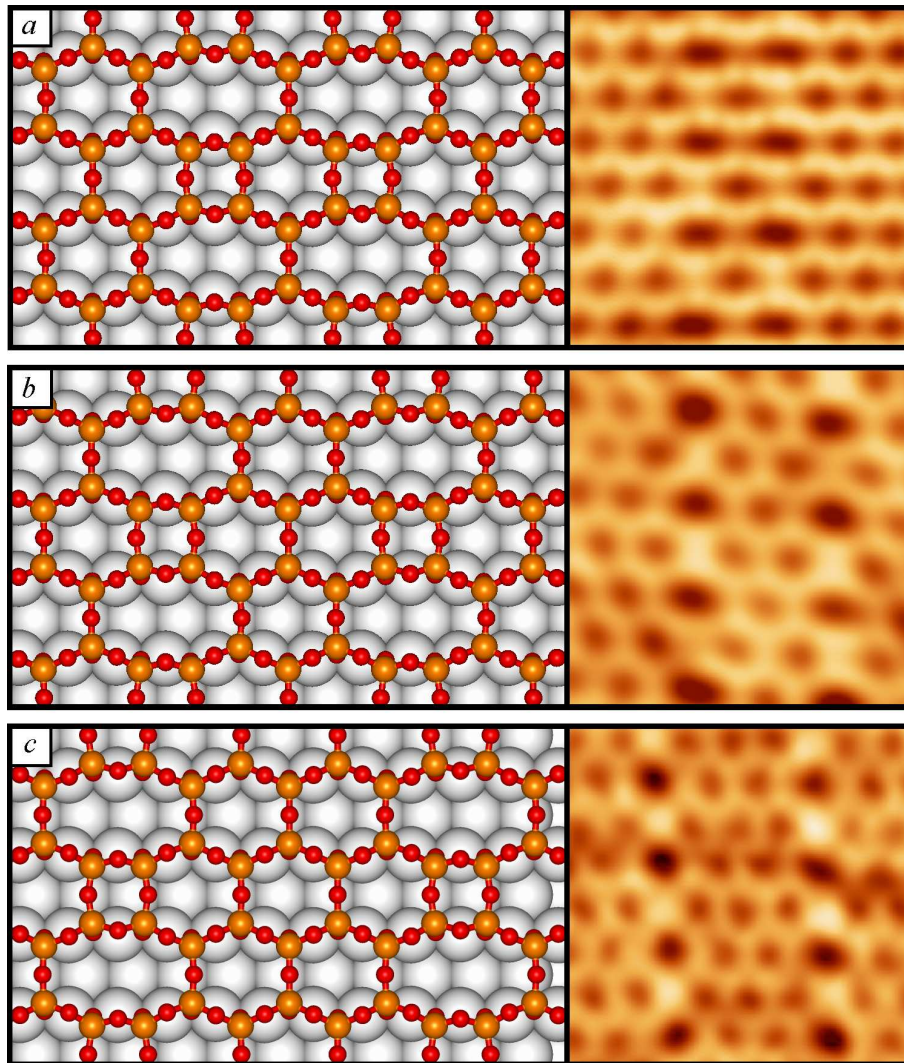


Figure 4.11: Simulated models of APDB (left) and experimental STM images (right, $3.5 \times 3.5 \text{ nm}^2$): (a) sharing edge; tunneling parameters: $V_s = 1.2 \text{ V}$, $I = 0.4 \text{ nA}$; (b) separated by one six-membered ring; $V_s = 2.78 \text{ V}$, $I = 0.42 \text{ nA}$; (c) separated by two six-membered rings; $V_s = 3.0 \text{ V}$, $I = 0.6 \text{ nA}$.

The model of APDB can be constructed in the following way. The 1 ML *A* film is cut along the $[\bar{1}10]$ direction. Then, one half of the structure is translated by half of the unit cell in the $[\bar{1}\bar{1}1]$ direction towards the other half. This results in the formation of a chain of interchanging octahedral and square rings containing eight and four Si atoms, respectively.

Surface unit cells with various sizes were used to simulate different separations between the antiphase domain boundaries. An (8×2) unit cell has two octahedra sharing an edge in the $[\bar{1}\bar{1}1]$ direction (Fig. 4.11a). In the (5×2) and (7×2) supercells (Figs. 4.11b and 4.11c), the APDB are separated by one and two six-membered rings

by 5.25 and 10.68 Å, respectively. The corresponding unit cell compositions of these defected structures are (SiO₂)₁₆·8O, (SiO₂)₁₀·5O, and (SiO₂)₁₄·7O. The sampling of the first Brillouin zone is done with a (1 × 4 × 1), (2 × 4 × 1), and (1 × 4 × 1) *k*-point mesh, respectively.

The three APDB structure models have very similar formation energies, i.e., $\Delta E_{\text{form}} = -10.7$ eV for (SiO₂)₁₆·8O, $\Delta E_{\text{form}} = -10.7$ eV for (SiO₂)₁₀·5O, and $\Delta E_{\text{form}} = -10.6$ eV for (SiO₂)₁₄·7O. They are only 0.1–0.2 eV less stable than the 1 ML model *A* ($\Delta E_{\text{form}} = -10.8$ eV). This strongly supports the proposed structure of APDB and provides further evidence for the atomic model of the SiO₂/Mo(112) film. The small difference in formation energies between the simulated APDB models is confirmed by STM measurements, where the coexistence of all three structures has been detected (Figure 4.11*a-c*).

4.6 Summary

Based on excellent agreement between the results of DFT calculations and new experimental data, the atomic structure of the ultrathin crystalline silica film on Mo(112) has been determined. It consists of a two-dimensional network of corner-sharing [SiO₄] tetrahedra, with one oxygen atom of each tetrahedron binding to the Mo(112) surface. The other three oxygen atoms form Si–O–Si bonds with the neighboring tetrahedra. There are three 2D-network models with bridge, top, and pseudo threefold hollow positions of the interface oxygen atoms with respect to the protruding Mo atoms running along the $[\bar{1}\bar{1}1]$ direction. The results of our calculations indicate that the most favorable model has oxygen atoms in bridge positions. Simulations of the IRAS spectra, O 1*s* core-level shifts, and STM images confirm this structure as the atomic model of the SiO₂/Mo(112) film. Its surface layer is fully saturated, which explains the essential inertness of the film towards water. The 2D-network has independently been proposed as the most viable candidate of the silica film by Giordano *et al.* [154]. However, their model corresponds to the less stable 1 ML model *B* with interface oxygen atoms in top positions (cf. Fig. 4.3*B*). The film has a SiO_{2.5} stoichiometry that does not naturally occur in bulk silica. A comparison to other known thin films and surface structures reveals that it is identical to the “dense reconstruction” of the α -quartz(0001) surface found in DFT simulations [160], the “silicate adlayer” on 4H and 6H SiC [161], and the “siloxane surface” of clay minerals [162]. However, the structure reported here is a new form of silica, which can be regarded as a new material with rather interesting and novel properties of its own [163].

Chapter 5

1D Silica Stripes on Mo(112) Substrate

Formation of crystalline silica structures with even further reduced dimensionality, i.e., one-dimensional (1D) stripes on the Mo(112) substrate has been observed. When they coalesce, particularly at increasing Si coverage, islands of 2D silica film are formed. The protrusions imaged by STM for both silica structures are in perfect registry, which implies the same nature of protrusions. In this chapter, DFT calculations are employed to determine the atomic structures of the crystalline SiO₂ stripes. Excellent agreement with the experimental STM, XPS, and IRAS data obtained in the group of Prof. Hans-Joachim Freund, FHI, Berlin is demonstrated. For more details the reader is referred to Ref. [27].

5.1 Experimental Findings on the Silica Stripes

First, the experimental findings for the 1D silica stripes formed on Mo(112) are briefly summarized. The preparation included deposition of ~ 0.5 ML of Si onto Mo(112) at 850 K in 5×10^{-8} mbar of O₂, followed by annealing in UHV at 1000 K. This resulted in the formation of long features running along the $[\bar{1}\bar{1}1]$ direction with a (1×3) periodicity as shown in Figure 5.1. High-resolution STM images reveal that each stripe consists of two rows of protrusions, with a distance between the protrusions of ~ 2.8 Å and ~ 4.5 Å in the $[\bar{1}\bar{1}1]$ and $[\bar{1}10]$ directions, respectively. The distances match well the unit cell of the Mo(112) surface (2.73×4.45 Å). In addition, ill-defined ridge-like features are randomly observed between the silica stripes and are tentatively assigned to MoO_x species.

The XPS study revealed a single peak for the Si 2*p* region with a binding energy of 103.0 eV, which is characteristic of a Si^{IV} oxidation state. The O 1*s* region showed at least three different oxygen species. Two components centered at 532.5 and 531.2 eV are essentially identical to those found for the 2D film (cf. Section 4.1). The higher BE component has previously been assigned to the oxygen atoms in the outermost

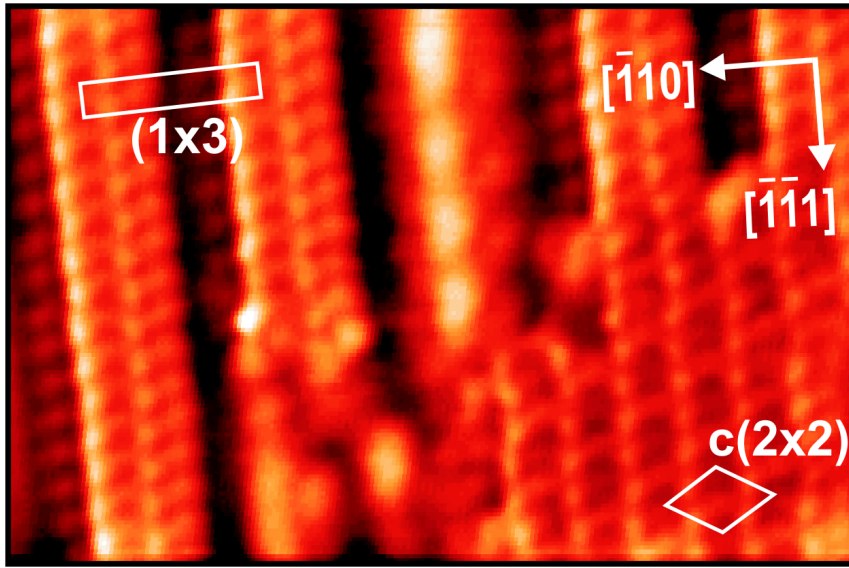


Figure 5.1: Experimental STM image of the crystalline silica stripes formed on the Mo(112) substrate. The 2D silica film is also atomically resolved. Image size and tunneling parameters: $6.5 \times 4.5 \text{ nm}^2$, $V_s = -0.5 \text{ V}$, $I = 0.4 \text{ nA}$.

layer (O1 and O2 in Fig. 4.3) and the lower BE component – to the interface oxygen atoms (O3) bound to the Mo(112) substrate. The third component at $\sim 530.2 \text{ eV}$ is observed for the Si-free surface, which is therefore assigned to oxygen chemisorbed on Mo(112).

Finally, the phonon region of the IRAS spectra revealed a strong signal at 1046 cm^{-1} , which is red-shifted with respect to the most intense band in the 2D film (1059 cm^{-1}), and weak absorption bands at 875 and 672 cm^{-1} (cf. Fig. 5.5). The weak signals at 1100 and 1030 cm^{-1} are attributed to 3D silica particles and/or ill-defined MoO_x structures present on the surface.

5.2 Structure Models

Based on the registry relationship between the 1D and 2D silica structures observed by STM (cf. Fig. 5.1), the stripes were modeled as paired rows of corner-sharing $[\text{SiO}_4]$ tetrahedra chemisorbed on the Mo(112) substrate along the $[\bar{1}\bar{1}1]$ direction. The surface structure between them, however, is not so straightforward to resolve. Various models with a (1×3) periodicity and a different number of oxygen atoms adsorbed on Mo(112) have been considered. Similar to the structure models in Section 4.2, the Mo(112) surface was modeled using seven atomic layers, with the four topmost fully relaxed and the three bottom layers kept frozen at their bulk positions. An energy cutoff of 400 eV and a $(16 \times 2 \times 1)$ Monkhorst-Pack grid were employed.

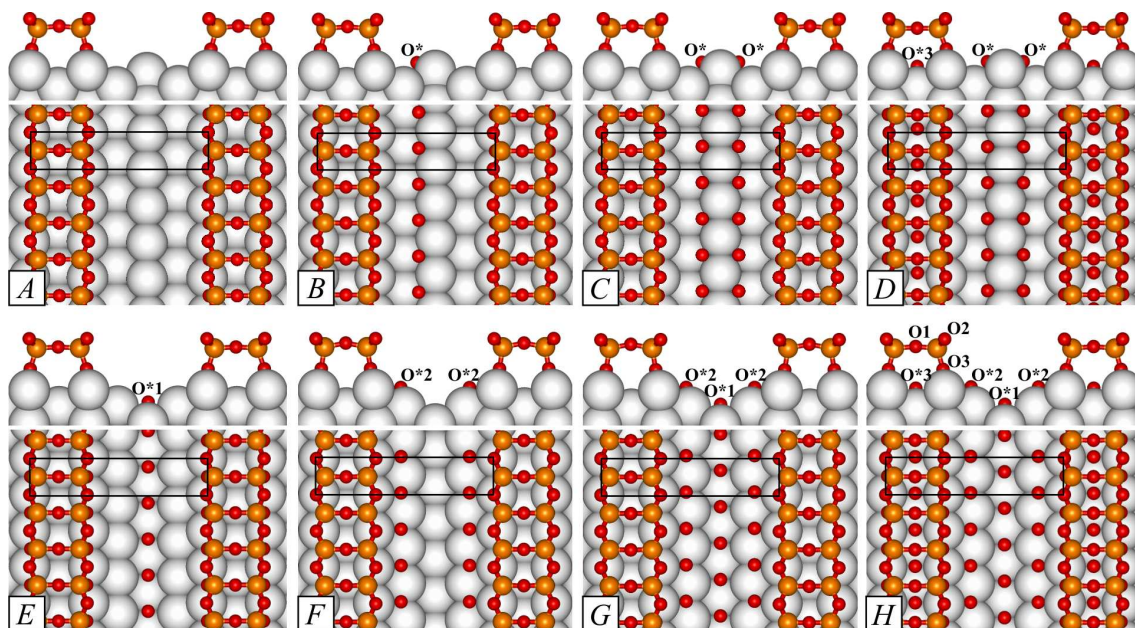


Figure 5.2: Top and side view of selected unreconstructed (*A-D*) and missing-row reconstructed (*E-H*) stripe models. The (1×3) unit cell is indicated.

Figure 5.2 shows selected models of silica stripes formed on the unreconstructed (*A-D*) and reconstructed (*E-H*) Mo(112) surface. Model *A* contains no additional chemisorbed oxygen atoms, whereas in models *B* to *D* the number of O atoms gradually increases from one to three per unit cell, respectively. They are located in threefold hollow (O^*) sites on one (model *B*) or both (model *C*) sides of the topmost protruding Mo rows bound to two first-layer and one second-layer Mo atoms. In model *D*, an additional oxygen atom is adsorbed in a short-bridge (O^{*3}) site under the silica stripes.

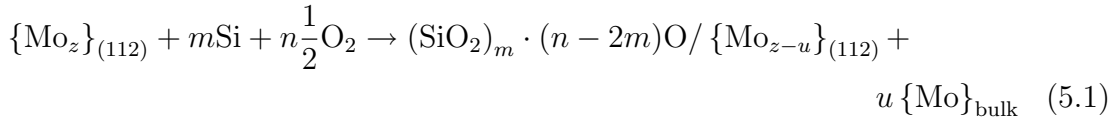
The Mo(112) surface in models *E* to *H* is reconstructed, i.e., every third topmost Mo row along the $[\bar{1}\bar{1}1]$ direction is removed. This type of reconstruction was experimentally suggested for the $p(2 \times 3)$ O/Mo(112) surface on the basis of LEED and STM results [164]. The calculations indicate that the first extra oxygen atom adsorbs in a short-bridge site on the third Mo row (O^{*1} in model *E*), whereas the preferential sites for two O atoms are the threefold hollow (O^{*2}) sites bound to one first-layer and two second-layer Mo atoms (cf. Fig. 5.2*F*). Gradually increasing the oxygen coverage yields the structure model *G*, in which the reconstructed surface is completely covered by O^{*1} and O^{*2} atoms. Finally, in model *H* an additional O atom is adsorbed in the O^{*3} site under the stripes.

It is noteworthy that the missing-row reconstructed stripe models closely resemble the most stable structure models of the oxygen-induced reconstructed $p(1 \times 3)$ Mo(112) surface (cf. Section 7).

5.3 Thermodynamic Stability

First, we note that the oxygen atoms located in different adsorption sites on the Mo(112) surface differ in their binding energies. The least bound O atoms are located in the O*3 sites under the silica stripes (2.6–2.8 eV). Removal of a short-bridge O*1 atom from the third Mo row requires between 3.4 and 3.7 eV, and increases to 3.5–4.2 eV for the threefold hollow (O* and O*2) sites.

In order to compare the stability of different silica stripe models, their formation energy, ΔE_{form} , from a clean Mo(112) surface, bulk silicon, and molecular oxygen is given as



where m and n are the number of Si and O atoms in the unit cell, respectively, and $(\text{SiO}_2)_m \cdot (n - 2m)\text{O} / \{\text{Mo}_{z-u}\}_{(112)}$ defines the composition of a particular 1D silica structure. The term $\{\text{Mo}\}_{\text{bulk}}$ appears for the stripes formed on the missing-row reconstructed Mo(112) surface, which is assumed to be in equilibrium with bulk Mo. This reconstruction, resulting in a change of Mo content in the unit cell, is indicated by z and u . As pointed out, the values of ΔE_{form} cannot be compared directly for structures with different chemical composition. Instead, the surface-related free energy change of reaction (5.1), $\Delta\gamma$, has to be used according to Eq. (4.3).

Figure 5.3 presents the surface-related free energy of formation $\Delta\gamma$ as a function of the oxygen chemical potential at $T = 1000$ K for the most stable 1D silica stripe models shown in Figure 5.2. At very reducing conditions ($\Delta\mu_{\text{O}} < -4.0$ eV), stripes on the clean unreconstructed Mo(112) surface are stabilized (Fig. 5.2A). The model is more stable than the corresponding reconstructed one by ~ 0.3 eV. At increasing oxygen chemical potential values (-4.0 eV $< \Delta\mu_{\text{O}} < -3.4$ eV), stripes on unreconstructed substrate that have oxygen atoms adsorbed on both sides of the topmost Mo rows running along the $[\bar{1}\bar{1}1]$ direction (Fig. 5.2C) become energetically favorable. The structure is by 1.1 eV more stable than the one with the same amount of oxygen atoms chemisorbed on the missing-row reconstructed Mo(112). Our calculations, however, suggest that model *H* is thermodynamically the most favorable structure at all experimentally relevant oxygen pressures. In this model the Mo(112) surface between the SiO₂ stripes is reconstructed and completely covered by O*1 and O*2 atoms as well as oxygen atoms in O*3 sites under the silica (cf. Fig. 5.2H).

5.4 Electronic and Vibrational Properties

In order to verify that the properties of the most energetically favorable 1D silica stripe model (Fig. 5.2H) agree with the experimental findings, vibrational fre-

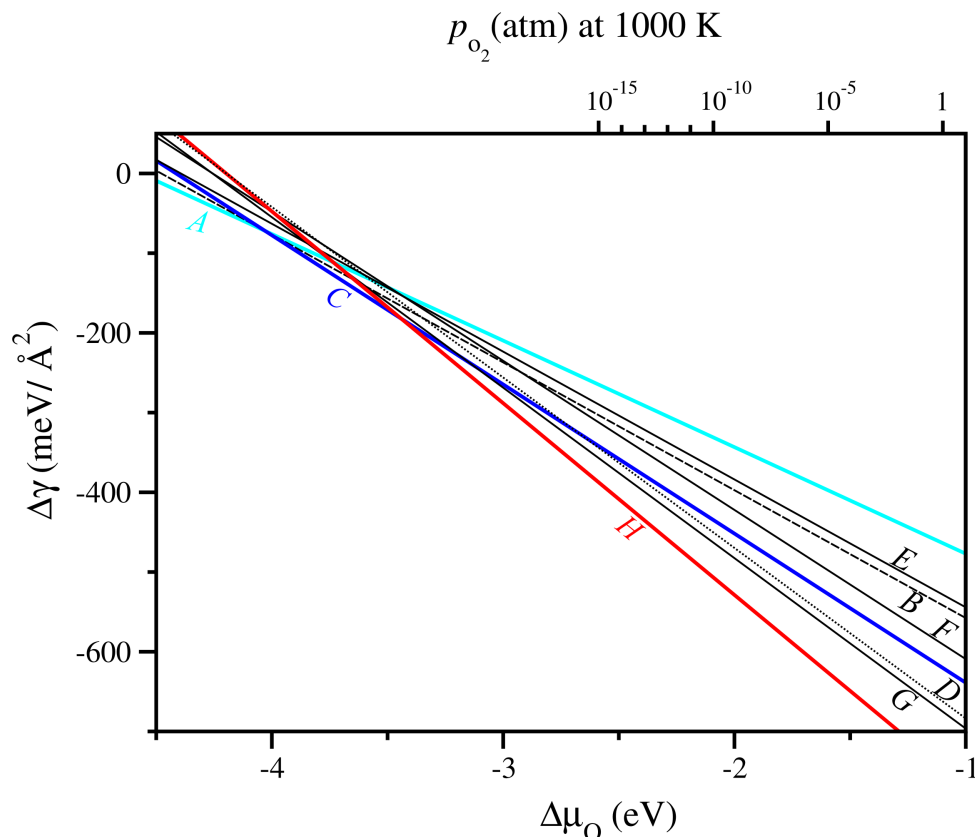


Figure 5.3: Surface-related free energy of formation $\Delta\gamma(T, p)$ as a function of the oxygen chemical potential for the 1D silica stripes. The $\Delta\mu_{\text{O}}$ axis has been translated into an oxygen pressure scale at $T = 1000$ K.

quency and O 1s core-level shift calculations as well as STM simulations have been performed.

The simulated STM image of this structure, shown in Fig. 5.4, matches very well the experimental image (Fig. 5.1). The protrusions are attributed to the bridging oxygen atoms (O2), whereas the depressions correspond to the missing-row reconstructed Mo(112) surface. Moreover, none of the oxygen atoms chemisorbed there (O*1 and O*2) is resolved in the STM image.

Furthermore, the difference in binding energies of O 1s core levels between different oxygen atoms present in the 1D stripe model was calculated. Similar to the 2D film, the surface O1 and O2 atoms in Si–O–Si bridging positions have nearly equal binding energies and the O 1s core-level shift between O1(O2) and interface O3 atoms is 1.3 eV. The difference appears due to the oxygen species chemisorbed on Mo(112), which are shifted by ~ 1 eV towards lower BEs as compared to the O3 atoms, in good agreement with the experimental XPS data.

Even stronger evidence for the proposed structure comes from the study of lattice vibrations. Calculated harmonic frequencies of the stripe model *H* reveal three

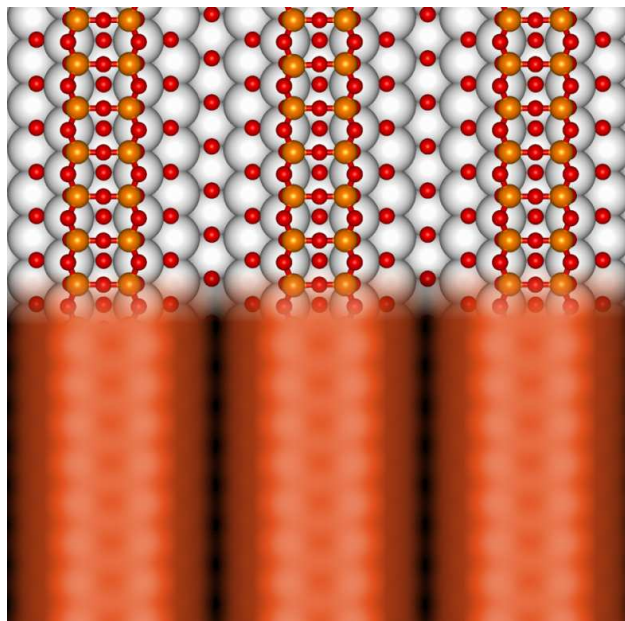


Figure 5.4: Top view of the thermodynamically most stable structure of silica stripes formed on the Mo(112) substrate. A simulated STM image is superimposed with the structure in order to show that the protrusions correspond to the position of the O2 atoms.

IRAS active modes at 1052, 879, and 654 cm^{-1} , in excellent agreement with the experimental results as shown in Figure 5.5. The origin of these modes is similar to that for the 2D silica film, for which the most intense band at 1061 cm^{-1} was assigned to the asymmetric Si–O–Mo stretching and the weak signals at 779 cm^{-1} to the Si–O–Si symmetric stretching coupled with Si–O–Si bending and at 672 cm^{-1} to coupled Si–O–Si bending modes. The major difference between stripes and film is observed for the mode at 879 cm^{-1} , which is shifted by 100 cm^{-1} towards higher wavenumbers as compared to the corresponding mode in the 2D film. This is due to the fact that this mode becomes essentially a Si–O–Si symmetric stretching vibration within the stripes and has less Si–O–Si bending character than in the film. The mode calculated at 654 cm^{-1} is a coupling of Si–O–Si bending with the Mo–O stretching involving the oxygen atoms chemisorbed on the Mo(112) surface. Due to the more coupled character, this vibration is 18 cm^{-1} red-shifted as compared to the corresponding mode in the silica film.

A number of vibrational modes is undetectable in the experiments because of the selection rule applied in IRAS, i.e., there is no dynamic dipole moment component perpendicular to the metal surface associated with these modes. They include combinations of asymmetric Si–O–Si stretching vibrations in the range of 985–1206 cm^{-1} (1008–1195 cm^{-1} for the 2D film), the out-of-phase Si–O–Mo asymmetric stretching at 928 cm^{-1} (863–912 cm^{-1} for the film), and the Si–O–Si bending mode at 787 cm^{-1} .

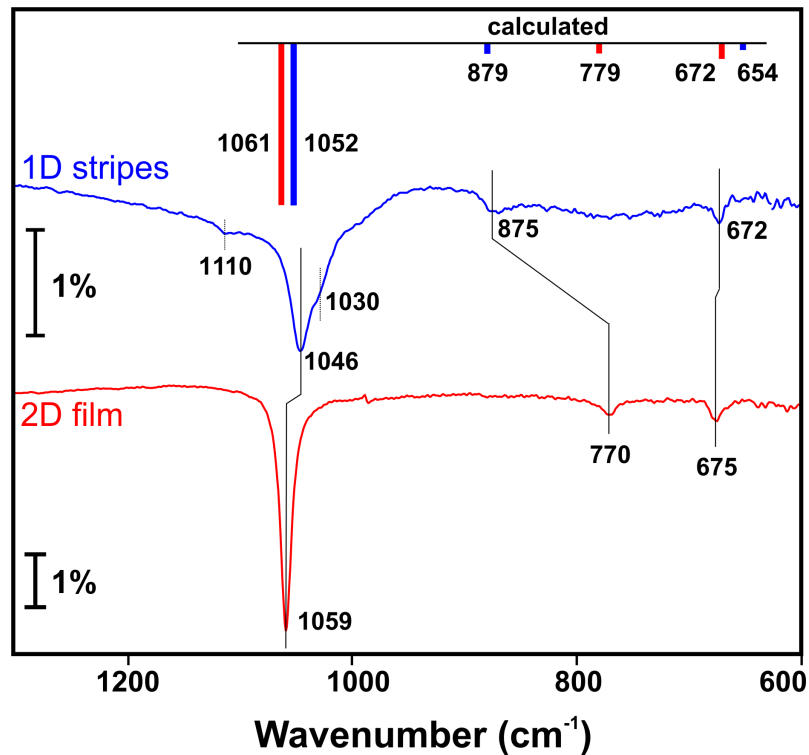


Figure 5.5: IRAS spectra of the 1D and 2D silica structures formed on Mo(112). The calculated frequencies are represented as bars with the height proportional to the intensity normal to the surface.

5.5 Summary

The atomic structure of the one-dimensional crystalline silica stripes formed on Mo(112) has been determined through a combination of experiment and theory. DFT and statistical thermodynamics suggest that the most energetically favorable structure at all experimentally relevant oxygen pressures consists of paired rows of corner-sharing $[\text{SiO}_4]$ tetrahedra chemisorbed on the Mo(112) surface, which is a missing-row type reconstructed and completely covered by oxygen atoms in short-bridge and threefold hollow sites, and also in short-bridge sites under the silica. Simulations of the STM image, O 1s core-level shifts, and vibrational frequencies confirm this structure as the atomic model of the $\text{SiO}_2/\text{Mo}(112)$ stripes.

Chapter 6

Oxygen-Rich Silica Film on Mo(112)

Owing to the variety of low-dimensional silica phases formed on the Mo(112) substrate under different conditions, statistical thermodynamics is applied to account for the effect of silicon activity (concentration) and oxygen partial pressure on the stability of the 1D stripes and 2D films considered in the previous two chapters. This work is also a joint effort with the experimental group of Prof. Hans-Joachim Freund, FHI, Berlin. The results presented here have been published in Ref. [28].

6.1 Thermodynamic Stability

Stability of the different SiO₂/Mo(112) structure models is evaluated using the surface-related free energy $\Delta\gamma$, defined as

$$\Delta\gamma(T, p) = \frac{1}{A}[\Delta E_{\text{form}} - m\Delta\mu_{\text{Si}}(T, a_{\text{Si}}) - n\Delta\mu_{\text{O}}(T, p_{\text{O}_2})] \quad (6.1)$$

where A is the area of the surface unit cell, and m and n are the numbers of Si and O atoms in the given silica model, respectively. The formation energy ΔE_{form} is the energy required to form a crystalline silica phase from the clean Mo(112) surface, silicon, and oxygen according to Eq. (5.1). The relative oxygen chemical potential $\Delta\mu_{\text{O}}$ is given in Eq. (3.5) and $\Delta\mu_{\text{Si}}$ is defined as

$$\Delta\mu_{\text{Si}}(T, a_{\text{Si}}) = \mu_{\text{Si}}(T, a_{\text{Si}}) - E_{\text{Si}} \quad (6.2)$$

where E_{Si} is the energy of face-centered cubic (fcc) bulk Si. The silicon chemical potential can be related to silicon activity, a_{Si} , using standard thermodynamics [114]. From a practical point of view, the silicon activity can be varied by controlling the amount of evaporated silicon forming the given crystalline SiO₂ phase and is related to the concentration through the activity coefficient [114].

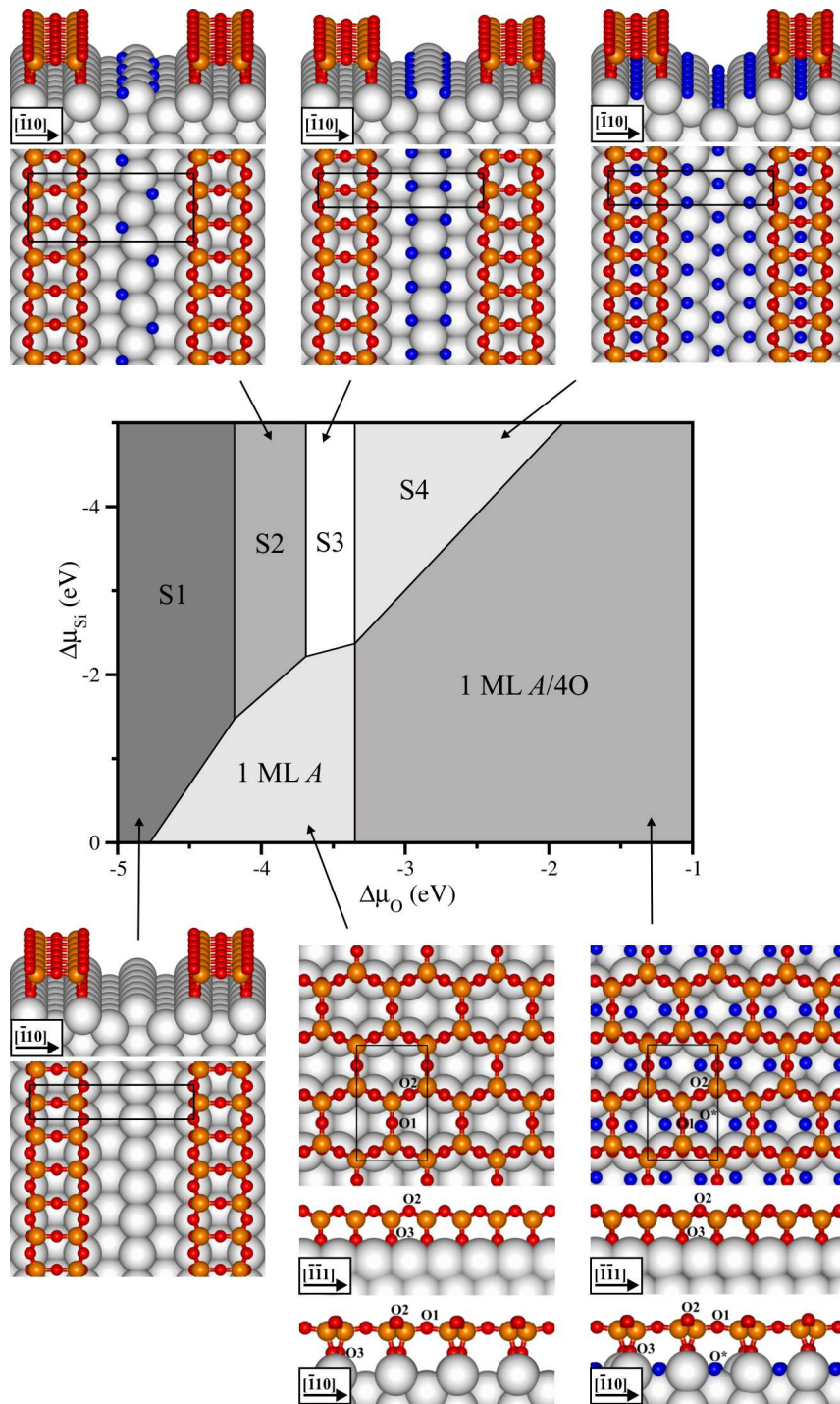


Figure 6.1: Phase diagram as a function of the $\Delta\mu_{\text{Si}}$ and $\Delta\mu_{\text{O}}$ chemical potentials for 1D and 2D crystalline silica on Mo(112). Si and O atoms are depicted in orange and red, respectively. O atoms adsorbed on the Mo(112) surface (O* species) are shown in blue. Black rectangle indicates the surface unit cell.

The most favorable structure for given values of $\Delta\mu_{\text{Si}}$ and $\Delta\mu_{\text{O}}$ chemical potentials is the one that corresponds to the lowest surface-related free energy $\Delta\gamma$ according to Eq. (6.1). The resulting 2D-phase diagram is shown in Figure 6.1. At low chemical potential values, the energetically stable silica structures that are predicted to form are one-dimensional stripes. At very reducing conditions ($\Delta\mu_{\text{O}} < -4.2$ eV), the (1×3) stripes on the clean, unreconstructed Mo(112) surface are the most stable structure (S1, Fig. 6.1). Increasing the oxygen pressure leads to adsorption of oxygen in threefold hollow sites on both sides of the protruding Mo rows running along the $[\bar{1}\bar{1}1]$ direction between the silica stripes. The adsorption occurs first on every second site in a “zigzag” manner with a (2×3) periodicity, and then on all threefold hollow sites, resulting in a (1×3) structure (S2 and S3, respectively, Fig. 6.1). Finally, at higher $\Delta\mu_{\text{O}}$ values ($\Delta\mu_{\text{O}} > -3.3$ eV), the most stable structure consists of paired rows of corner-sharing $[\text{SiO}_4]$ tetrahedra chemisorbed on the Mo(112) surface, which is a missing-row type reconstructed and completely covered by oxygen atoms in short-bridge and threefold hollow sites, and also in short-bridge sites under the silica stripes (S4, Fig. 6.1). In fact, this is the most energetically favorable model of 1D crystalline SiO_2 at all experimentally relevant oxygen pressures predicted in our calculations (Fig. 5.3). Simulations of the STM image, O 1s core-level shifts, and vibrational frequencies confirm this structure as the atomic model of the $\text{SiO}_2/\text{Mo}(112)$ stripes (cf. Section 5.4). We also note the same ordering of the stable stripe structures as obtained in Figure 5.3, where only the amount of oxygen was varied.

At high $\Delta\mu_{\text{Si}}$ and low $\Delta\mu_{\text{O}}$ values, the 2D crystalline silica film of corner-sharing $[\text{SiO}_4]$ tetrahedra is formed, which corresponds to the 1 ML *A* structure (Fig. 4.3). At increasing oxygen chemical potentials ($\Delta\mu_{\text{O}} > -3.3$ eV), a new phase, denoted here as 1 ML *A*/*n*O and referred to as “O-rich” film, is predicted to be the most stable. It contains four additional oxygen atoms per surface unit cell, located in bridging positions in the trenches of the Mo(112) surface along the $[\bar{1}\bar{1}1]$ direction (Fig. 6.1). Models with one, two, and three O atoms are always less stable, as becomes evident from the stability plot in Figure 6.2. Adsorption of more than four oxygen atoms, on the other hand, results in a subsurface oxidation of the Mo(112) substrate and a partial decomposition of the silica film.

6.2 New Phase of the Silica Film

Table 6.1 compiles selected calculated structural parameters for the original “O-poor” (1 ML *A*) and the new 1 ML *A*/*n*O silica film models. It is evident that the additional *n* oxygen atoms chemisorbed on the Mo(112) surface have virtually no influence on the structure of the film. Thus, the properties of the two thermodynamically stable SiO_2 phases (cf. Fig. 6.1) are expected to be very similar.

Both simulated and experimental STM images for the O-rich film reveal no discernible differences and are identical to those shown in Fig. 4.10 for the O-poor

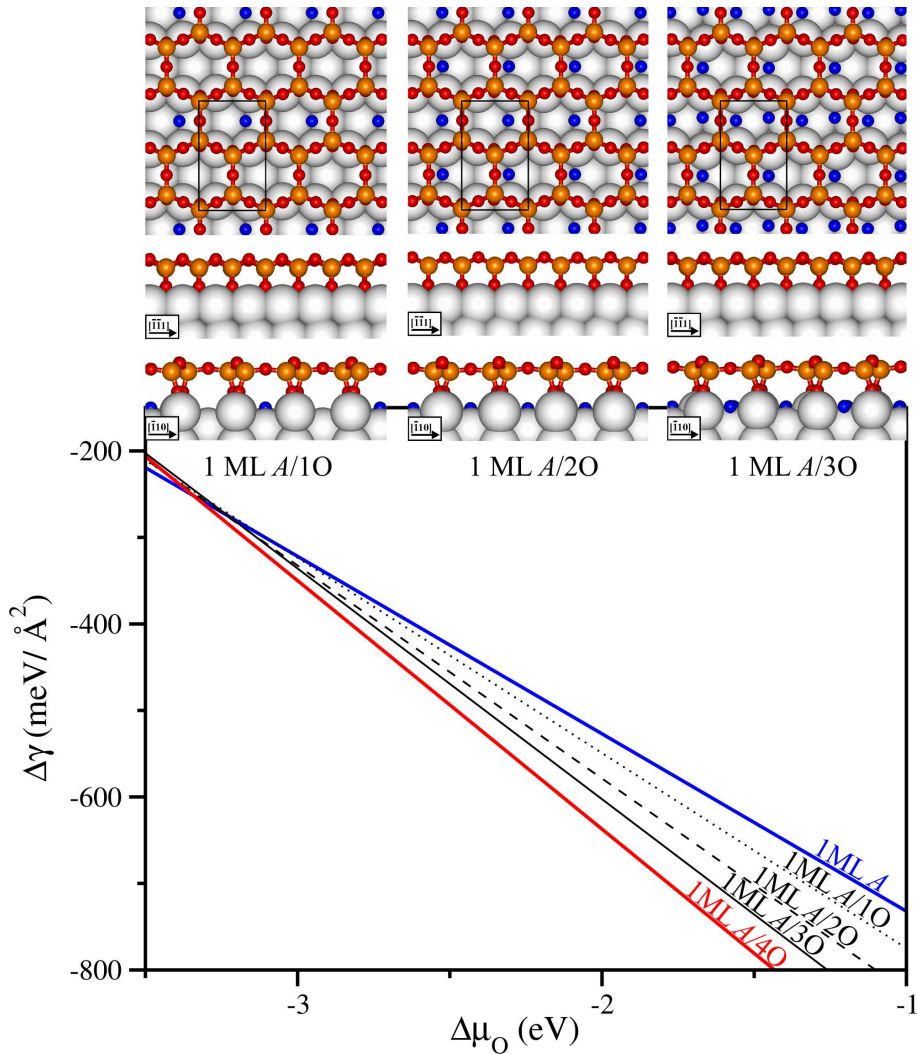


Figure 6.2: Surface-related free energy of formation $\Delta\gamma(T, p)$ as a function of the oxygen chemical potential $\Delta\mu_{\text{O}}$ for the original 1 ML *A* and the 1 ML *A*/*n*O models of the $\text{SiO}_2/\text{Mo}(112)$ film, containing additional *n* oxygen O^* atoms chemisorbed on the Mo(112) surface (depicted in blue). The 1 ML *A* and 1 ML *A*/4O models are illustrated in Fig. 6.1. Black rectangle indicates the unit cell.

phase. Also, no changes are observed in the LEED pattern, confirming that the O^* species chemisorbed on Mo(112) under the silica do not change a $c(2 \times 2)$ -Mo(112) symmetry. However, the analysis of the vibrational frequencies and O 1s core-level shifts indicates some differences.

As mentioned in Section 4.4, the calculated IRAS spectrum of the O-poor (1 ML *A*) film shows a very sharp and intense band at 1061 cm^{-1} and two weak signals at 779 and 672 cm^{-1} . These bands were assigned to Si–O–Mo asymmetric stretching, Si–O–Si symmetric stretching coupled with Si–O–Si bending, and to a coupling of Si–O–Si bending modes, respectively, as schematically illustrated in Fig. 6.3. Similarly,

Table 6.1: Selected structural parameters (Å, deg) of the 1 ML *A* and 1 ML *A/nO* models of the SiO₂/Mo(112) film.

Model	Si–O1	Si–O2	Si–O3	Mo–O3	Si–O1–Si	Si–O2–Si	Si–O–Mo
1 ML <i>A</i>	1.62	1.64	1.65	2.11	163.2	132.9	139.2–139.6
1 ML <i>A/1O</i>	1.62	1.64	1.65	2.07–2.13	163.3–166.7	132.9	137.6–140.4
1 ML <i>A/2O</i>	1.62	1.64	1.65	2.07–2.13	163.8–167.9	133.4	135.4–140.3
1 ML <i>A/3O</i>	1.62	1.64	1.65	2.08–2.11	163.7–169.1	132.4	135.2–136.5
1 ML <i>A/4O</i>	1.62	1.64	1.65	2.08–2.10	166.8	130.8	135.8–137.3

the calculated vibrational frequencies of the O-rich (1 ML *A/4O*) film reveal only three IRAS active modes with the same origin as for the 1 ML *A* film. The Si–O–Mo asymmetric stretching vibration is shifted to 1046 cm⁻¹, whereas the positions of the other two bands remain virtually unchanged (Fig. 6.3). In line with our theoretical predictions, the main peak in the experimental IRAS spectrum of the O-rich film is red-shifted by about 10 cm⁻¹ with respect to the mode at 1059 cm⁻¹ present in the O-poor film. No discernible differences are observed for the low-frequency vibrations at 771 and 675 cm⁻¹.

In perfect agreement with the XPS results, the calculated difference in binding energies of O 1s core levels in the O-poor film reveals that the two oxygen species, i.e., the surface O1 and O2 atoms and the interface O3 atoms bound to the Mo substrate differ by 1.3 eV (cf. Section 4.4). For the O-rich film, the presence of the O* species chemisorbed on the Mo(112) surface gives rise to a new peak, which is shifted by ~0.7 eV towards lower BEs as compared to the O3 atoms, in excellent agreement with the O 1s XPS data [28]. These O* species have virtually no influence on the binding energy of the oxygen atoms within the silica layer. However, they partially oxidize the surface Mo atoms, leading to the prominent shoulder at higher BEs for the Mo 3d core level, as has been resolved in the difference spectrum [28].

It is important to note that the O-rich silica film can easily be obtained by post-annealing of the O-poor phase in oxygen ambient [28]. However, once prepared the O-rich film cannot be converted back to the O-poor state. This is a consequence of the high binding energy of the O* species on the Mo(112) surface (3.1–3.7 eV/O atom).

6.3 Summary

Combining DFT and statistical thermodynamics, a 2D-phase diagram showing the stability of various 1D and 2D crystalline silica structures depending on the silicon coverage and oxygen pressure has been derived. The calculations predict formation of a new, previously not considered “O-rich” phase of the SiO₂/Mo(112) film, whose

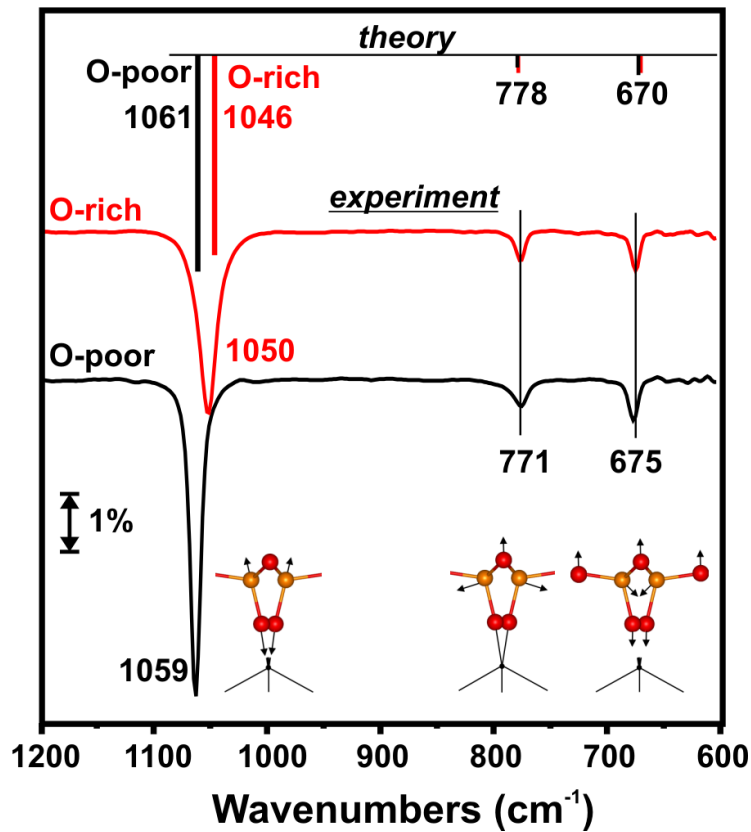


Figure 6.3: Experimental IRAS spectra of the O-poor and O-rich silica films grown on Mo(112). Calculated frequencies for the three IRAS active vibrations of the 1 ML *A* and 1 ML *A/4O* structure models are represented as bars with the height proportional to the intensity normal to the surface.

existence was subsequently confirmed by IRAS and XPS. In addition to the network of corner-sharing $[\text{SiO}_4]$ tetrahedra, the structure contains oxygen atoms adsorbed in bridging positions in the trenches of the Mo(112) surface under the silica layer. Due to very subtle differences between the properties of the O-poor and O-rich films, the existence of the latter may not have been discovered without the aid of theory. Even though the O^* species have virtually no influence on the 2D-network structure, they should be taken into account in studies of reactivity of metal ad-atoms deposited on the silica surface (e.g., Ref. [165]).

Moreover, the existence of slightly different SiO_2 structures with the same surface symmetry may shed light on the somewhat controversial results reported in the literature. Since one of the main arguments in these discussions concerns the vibrational properties of the well-ordered crystalline silica film, it appears that the experimental data may critically depend on the exact preparation procedure, such as the annealing temperature and whether annealing is performed in UHV or O_2 atmosphere.

Chapter 7

Oxygen Adsorption on Mo(112)

Molybdenum single-crystals have been successfully used as a model support for the preparation of ultrathin oxide films, e.g., SiO₂ [20, 22], Al₂O₃ [166], TiO₂ [167], and MgO [168]. The synthesis of such films usually starts with oxygen adsorption on a clean metal surface. Therefore, the dissociation and adsorption of oxygen, the oxygen-induced structures, and oxide formation on the stable low-index molybdenum surfaces have been subject of a number of experimental and theoretical studies [33, 36, 164, 169–171].

The work here is focused on the Mo(112) surface as it has proved to be a successful substrate for the crystal growth of low-dimensional SiO₂ structures. It shows a ridge-and-through structure with the top layer Mo atoms forming close-packed rows along the $[\bar{1}\bar{1}1]$ direction separated from each other by 4.45 Å in the $[\bar{1}10]$ direction. Depending on the experimental conditions, various surface structures have been observed upon oxygen adsorption on Mo(112): $p(3 \times 9)$ [169], $p(6 \times 12)$ [169], $p(1 \times 2)$ [36, 170], $p(1 \times 3)$ [36], $p(2 \times 1)$ [33], $c(4 \times 2)$ [33], and $p(2 \times 3)$ [164]. Their precise atomic structure, however, is still under debate. Even for the simplest $p(1 \times 2)$ surface, several models have been proposed based either on experimental data [36, 170] or theoretical calculations [171], involving unreconstructed [170, 171] or reconstructed [36] surfaces. Similarly, for the $p(1 \times 3)$ - and $p(2 \times 3)$ -Mo(112) surface structures, oxygen-induced reconstructions have been postulated [36, 164].

Obviously, the problem in deriving reliable atomic structure models from theoretical calculations arises from the large number of possible adsorption sites and surface configurations (reconstructed vs. unreconstructed). Even the simplest $p(1 \times 2)$ surface unit cell has 16 potential adsorption sites and may lead to a large number of possible structures. Their manual construction followed by structure optimization would be a formidable task. In many cases experimental data, such as atomically resolved STM images, can provide some information about possible arrangement of atoms, but data interpretation relies to a large extent on intuition. Recently, several techniques for automatic determination of the most stable surface structures, such as genetic algorithm (GA) [172, 173] and Monte Carlo [174] methods have been proposed. The GA approach appears particularly efficient. It requires only the periodic

vectors of the surface unit cell and the chemical potentials of the constituent species as input. The number of atoms involved in the adsorption and reconstruction as well as their most favorable bonding geometry under different conditions is obtained automatically within the GA search.

In this chapter, such global optimization method for dealing with unknown atomic structures is presented. The aim is to determine the $p(1 \times 2)$ and $p(1 \times 3)$ surface structures observed upon oxygen adsorption on Mo(112), thus gaining further insight into formation of the crystalline silica phases. The simulations reveal unusual flexibility of the Mo(112) surface, resulting in oxygen-induced reconstructions and leading to more stable structures than any suggested so far. The results are fully supported by a multitude of experimental data. For more details the reader is referred to Ref. [37].

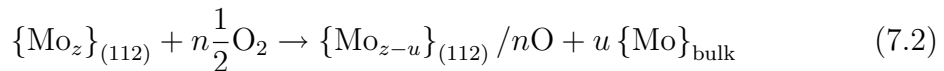
7.1 Genetic Algorithm Method

The genetic algorithm method used throughout this work was implemented in the VASP code by Dr. Marek Sierka [37]. Following the original idea of Chuang *et al.* [172], it is based on the evolutionary approach in which different surface structures form a population. The algorithm starts with a population of M randomly generated structures. In the present case, $M = 20$ initial models are obtained by random distribution of oxygen atoms on a given Mo(112) surface. The number of oxygen atoms for each structure is between 1 and k . The algorithm is quite insensitive to the choice of k ; $k = 3$ oxygen atoms per (1×1) Mo(112) surface unit cell is used. The structures in the initial pool are optimized using a conjugate-gradient technique. The subsequent algorithm steps proceed as follows:

Fitness evaluation: The fitness f_i of each individual in the current population is evaluated based on the surface-related free energy change $\Delta\gamma$:

$$f_i = \frac{\exp[-\Delta\gamma/\beta(\Delta\gamma_{\max} - \Delta\gamma_{\min})]}{\sum_i^M f_i} \quad (7.1)$$

where $\Delta\gamma_{\max}$ and $\Delta\gamma_{\min}$ are the maximum and minimum values of $\Delta\gamma$ in the population and β is an adjustable parameter ($\beta = 0.5$ in the calculations). $\Delta\gamma$ is derived from Eq. (3.5) using the formation energy ΔE_{form} from a clean Mo(112) surface and molecular oxygen:



where u defines the number of Mo atoms removed to form a missing-row reconstructed surface. Thus, ΔE_{form} is given as

$$\Delta E_{\text{form}} = E_{\{\text{Mo}_{z-u}\}_{(112)}/n\text{O}} + uE_{\{\text{Mo}\}_{\text{bulk}}} - E_{\{\text{Mo}_z\}_{(112)}} - n\frac{1}{2}E_{\text{O}_2} \quad (7.3)$$

where $E_{\{\text{Mo}_{z-u}\}_{(112)}/n\text{O}}$ corresponds to the energy of the given Mo(112)/ $n\text{O}$ model, $E_{\{\text{Mo}_z\}_{(112)}}$ and $E_{\{\text{Mo}\}_{\text{bulk}}}$ are the energies of the clean Mo(112) surface with z atoms in the unit cell and bulk Mo, respectively.

Crossover: The evolution from one generation to the next one takes place by crossover. Two structures from the population are selected to be parents. A roulette wheel selection with selection probability proportional to the value of the fitness function is used [175]. The topmost parts of the parent structures are sectioned by an arbitrary plane and then combined to create a child structure. To prevent creation of children structures with too small interatomic distances at the junction between the two parent substructures, atoms with unreasonably small interatomic distances are discarded. In each generation, a number of m ($m = 8$) crossover operations are performed. The resulting m children structures are then optimized.

Mutation: Mutation operations prevent premature convergence of the GA and provide additional structural diversity. The mutation is performed by removing or adding atoms at random positions of randomly chosen parent structures. Mutated structures are optimized and added to the population. The mutation rate is kept below 1% in all GA runs.

Selection of the next generation: The parent structures of the current generation, optimized children structures obtained by the crossover operations, and mutated structures form a new population. In order to maintain a maximum diversity during the GA runs, the population is sorted into groups of similar structures. This is achieved by comparing the number and positions of the atoms in the unit cell as well as the interatomic bond distances. Next, the structures are ordered in a list that includes the most stable structure (in terms of $\Delta\gamma$) from each group, then the second most stable, and so on. The next generation of parent structures is created by choosing M topmost structures from the list.

Dual computational strategy has been employed. For the GA runs, a plane-wave basis set with an energy cutoff of 200 eV and a $(2 \times 2 \times 1)$ Monkhorst-Pack grid for the integration of the Brillouin zone were used. The final structure optimization of the models was performed with a 400 eV cutoff and a $(12 \times 4 \times 1)$ k -point grid. The energies obtained with the lower accuracy setup exactly reproduce (with a deviation of less than 0.1 eV) the structure ordering at the higher level.

7.2 Models

The surface unit cells were modeled using orthorhombic (1×2) and (1×3) supercells with the lattice constants $a_0 = 2.73$, $b_0 = 8.92 \text{ \AA}$, and $a_0 = 2.73$, $b_0 = 13.39 \text{ \AA}$, respectively. In all structure optimizations, the two bottom layers of the Mo(112) substrate were kept fixed at their bulk positions. The abbreviations $p(1 \times 2)\text{-Mo(112)}/n\text{O}$ and $p(1 \times 3)\text{-Mo(112)}/n\text{O}$ are used to distinguish models with n oxygen atoms adsorbed per surface unit cell of a given periodicity.

7.2.1 $p(1 \times 2)$ -Mo(112)/ n O

Figure 7.1 summarizes the $p(1 \times 2)$ -Mo(112)/ n O structure models obtained in the GA simulations. The Mo(112) surface in models A to D is reconstructed, i.e., every third topmost Mo row along the $[\bar{1}\bar{1}1]$ direction is missing and a different number of oxygen atoms is adsorbed in pseudo threefold hollow (O2) and short-bridge (O1 and O3) sites. Model A contains four oxygen atoms ($n = 4$), adsorbed in short-bridge sites on the first and third Mo rows (O1 and O3) and pseudo threefold hollow sites bound to one first-layer and two second-layer Mo atoms (O2). In model B, a single short-bridge oxygen (O1) is removed from the outermost Mo layer ($n = 3$). Model

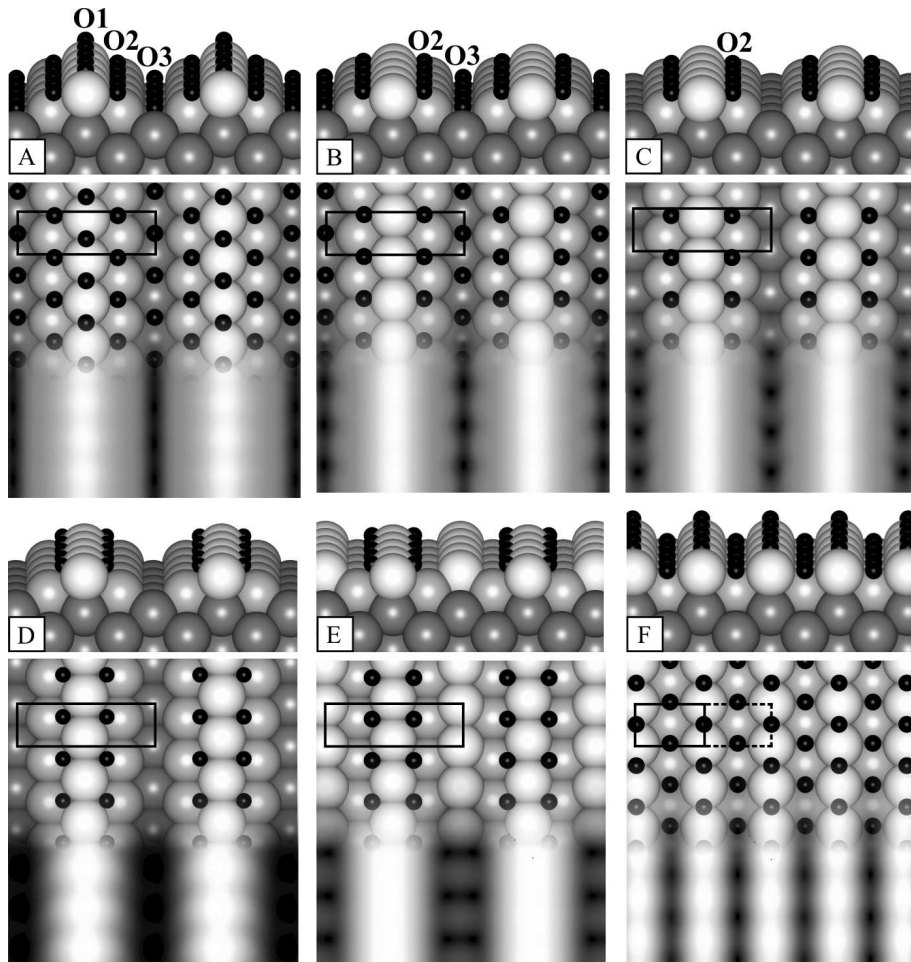


Figure 7.1: Perspective and top view of the calculated $p(1 \times 2)$ -Mo(112)/ n O structure models along with their simulated STM images (lower panels). Models A, B, C, and D are characterized by a missing-row reconstructed Mo(112) surface and $n = 4, 3, 2,$ and $2,$ respectively. Models E ($n = 2$) and F ($n = 4$) involve unreconstructed surfaces. D is the model of Santra *et al.* [36] and E is the model of Sasaki *et al.* [170]. Black rectangle indicates the surface unit cell.

C contains two oxygen atoms (O2) per unit cell ($n = 2$) located in pseudo threefold hollow sites on both sides of the topmost Mo rows. Models D and E have been suggested by Santra *et al.* [36] and Sasaki *et al.* [170], respectively. The former structure (Fig. 7.1, model D) is similar to model C, but has a different bonding geometry of the oxygen atoms (two bonds to the first-layer and one to the second-layer Mo atoms). It is also similar to model E, which contains the same amount of oxygen atoms ($n = 2$) in the same adsorption sites, but involves the unreconstructed Mo(112) surface.

7.2.2 $p(1 \times 3)$ -Mo(112)/ n O

The most stable $p(1 \times 3)$ -Mo(112)/ n O structure models obtained in the GA simulations are displayed in Figure 7.2. All of them are characterized by a missing-row reconstructed Mo(112) surface forming two reconstruction patterns. In the first pattern, denoted as the single missing-row reconstruction, every third row of Mo atoms along the $[\bar{1}\bar{1}1]$ direction is missing (Fig. 7.2, models A.1, B.1, C.1, D, and E). In the second one, the double missing-row reconstruction, two missing rows are separated by one protruding Mo row (Fig. 7.2, models A.2, B.2, and C.2). Models A.1 and A.2 contain six O atoms ($n = 6$) located in the same adsorption sites as in the $p(1 \times 2)$ -Mo(112)/4O structure (Fig. 7.1, model A), i.e., short-bridge sites on the first and third Mo rows and pseudo threefold hollow sites bound to one first-layer and two second-layer Mo atoms. Additionally, model A.2 contains O atoms adsorbed in short-bridge positions on the second Mo layer (O'1). In models B.1 and B.2 ($n = 5$), a single short-bridge oxygen atom is removed from the topmost Mo layer. In models C.1 and C.2 ($n = 4$), all short-bridge oxygen atoms from the first Mo layer (C.1) or first and second Mo layer (C.2) are removed. Further removal of the O atoms on the third Mo layer (O3) results in model D ($n = 3$). The model of Santra *et al.* [36] (Fig. 7.2, model E) contains three oxygen atoms adsorbed in pseudo threefold hollow sites bound to two first-layer and one second-layer Mo atoms as well as one oxygen bound to two second-layer and one third-layer Mo atoms ($n = 4$).

7.3 Thermodynamic Stability

The binding energies of the oxygen atoms located in different adsorption sites on the Mo(112) surface vary between 2.8 and 3.6 eV. For both $p(1 \times 2)$ and $p(1 \times 3)$ phases, the removal of first short-bridge O1 atom requires energies in the range of 2.8–2.9 eV. Removal of the second O1 atom from the $p(1 \times 3)$ -Mo(112)/5O model B.1 costs 3.2 eV. Similar amount of energy (3.3 eV) is obtained for the short-bridge oxygen atom on the second Mo layer (O'1) in model B.2. The binding energy of the O3 atom adsorbed on the third Mo layer is ~ 3.6 eV in all models.

Figure 7.3 shows the surface-related free energy change of formation $\Delta\gamma(T, p)$ as a function of the oxygen chemical potential $\Delta\mu_{\text{O}}$ for the most stable $p(1 \times 2)$ -

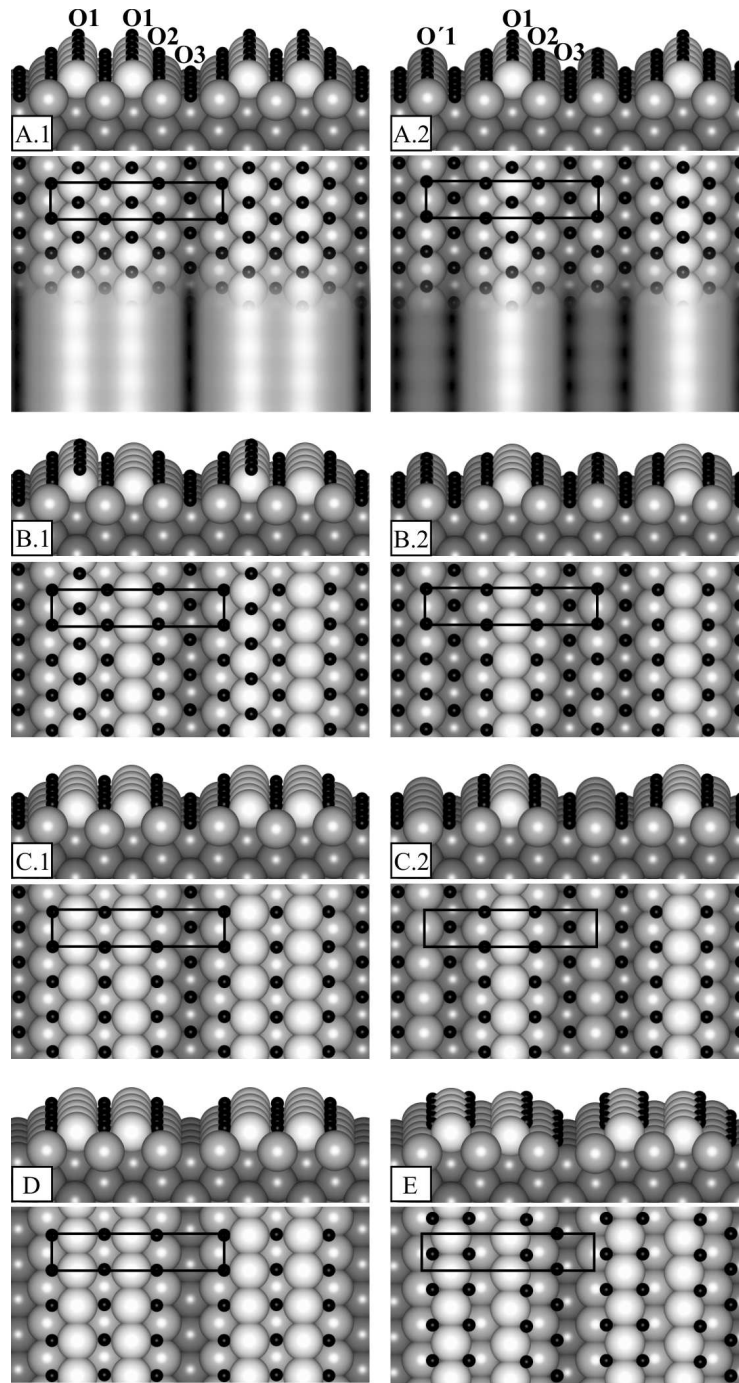


Figure 7.2: Perspective and top view of the calculated $p(1 \times 3)$ -Mo(112)/ n O structure models along with simulated STM images (lower panel of A.1 and A.2). All models are characterized by a missing-row reconstructed Mo(112) surface and varying amount of oxygen atoms per unit cell; $n = 6$ (models A.1 and A.2), $n = 5$ (models B.1 and B.2), $n = 4$ (models C.1, C.2, and E), and $n = 3$ (model D). E is the model of Santra *et al.* [36]. Black rectangle indicates the surface unit cell.

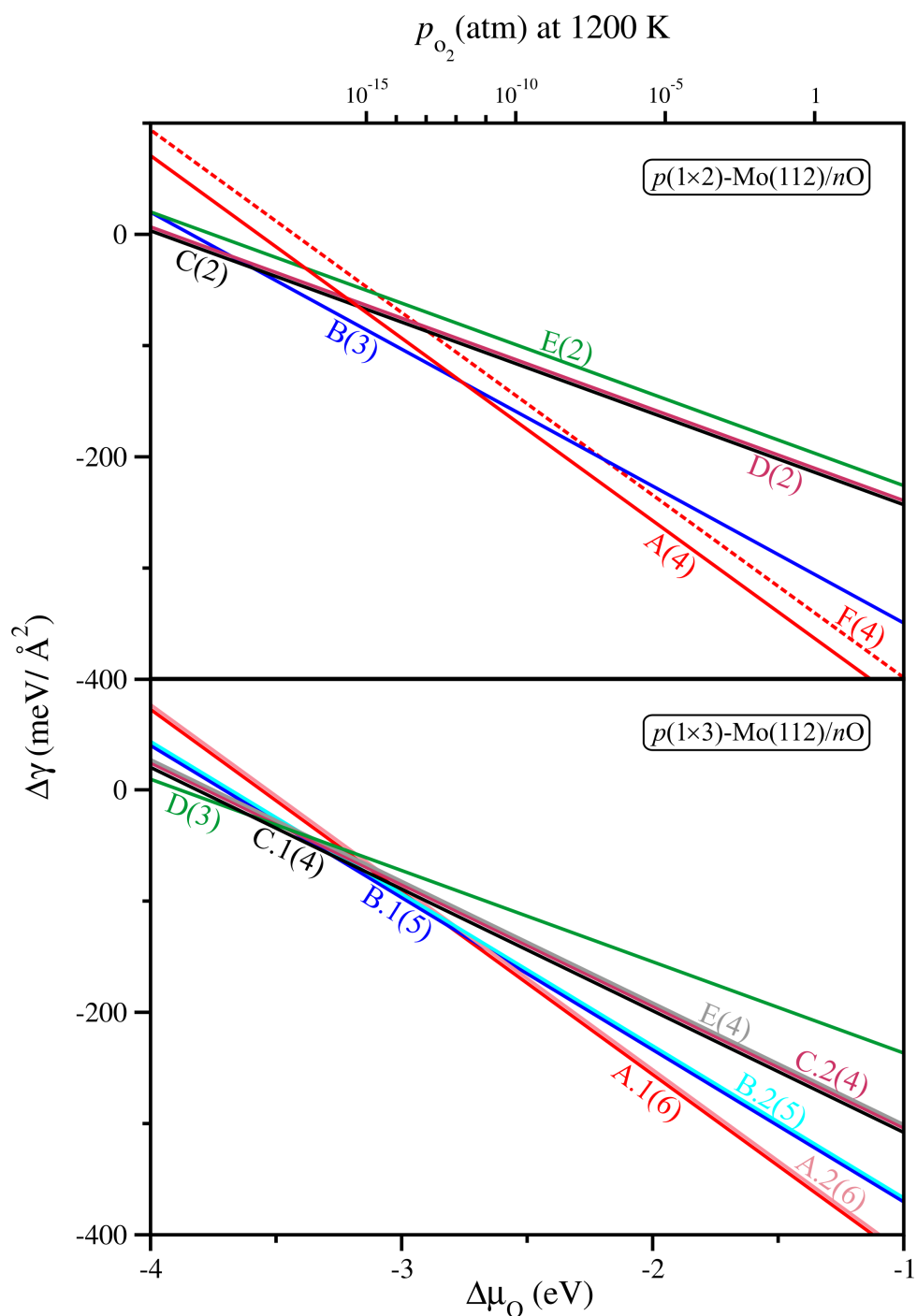


Figure 7.3: Surface-related free energy change of formation $\Delta\gamma(T, p)$ as a function of the oxygen chemical potential $\Delta\mu_{\text{O}}$ for the most stable $p(1 \times 2)$ -Mo(112)/ $n\text{O}$ (upper panel) and $p(1 \times 3)$ -Mo(112)/ $n\text{O}$ (lower panel) structure models. Numbers in parenthesis indicate the amount of oxygen atoms (n) per surface unit cell. The $\Delta\mu_{\text{O}}$ axis has been cast into a pressure scale at 1200 K.

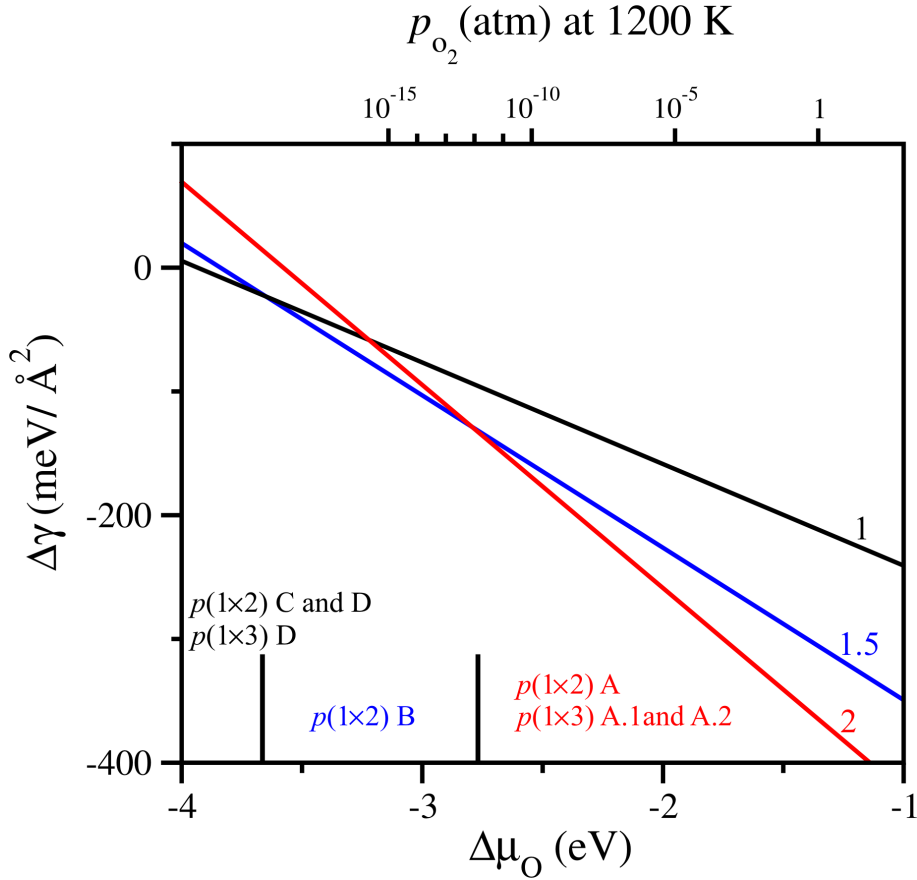


Figure 7.4: Combined stability plot for the most stable $p(1 \times 2)$ - and $p(1 \times 3)$ -Mo(112)/ n O structure models. Numbers above the lines indicate the amount of oxygen atoms per (1×1) Mo(112) unit cell.

Mo(112)/ n O and $p(1 \times 3)$ -Mo(112)/ n O structure models. The $\Delta\mu_{\text{O}}$ axis has been cast into an oxygen pressure scale at 1200 K. At high oxygen chemical potentials ($\Delta\mu_{\text{O}} > -2.8$ eV), the most favorable structure is $p(1 \times 2)$ -Mo(112)/4O (Fig. 7.1, model A). The $p(1 \times 2)$ /3O model (Fig. 7.1, model B) becomes stable at lower $\Delta\mu_{\text{O}}$ values ($-3.7 < \Delta\mu_{\text{O}} < -2.8$ eV). Finally, at very reducing conditions ($\Delta\mu_{\text{O}} < -3.7$ eV), missing-row reconstructed structures with only two oxygen atoms per unit cell (Fig. 7.1, models C and D) are stabilized. Both models are almost equally stable (ΔE_{form} differ by about 30 meV), which indicates that it is difficult to determine the precise bonding geometry of the oxygen atoms located in pseudo threefold hollow sites on the Mo(112) surface. The two structures are more stable than the unreconstructed model suggested by Sasaki *et al.* [170] (Fig. 7.1, model E). It should be stressed that for the same unit cell composition, the missing-row reconstructed structures are by 0.36 eV ($n = 2$) and 0.56 eV ($n = 4$) more stable than the corresponding unreconstructed models.

Very similar results are obtained for the $p(1 \times 3)$ -Mo(112)/ n O structure models

(cf. Fig. 7.3). At high oxygen chemical potentials ($\Delta\mu_{\text{O}} > -2.9$ eV), structures with a maximum oxygen occupancy ($n = 6$), i.e., A.1 and A.2 are predicted to be stable. They are characterized by different reconstruction patterns (single vs. double missing-row reconstruction). However, their formation energies differ by less than 0.15 eV. Interestingly, the energy gain due to the reconstruction of the Mo(112) surface is 0.42 and 0.57 eV for the models A.1 and A.2, respectively. At lower $\Delta\mu_{\text{O}}$ values, structures with $n = 5$ (models B.1 and B.2) and $n = 4$ (models C.1, C.2, and E) are energetically favorable. The model proposed by Santra *et al.* [36] (Fig. 7.2, model E), which has the same amount of oxygen atoms per surface unit cell as models C.1 and C.2 is almost equally stable. Finally, at even further reducing conditions ($\Delta\mu_{\text{O}} < -3.6$ eV), model D ($n = 3$) is stabilized.

Figure 7.4 presents a combined stability plot for the most stable $p(1 \times 2)$ - and $p(1 \times 3)$ -Mo(112)/ $n\text{O}$ structure models. The calculations indicate that in all cases, oxygen adsorption on the Mo(112) surface induces missing-row-type reconstructions. Moreover, a coexistence of different $p(1 \times 2)$ and $p(1 \times 3)$ structures is predicted. Interestingly, such phases have the same amount of oxygen atoms per (1×1) Mo(112) unit cell. For $\Delta\mu_{\text{O}} > -2.8$ eV, structures with the maximum oxygen occupancy (Fig. 7.1, model A and Fig. 7.2, models A.1 and A.2) become energetically most favorable. There is a range of oxygen chemical potentials (-3.6 eV $< \Delta\mu_{\text{O}} < -2.8$ eV), for which only $p(1 \times 2)$ model B is favored. At very reducing conditions, $p(1 \times 2)$ models C and D as well as $p(1 \times 3)$ model D, all of them exclusively containing pseudo threefold hollow oxygen atoms on both sides of the protruding Mo rows along the $[\bar{1}\bar{1}1]$ direction, are predicted to be the most stable.

7.4 Properties

Experimental support for our findings was provided by LEED measurements, which revealed diffuse patterns interpreted as a combination of $p(1 \times 2)$ and $p(1 \times 3)$ phases [37]. Attempts to form a pure $p(1 \times 3)$ structure always resulted in the formation of a $p(2 \times 3)$ phase. Therefore, the LEED results confirmed that the $p(1 \times 3)$ structure is metastable and coexists with either $p(1 \times 2)$ or $p(2 \times 3)$ phases.

The XPS measurements of the O 1s region for the $p(1 \times 2)$ surface revealed an asymmetric peak, indicating the existence of at least two different O species [37]. This finding rules out the $p(1 \times 2)$ models C, D, and E, which contain only one type of oxygen atoms, and leaves the $p(1 \times 2)$ models A, B, and F as possible candidates (cf. Fig. 7.1). However, the calculations predict that $p(1 \times 2)$ model A coexists with $p(1 \times 3)$ models A.1 and A.2, and that model F is not thermodynamically stable under any conditions. Therefore, based on the XPS data, we conclude that model B corresponds to the atomic structure of the observed pure $p(1 \times 2)$ phase.

Finally, verification of the structure models obtained in the generic algorithm simulations is provided by comparison of the calculated and experimental STM images and vibrational spectra.

7.4.1 STM

Figure 7.1 shows the simulated STM images of the $p(1 \times 2)$ -Mo(112)/ n O structure models. The tip height is set to $\sim 4 \text{ \AA}$ above the highest atom and the voltage is 1.5 V. Tunneling towards occupied or empty states as well as increasing the tip-sample distance up to 5 \AA do not affect the simulated images. In agreement with the experiment, all structures show an alternation of bright and dark stripes. The protrusions are attributed to the topmost Mo rows, whereas the trenches are imaged as dark stripes. Simulations of the reconstructed $p(1 \times 2)$ models A–D give rise to virtually identical images, indicating that on the basis of the STM results these structures cannot be distinguished. On the other hand, the unreconstructed models E and F are inconsistent with the experimental data [37].

Figure 7.2 shows the simulated STM images of the $p(1 \times 3)$ models A.1 and A.2. The single and double missing-row reconstructed surface models have different ratios of bright and dark stripes, i.e., 2:1 in the single A.1 and 1:2 in the double A.2 missing-row model. Likewise in reconstructed $p(1 \times 2)$ structures, the calculated height difference between bright and dark stripes is $\sim 1 \text{ \AA}$, in a very good agreement with the experimentally measured corrugation.

7.4.2 Vibrational Frequencies

The experimental HREEL spectrum of the $p(1 \times 2)$ -Mo(112)/ n O surface revealed three main vibrational features at 220, 460, and 620 cm^{-1} , and a shoulder at 670 cm^{-1} [170]. Oxygen exposure and annealing at 1000 K yielded two additional peaks at 770 and 970 cm^{-1} [170]. The signal at 220 cm^{-1} is typical for the clean Mo(112) surface and has previously been assigned to a dipole active surface resonance [176]. The modes at 460 and 620 cm^{-1} were assigned to vibrations of oxygen atoms adsorbed in pseudo threefold sites, whereas the mode at 670 cm^{-1} to molecularly adsorbed oxygen in form of bridging peroxo species. The 770 cm^{-1} mode, which appears after high-temperature annealing, was associated with the loss of surface order and formation of three-dimensional Mo_xO_y phases [170]. Finally, the vibration at 970 cm^{-1} is a characteristic stretching mode of oxygen atoms adsorbed in top positions on the molybdenum surface and forming Mo=O double bonds [164, 177, 178].

Table 7.1 summarizes the calculated oxygen-related vibrational modes along with the corresponding frequencies for the most stable $p(1 \times 2)$ models A–D. To compensate for systematic errors of DFT, the frequencies are scaled by an empirical factor of 1.0382 derived from experimental [179] and calculated vibrations of bulk MoO_2 . Graphical representation of the normal modes is shown in Figure 7.5. The frequencies of all four models fall into the range of observed HREELS vibrations. In model B (cf. Fig. 7.1), which is the most stable structure for the pure $p(1 \times 2)$ phase, the frequencies at 671 and 651 cm^{-1} are associated with symmetric and asymmetric stretching modes of the threefold coordinated O2 atoms ($\nu^s(\text{Mo-O2})$ and $\nu^{as}(\text{Mo-O2})$, Figs. 7.5a,b, respectively). The stretching mode of the short-bridge O3 atoms

Table 7.1: Calculated scaled [scaling factor 1.0382] harmonic vibrational frequencies (cm^{-1}) and their assignment for the most stable $p(1 \times 2)$ -Mo(112)/ $n\text{O}$ structure models.

$p(1 \times 2)$ -A		$p(1 \times 2)$ -B		$p(1 \times 2)$ -C	$p(1 \times 2)$ -D
$\nu^s(\text{Mo-O1/O2})$	717	$\nu^s(\text{Mo-O2})$	671	$\nu^s(\text{Mo-O2})$	614
$\nu^{as}(\text{Mo-O2})$	669	$\nu^{as}(\text{Mo-O2})$	651	$\nu^{as}(\text{Mo-O2})$	648
$\nu^{as}(\text{Mo-O1/O2})$	662				
$\nu^s(\text{Mo-O3})$	636	$\nu^s(\text{Mo-O3})$	611		
$\sigma(\text{Mo-O2})$	505	$\sigma(\text{Mo-O2})$	504	$\sigma(\text{Mo-O2})$	443
$\omega(\text{Mo-O2})$	481			$\omega(\text{Mo-O2})$	472
$\tau(\text{Mo-O2})$	471			$\tau(\text{Mo-O2})$	428
$\rho(\text{Mo-O2})$	457	$\rho(\text{Mo-O2})$	492	$\rho(\text{Mo-O2})$	448
$\delta_1^s(\text{Mo-O3/O1})$	456	$\delta_1^s(\text{Mo-O3})$	454		
$\delta(\text{Mo-O1/O2})$	434	$\delta(\text{Mo-O2})$	438/437		
$\delta_2^s(\text{Mo-O3/O1})$	299	$\delta_2^s(\text{Mo-O3})$	307		
$\delta_2^{as}(\text{Mo-O1/O3})$	276				

($\nu^s(\text{Mo-O3})$, Fig. 7.5d) is located at 611 cm^{-1} . In addition, the vibrational spectrum of model B reveals deformation modes of the O2 species, such as scissoring (Fig. 7.5e) at 504 cm^{-1} and rocking (Fig. 7.5h) at 492 cm^{-1} as well as deformation modes involving the O3 atoms (Figs. 7.5i–k) in the range of 307 – 454 cm^{-1} . Vibrational spectra of models C and D are similar, but additionally involve wagging modes (Fig. 7.5f) at 418 and 472 cm^{-1} and twisting modes (Fig. 7.5g) at 404 and 428 cm^{-1} , respectively. Oxidation of the $p(1 \times 2)$ model B results in adsorption of oxygen atoms in the short-bridge O1 sites on the topmost Mo rows (cf. Fig. 7.1 model A). For this model, the highest vibration at 717 cm^{-1} is associated with a coupled symmetric stretching of the O1 and O2 atoms on the Mo(112) surface (Fig. 7.5a). The corresponding asymmetric mode (Fig. 7.5c) is located at 662 cm^{-1} and has very similar frequencies as the asymmetric stretching involving only O2 atoms. At the same time, the pure stretching vibration of the O3 atoms ($\nu^s(\text{Mo-O3})$, Fig. 7.5d) is shifted by about 25 cm^{-1} towards higher wavenumbers as compared to the same mode in the $p(1 \times 2)$ model B. Finally, the deformation modes of model A vary between 276 and 505 cm^{-1} , with the lowest vibration assigned to asymmetric translational movements of O1 and O3 atoms (Fig. 7.5l).

7.5 Summary

The power of genetic algorithm method combined with density functional theory in determining unknown atomic structures has been demonstrated for the example of $p(1 \times 2)$ and $p(1 \times 3)$ surface structures observed upon oxygen adsorption on Mo(112). The simulations reveal unusual flexibility of the Mo(112) surface, resulting

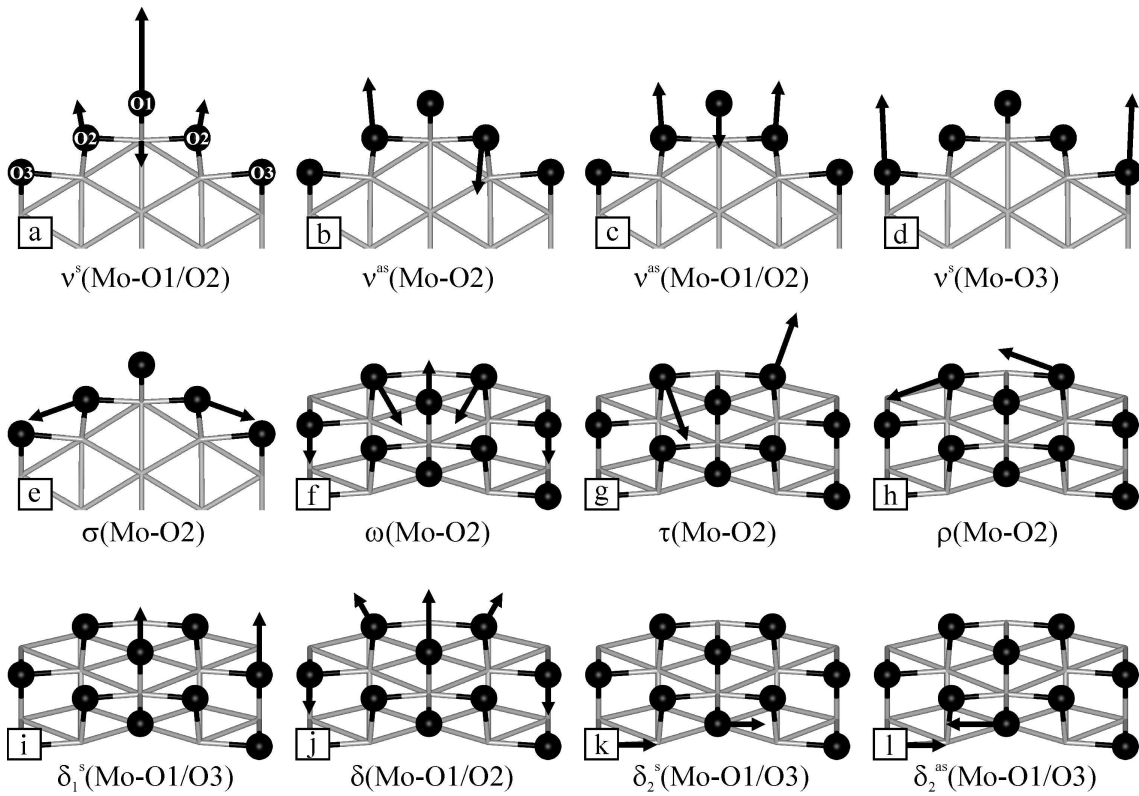


Figure 7.5: Graphical representation of the vibrational normal modes of the $p(1 \times 2)$ model A. Side view images (a)–(d) show the stretching modes, whereas the side view image (e) is the scissoring mode. (f)–(l) are top views of different deformation modes. O atoms are depicted in black and the Mo(112) surface is shown as gray sticks.

in oxygen-induced reconstructions and leading to more stable structure models than any suggested so far. Statistical thermodynamics indicates that only in a narrow region of oxygen pressures, a pure $p(1 \times 2)$ phase can be obtained. In contrast, a $p(1 \times 3)$ phase is metastable and always coexists with $p(1 \times 2)$. These findings are supported by LEED results. Combined with experimental STM and XPS data, our calculations allow for an unequivocal determination of the atomic structure of the $p(1 \times 2)$ phase. It contains three oxygen atoms per unit cell adsorbed in short-bridge and threefold hollow sites on the missing-row reconstruction Mo(112) surface (Fig. 7.1, model B). Additionally, assignment of the vibrational modes observed in HREELS experiments is provided for the most stable $p(1 \times 2)$ -Mo(112)/ n O surface structures.

Chapter 8

Vanadium Oxides on a Thin Silica Film

The experimental silica-supported vanadium oxide particles prepared by physical vapor deposition of vanadium in oxygen ambient onto well-ordered thin silica film under UHV conditions are characterized as vanadia sesquioxide nanoparticles with the vanadyl terminated surface [72, 180]. The deposited vanadia does not spread to wet the surface. Imaged on the atomically-resolved silica substrate, the size of the particles is estimated rather precisely as 10–12 Å, suggesting vanadia aggregates such as V₂O₅ or V₄O₁₀ clusters [181]. The stoichiometry is consistent with estimates based on the amount of deposited vanadium and the number of structures seen in the STM. At increasing V coverages, formation of particles with apparent height and lateral size distribution in the range of 4–15 Å and 15–40 Å, respectively, is observed [180].

Interestingly, the morphology of the VO_x species as imaged with STM is almost indistinguishable on both alumina and silica supports [72, 181]. However, there is a substantial difference in their vibrational spectra, and that is the absence of the 950 cm⁻¹ band for VO_x/SiO₂. Since this feature has been used as a fingerprint for the polymeric vanadia species, its absence was interpreted as a result of the absence of polymeric vanadia on the silica support and exclusive formation of monomeric VO_x species [3].

Elucidation of the precise atomic structure of the thin-film silica support allows investigation of the VO_x/SiO₂ model catalyst systems in much greater detail. Different model structures are constructed and their vibrational spectra are investigated using density functional theory. The aim is to develop an understanding of the effect of different types of aggregation on the structure, stability, and vibrational frequencies of the silica-supported VO_x species. Such theoretical studies have proven to be indispensable in identifying trends in the properties of systems as complex as supported vanadium oxides and in providing assignments of characteristic vibrational features of the experimental systems [72, 102, 136].

8.1 Models

In the same way as for alumina-supported vanadium oxides, vanadia on a thin SiO₂/Mo(112) film can be created by either replacing Si atoms of the 2D network by V=O groups or by “landing” gas-phase V_nO_m clusters on the clean silica surface. Monomeric and dimeric VO_x species as well as large particles are thus created. Such species are modeled using a (4 × 2) unit cell with respect to (1 × 1) Mo(112), i.e., a Si₈O₂₀/Mo(112) composition, an energy cutoff of 400 eV, and the sampling of the Brillouin zone is performed with a (4 × 4 × 1) *k*-point mesh.

8.1.1 Vanadium Oxides Modeled by Replacement

Low-coverage VO_x species, such as monomers and dimers, constructed by replacement of Si atoms by V=O groups are illustrated in Figure 8.1. The monomeric species (Fig. 8.1A) are separated by 8.92 and 10.93 Å in the $[\bar{1}10]$ and $[\bar{1}\bar{1}1]$ direction, respectively. As a result of the substitution, the bond to the interface oxygen is broken. The oxygen atom is retained in a short-bridge site on the Mo(112) surface with a distance of 3.05 Å from the V atom. The V–O1–Si angle is 152.2° and the three V–O bonds have the same length (1.78 Å). Thus, the VO₄ unit maintains its usual tetrahedral coordination.

Replacement of one additional Si atom in a nearest-neighbor position results in formation of two different dimeric VO_x species with adjacent V=O groups along the $[\bar{1}\bar{1}1]$ and $[\bar{1}10]$ crystallographic direction, respectively. The calculations indicate that the dimer along the $[\bar{1}10]$ direction is by about 0.2 eV more stable. Its structure is shown in Figure 8.1B. The separations between two dimeric sites are 5.56 Å in the $[\bar{1}10]$ and 10.93 Å in the $[\bar{1}\bar{1}1]$ direction. Again, upon replacement of Si atoms by V=O groups the bonds to the interface are broken and the O atoms are left on the Mo(112) surface with a distance of 3.20 Å from the corresponding V centers. The substitution results in a relaxation of the vanadia unit away from the surface, creating a much more open structure as seen from the side view along the $[\bar{1}10]$ direction. The V–O1–V angle is 141.0°, but the two vanadyl groups are almost parallel. The structure resembles that of dimeric vanadium oxides on various clusters of silica modifications, e.g., edingtonite and cristobalite, investigated in Ref. [182].

8.1.2 Vanadium Oxides Modeled by Adsorption

As a second approach to model silica-supported vanadia species, different V_nO_m gas-phase clusters, with vanadium in a V^{IV} or V^V oxidation state, are adsorbed on the SiO₂/Mo(112) film surface. Their adsorption energy, E_{ad} , is defined as

$$E_{ad} = E_{V_nO_m/Si_8O_{20}/Mo(112)} - E_{Si_8O_{20}/Mo(112)} - E_{V_nO_m(gas)} \quad (8.1)$$

where $E_{V_nO_m/Si_8O_{20}/Mo(112)}$, $E_{Si_8O_{20}/Mo(112)}$, and $E_{V_nO_m(gas)}$ are the energies of the silica-supported vanadia slab, the clean SiO₂/Mo(112) surface, and the most stable

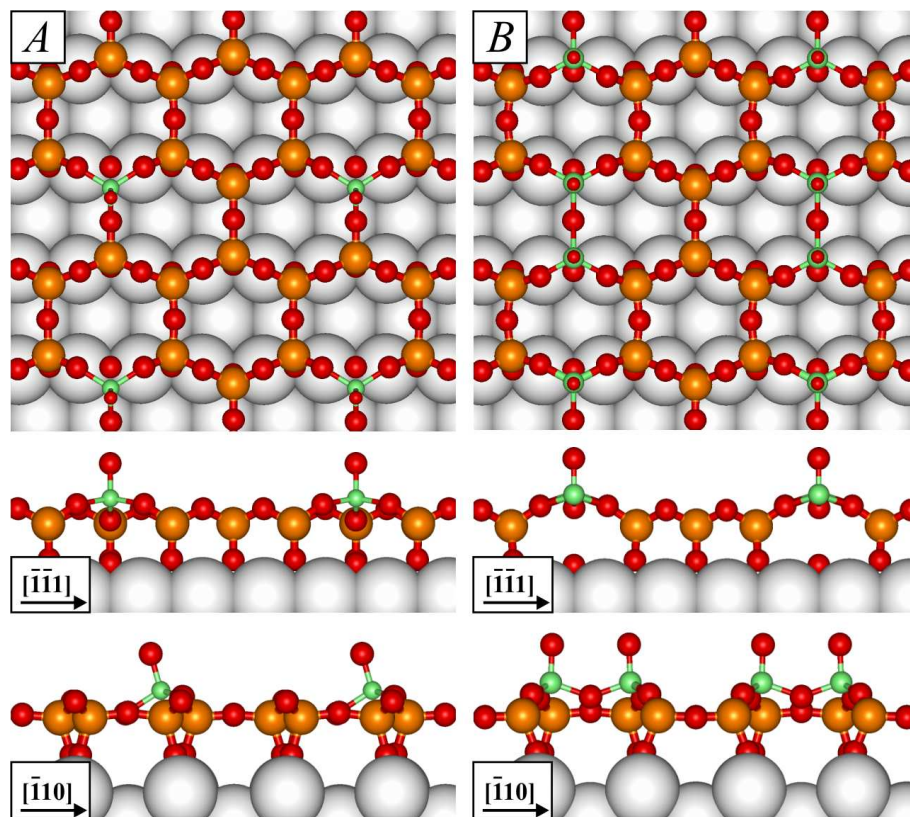


Figure 8.1: Top and side views of the most stable monomeric (*A*) and dimeric (*B*) vanadia species on the $\text{SiO}_2/\text{Mo}(112)$ surface. V atoms are depicted in green, Si in orange, and O in red.

V_nO_m cluster in the gas phase, respectively. The different V_nO_m gas-phase structures are calculated in a cubic box with $a = 15 \text{ \AA}$ using only the Γ -point. The obtained geometries are in a very good agreement with previously reported B3LYP (TZVP basis set) results [183].

The most stable $\text{VO}_2/\text{Si}_8\text{O}_{20}/\text{Mo}(112)$ cluster, regarded as a monomeric species, is shown in Figure 8.2A. It has one $\text{V}=\text{O}$ bond and forms one $\text{V}-\text{O}^{(2)}-\text{Si}$ interface bond with a Si atom from the film, which becomes 5-fold coordinated. Although fivefold coordinated silicon is not a common feature in crystalline phases, its existence has been reported for triclinic CaSi_2O_5 [184, 185], *K*-silicate glass quenched from high pressure [186], organosilane and organosilicate structures [187, 188]. The length of the new Si–O bond is 1.84 \AA , which is about 0.2 \AA elongated with respect to its typical value. The V atom, which is originally in a V^{IV} oxidation state, forms an additional bond to an O2 atom from the silica network at a distance of 2 \AA . The adsorption energy of this cluster given with respect to the most stable gas-phase VO_2 is -0.94 eV .

As far as dimeric VO_x species are considered, two different clusters, i.e., V_2O_4 and V_2O_5 , in which vanadium is in a V^{IV} and V^{V} oxidation state, respectively,

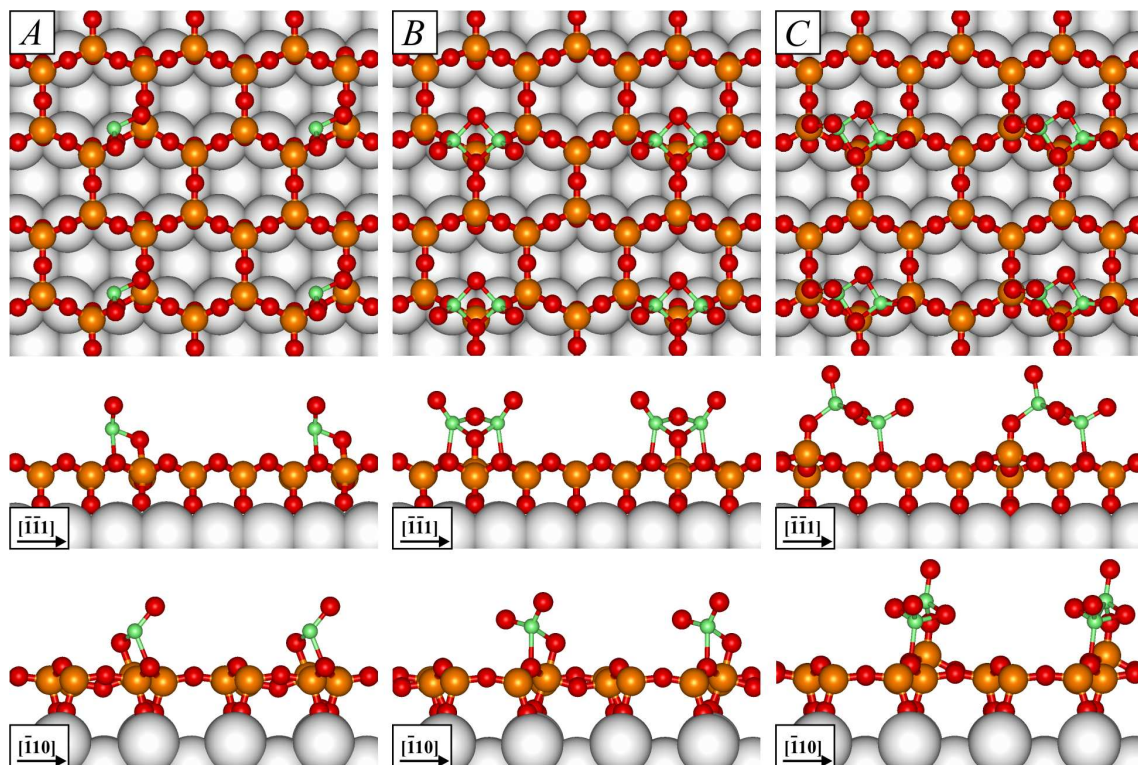


Figure 8.2: Top and side views of the most stable monomeric (VO_2) and dimeric (V_2O_4 and V_2O_5) clusters adsorbed on the $\text{SiO}_2/\text{Mo}(112)$ surface. See Figure 8.1 for color coding.

are adsorbed on the $\text{SiO}_2/\text{Mo}(112)$ surface. The resulting structures are shown in Figs. 8.2B and C. The most stable V_2O_4 cluster has a cyclic structure and two $\text{V}=\text{O}$ bonds, one $\text{V}-\text{O}^{(2)}-\text{V}$ bond, and one $\text{V}-\text{O}^{(3)}-\text{Si}$ interface bond to Si atom, which becomes 5-fold coordinated (Si-O distance is 1.81 Å). Again, the two V atoms are bound to O2 atoms from the silica network. This cluster is slightly more strongly bound to the surface ($E_{ad} = -1.08$ eV) than the VO_2 structure. Its adsorption energy is calculated with respect to the most stable gas-phase V_2O_4 cyclic-trans isomer (see Section 3.2.2).

The most stable V_2O_5 cluster adsorbed on the silica surface has a cyclic structure (Fig. 8.2C) and is by 1.43 eV more stable than the linear adsorbed V_2O_5 . It contains two $\text{V}=\text{O}$ bonds, two $\text{V}-\text{O}^{(2)}-\text{V}$ bonds, and one $\text{V}-\text{O}^{(2)}-\text{Si}$ interface bond. Only one of the V atoms is bound to an O2 atom from the silica surface. Upon formation of the new Si-O bond, in contrast to the previous two models (Figs. 8.2A and B), the Si atom remains tetrahedrally coordinated. This is due to the fact that the bond to the interface oxygen is replaced by one to a vanadyl oxygen atom from the vanadia cluster. The distance between silicon and the interface oxygen increases to 3.08 Å; virtually no bond exists between these two atoms. This cluster is much more strongly bound to the silica surface ($E_{ad} = -1.94$ eV) as compared to the V_2O_4 one.

Larger V_nO_m clusters, where n is 4 and 6, are also investigated. Attempts to

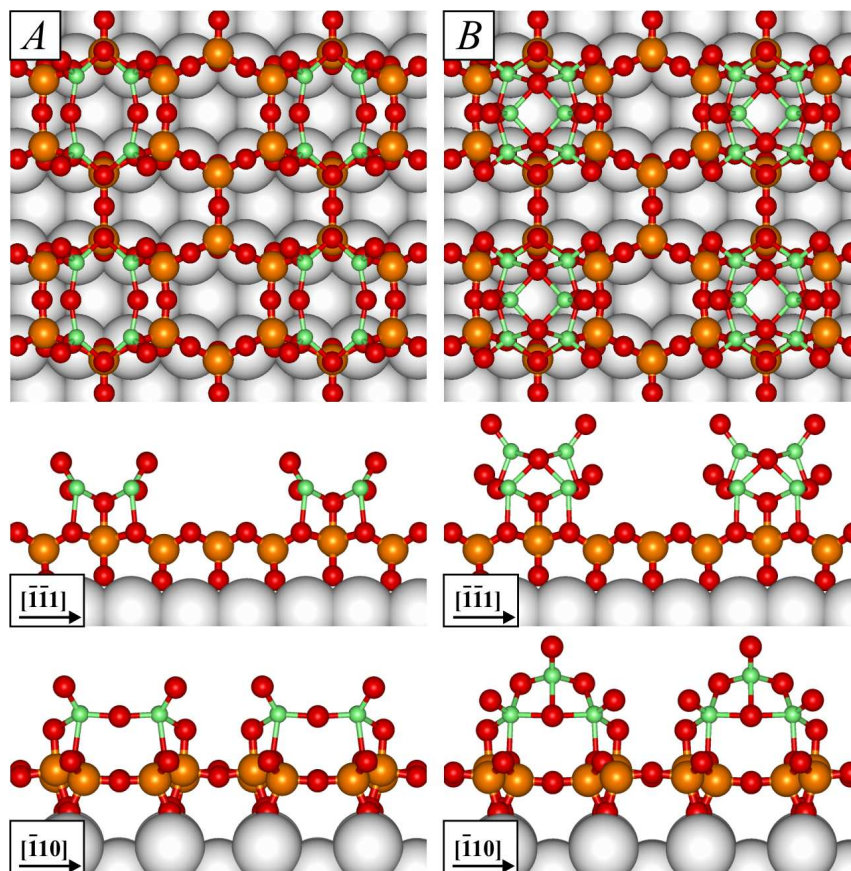


Figure 8.3: Top and side views of the V_4O_8 (A) and V_6O_{12} (B) clusters adsorbed on the $SiO_2/Mo(112)$ surface. See Figure 8.1 for color coding.

strongly bind such clusters to the silica surface resulted in structure models shown in Figure 8.3. The V_4O_8 cluster is in the form of a flat particle located on top of the six-membered silica rings of the $[SiO_4]$ network. It has four $V=O$ bonds, two $V-O^{(2)}-V$ bonds, and two $V-O^{(3)}-Si$ interface bonds with Si atoms, which increase their coordination to 5-fold (cf. Fig. 8.3A). The structure, however, is quite unstable with respect to the gas-phase V_4O_8 cage-like structure, with an adsorption energy of 1.78 eV. Decreasing by a half the dispersion of V_4O_8 clusters along the $[\bar{1}10]$ direction increases slightly the adsorption energy to $E_{ad} = 1.56$ eV.

The V_6O_{12} cluster is constructed by placing a V_2O_4 cyclic unit on top of the $V_4O_8/Si_8O_{20}/Mo(112)$ structure and is visualized in Fig. 8.3B. It is in the form of 3D particles, which are about 6 Å in height. However, similar to the aforementioned V_4O_8 structure the cluster is weakly bound to the silica surface, with the adsorption energy of only -0.08 eV. The latter is given with respect to the V_6O_{12} gas-phase cluster obtained by removal of three vanadyl oxygen atoms from the most stable V_6O_{15} cage-like structure [183].

Our studies indicate that V_nO_m clusters are weakly bound to the $SiO_2/Mo(112)$

film, which is coordinatively saturated and oxygen terminated. Additionally, the binding to the surface does not offset the structural differences from their most favorable geometry in the gas phase. Therefore, a different approach to anchor vanadia particles is used in order to increase their binding to the silica support. One Si atom from the 2D network is pulled out of the plane and its bond with the interface oxygen atom is broken. The dangling bond is saturated by forming a bond with vanadyl oxygen from the vanadia cluster. Note that such anchored species were obtained by “landing” the V_2O_5 cluster (cf. Fig. 8.2). The most stable V_4O_8 cluster created in such a way is shown in Figure 8.4A and has a cage-like structure with one $V=O$ group, five $V-O^{(2)}-V$ bonds, and one $V-O^{(2)}-Si$ interface bond. Interestingly, this model is by 2.6 eV energetically more favorable than the V_4O_8 cluster shown in Fig. 8.3A. In contrast to the latter, its adsorption on the silica surface is an exothermic process ($E_{ad} = -0.68$ eV).

Another possibility is to anchor the V_4O_8 cluster to the $SiO_2/Mo(112)$ surface by its two vanadyl oxygen atoms. Four different structures depending on the orientation of the vanadia cluster are thus obtained, as shown in Figure 8.5. However, they differ by less than 0.1 eV because of the similar distances between any two Si atoms involved in interface bond formation. As a result of the strong binding to the surface, the adsorption energy of such cluster (Fig. 8.4B) increases to $E_{ad} = -0.89$ eV. Thus, the energy gain due to formation of the second $V-O-Si$ interface bond is about 0.3 eV.

V_4O_{10} clusters are also considered and the most favorable $V_4O_{10}/Si_8O_{20}/Mo(112)$ structure is shown in Figure 8.4C. It has two surface $V=O$ groups and is anchored to the silica surface by two $V-O^{(2)}-Si$ interface bonds. Thus, its bonding geometry is practically the same as of the V_4O_8 structure and its adsorption energy is $E_{ad} = -0.68$ eV.

Finally, even larger vanadia species, such as V_6O_{15} , are considered and the most stable one is illustrated in Figure 8.4D. It is terminated by four $V=O$ groups and

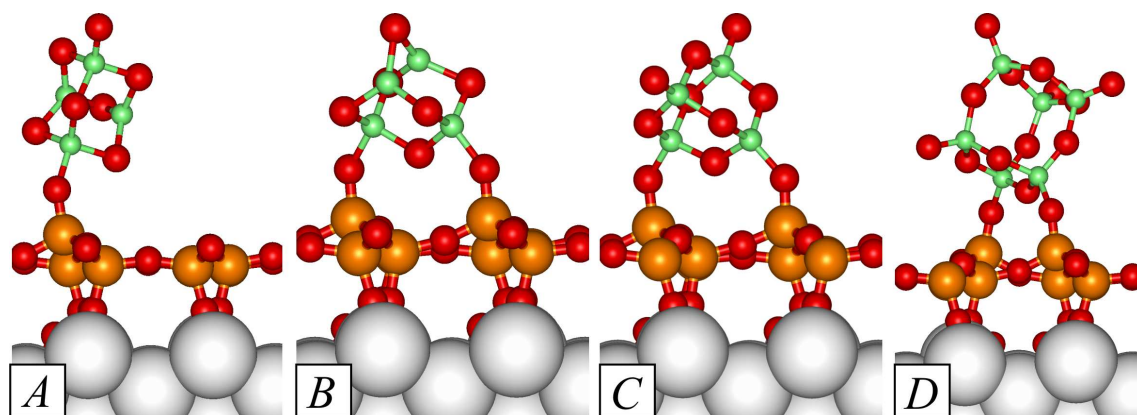


Figure 8.4: V_4O_8 cluster anchored to the $SiO_2/Mo(112)$ surface by one (model A) and two (model B) $V-O-Si$ interface bonds, V_4O_{10} (model C), and V_6O_{15} (model D) clusters.

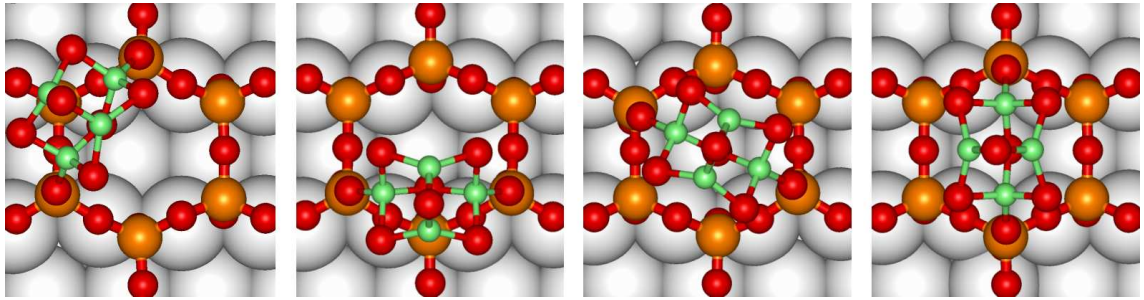


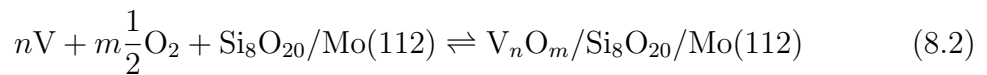
Figure 8.5: Top view of the differently oriented V_4O_8 clusters anchored to the $SiO_2/Mo(112)$ surface by two interface bonds.

is anchored to the $SiO_2/Mo(112)$ surface by two $V-O^{(2)}-Si$ interface bonds. The adsorption energy is -0.65 eV and is given with respect to the most stable V_6O_{15} trigonal prism in the gas-phase.

8.2 Thermodynamic Stability

As with the studies on alumina-supported vanadium oxides, statistical thermodynamics is applied to account for the effect of oxygen partial pressure and vanadium concentration at a given temperature on the stability of the vanadia aggregates supported on the thin crystalline SiO_2 film grown on $Mo(112)$.

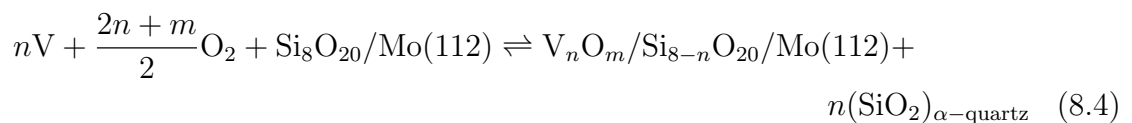
The following equilibrium reaction is considered



The corresponding reaction energy is

$$\Delta E = E_{V_nO_m/Si_8O_{20}/Mo(112)} - E_{Si_8O_{20}/Mo(112)} - nE_V^{bulk} - m\frac{1}{2}E_{O_2} \quad (8.3)$$

where $E_{V_nO_m/Si_8O_{20}/Mo(112)}$ and $E_{Si_8O_{20}/Mo(112)}$ are the total energies of the system with a given vanadia/ $Si_8O_{20}/Mo(112)$ composition and the clean silica slab, respectively. The reaction energy ΔE is the energy needed to form a silica-supported vanadium oxide from a silica thin film, metallic vanadium, and oxygen. This equation, however, holds only when the number of Si atoms does not change. If one or two Si atoms are replaced by $V=O$ groups forming monomeric and dimeric VO_x species, respectively, Eq. (8.2) is reformulated as



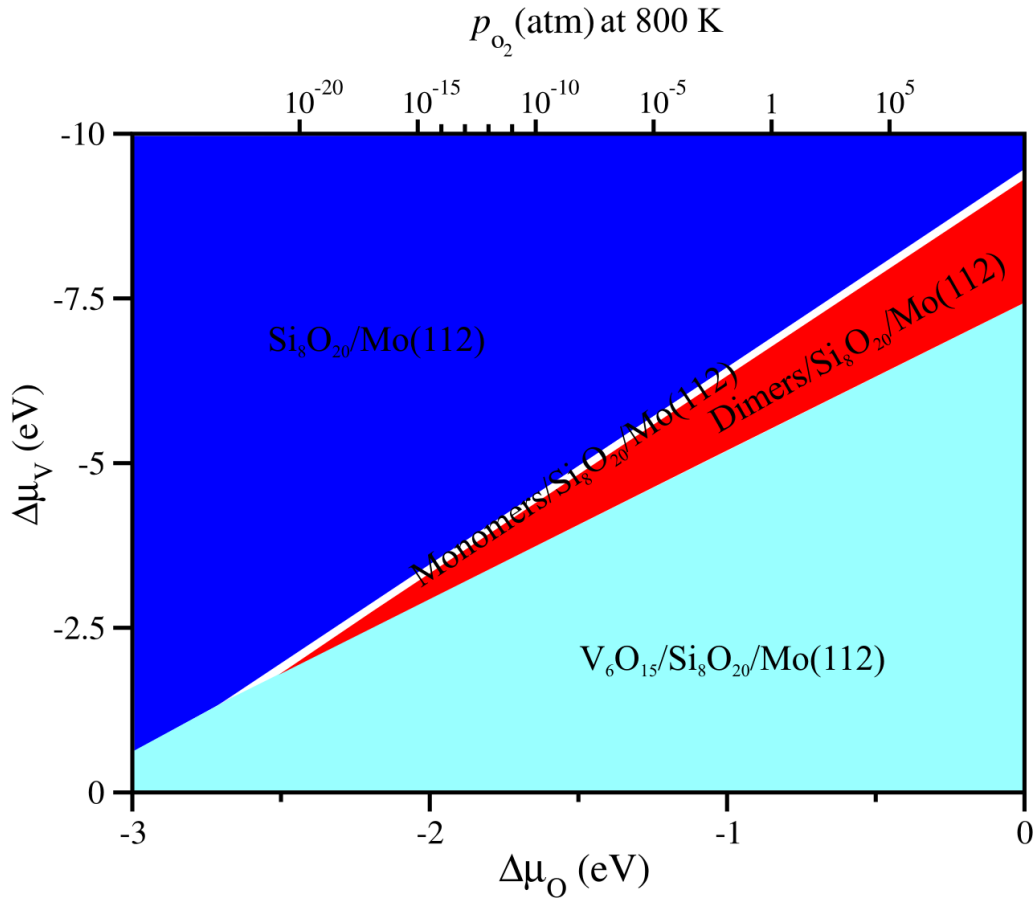


Figure 8.6: Phase diagram as a function of the $\Delta\mu_{\text{O}}$ and $\Delta\mu_{\text{V}}$ chemical potentials for vanadia aggregates supported on the $\text{SiO}_2/\text{Mo}(112)$ surface. $\Delta\mu_{\text{O}}$ is translated into a pressure scale at $T = 800$ K.

The accompanying change in the surface-related free energy $\Delta\gamma$ is given by Eq. (3.3). The most favorable structure is the one that minimizes $\Delta\gamma$ for given values of vanadium and oxygen chemical potentials. The resulting phase diagram is shown in Figure 8.6 with values of the oxygen potential related to an oxygen pressure at $T = 800$ K.

At low vanadium chemical potentials, monomeric VO_x species obtained by replacement of Si atoms of the $\text{SiO}_2/\text{Mo}(112)$ film surface by $\text{V}=\text{O}$ groups (see Figure 8.1A) become energetically stable. Upon increasing the $\Delta\mu_{\text{V}}$ values, dimers that are also modeled by replacement are predicted to be stable (Fig. 8.1B). At even higher vanadium chemical potentials, the largest vanadia clusters considered (V_6O_{15}) form. A characteristic feature of all stable structures is the presence of surface vanadyl groups. Furthermore, among the various structure models investigated here, the clusters “landed” on the silica surface do not appear in the stability plot. The reason is that the thin-film silica support is oxygen-terminated and coordina-

tively saturated, and thus, the binding of the vanadia species is very weak. The results suggest that initially, depositing vanadium in oxygen atmosphere would result in formation of low-coverage VO_x species, such as monomers and dimers created by replacement of Si atoms from the crystalline $\text{SiO}_2/\text{Mo}(112)$ film. Upon increasing the amount of deposited vanadium, large vanadia clusters that are anchored to the surface via interface $\text{V}-\text{O}^{(2)}-\text{Si}$ bonds would form. Note, however, that in this work clusters anchored to already existing VO_x sites on the film surface have not been investigated.

At low V exposures, the formation of vanadia particles consisting of 1-2 V atoms was reported, based on the amount of deposited vanadium and the determined particle density [72]. In Ref. [180], high-resolution STM images showed atomic-size features suggested to be monomeric VO_x species. Registry analysis revealed that they are located above the outermost $\text{Si}-\text{O1}-\text{Si}$ bonds of the $[\text{SiO}_4]$ network. The results of our calculation can explain these experimental observations by formation of monomeric VO_x species created by replacement (cf. Fig. 8.1A). Thus, the protrusions imaged by STM in Ref. [180] might be attributed to the vanadyl oxygen atoms of the monomers, which are indeed located above the O1 atoms of the SiO_2 network.

8.3 Vibrational Analysis

The aim of this section is to develop an understanding of the vibrational spectra of the model silica-supported vanadia catalysts. Therefore, based on DFT calculations a frequency analysis on the various structure models considered is performed and the results are compared to the experimental data. Such study on the different types of aggregation of the VO_x species gives an insight into the variability of the vibrational frequencies and provides a qualitative understanding of the characteristic structural features of the experimental systems.

Table 8.1 shows the frequencies and intensities obtained for selected models, i.e., low-coverage (monomeric and dimeric) VO_x species and large V_4O_{10} and V_6O_{15} clusters, which are differently supported on the surface. Statistical thermodynamics suggests that these structures are stable phases. Note, however, that at high $\Delta\mu_V$ values, V_4O_{10} is always less favorable than V_6O_{15} . In order to compensate for systematic errors of DFT, the frequencies are scaled by two different empirical factors. A scaling factor of 1.0312 is used for the modes of the SiO_2 film (see Section 4.4), whereas the vanadyl stretching vibrations are scaled by a factor of 0.985 derived from BP86 calculations on $\text{O}=\text{VF}_3$, $\text{O}=\text{VCl}_3$, and V_4O_{10} [182]. The experimental IRAS frequencies as obtained in Ref. [180] are given for comparison.

For the clean $\text{SiO}_2/\text{Mo}(112)$ film, a very intense band at 1061 cm^{-1} and two weak signals at 779 and 672 cm^{-1} were obtained, in perfect agreement with the experimental IRAS results (see Section 4.4). They were assigned to $\text{Si}-\text{O}-\text{Mo}$ asymmetric stretching, $\text{Si}-\text{O}-\text{Si}$ symmetric stretching coupled with $\text{Si}-\text{O}-\text{Si}$ bending, and

Table 8.1: Calculated scaled harmonic vibrational frequencies (cm^{-1}) and IR intensities (in parentheses, normalized to 1.00) for the most intense vibrational modes of the $\text{SiO}_2/\text{Mo}(112)$ film, monomeric and dimeric VO_x species, V_4O_{10} and V_6O_{15} clusters. Experimental IRAS frequencies are given for comparison.

Frequency	Support	Monomer	Dimer	V_4O_{10}	V_6O_{15}	Exp.
V–O–Si stretch		1075(0.01) 947(0.008)	1100(0.21)			
V=O stretch		1056(0.30)	1064(0.15)	1048(0.18) 1034(0.05)	1037(0.05) 1006(0.11)	1046
Si–O–Mo stretch	1061(0.79)	1032(1.00)	1004(0.83)	1015(0.002) 933(0.003)		
Si–O–Si stretch	779(0.05)	801(0.03) 757(0.04)	812(0.04)			
V–O–V stretch				726(0.02) 637(0.02)	858(0.13) 805(0.11) 733(0.03)	720
Si–O–Si bending	672(0.07)	659(0.06)	655(0.04)			

to a coupling of Si–O–Si bending modes. Upon creation of monomeric VO_x species (cf. Fig. 8.1A), the main phonon of the silica film, which is strongly influenced by the replacement of silicon by vanadium, shifts by $\sim 30 \text{ cm}^{-1}$ toward lower wavenumbers (1032 cm^{-1}). Concomitantly, a new vibration emerges at 1056 cm^{-1} , which corresponds to stretching of the V=O species. Its intensity is about three times lower than that of the Si–O–Mo phonon. The coupled Si–O–Si symmetric stretching and bending mode is split into two bands at 801 and 757 cm^{-1} , and the Si–O–Si bending mode appears at 659 cm^{-1} . Table 8.1 shows that the intensities of these modes are almost unchanged with respect to the corresponding modes in the silica support. In addition, two weak signals at 1075 and 947 cm^{-1} are attributed to the in-phase V–O–Si vibration coupled with stretching of the V=O group, and the out-of-phase V–O–Si stretching mode, respectively.

Upon formation of dimeric VO_x species, the main silica phonon shifts to even lower wavenumbers (1004 cm^{-1}) and its intensity is slightly reduced. The vanadyl stretching mode appears at similar frequencies (1064 cm^{-1}) as in the monomeric species, but its intensity is reduced by a half (see Table 8.1). In fact, this vibration corresponds to an in-phase stretching of the two vanadyl groups. The corresponding out-of-phase mode at 1055 cm^{-1} is IRAS inactive because it does not produce a change in the dipole moment component perpendicular to the surface. The coupled Si–O–Si symmetric stretching and bending vibration appears at 812 cm^{-1} , and the coupling of bending modes is red-shifted (655 cm^{-1}) as compared to the same mode in the silica film. The vibration at 1100 cm^{-1} in the dimeric structure is an in-

phase V–O–Si stretching mode and has a significant intensity, whereas the V–O–V vibration at 795 cm^{-1} is parallel to the surface and is IRAS inactive.

It is evident that the models considered so far cannot explain the experimental vibrational spectra of vanadia/silica systems [72, 180, 181], for which the single band at 1046 cm^{-1} is assigned to stretching vibration of V=O species, whereas the broad signal at 720 cm^{-1} that appears at higher vanadium coverages is attributed to the V–O–V stretching vibrations. However, it is important to realize that the IRAS spectra reported in the literature are always taken on vanadia particles with higher vanadia coverage than that of the monomeric and dimeric VO_x species.

Thus, as a next step, the vibrational frequencies of large vanadia clusters, such as V_4O_{10} and V_6O_{15} , anchored to the $\text{SiO}_2/\text{Mo}(112)$ surface by two V–O⁽²⁾–Si interface bonds (see Figure 8.4 C and D) are calculated. The spectrum of the former structure is characterized by a vibrational mode at 1048 cm^{-1} assigned to the in-phase stretching of the two vanadyl groups, and a mode at 1034 cm^{-1} , which is the corresponding out-of-phase vibration. Interestingly, the asymmetric Si–O–Mo stretching modes at 1015 and 933 cm^{-1} , which are strongly coupled with the V–O⁽²⁾–Si interface modes have negligible intensities because they do not produce a change in the dipole moment component perpendicular to the surface. The frequency analysis also reveals no IRAS active Si–O–Si symmetric stretching and bending modes, which is in agreement with the experimental spectra obtained upon deposition of vanadium onto pristine silica surface. The lack of these two signals was interpreted as an indication of long-range order loss in the crystalline silica film [180]. Therefore, very recently, a new ice-assisted preparation of silica-supported vanadia particles has been developed [180]. In our work, the role of the H_2O layer in protecting the silica film and the properties of vanadia grown on ice-assisted silica support are not investigated. However, the calculations suggest that the loss of the three IRAS active bands characteristic for the silica support does not necessarily indicate a destruction of the film. The quenching of these modes upon formation of vanadia-deposited particles is governed by the metal surface selection rule. Finally, the new bands that emerge at 726 and 637 cm^{-1} are attributed to vibrations of the entire V–O–V framework and the outermost V–O–V bond, respectively. Thus, the V_4O_{10} cluster anchored to the $\text{SiO}_2/\text{Mo}(112)$ surface by two V–O⁽²⁾–Si interface bonds, despite the fact that is not the most thermodynamically stable phase (see Figure 8.6), can account for all vibrational features in the spectra of experimental vanadia/silica model systems. However, one should keep in mind that the phase diagram shows only the stable species under equilibrium conditions and that the exact mechanism of vanadia particle formation is unknown.

Similar to V_4O_{10} , the vibrational spectrum of $\text{V}_6\text{O}_{15}/\text{Si}_8\text{O}_{20}/\text{Mo}(112)$ reveals no IRAS active Si–O–Mo stretching modes as well as vibrations associated with Si–O–Si symmetric stretching and bending modes of the thin silica film. The highest wavenumber frequencies involve stretching vibrations of different vanadyl groups present in the structure, whereas those at 858 , 805 , and 733 cm^{-1} are stretching modes of the V–O–V framework (see Table 8.1). The existence of two very intense

bands in the region of 800–850 cm^{-1} is a main discrepancy with the measured IRAS spectra. Therefore, despite the thermodynamic stability of the V_6O_{15} clusters at high $\Delta\mu_{\text{V}}$ values, the frequency analysis indicates that these are not the experimentally formed vanadia species.

8.4 Summary

Low-coverage vanadia species (monomers and dimers) as well as large vanadia clusters, differently anchored to the thin-film silica support have been investigated by DFT combined with statistical thermodynamics. The vanadia/silica phase diagram as a function of vanadium activity and oxygen partial pressure shows that at low $\Delta\mu_{\text{V}}$ values, monomeric and then in turn dimeric VO_x species become stable. They are modeled by replacement of Si atoms from the 2D network of the $\text{SiO}_2/\text{Mo}(112)$ film by $\text{V}=\text{O}$ groups. At high values of the vanadium chemical potentials, the largest vanadia clusters considered (V_6O_{15}) form. A characteristic feature of all stable species is the presence of surface vanadyl groups.

Vibrational frequency analysis of different models considered in this work provides a valuable insight into the structural features of the vanadia/silica model catalysts. The calculations suggest that the V_4O_{10} cluster anchored to the $\text{SiO}_2/\text{Mo}(112)$ surface by two $\text{V}-\text{O}^{(2)}-\text{Si}$ interface bonds can account for all vibrational frequencies of the experimental model systems. Its spectrum reveals a single band at 1048 cm^{-1} corresponding to a stretching of the $\text{V}=\text{O}$ groups and a broad band in the range of 630–730 cm^{-1} attributed to $\text{V}-\text{O}-\text{V}$ vibrations, well-known for the V_2O_3 bulk. Moreover, the three characteristic for the thin-film silica support bands are IRAS inactive because of the metal surface selection rule, which is in an agreement with the experimental observations.

Chapter 9

Summary

Although supported vanadium oxide catalysts have been a subject of detailed investigations for many decades, the exact atomic structure and the way these species are anchored to the surface of the support oxide have not been unambiguously determined. The results presented in this work aimed to provide a step towards better understanding of two such systems, namely, the alumina- and silica-supported vanadium oxides on the atomic scale.

In the first step of this context (Chapter 3), low-coverage VO_x species as well as vanadia films of varying thickness supported on the stable $\alpha\text{-Al}_2\text{O}_3(0001)$ and the metastable $\kappa\text{-Al}_2\text{O}_3(001)$ surface have been investigated by DFT in combination with statistical thermodynamics. Compared to $\alpha\text{-Al}_2\text{O}_3$, the presence of tetrahedrally coordinated Al sites (25 %) in $\kappa\text{-Al}_2\text{O}_3$ results in a much more open structure that facilitates significant lattice-induced relaxation effects upon formation of oxygen defects in the vanadia phase. Our findings indicate that the vanadyl-terminated low-coverage VO_x species on $\kappa\text{-Al}_2\text{O}_3$, which possess very labile oxygen atoms, are expected to exist at catalytically relevant conditions and are likely to show higher reactivity than the stable species on the $\alpha\text{-Al}_2\text{O}_3$ support. Moreover, under typical reducing conditions, such aggregates on $\kappa\text{-Al}_2\text{O}_3$ are partially reduced, whereas the α -alumina-supported reduced species would only become stable in UHV at very high temperatures (1200 K). Using the calculated vibrational spectra of VO_x species anchored via $\text{V-O}^{(2)}\text{-Al}$ interface bonds to the α - and $\kappa\text{-Al}_2\text{O}_3$ supports, the studies show that the sole presence of such bonds at the vanadia/alumina interface does *not* necessarily lead to interface-localized vibrations at $\sim 950\text{ cm}^{-1}$, and that additional factors, such as the $\text{V-O}^{(2)}$ bond lengths, couplings, and the specific oxide support structure play a role. Moreover, on the basis of the structure of models that produced this band, the nature of the interface cannot be unequivocally assigned.

An important achievement of this work is that in collaboration with the experimental group of Prof. Hans-Joachim Freund at the Fritz-Haber-Institut der Max-Planck-Gesellschaft, the precise atomic structure of the model silica support, namely, the ultrathin crystalline SiO_2 film grown on $\text{Mo}(112)$ substrate has been resolved (Chapter 4). Based on excellent agreement between the results of DFT calculations,

and experimental data obtained from STM, IRAS, and XPS, it has been shown that the film consists of a monolayer of 2D network of corner-sharing $[\text{SiO}_4]$ tetrahedra. It resembles the sheet structure of monolayer silicates and has a $\text{SiO}_{2.5}$ stoichiometry that does not naturally occur in bulk silica. Additionally, it has been demonstrated that the previously proposed model of isolated $[\text{SiO}_4]$ clusters cannot account for all the available experimental data, and thus, it does not correspond to the atomic structure of the epitaxially grown $\text{SiO}_2/\text{Mo}(112)$ film.

The study of low-dimensional crystalline silica on $\text{Mo}(112)$ was further extended to 1D stripes, which coexist with islands of the 2D films (Chapter 5). Their atomic structure is determined as paired-rows of $[\text{SiO}_4]$ units chemisorbed on the missing-row-type reconstructed $\text{Mo}(112)$ surface, and the calculated vibrational frequencies, O 1s core-level shifts, and simulated STM images are in excellent agreement with the experimental results. A phase diagram showing the stability of various 1D and 2D crystalline silica depending on the silicon coverage and oxygen pressure has been derived (Chapter 6). At elevated O_2 pressures the calculations predicted formation of a new, “O-rich” phase of the silica film, whose existence was subsequently confirmed by IRAS and XPS. The structure contains additional oxygen atoms adsorbed in bridging positions in the trenches of the $\text{Mo}(112)$ surface under the silica layer. Due to the very subtle differences between the properties of the O-poor and O-rich films, the existence of the latter may not have been discovered without the aid of theory.

In Chapter 7, the power of genetic algorithm method in determining unknown atomic structures has been demonstrated for the $p(1 \times 2)$ and $p(1 \times 3)$ models observed upon oxygen adsorption on $\text{Mo}(112)$. The only required parameters are the periodic vectors of the unit cell and the chemical potentials of the constituent species. The number of atoms involved in the adsorption and reconstruction as well as their most favorable bonding geometry is obtained automatically within the GA search. The simulations reveal unusual flexibility of the $\text{Mo}(112)$ surface and yield oxygen-induced reconstructed structures that are more stable than any models suggested so far. The results are fully supported by a multitude of experimental data.

Finally, in Chapter 8, differently anchored silica-supported vanadia aggregates have been investigated. The vanadia/silica phase diagram reveals that the stable VO_x species are terminated by vanadyl groups. The frequency analysis indicates that the V_4O_{10} clusters anchored to the $\text{SiO}_2/\text{Mo}(112)$ surface by two $\text{V}-\text{O}^{(2)}-\text{Si}$ interface bonds can account for all vibrational frequencies of the experimental model systems. Moreover, it is suggested that the loss of the three IRAS active bands characteristic for the silica support does not necessarily indicate a destruction of the film. The quenching of these modes upon formation of vanadia-deposited particles is governed by the metal surface selection rule.

The present work demonstrates the importance of combining theory and experiment in the identification and characterization of complex, novel structures on the atomic scale.

Bibliography

- [1] R. A. VanSanten, P. W. N. M. van Leeuwen, J. Moulijn, and B. A. Averill, editors. *Catalysis: An Integrated Approach*. Elsevier, Amsterdam, 2nd edition, 1999.
- [2] G. Deo, I. E. Wachs, and J. Haber. Supported Vanadium-Oxide Catalysts-Molecular Structural Characterization and Reactivity Properties. *Crit. Rev. Surf. Chem.*, 4:141–187, 1994.
- [3] B. M. Weckhuysen and D. E. Keller. Chemistry, Spectroscopy and the Role of Supported Vanadium Oxides in Heterogeneous Catalysis. *Catal. Today*, 78: 25–46, 2003.
- [4] G. Martra, F. Arena, S. Coluccia, F. Frusteri, and A. Parmaliana. Factors Controlling the Selectivity of V₂O₅ Supported Catalysts in the Oxidative Dehydrogenation of Propane. *Catal. Today*, 63:197–207, 2000.
- [5] E. A. Mamedov and V. C. Corberán. Oxidative Dehydrogenation of Lower Alkanes on Vanadium Oxide-Based Catalysts. The Present State of the Art and Outlooks. *Appl. Catal. A*, 127:1–40, 1995.
- [6] M. A. Bañares, M. V. Martínez-Huerta, X. Gao, J. L. G. Fierro, and I. E. Wachs. Dynamic Behavior of Supported Vanadia Catalysts in the Selective Oxidation of Ethane. In situ Raman, UV-Vis DRS and Reactivity Studies. *Catal. Today*, 61:295–301, 2000.
- [7] A. Khodakov, B. Olthof, A. T. Bell, and E. Iglesia. Structure and Catalytic Properties of Supported Vanadium Oxides: Support Effects on Oxidative Dehydrogenation Reactions. *J. Catal.*, 181:205–216, 1999.
- [8] I. E. Wachs. Recent Conceptual Advances in the Catalysis Science of Mixed Metal Oxide Catalytic Materials. *Catal. Today*, 100:79–94, 2005.
- [9] M. Bäumer and H.-J. Freund. Metal Deposits on Well-Ordered Oxide Films. *Prog. Surf. Sci.*, 61:127–198, 1999.

-
- [10] C. T. Campbell. Ultrathin Metal Films and Particles on Oxide Surfaces: Structural, Electronic and Chemisorptive Properties. *Surf. Sci. Rep.*, 27:1–111, 1997.
- [11] K. Kishi, K. Hirai, and T. Yamamoto. XPS and XAES Study for Oxidation of V/Cu(100) and V,Na/Cu(100) Surfaces. *Surf. Sci.*, 290:309–318, 1993.
- [12] A.-C. Dupuis, M. A. Haija, B. Richter, H. Kuhlenbeck, and H.-J. Freund. V₂O₃(0001) on Au(111) and W(110): Growth, Termination and Electronic Structure. *Surf. Sci.*, 539:99–112, 2003.
- [13] H. Niehus, R.-P. Blum, and D. Ahlbehrendt. Structure of Vanadium Oxide (V₂O₃) Grown on Cu₃Al(100). *Surf. Rev. Lett.*, 10:353–359, 2003.
- [14] S. Surnev, L. Vitali, M. G. Ramsey, F. P. Netzer, G. Kresse, and J. Hafner. Growth and Structure of Ultrathin Vanadium Oxide Layers on Pd(111). *Phys. Rev. B*, 61:13945–13954, 2000.
- [15] M. Sambti, M. Della Negra, and G. Granozzi. Growth and Structural Characterisation of Vanadium Oxide Ultrathin Films on TiO₂(110). *Thin Solid Films*, 400:26–36, 2001.
- [16] N. Magg, J. B. Giorgi, T. Schroeder, M. Bäumer, and H.-J. Freund. Model Catalyst Studies on Vanadia Particles Deposited onto a Thin-Film Alumina Support. 1. Structural Characterization. *J. Phys. Chem. B*, 106:8756–8761, 2002.
- [17] N. Magg, J. B. Giorgi, A. Hammoudeh, T. Schroeder, M. Bäumer, and H.-J. Freund. Model Catalyst Studies on Vanadia Particles Deposited onto a Thin-Film Alumina Support. 2. Interaction with Carbon Monoxide. *J. Phys. Chem. B*, 107:9003–9010, 2003.
- [18] S. Guimond, M. Abu Haija, S. Kaya, J. Lu, J. Weissenrieder, S. Shaikhutdinov, H. Kuhlenbeck, H.-J. Freund, J. Döbler, and J. Sauer. Vanadium Oxide Surfaces and Supported Vanadium Oxide Nanoparticles. *Top. Catal.*, 38:117–125, 2006.
- [19] Y. Yourdshahyan, C. Ruberto, M. Halvarsson, L. Bengtsson, V. Langer, B. I. Lundqvist, S. Rупpi, and U. Rolander. Theoretical Structure Determination of a Complex Material: κ -Al₂O₃. *J. Am. Ceram. Soc.*, 82:1365–1380, 1999.
- [20] T. Schroeder, M. Adelt, B. Richter, M. Naschitzki, M. Bäumer, and H.-J. Freund. Epitaxial Growth of SiO₂ on Mo(112). *Surf. Rev. Lett.*, 7:7–14, 2000.
- [21] T. Schroeder, J. B. Giorgi, M. Bäumer, and H.-J. Freund. Morphological and Electronic Properties of Ultrathin Crystalline Silica Epilayers on a Mo(112) Substrate. *Phys. Rev. B*, 66:165422, 2002.

-
- [22] M. S. Chen, A. K. Santra, and D. W. Goodman. Structure of Thin SiO₂ Film Grown on Mo(112). *Phys. Rev. B*, 69:155404, 2004.
- [23] D. Ricci and G. Pacchioni. Structure of Ultrathin Crystalline SiO₂ Films on Mo(112). *Phys. Rev. B*, 69:161307, 2004.
- [24] S. Wendt, E. Ozensoy, T. Wei, M. Frerichs, Y. Cai, M. S. Chen, and D. W. Goodman. Electronic and Vibrational Properties of Ultrathin SiO₂ Films Grown on Mo(112). *Phys. Rev. B*, 72:115409, 2005.
- [25] J. Weissenrieder, S. Kaya, J.-L. Lu, H.-J. Gao, S. Shaikhutdinov, H.-J. Freund, M. Sierka, T. K. Todorova, and J. Sauer. Atomic Structure of a Thin Silica Film on a Mo(112) Substrate: A Two-Dimensional Network of SiO₄ Tetrahedra. *Phys. Rev. Lett.*, 95:076103, 2005.
- [26] T. K. Todorova, M. Sierka, J. Sauer, S. Kaya, J. Weissenrieder, J.-L. Lu, H.-J. Gao, S. Shaikhutdinov, and H.-J. Freund. Atomic Structure of a Thin Silica Film on a Mo(112) Substrate: A Combined Experimental and Theoretical Study. *Phys. Rev. B*, 73:165414, 2006.
- [27] J.-L. Lu, S. Kaya, J. Weissenrieder, T. K. Todorova, M. Sierka, J. Sauer, H.-J. Gao, S. Shaikhutdinov, and H.-J. Freund. Formation of One-Dimensional Crystalline Silica on a Metal Substrate. *Surf. Sci.*, 600:L164–L168, 2006.
- [28] M. Sierka, T. K. Todorova, S. Kaya, D. Stacchiola, J. Weissenrieder, J.-L. Lu, H.-J. Gao, S. Shaikhutdinov, H.-J. Freund, and J. Sauer. Interplay between Theory and Experiment in the Quest for Silica with Reduced Dimensionality Grown on a Mo(112) Surface. *Chem. Phys. Lett.*, 424:115–119, 2006.
- [29] E. Lundgren, G. Kresse, C. Klein, M. Borg, J. N. Andersen, M. De Santis, Y. Gauthier, C. Konvicka, M. Schmid, and P. Varga. Two-Dimensional Oxide on Pd(111). *Phys. Rev. Lett.*, 88:246103, 2002.
- [30] M. Todorova, E. Lundgren, V. Blum, A. Mikkelsen, S. Gray, J. Gustafson, M. Borg, J. Rogal, K. Reuter, J. N. Andersen, and M. Scheffler. The Pd(100)-($\sqrt{5} \times \sqrt{5}$)R27°-O Surface Oxide Revisited. *Surf. Sci.*, 541:101–112, 2003.
- [31] J. Schnadt, A. Michaelides, J. Knudsen, R. T. Vang, K. Reuter, L. Lægsgaard, M. Scheffler, and F. Besenbacher. Revisiting the Structure of the $p(4 \times 4)$ Surface Oxide on Ag(111). *Phys. Rev. Lett.*, 96:146101, 2006.
- [32] M. Schmid, A. Reicho, A. Stierle, I. Costina, J. Klikovits, P. Kostelnik, O. Dubay, G. Kresse, J. Gustafson, E. Lundgren, J. N. Andersen, H. Dosch, and P. Varga. Structure of Ag(111)- $p(4 \times 4)$ -O: No Silver Oxide. *Phys. Rev. Lett.*, 96:146102, 2006.

-
- [33] K. Fukui, T. Aruga, and Y. Iwasawa. Chemisorption of CO and H₂ on Clean and Oxygen-Modified Mo(112). *Surf. Sci.*, 281:241–252, 1993.
- [34] K. Fukui, K. Motoda, and Y. Iwasawa. Selective Oxidation of Methanol by Extra Oxygen Species on One-Dimensional Mo Rows of a Mo(112)-(1 × 2)-O Surface. *J. Phys. Chem. B*, 102:8825–8833, 1998.
- [35] T. Schroeder, J. Zegenhagen, N. Magg, B. Immaraporn, and H.-J. Freund. Formation of a Faceted MoO₂ Epilayer on Mo(112) Studied by XPS, UPS and STM. *Surf. Sci.*, 552:85–97, 2004.
- [36] A. K. Santra, B. K. Min, and D. W. Goodman. Oxygen-Induced $p(1 \times 3)$ -O Reconstruction on Mo(112): A Precursor to the Epitaxial Formation of MoO₂(100). *Surf. Sci.*, 513:L441–L444, 2002.
- [37] M. Sierka, T. K. Todorova, J. Sauer, S. Kaya, D. Stacchiola, J. Weissenrieder, S. Shaikhutdinov, and H.-J. Freund. Oxygen Adsorption on Mo(112) Surface Studied by Ab Initio Genetic Algorithm and Experiment. *J. Chem. Phys.*, 2007.
- [38] R. G. Parr and W. Yang. *Density-Functional Theory of Atoms and Molecules*, volume 16 of International series of monographs on chemistry. Oxford University Press, Inc., New York, 1989.
- [39] C. J. Cramer. *Essentials of Computational Chemistry*. John Wiley and Sons, Ltd, Chichester, 2nd edition, 2004.
- [40] W. Koch and M. C. Holthausen. *A Chemist's Guide to Density Functional Theory*. Wiley-VCH, Weinheim, 2000.
- [41] L. H. Thomas. The Calculation of Atomic Fields. *Proc. Camb. Phil. Soc.*, 23: 542–548, 1927.
- [42] E. Fermi. Un Metodo Statistiche per la Determinazione di Alcune Proprieta Dell'atomo. *Rend. Accad. Lincei*, 6:602–607, 1927.
- [43] P. Hohenberg and W. Kohn. Inhomogeneous Electron Gas. *Phys. Rev.*, 136: B864–B871, 1964.
- [44] W. Kohn and L. J. Sham. Self-Consistent Equations Including Exchange and Correlation Effects. *Phys. Rev.*, 140:A1133–A1138, 1965.
- [45] D. M. Ceperley and B. J. Alder. Ground State of the Electron Gas by a Stochastic Method. *Phys. Rev. Lett.*, 45:566–569, 1980.
- [46] A. D. Becke. A New Mixing of Hartree-Fock and Local Density-Functional Theories. *J. Chem. Phys.*, 98:1372–1377, 1993.

-
- [47] J. Paier, M. Marsman, K. Hummer, G. Kresse, I. C. Gerber, and J. G. Ángyán. Screened Hybrid Density Functionals Applied to Solids. *J. Chem. Phys.*, 124:154709, 2006.
- [48] J. Sauer and J. Döbler. Structure and Reactivity of V_2O_5 : Bulk Solid, Nanosized Clusters, Species Supported on Silica and Alumina, Cluster Cations and Anions. *Dalton Trans.*, 19:3116–3121, 2004.
- [49] M. V. Ganduglia-Pirovano, A. Hofmann, and J. Sauer. Oxygen Vacancies in Transition Metal and Rare Earth Oxides: Current State of Understanding and Remaining Challenges. *Surf. Sci. Rep.*, 62:219–270, 2007.
- [50] G. Kresse and J. Furthmüller. Efficiency of Ab-initio Total Energy Calculations for Metals and Semiconductors Using a Plane-Wave Basis Set. *Comput. Mater. Sci.*, 6:15–50, 1996.
- [51] G. Kresse and J. Furthmüller. Efficient Iterative Schemes for Ab initio Total-Energy Calculations Using a Plane-Wave Basis Set. *Phys. Rev. B*, 54:11169–11186, 1996.
- [52] <http://cms.mpi.univie.ac.at/vasp/>.
- [53] J. P. Perdew, J. A. Chevary, S. H. Vosko, K. A. Jackson, M. R. Pederson, D. J. Singh, and C. Fiolhais. Atoms, Molecules, Solids, and Surfaces: Applications of the Generalized Gradient Approximation for Exchange and Correlation. *Phys. Rev. B*, 46:6671–6687, 1992.
- [54] P. Pulay. Ab initio Calculation of Force Constants and Equilibrium Geometries in Polyatomic Molecules.I. Theory. *Mol. Phys.*, 17:197–204, 1969.
- [55] G. P. Francis and M. C. Payne. Finite Basis Set Corrections to Total Energy Pseudopotential Calculations. *J. Phys.: Condens. Matter*, 2:4395–4404, 1990.
- [56] S. Froyen and M. L. Cohen. Structural Properties of NaCl and KCl under Pressure. *J. Phys. C: Solid State Phys.*, 19:2623–2632, 1986.
- [57] D. R. Hamann, M. Schlüter, and C. Chiang. Norm-Conserving Pseudopotentials. *Phys. Rev. Lett.*, 43:1494–1497, 1979.
- [58] D. Vanderbilt. Soft Self-Consistent Pseudopotentials in a Generalized Eigenvalue Formalism. *Phys. Rev. B*, 41:7892–7895, 1990.
- [59] O. K. Andersen. Linear Methods in Band Theory. *Phys. Rev. B*, 12:3060–3083, 1975.
- [60] P. E. Blöchl. Projector Augmented-Wave Method. *Phys. Rev. B*, 50:17953–17979, 1994.

-
- [61] G. Kresse and D. Joubert. From Ultrasoft Pseudopotentials to the Projector Augmented-Wave Method. *Phys. Rev. B*, 59:1758–1775, 1999.
- [62] D. J. Singh. *Planewaves, Pseudopotentials and the LAPW Method*. Kluwer Academic, Norwell, MA, 1994.
- [63] M. Marsman and G. Kresse. Relaxed Core Projector-Augmented-Wave Method. *J. Chem. Phys.*, 125:104101, 2006.
- [64] H. J. Monkhorst and J. D. Pack. Special Points for Brillouin-Zone Integrations. *Phys. Rev. B*, 13:5188–5192, 1976.
- [65] M. Methfessel and A. T. Paxton. High-Precision Sampling for Brillouin-Zone Integration in Metals. *Phys. Rev. B*, 40:3616–3621, 1989.
- [66] J. Schoiswohl, M. Sock, S. Surnev, M. G. Ramsey, F. Netzer, G. Kresse, and J. N. Andersen. $V_2O_3(0001)$ Surface Terminations: from Oxygen- to Vanadium-Rich. *Surf. Sci.*, 555:101–117, 2004.
- [67] S. Surnev, G. Kresse, M. G. Ramsey, and F. P. Netzer. Novel Interface-Mediated Metastable Oxide Phases: Vanadium Oxides on Pd(111). *Phys. Rev. Lett.*, 87:086102, 2001.
- [68] G. Kresse, S. Surnev, M. G. Ramsey, and F. P. Netzer. First-Principles Calculations for V_xO_y Grown on Pd(111). *Surf. Sci.*, 492:329–344, 2001.
- [69] S. Surnev, M. G. Ramsey, and F. P. Netzer. Vanadium Oxide Surface Studies. *Prog. Surf. Sci.*, 73:117–165, 2003.
- [70] J. Schoiswohl, M. Sock, S. Eck, S. Surnev, M. G. Ramsey, F. P. Netzer, and G. Kresse. Atomic-Level Growth Study of Vanadium Oxide Nanostructures on Rh(111). *Phys. Rev. B*, 69:155403, 2004.
- [71] H. Niehus, R.-P. Blum, and D. Ahlbehrendt. Formation of Vanadium Oxide Films on $Cu_3Al(100)$. *Phys. Stat. Sol. (a)*, 187:151–159, 2001.
- [72] N. Magg, B. Immaraporn, J. B. Giorgi, T. Schroeder, M. Bäumer, J. Döbler, Z. Wu, E. Kondratenko, M. Cherian, M. Baerns, P. C. Stair, J. Sauer, and H.-J. Freund. Vibrational Spectra of Alumina- and Silica-Supported Vanadia Revisited: An Experimental and Theoretical Model Catalyst Study. *J. Catal.*, 226:88–100, 2004.
- [73] R. M. Jaeger, H. Kühlenbeck, H.-J. Freund, M. Wuttig, W. Hoffmann, R. Franchy, and H. Ibach. Formation of a Well-Ordered Aluminium Oxide Overlayer by Oxidation of NiAl(110). *Surf. Sci.*, 259:235–252, 1991.

-
- [74] M. Frank, K. Wolter, N. Magg, M. Heemeier, R. Kühnemuth, M. Bäumer, and H.-J. Freund. Phonons of Clean and Metal-Modified Oxide Films: An Infrared and HREELS Study. *Surf. Sci.*, 492:270–284, 2001.
- [75] M. Klimenkov, S. Nepijko, H. Kuhlenbeck, and H.-J. Freund. Transmission Electron Microscopic Investigation of an Ordered Al_2O_3 film on NiAl(110). *Surf. Sci.*, 385:66–76, 1997.
- [76] G. Ceballos, Z. Song, J. I. Pascual, H.-P. Rust, H. Conrad, M. Bäumer, and H.-J. Freund. Structure Investigation of the Topmost Layer of a Thin Ordered Alumina Film Grown on NiAl(110) by Low Temperature Scanning Tunneling Microscopy. *Chem. Phys. Lett.*, 359:41–47, 2002.
- [77] J. Libuda, F. Winkelmann, M. Bäumer, H.-J. Freund, Th. Bertrams, H. Neddermeyer, and K. Müller. Structure and Defects of an Ordered Alumina Film on NiAl(110). *Surf. Sci.*, 318:61–73, 1994.
- [78] M. Kulawik, N. Nilius, H.-P. Rust, and H.-J. Freund. Atomic Structure of Antiphase Domain Boundaries of a Thin Al_2O_3 Film on NiAl(110). *Phys. Rev. Lett.*, 91:256101, 2003.
- [79] A. Stierle, F. Renner, R. Streitl, H. Dosch, W. Drube, and B. C. Cowie. X-ray Diffraction Study of the Ultrathin Al_2O_3 Layer on NiAl(110). *Science*, 303:1652–1656, 2004.
- [80] G. Kresse, M. Schmid, E. Napetschnig, M. Shishkin, L. Köhler, and P. Varga. Structure of the Ultrathin Aluminum Oxide Film on NiAl(110). *Science*, 308:1440–1442, 2005.
- [81] M. Schmid, M. Shishkin, G. Kresse, E. Napetschnig, P. Varga, M. Kulawik, N. Nilius, H.-P. Rust, and H.-J. Freund. Oxygen-Deficient Line Defects in an Ultrathin Aluminum Oxide Film. *Phys. Rev. Lett.*, 97:046101, 2006.
- [82] C. Wolverton and K. C. Hass. Phase Stability and Structure of Spinel-Based Transition Aluminas. *Phys. Rev. B*, 63:024102, 2000.
- [83] G. Paglia, C. E. Buckley, A. L. Rohl, B. A. Hunter, R. D. Hart, J. V. Hanna, and L. T. Byrne. Tetragonal Structure Model for Boehmite-Derived γ -alumina. *Phys. Rev. B*, 68:144110, 2003.
- [84] G. Paglia, A. L. Rohl, C. E. Buckley, and J. D. Gale. Determination of the Structure of γ -alumina from Interatomic Potential and First-Principles Calculations: The Requirement of Significant Numbers of Nonspinel Positions to Achieve an Accurate Structural Model. *Phys. Rev. B*, 71:224115, 2005.
- [85] H. P. Pinto, R. M. Nieminen, and S. D. Elliott. Ab Initio Study of γ - Al_2O_3 Surfaces. *Phys. Rev. B*, 70:125402, 2004.

- [86] X. Krokidis, P. Raybaud, A.-E. Gobichon, B. Rebours, P. Euzen, and H. Toulhoat. Theoretical Study of the Dehydration Process of Boehmite to γ -alumina. *J. Phys. Chem. B*, 105:5121–5130, 2001.
- [87] T. K. Todorova, M. V. Ganduglia-Pirovano, and J. Sauer. Vanadium Oxides on Aluminum Oxide Supports. 1. Surface Termination and Reducibility of Vanadia Films on α -Al₂O₃(0001). *J. Phys. Chem. B*, 109:23523–23531, 2005.
- [88] T. K. Todorova, M. V. Ganduglia-Pirovano, and J. Sauer. Vanadium Oxides on Aluminum Oxide Supports. 3. Metastable κ -Al₂O₃(001) Compared to α -Al₂O₃(0001). *J. Phys. Chem. C*, 111:5141–5153, 2007.
- [89] A. Kirfel and K. Eichhorn. Accurate Structure Analysis with Synchrotron Radiation. The Electron Density in Al₂O₃ and Cu₂O. *Acta Cryst.*, A46:271–284, 1990.
- [90] F. D. Murnaghan. The Compressibility of Media under Extreme Pressures. *Proc. Nat. Acad. Sci.*, 30:244–247, 1944.
- [91] P. Guénard, G. Renaud, A. Barbier, and M. Gautier-Soyer. Determination of the α -Al₂O₃(0001) Surface Relaxation and Termination by Measurements of Crystal Truncation Rods. *Surf. Rev. Lett.*, 5:321–324, 1998.
- [92] J. Ahn and J. W. Rabalais. Composition and Structure of the Al₂O₃{0001}-(1 × 1) Surface. *Surf. Sci.*, 388:121–131, 1997.
- [93] G. Renaud. Oxide Surfaces and Metal/Oxide Interfaces Studied by Grazing Incidence X-ray Scattering. *Surf. Sci. Rep.*, 32:5–90, 1998.
- [94] P. W. Tasker. Stability of Ionic-Crystal Surfaces. *J. Phys. C*, 12:4977–4984, 1979.
- [95] M. Causà, R. Dovesi, C. Pisani, and C. Roetti. Ab Initio Characterization of the (0001) and (10 $\bar{1}$ 0) Crystal Faces of α -alumina. *Surf. Sci.*, 215:259–271, 1989.
- [96] T. J. Godin and J. P. LaFemina. Atomic and Electronic Structure of the Corundum (α -alumina)(0001) Surface. *Phys. Rev. B*, 49:7691, 1994.
- [97] C. Verdozzi, D. R. Jennison, P. A. Schultz, and M. P. Sears. Sapphire (0001) Surface, Clean and with d-Metal Overlayers. *Phys. Rev. Lett.*, 82:799, 1999.
- [98] X.-G. Wang, A. Chaka, and M. Scheffler. Effect of the Environment on α -Al₂O₃(0001) Surface Structures. *Phys. Rev. Lett.*, 84:3650, 2000.
- [99] C. Ruberto, Y. Yourdshadyan, and B. I. Lundqvist. Surface Properties of Metastable Alumina: A Comparative Study of κ - and α -Al₂O₃. *Phys. Rev. B*, 67:195412, 2003.

- [100] I. Manassidis, A. De Vita, and M. J. Gillan. Structure of the (0001) Surface of α -Al₂O₃ from First Principles Calculations. *Surf. Sci.*, 285:L517–L521, 1993.
- [101] D. J. Siegel, L. G. Jr. Hector, and J. B. Adams. Adhesion, Atomic Structure, and Bonding at the Al(111)/ α -Al₂O₃(0001) Interface: A First Principles Study. *Phys. Rev. B*, 65:085415, 2002.
- [102] V. Brázdová, M. V. Ganduglia-Pirovano, and J. Sauer. Periodic Density Functional Study on Structural and Vibrational Properties of Vanadium Oxide Aggregates. *Phys. Rev. B*, 69:165420, 2004.
- [103] D. B. McWhan, T. M. Rice, and J. P. Remeika. Mott Transition in Cr-Doped V₂O₃. *Phys. Rev. Lett.*, 23:1384–1387, 1969.
- [104] N. F. Mott. *Metal-Insulator Transitions*. Taylor and Francis, London, 2nd edition, 1990.
- [105] R. Enjalbert and J. Galy. A Refinement of the Structure of V₂O₅. *Acta Cryst. C*, 42:1467–1469, 1986.
- [106] P. D. Dernier. The Crystal Structure of V₂O₃ and (V_{0.962}Cr_{0.0382})₂O₃ near the Metal-Insulator Transition. *J. Phys. Chem. Solids*, 31:2569–2575, 1970.
- [107] G. Kresse, S. Surnev, J. Schoiswohl, and F. P. Netzer. V₂O₃(0001) Surface Terminations: A Density Functional Study. *Surf. Sci.*, 555:118–134, 2004.
- [108] I. Czekaj, K. Hermann, and M. Witko. Ab Initio Density Functional Theory Studies on Oxygen Stabilization at the V₂O₃(0001) Surface. *Surf. Sci.*, 545: 85–98, 2003.
- [109] V. Brázdová, M. V. Ganduglia-Pirovano, and J. Sauer. Vanadium Oxides on Aluminum Oxide Supports. 2. Structure, Vibrational Properties, and Reducibility of V₂O₅ Clusters on α -Al₂O₃(0001). *J. Phys. Chem. B*, 109:23532–23542, 2005.
- [110] G. Herzberg. *Molecular Spectra and Molecular Structure. I. Spectra of Diatomic Molecules*. Robert E. Krieger Publishing Co., Inc., Malabar, FL, 2nd edition, 1989.
- [111] J. P. Perdew, K. Burke, and M. Ernzerhof. Generalized Gradient Approximation Made Simple. *Phys. Rev. Lett.*, 77(18):3865–3868, 1996.
- [112] X.-G. Wang, A. Chaka, and M. Scheffler. Effect of the Environment on α -Al₂O₃(0001) Surface Structures. *Phys. Rev. Lett.*, 84:3650–3653, 2000.
- [113] K. Reuter and M. Scheffler. Composition, Structure, and Stability of RuO₂(110) as a Function of Oxygen Pressure. *Phys. Rev. B*, 65:035406, 2002.

- [114] W. Zhang, J. R. Smith, and X.-G. Wang. Thermodynamics from *ab initio* Computations. *Phys. Rev. B*, 70:024103, 2004.
- [115] D. R. Stull and H. Prophet, editors. *JANAF Thermochemical Tables*. U.S. National Bureau of Standards, Washington DC, 2nd edition, 1971.
- [116] P. J. Linstrom and W. G. Mallard, editors. *NIST Chemistry WebBook*. National Institute of Standards and Technology, Gaithersburg MD, 2001. URL <http://webbook.nist.gov>.
- [117] D. D. Wagman, W. H. Evans, V. B. Parker, R. H. Schumm, I. Halow, S. M. Bailey, K. L. Churney, and R. L. Nuttall. The NBS Tables of Chemical Thermodynamic Properties. *J. Phys. Chem. Ref. Data*, 11:Supplement 2, 1982.
- [118] W. Brückner, H. Oppermann, W. Reichelt, J. I. Terukow, F. A. Tschudnowski, and E. Wolf, editors. *Vanadiumoxide Darstellung, Eigenschaften, Anwendung*. Akademie-Verlag, Berlin, 1983.
- [119] M. V. Ganduglia-Pirovano and J. Sauer. Stability of Reduced $V_2O_5(001)$ Surfaces. *Phys. Rev. B*, 70:045422, 2004.
- [120] K. Chen, A. Khodakov, J. Yang, A. T. Bell, and E. Iglesia. Isotopic Tracer and Kinetic Studies of Oxidative Dehydrogenation Pathways on Vanadium Oxide Catalysts. *J. Catal.*, 186:325–333, 1999.
- [121] K. Chen, E. Iglesia, and A. T. Bell. Kinetic Isotopic Effects in Oxidative Dehydrogenation of Propane on Vanadium Oxide Catalysts. *J. Catal.*, 192:197–203, 2000.
- [122] J. C. Slater. *In Quantum Theory of Molecules and Solids*. McGraw-Hill, New York, 1974.
- [123] J. F. Janak. Proof that $\partial E/\partial n_i = \varepsilon$ in Density-Functional Theory. *Phys. Rev. B*, 18:7165–7168, 1978.
- [124] P. Liu and J. Skogsmo. Space-Group Determination and Structure Model for κ - Al_2O_3 by Convergent-Beam Electron Diffraction (CBED). *Acta Cryst.*, B47:425–433, 1991.
- [125] H.-L. Gross and W. Mader. On the Crystal Structure of κ -alumina. *Chem. Commun.*, 1:55–56, 1997.
- [126] B. Ollivier, R. Retoux, P. Lacorre, D. Massiot, and G. Férey. Crystal Structure of κ -alumina: an X-ray Powder Diffraction, TEM and NMR Study. *J. Mater. Chem.*, 7:1049, 1997.

- [127] C. Ruberto, Y. Yourdshadyan, and B. I. Lundqvist. Stability of a Flexible Polar Ionic Crystal Surface: Metastable Alumina and One-Dimensional Surface Metallicity. *Phys. Rev. Lett.*, 88:226101, 2002.
- [128] M. Halvarsson and S. Vuorinen. The Influence of the Nucleation Surface on the Growth of CVD κ -Al₂O₃ and α -Al₂O₃. *Surf. Coat. Technol.*, 76-77:287–296, 1995.
- [129] P. Hyldgaard, N. Jacobson, C. Ruberto, B. Razaznejad, and B. I. Lundqvist. One-Dimensional Electron Systems for Anchoring Growth of Carbon Nanostructures. *Comput. Mater. Sci.*, 33:356–361, 2005.
- [130] S. F. Vyboishchikov and J. Sauer. Gas-phase Vanadium Oxide Anions: Structure and Detachment Energies from Density Functional Calculations. *J. Phys. Chem. A*, 104:10913–10922, 2000.
- [131] M. Calatayud, B. Mguig, and C. Minot. A Periodic Model for the V₂O₅–TiO₂ (anatase) Catalyst. Stability of Dimeric Species. *Surf. Sci.*, 526:297–308, 2003.
- [132] M. Pykavy, C. van Wüllen, and J. Sauer. Electronic Ground States of the V₂O₄^{+0/-} Species from Multireference Correlation and Density Functional Studies. *J. Phys. Chem. A*, 120:4207–4215, 2004.
- [133] M. V. Ganduglia-Pirovano and J. Sauer. Reduction of the (001) Surface of γ -V₂O₅ Compared to α -V₂O₅. *J. Phys. Chem. B*, 109:374–380, 2005.
- [134] M. D. Argyle, K. Chen, A. T. Bell, and E. Iglesia. Effect of Catalyst Structure on Oxidative Dehydrogenation of Ethane and Propane on Alumina-Supported Vanadia. *J. Catal.*, 208:139–149, 2002.
- [135] V. Brázdová, M. V. Ganduglia-Pirovano, and J. Sauer. Vanadia Aggregates on an Ultrathin Aluminum Oxide Film on NiAl(110), 2007. in preparation.
- [136] V. Brázdová, M. V. Ganduglia-Pirovano, and J. Sauer. Crystal Structure and Vibrational Spectra of AlVO₄. A DFT Study. *J. Phys. Chem. B*, 109:394–400, 2005.
- [137] T. R. Gilson, O. F. Bizri, and N. Cheetham. Single-crystal Raman and Infrared Spectra of Vanadium(V) Oxide. *J. Chem. Soc. Dalton Trans.*, 3:291–294, 1973.
- [138] J.-W. He, X. Xu, J. S. Corneille, and D. W. Goodman. X-ray Photoelectron Spectroscopic Characterization of Ultra-Thin Silicon Dioxide Films on a Mo(100) Surface. *Surf. Sci.*, 279:119–126, 1992.
- [139] X. Xu and D. W. Goodman. The Preparation and Characterization of Ultra-Thin Silicon Dioxide Films on a Mo(110) Surface. *Surf. Sci.*, 282:323–332, 1993.

-
- [140] T. Schroeder, M. Adelt, B. Richter, M. Naschitzki, M. Bäumer, and H.-J. Freund. Growth of Well-Ordered Silicon Dioxide Films on Mo(112). *Microelectr. Rel.*, 40:841–844, 2000.
- [141] T. Schroeder, A. Hammoudeh, M. Pykavy, N. Magg, M. Adelt, M. Bäumer, and H.-J. Freund. Single Crystalline Silicon Dioxide Films on Mo(112). *Solid State Electron.*, 45:1471–1478, 2001.
- [142] B. K. Min, A. K. Santra, and D. W. Goodman. Understanding Silica-Supported Metal Catalysts: Pd/silica as a Case Study. *Catal. Today*, 85: 113–124, 2003.
- [143] B. K. Min, W. T. Wallace, A. K. Santra, and D. W. Goodman. Role of Defects in the Nucleation and Growth of Au Nanoclusters on SiO₂ Thin Films. *J. Phys. Chem. B*, 108:16339–16343, 2004.
- [144] B. K. Min, W. T. Wallace, and D. W. Goodman. Synthesis of a Sinter-Resistant, Mixed-Oxide Support for Au Nanoclusters. *J. Phys. Chem. B*, 108: 14609–14615, 2004.
- [145] S. Wendt, M. Frerichs, T. Wei, M. S. Chen, V. Kempter, and D. W. Goodman. The Interaction of Water with Silica Thin Films Grown on Mo(112). *Surf. Sci.*, 565:107–120, 2004.
- [146] F. Liebau. *Structural Chemistry of Silica*. Springer-Verlag, Berlin, 1985.
- [147] S. Kaya, M. Baron, D. Stacchiola, J. Weissenrieder, S. Shaikhutdinov, T. K. Todorova, M. Sierka, J. Sauer, and H.-J. Freund. On the Geometrical and Electronic Structure of an Ultrathin Crystalline Silica Film Grown on Mo(112). *Surf. Sci.*, 2007.
- [148] L. Giordano, G. Ricci, D. Pacchioni, and P. Ugliengo. Structure and Vibrational Spectra of Crystalline SiO₂ Ultrathin Films on Mo(112). *Surf. Sci.*, 584: 225–236, 2005.
- [149] M. S. Chen and D. W. Goodman. The Structure of Monolayer SiO₂ on Mo(112): A 2-D [Si–O–Si] Network or Isolated [SiO₄] Units? *Surf. Sci.*, 600:L255–L259, 2006.
- [150] A. P. Scott and L. Radom. Harmonic Vibrational Frequencies: An Evaluation of Hartree-Fock, Møller-Plesset, Quadratic Configuration Interaction, Density Functional Theory, and Semiempirical Scale Factors. *J. Phys. Chem.*, 100: 16502–16513, 1996.
- [151] J. F. Scott and S. P. S. Porto. Longitudinal and Transverse Optical Lattice Vibrations in Quartz. *Phys. Rev.*, 161:903–910, 1967.

-
- [152] R. K. Sato and P. F. McMillan. An Infrared and Raman Study of the Isotopic Species of α -Quartz. *J. Phys. Chem.*, 91:3494–3498, 1987.
- [153] I. N. Yakovkin. Favorable Silica Monolayer Structures on the Mo(112) Surface. *Surf. Rev. Lett.*, 12:449–456, 2005.
- [154] L. Giordano, D. Ricci, G. Pacchioni, and P. Ugliengo. Structure and Vibrational Spectra of Crystalline SiO₂ Ultra-Thin Films on Mo(112). *Surf. Sci.*, 584:225–236, 2005.
- [155] F. M. Hoffmann. Infrared Reflection-Absorption Spectroscopy of Adsorbed Molecules. *Surf. Sci. Rep.*, 3:107–192, 1983.
- [156] N. Sheppard and J. Erkelens. Vibrational-Spectra of Species Adsorbed on Surfaces-Forms of Vibrations and Selection Rules for Regular Arrays of Adsorbed Species. *Appl. Spectroscopy*, 38:471–485, 1984.
- [157] A. M. Bradshaw and N. V. Richardson. Symmetry, Selection Rules and Nomenclature in Surface Spectroscopies. *Pure and Appl. Chem.*, 68:457–467, 1996.
- [158] M. S. Chen and D. W. Goodman. Reply to Comment on “The Structure of Monolayer SiO₂ on Mo(112): A 2-D [Si–O–Si] Network or Isolated [SiO₄] Units?”. *Surf. Sci.*, 601:591–593, 2007.
- [159] J. Tersoff and D. R. Hamann. Theory of the Scanning Tunneling Microscope. *Phys. Rev. B*, 31:805–813, 1985.
- [160] G.-M. Rignanese, A. De Vita, J.-C. Charlier, X. Gonze, and R. Car. First-Principles Molecular-Dynamics Study of the (0001) α -Quartz Surface. *Phys. Rev. B*, 61:13250–13255, 2000.
- [161] J. Bernhardt, J. Schardt, U. Starke, and K. Heinz. Epitaxial Ideal Oxide-Semiconductor Interface: Silicate Adlayers on Hexagonal (0001) and (000 $\bar{1}$) SiC Surfaces. *Appl. Phys. Lett.*, 74:1084–1086, 1999.
- [162] G. Sposito. *The Surface Chemistry of Soils*. Oxford Univ. Press., New York, 1984.
- [163] C. Freysoldt, P. Rinke, and M. Scheffler. , 2007. submitted.
- [164] T. Schroeder, J. B. Giorgi, A. Hammoudeh, N. Magg, M. Bäumer, and H.-J. Freund. Oxygen-Induced $p(2 \times 3)$ Reconstruction on Mo(112) Studied by LEED and STM. *Phys. Rev. B*, 65:115411, 2002.
- [165] L. Giordano, A. Del Vitto, and G. Pacchioni. Au and Pd Atoms Adsorbed on Pure and Ti-Doped SiO₂/Mo(112) Films. *J. Chem. Phys.*, 124:034701, 2006.

- [166] M.-C. Wu and D. W. Goodman. Particulate Cu on Ordered Al₂O₃: Reactions with Nitric Oxide and Carbon Monoxide. *J. Phys. Chem.*, 98:9874–9881, 1994.
- [167] M. S. Chen, W. T. Wallace, D. Kumar, Z. Yan, K. K. Gath, Y. Cai, Y. Kuroda, and D. W. Goodman. Synthesis of Well-Ordered Ultra-Thin Titanium Oxide Films on Mo(112). *Surf. Sci.*, 581:L115–L121, 2005.
- [168] M.-C. Wu, J. S. Corneille, C. A. Estrada, J.-W. He, and D. W. Goodman. Synthesis and Characterization of Ultra-Thin MgO Films on Mo(100). *Chem. Phys. Lett.*, 182:472–478, 1991.
- [169] T. McAvoy, J. Zhang, C. Waldfried, D. N. McIlroy, P. A. Dowben, O. Zeybek, T. Bertrams, and S. D. Barrett. The Interplay between the Surface Band Structure and Possible Surface Reconstructions of Mo(112). *Eur. Phys. J. B*, 14:747–755, 2000.
- [170] T. Sasaki, Y. Goto, R. Tero, K. Fukui, and Y. Iwasawa. Oxygen Adsorption States on Mo(112) Surface Studied by HREELS. *Surf. Sci.*, 502-503:136–143, 2002.
- [171] A. Kiejna and R. M. Nieminen. Density-Functional Study of Oxygen Adsorption on Mo(112). *J. Chem. Phys.*, 122:044712, 2005.
- [172] F. C. Chuang, C. V. Ciobanu, V. B. Shenoy, C. Z. Wang, and K. M. Ho. Finding the Reconstructions of Semiconductor Surfaces via a Genetic Algorithm. *Surf. Sci.*, 573:L375–L381, 2004.
- [173] F. C. Chuang, C. V. Ciobanu, C. Predescu, C. Z. Wang, and K. M. Ho. Structure of Si(114) Determined by Global Optimization Methods. *Surf. Sci.*, 578:183–195, 2005.
- [174] C. V. Ciobanu and C. Predescu. Reconstruction of Silicon Surfaces: A Stochastic Optimization Problem. *Phys. Rev. B*, 70:085321, 2004.
- [175] D. E. Goldberg. *Genetic Algorithms in Search, Optimization and Machine Learning*. Addison-Wesley, Boston, 2005.
- [176] J. Kröger, S. Lehwald, and H. Ibach. EELS Study of the Clean and Hydrogen-Covered Mo(110) Surface. *Phys. Rev. B*, 55:10895–10904, 1997.
- [177] P. K. Stefanov and T. S. Marinova. HREELS Study of the Interaction of Oxygen with a Mo(111) Surface. *Surf. Sci.*, 200:26–34, 1988.
- [178] K. T. Queeney and C. M. Friend. The Role of Oxygen Vacancies in Methanol Reaction on Oxidized Mo(110). *J. Phys. Chem. B*, 102:5178–5181, 1998.

-
- [179] R. Srivastava and L. L. Chase. Raman Spectra of CrO_2 and MoO_2 Single Crystals. *Solid State Comm.*, 11:349–353, 1972.
- [180] S. Kaya, Y.-N. Sun, J. Weissenrieder, D. Stacchiola, S. Shaikhutdinov, and H.-J. Freund. Ice-Assisted Preparation of Silica-Supported Vanadium Oxide Particles. *J. Phys. Chem. C*, 111:5337–5344, 2007.
- [181] S. Guimond, M. Abu Haija, S. Kaya, J. Lu, J. Weissenrieder, S. Shaikhutdinov, H. Kuhlenbeck, H.-J. Freund, J. Döbler, and J. Sauer. Vanadium Oxide Surfaces and Supported Vanadium Oxide Nanoparticles. *Top. Catal.*, 38:117–125, 2006.
- [182] J. Döbler, M. Pritzsche, and J. Sauer. Vibrations of Silica Supported Vanadia: A Comparison of Cluster and Embedded Cluster Calculations, 2007. in preparation.
- [183] S. F. Vyboishchikov and J. Sauer. $(\text{V}_2\text{O}_5)_n$ Gas-Phase Clusters ($n = 1-12$) Compared to V_2O_5 Crystal: DFT Calculations. *J. Phys. Chem. A*, 105:8588–8598, 2001.
- [184] M. Kanzaki, J. F. Stebbins, and X. Xue. Characterization of Quenched High Pressure Phases in CaSiO_3 System by XRD and ^{29}Si NMR. *Geophys. Res. Lett.*, 18:463–466, 1991.
- [185] R. J. Angel, N. L. Ross, F. Seifert, and T. F. Fliervoet. Structural Characterization of Ppentacoordinate Silicon in a Calcium Silicate. *Nature*, 384:441–444, 1996.
- [186] J. F. Stebbins and P. McMillan. Five- and Six-Coordinated Si in $\text{K}_2\text{Si}_4\text{O}_9$ Glass Quenched from 1.9 GPa and 1200°C . *Am. Mineral.*, 74:965–968, 1989.
- [187] J. W. Turley and F. P. Boer. Structural Studies of Pentacoordinate Silicon. I. Phenyl-(2,2',2''-Nitrilotriethoxy) Silane. *J. Am. Chem. Soc.*, 90:4026–4030, 1968.
- [188] R. Tacke, C. Burschka, I. Richter, B. Wagner, and R. Willeke. Pentacoordinate Silicon Compounds with SiO_5 Skeletons Containing SiOH or SiOSi Groups: Derivatives of the Pentahydroxosilicate(1-) Anion $[\text{Si}(\text{OH})_5]^-$ and its Anhydride $[(\text{HO})_4\text{Si}-\text{O}-\text{Si}(\text{OH})_4]^{2-}$. *J. Am. Chem. Soc.*, 122:8480–8485, 2000.

Selbständigkeitserklärung

Hiermit erkläre ich, die vorliegende Arbeit selbständig verfasst und nur die aufgeführte Literatur sowie die angegebenen Hilfsmittel verwendet zu haben.

Berlin, den 30. Mai 2007

Acknowledgments

First, I would like to express my sincere gratitude to Prof. Joachim Sauer for giving me the opportunity to work in his group and for his continuous support.

I am most grateful to my supervisors, Dr. Maria Veronica Ganduglia-Pirovano and Dr. Marek Sierka, for their great guidance and huge enthusiasm. Their experience was invaluable for the successful development of the present work.

I would like also to acknowledge the collaborators with whom I had the pleasure to work – Sarp Kaya, Dr. Jonas Weissenrieder, Dr. Dario Stacchiola, Dr. Shamil Shaikhutdinov, Dr. Helmut Kuhlenbeck, and Prof. Hans-Joachim Freund.

Fonds der Chemischen Industrie (04/2003 – 03/2005) as well as the International Max Planck Research School “Complex Surfaces in Materials Science” (04/2005 – 09/2007) provided the financial support, for which I am very grateful.

I thank Thomas Dargel for the invaluable technical assistance and the Norddeutscher Verbund für Hoch- und Höchstleistungsrechnen for the computing time.

I am much indebted to Silvana Pophal for always being helpful with any administrative concerns.

I also express my gratitude to Dr. Jens Döbler, Dr. Alexander Hofmann, Dr. Xavier Rosanska, Dr. Veronika Brázdová, Dr. Remy Fortrie, Dr. Gernot Katzer, Dr. Christian Tuma, and Dr. Laurence Gregoriades for many fruitful discussions and advises. Jens, you are the best office mate and I thank you for the fun and fascinating countless discussions, which sometimes extended beyond the field of science!

Special thanks go to Torsten Kerber for providing the vital “German language support” which I sometimes desperately needed as well as to Asbjörn Burow for translating the Abstract into German.

It is a pleasure to acknowledge all my colleagues from the “Arbeitsgruppe Quantenchemie” as well as the IMPRS students who really made me enjoy my stay here.

My deepest gratitude goes to my family, who unconditionally stood behind me in all my endeavors and to the most special person in my life, Deyan, for always being there for me, for his love and support.

Lebenslauf

Tanya Kumanova Todorova
geboren am 29. Januar 1980 in Bulgarien

Schulbildung

1986 – 1993
1993 – 1997
05/1997

Grundschule “Kliment Ohridski”, Byala Slatina, Bulgarien
Gymnasium “Vasil Levski”, Byala Slatina, Bulgarien
Abitur

Hochschulbildung

1997 – 2002
07/2002

Studium der Chemie (Magister) an der Sofia Universität
“St. Kliment Ohridski”, Sofia, Bulgarien
Diplomarbeit unter Betreuung von Prof. Nikolai Tyutyulkov
und Assoc. Prof. Alia Tadjer
Abschluß als Magister-Chemikerin

Promotion

seit 01/2003

Promotion an der Humboldt-Universität zu Berlin in der
Arbeitsgruppe Quantenchemie unter Betreuung von Herrn
Prof. Joachim Sauer
Titel der Dissertation: *Periodic Density Functional Study
on Supported Vanadium Oxides*

04/2003 – 03/2005 Kekulé-Stipendium des Fonds der Chemischen Industrie

04/2005 – 09/2007 Stipendiantin der International Max Planck Research School
“Complex Surfaces in Materials Science”

Publications

1. *Vanadium Oxides on Aluminum Oxide Support. 1. Surface Termination and Reducibility of Vanadia Films on α - $Al_2O_3(0001)$.*
T. K. Todorova, M. V. Ganduglia-Pirovano, and J. Sauer, J. Phys. Chem. B 109, 23523 (2005).
2. *Low Temperature Adsorption of Oxygen on Reduced $V_2O_3(0001)$ Surfaces.*
M. Abu Haija, S. Guimond, Y. Romanyshyn, A. Uhl, H. Kuhlenbeck, **T. K. Todorova**, M. V. Ganduglia-Pirovano, J. Döbler, J. Sauer, and H.-J. Freund, Surf. Sci. 600, 1497 (2006).
3. *Atomic Structure of a Thin Silica Film on a $Mo(112)$ Substrate: A Two-Dimensional Network of SiO_4 Tetrahedra.*
J. Weissenrieder, S. Kaya, J.-L. Lu, H.-J. Gao, S. Shaikhutdinov, H.-J. Freund, M. Sierka, **T. K. Todorova**, and J. Sauer, Phys. Rev. Lett. 95, 076103 (2005).
4. *Atomic Structure of a Thin Silica Film on a $Mo(112)$ Substrate: A Combined Experimental and Theoretical Study.*
T. K. Todorova, M. Sierka, J. Sauer, S. Kaya, J. Weissenrieder, J.-L. Lu, H.-J. Gao, S. Shaikhutdinov, and H.-J. Freund, Phys. Rev. B 73, 165414 (2006).
5. *Formation of One-Dimensional Crystalline Silica on a Metal Substrate.*
J.-L. Lu, S. Kaya, J. Weissenrieder, **T. K. Todorova**, M. Sierka, J. Sauer, H.-J. Gao, S. Shaikhutdinov, and H.-J. Freund, Surf. Sci. Lett. 600, L164 (2006).
6. *Interplay Between Theory and Experiment in the Quest for Silica with Reduced Dimensionality Grown on a $Mo(112)$ Surface.*
M. Sierka, **T. K. Todorova**, S. Kaya, D. Stacchiola, J. Weissenrieder, J.-L. Lu, H.-J. Gao, S. Shaikhutdinov, H.-J. Freund, and J. Sauer, Chem. Phys. Lett. 424, 115 (2006).
7. *Synthesis and Structure of Ultrathin Aluminosilicate Films.*
D. Stacchiola, S. Kaya, J. Weissenrieder, H. Kuhlenbeck, S. Shaikhutdinov,

- H.-J. Freund, M. Sierka, **T. K. Todorova**, and J. Sauer, *Angew. Chem. Int. Ed.* 45, 7636 (2006); *Angew. Chem.* 118, 7798 (2006).
8. *Vanadium Oxides on Aluminum Oxide Supports. 3. Metastable κ -Al₂O₃(001) Compared to α -Al₂O₃(0001).*
T. K. Todorova, M. V. Ganduglia-Pirovano, and J. Sauer, *J. Phys. Chem. C* 111, 5141 (2007).
9. *Oxygen Adsorption on Mo(112) Surface Studied by Ab Initio Genetic Algorithm and Experiment.*
M. Sierka, **T. K. Todorova**, J. Sauer, S. Kaya, D. Stacchiola, J. Weissenrieder, S. Shaikhutdinov, and H.-J. Freund, *J. Chem. Phys.* 126, 234710 (2007).
10. *On the Geometrical and Electronic Structure of an Ultrathin Crystalline Silica Film Grown on Mo(112).*
S. Kaya, M. Baron, D. Stacchiola, J. Weissenrieder, S. Shaikhutdinov, **T. K. Todorova**, M. Sierka, J. Sauer, and H.-J. Freund, *Surf. Sci.* (in press).
11. *Vanadium Oxides Supported on a Thin Silica Film Grown on Mo(112): Insights from DFT.*
T. K. Todorova, J. Döbler, M. Sierka, and J. Sauer, in preparation.